UNIVERSIDAD AUTONOMA DE MADRID

Facultad de Ciencias
Departamento de Física Teórica

Precise determinations of the strong coupling constant at HERA

Submitted in partial fullfilment of the requirements
for the degree "Doctor en Ciencias Físicas" by

Oscar González López

Director: Juan Terrón Cuadrado

20/03/2002

UNIVERSIDAD AUTONOMA DE MADRID

Facultad de Ciencias
Departamento de Física Teórica

Medidas de precisión de la constante de acoplamiento fuerte en HERA

Memoria presentada para la obtención del
título de Doctor en Ciencias Físicas por

Oscar González López

Director: Juan Terrón Cuadrado

20/03/2002

This work has been carried out in the frame of the ZEUS Collaboration
through the High Energy Physics group of the Universidad Autónoma de Madrid (Spain).

The author was financially supported by the "Ministerio de Educación, Cultura y Deporte."

Este trabajo ha sido desarrollado en la Colaboración ZEUS
a través del grupo de Altas Energías de la Universidad Autónoma de Madrid

El autor ha sido financiado por el Ministerio de Educación, Cultura y Deporte.

A mis padres

que me enseñaron el aprecio
por las ciencias naturales
sin el cual esta tesis
nunca se habría realizado.

La rutina que desdeña a la ciencia muestra con semejante desdén un orgullo necio, hijo de la ignorancia (...).
Verdad es que hay en las ciencias una parte meramente especulativa y que difícilmente puede conducir a resultados prácticos; sin embargo, es preciso no olvidar que aun esta parte, al parecer inútil y como si dijéramos de mero lujo, se liga muchas veces con otras que tiene inmediata relación con las artes. Por manera que su inutilidad es sólo aparente, pues andando el tiempo se descubren consecuencias en que no se había reparado. La historia de las ciencias naturales y exactas nos ofrece abundantes pruebas de esta verdad.

JAIME BALMES [1]

Introduction

Jet production in neutral current deep inelastic ep scattering at high Q^2 (being Q^2 the virtuality of the exchanged boson) provides a testing ground of the theory of the strong interactions. In the analyses presented in this thesis, jet production has been studied in two different ways. In the first analysis, the study was done on the measurements of the inclusive jet cross sections in the Breit frame, which are directly related to those interactions.

In the second analysis, the strong interaction is studied by means of the internal structure of the jets produced in high-energy processes, which gives direct insight into the transition from the partons taking part in the hard scattering to the hadrons that are observed in the detectors.

Thus, measurements of the jet internal structure provide very stringent tests on the predictions given by the theory and the phenomenological approaches used to describe the processes that drive this transition.

For both analyses, the events are selected in the deep inelastic scattering regime, and the results are presented, in the first case, in terms of cross secions for inclusive jet production, whilst in the second, in terms of the mean subjet multiplicity, which has become the standard variable for the studies of the internal structure of jets.

The measurements are corrected for detector effects and compared with the theoretical predictions in the frame of the Standard Model, namely with the predictions of Quantum Chromodynamics (QCD). After the comparison is made, a QCD analysis is performed and values of the strong coupling constant are extracted from both analyses. This constant is one of the fundamental parameters of the theory to describe the strong interaction and, hence, of the Standard Model. The determinations of this coupling constant presented here provide a new contribution to the world average value, which still presents a relatively large uncertainty. This is especially true for the determination from the inclusive jet cross sections in the Breit frame, for which a very precise value of the strong coupling contant is extracted.

Regarding the second analysis, although the uncertainty of the extracted value is not so precise, its uncertainty is still comparable to most of the determination of this constant. It is especially remarkable that it is the first time that this determination is done by using the internal structure of jets at HERA,

The structure of this document is as follows. After describing the theoretical concepts related to the subject in chapter 1, the experimental infrastructure is described in chapter 2. In chapter 3, the main aspects of physics simulation, phenomenological models and generation of simulated events are introduced. The complete description of the analyses is presented in chapter 4. This chapter contains the results of the experimental analyses, which are discussed and compared with theory in chapter 5. In this chapter, the comparison between the measurements and the theory is used to extract the value of the strong coupling constant α_s. Finally, chapter 6 is devoted to the last remarks and a brief summary.

The results related to the measurement of the mean subjet multiplicity have been presented by the author in the DIS'2001 conference in Bologna, April 2001 [2]. Furthermore, they have been published by ZEUS as a contributed paper to the International Europhysics Conference on High Energy Physics, Budapest, Hungary (July, 2001) [3]. Those results related to the inclusive jet cross sections in the Breit frame have been published by ZEUS as a contributed paper to the same conference [4], and previously as a contributed paper to the International Conference on High Energy Physics, Osaka, Japan (August, 2000)[5].

Introducción

La producción de chorros colimados de hadrones ("jets") en procesos de dispersión profundamente inelástica ep para valores grandes de la virtualidad del bosón intercambiado es una fuente valiosa para verificar la validez de la teoría que describe las interacciones fuertes. En los análisis presentados en esta tesis, la producción de jets ha sido estudiada de dos maneras diferentes. En el primero de ellos, se realizaron las medidas de las secciones eficaces de producción inclusiva de jets en el sistema de referencia de Breit, las cuales están relacionadas de forma directa con procesos mediados por la interacción fuerte.

En el segundo análisis, se estudia la interacción fuerte a partir de las medidas de la estructura interna de los jets producidos en procesos de energías grandes. El estudio de esta estructura interna proporciona de forma directa información sobre los procesos que transforman los partones que participan en la interacción dura, y los hadrones que son observados en los detectores.

De esta forma, las medidas de la estructura interna de los jets proporcionan pruebas adicionales y muy exigentes para verificar la validez de la teoría y las diferentes aproximaciones fenomenológicas utilizadas para simular esos procesos.

En ambos análisis, los sucesos se seleccionan en el régimen de dispersión profundamente inelástica, y los resultados se presentan, para el primer análisis con la medida de las secciones eficaces de producción de jets en el sistema de referencia de Breit. Para el segundo las medidas se realizan sobre la multiplicidad media de subjets, que es un observable muy utilizado cuando la estructura interna de los jets se caracteriza por medio de subjets.

Las medidas realizadas han sido corregidas por efectos del detector y son comparadas con las predicciones teóricas obtenidas a partir del Modelo Estándar, concretamente con cálculos realizados en el contexto de la Cromodinámica Cuántica. Después de realizar la comparación para cada análisis, la misma es utilizada para realizar la medida de la constante de acoplamiento fuerte, α_s. Este es uno de los parámetros fundamentales de la teoría para describir la interacción fuerte, y por lo tanto del Modelo Estándar. Las medidas de esta constante realizadas son contribuciones adicionales a las realizadas previamente en muy diferentes procesos y que se resumen en el valor promedio mundial, que aún presenta una incertidumbre relativamente grande. Por ello, estas contribuciones son de gran importancia, en especial la medida obtenida a partir de la secciones eficaces de producción de jets en el sistema de referencia de Breit, donde el valor presenta unas incertidumbres mucho menores que las que se tienen en otras medidas.

Respecto al segundo de los análisis, la medida de α_s no es tan precisa como la anterior, pero aún así, su error es comparable a la mayoría de las medidas de esta constante. Además, hay que destacar que ésta es la primera vez que la constante de acoplamiento fuerte se mide a partir de la estructura interna de los jets producidos en los procesos de dispersión de HERA.

Este documento está estructurado de la siguiente manera: en el capítulo 1 se describen los conceptos teóricos. Posteriormente se da una descripción completa de los dispositivos experimentales utilizados para las diferentes medidas (capítulo 2). En el capítulo 3 se da una descripción de las técnicas utilizadas para la simulación de sucesos y de correcciones basadas en modelos fenomenológicos. Los análisis en sí se describen en el capítulo 4, y posteriormente, en el siguiente capítulo se presentan tanto la discusión de los resultados como la comparación con las predicciones teóricas. Finalmente, en el capítulo 6 se da un breve resumen y unos comentarios finales. Hay que mencionar que en el apéndice B se da un resumen de toda la tesis en castellano siguiéndose una estructura similar.

Los resultados obtenidos en relación con el análisis de la multiplicidad media de subjets fueron presentados por el autor en la conferencia "DIS'2001 Workshop" celebrado en Bolonia, en abril de 2001 [2]. Además dichos resultados han sido publicados por la Colaboración ZEUS como una contribución a la conferencia "International Europhysics Conference on High Energy Physics", celebrada en Budapest (Hungría) en julio de 2001 [3]. Los resultados del análisis de la sección eficaz inclusiva de jets en el sistema de referencia de Breit fueron publicados por la Colaboración ZEUS como una contribución a la misma conferencia [4], y anterioremente como una contribución a la conferencia "International Conference on High Energy Physics", celebrada en Osaka (Japón) en agosto de 2000.

Contents

1 Theoretical introduction **1**

1.1 The Standard Model of particle interactions . . . 1

1.1.1 The internal structure of atoms . . . 1

1.1.2 The electromagnetic interaction and QED . . . 2

1.1.3 The strong and weak interactions . . . 3

1.1.4 Hadron spectroscopy and the Quark-Parton Model . . . 4

1.1.5 Quantum Chromodynamics . . . 7

1.1.6 The electroweak unification . . . 8

1.1.7 Summary: the Standard Model and beyond . . . 11

1.2 Deep Inelastic Processes . . . 13

1.2.1 DIS processes . . . 14

1.2.2 The Quark-Parton Model and Bjorken scaling . . . 16

1.2.3 DIS and Quantum Chromodynamics . . . 18

1.2.4 The Breit or brick-wall frame . . . 22

1.3 The perturbative QCD framework . . . 24

1.3.1 The perturbative QCD approach . . . 24

1.3.2 Renormalisation . . . 25

1.3.3 Factorisation . . . 26

1.3.4 Evolution equations . . . 27

1.3.5 Modern parametrisations of parton densities . . . 31

1.4 Jet physics . . . 32

1.4.1 Jet algorithms . . . 33

1.4.2 Jet production in the Breit frame . . . 38

1.4.3 The azimuthal asymmetry . . . 39

1.4.4 Determination of α_s from jet production in the Breit frame . . . 41

1.4.5 The internal structure of jets . . . 41

1.4.6 Quark- and gluon-initiated jets . . . 44

1.4.7 Determination of α_s from the internal structure of jets . . . 44

2 Experimental setup **47**

2.1 The HERA collider . . . 47

2.2 The ZEUS detector . . . 49

2.2.1 The Central Tracking Detector (CTD) . . . 53

2.2.2 The Uranium-Scintillator Calorimeter (UCAL) . . . 54

2.2.3 The Backing Calorimeter and the Muon Chambers . . . 61

2.2.4 Luminosity measurement . . . 61

2.2.5 Other components . . . 63

2.2.6 Trigger and Data Acquisition Systems . . . 64

2.2.7 Offline and detector simulation . . . 65

2.3 Reconstruction of the kinematic variables . . . 66

2.3.1 Reconstruction using the scattered electron variables . . . 66

2.3.2 Reconstruction using the hadronic system . . . 67

2.3.3 Reconstruction from mixed variables . . . 68

3 Event simulation **71**

3.1 Global description . . . 71

3.2 Multipartonic production . . . 73

3.2.1 The Parton Shower approach . . . 73

3.2.2 The Colour Dipole Model . . . 75

3.3 Hadronisation models . . . 76

3.3.1 The independent fragmentation model . . . 76

3.3.2 The string model . . . 77

3.3.3 The cluster fragmentation model . . . 78

3.4 Event generators for neutral current DIS . . . 78

4 Description of the analyses **81**

4.1 Event selection . . . 81

4.1.1 Identification of the scattered positron . . . 81

4.1.2 Selection of the neutral current DIS event sample . . . 83

4.1.3 Final selection of the jets in the laboratory frame . . . 89

4.1.4 Final selection of the jets in the Breit frame . . . 90

4.1.5 Event selection at the hadron level in the MC samples . . . 92

4.1.6 Jet energy corrections . . . 93

4.2 Analysis I: Measurement of the inclusive jet cross sections... 97
4.2.1 Description of the measurements 97
4.2.2 Preliminary studies using Monte Carlo samples 98
4.2.3 Comparison between the data and Monte Carlo predictions 100
4.2.4 Correction for detector and QED effects 103
4.2.5 Systematic uncertainties 103
4.2.6 Measurement of the inclusive jet cross sections 105
4.3 Analysis II: Measurement of the subjet multiplicity... 106
4.3.1 Description of the measurements 107
4.3.2 Preliminary studies using Monte Carlo samples 107
4.3.3 Comparison between data and Monte Carlo predictions 108
4.3.4 Correction for detector and QED effects 108
4.3.5 Systematic uncertainties 110
4.3.6 Measurement of the mean subjet multiplicity 116

5 Discussion of the results **119**
5.1 NLO QCD predictions 119
5.1.1 Description of the NLO QCD calculation 119
5.1.2 The program DISENT 120
5.1.3 Estimation of the theoretical uncertainties 122
5.1.4 Theoretical predictions for inclusive jet cross sections in the Breit frame . 123
5.1.5 Theoretical predictions for the subjet multiplicity in the laboratory frame 125
5.2 Comparison of the inclusive jet cross... 126
5.2.1 Parton-to-hadron and Z° corrections 126
5.2.2 Theoretical uncertainties 128
5.2.3 Final results 130
5.3 Comparison of the subjet multiplicity... 135
5.3.1 Parton-to-hadron and Z° corrections 135
5.3.2 Theoretical uncertainties 135
5.3.3 Final results 137
5.4 Extraction of $\alpha_s(M_Z)$ from the measurements 138
5.4.1 Description of the method 138
5.4.2 $\alpha_s(M_Z)$ from the inclusive jet cross sections 139
5.4.3 $\alpha_s(M_Z)$ from the subjet multiplicity 142

6 Summary and conclusions **147**

A Some remarks on conventions **149**

B Resumen en castellano **153**

B.1 Introducción teórica . . . 153

B.1.1 El Modelo Estándar de las interacciones fundamentales . . . 153

B.1.2 Procesos de dispersión profundamente inelástica . . . 156

B.1.3 Producción de jets de hadrones . . . 159

B.1.4 La estructura interna de los jets . . . 160

B.1.5 Medida de la constante de acoplamiento fuerte . . . 161

B.2 Dispositivo experimental . . . 162

B.2.1 El acelerador HERA . . . 162

B.2.2 Descripción del detector ZEUS . . . 163

B.2.3 El calorímetro central de ZEUS . . . 166

B.3 Simulación de procesos y cálculos teóricos . . . 167

B.3.1 Modelos de simulación de la radiación de partones . . . 168

B.3.2 Modelos de simulación de la hadronización . . . 169

B.3.3 Cálculo de predicciones NLO en QCD perturbativa . . . 170

B.4 Descripción de los análisis . . . 171

B.4.1 Selección de los sucesos . . . 171

B.4.2 Descripción de las medidas experimentales . . . 174

B.4.3 Correcciones aplicadas a las medidas . . . 174

B.4.4 Comparación de las medidas con las predicciones teóricas . . . 176

B.4.5 La asimetría azimutal . . . 177

B.4.6 Determinación de α_s . . . 177

B.5 Conclusiones . . . 178

Bibliography **181**

Acknowledgments **189**

List of Figures

1.1 Two examples of the 'Eightfold Way' classification of hadrons 5

1.2 The multiplets for the quarks and the antiquarks as introduced in the original Quark model 7

1.3 Feynman diagrams for the lowest order of neutral and charged current DIS interactions with a positron being scattered by a proton. 15

1.4 The structure function F_2 is shown as a function of Q^2 for $\omega = \frac{1}{x} = 4$ as measured at SLAC 16

1.5 The structure of a proton interacting with a virtual photon 18

1.6 Running of the strong cupling constant with the scale 21

1.7 The results from ZEUS for F_2^{em} versus Q^2, for six values of x, are compared with results from NMC, BCDMS, E665 and H1 results 23

1.8 Schematic diagrams of the Born, QCD Compton and Boson-Gluon fusion processes in the Breit frame 24

1.9 The splitting functions at lowest order in α_s 29

1.10 A ladder diagram initiated by a gluon in the proton 30

1.11 Sterman-Weinberg jet algorithm for e^+e^- interactions 35

1.12 The first order QCD Compton process $\gamma^* q \rightarrow qg$, as viewed in the Breit frame . 39

1.13 The first-order contribution to the azimuthal distribution for the two possible processes: Boson-Gluon Fusion and QCD Compton 40

1.14 Schematic representation of the integrated and differential jet shape 42

1.15 Schematic representation of the subjet structure within a jet 43

2.1 Layout of the HERA collider. 48

2.2 Scheme of the injection facilities at DESY. 49

2.3 Bunch distribution for electrons and protons. 50

2.4 Accumulated luminosity delivered by HERA during RUN I divided in periods with equal lepton charge and proton beam energy. 50

2.5 Longitudinal cut of the ZEUS detector 52

2.6 Cross section of the ZEUS detector perpendicular to the beam direction 52

2.7 Layout of a CTD octant 53
2.8 Layout of the ZEUS high resolution uranium-scintillator calorimeter 59
2.9 Internal structure of an FCAL module 59
2.10 Layout of the ZEUS luminosity monitor. 62
2.11 Scheme of the ZEUS data adquisition system 65
2.12 Contours of constant electron energy and scattering angle in the (x, Q^2) plane . 70
2.13 Contours of constant current jet energy and hadronic angle obtained in the QPM approach in the (x, Q^2) plane 70

3.1 Representation of the different steps in the generation of an $e^+e^- \to$ hadrons event 72
3.2 Schematic representation of the parton shower approach to the simulation of the parton cascade 74
3.3 Schematic representation of the Colour Dipole Model for the simulation of the parton cascade of an $e^+e^- \to q\,\bar{q}$ event 75
3.4 Schematic picture showing a parton shower followed by cluster hadronisation and Lund-string hadronisation for $e^+e^- \to$ hadrons 78

4.1 Distribution in the $x - Q^2$ plane of the selected events for the analysis of jets in the Breit frame. The line shows the kinematic limit $y = 1$. 89
4.2 Distribution in the $x - Q^2$ plane of the selected events for the analysis of the subjet multiplicity. The lines shows Q^2 cut applied ($Q^2 = 125$ GeV^2) and the kinematic limit $y = 1$. 89
4.3 An event taken with the ZEUS detector and selected in the analysis of the subjet multiplicity 95
4.4 An event taken with the ZEUS detector and selected in the analysis of the inclusive jet cross sections in the Breit frame 96
4.5 Other example of event selected for the analysis of inclusive jet cross sections in the Breit frame 96
4.6 Values of the correction factor to be applied to the data to correct for detector effects obtained with the ARIADNE sample. 99
4.7 Values of the correction factor to be applied to the data to correct for detector effects obtained with the LEPTO-MEPS sample. 100
4.8 Control plots showing the comparison between the data and the ARIADNE sample for the jet variables in the laboratory and Breit frames 101
4.9 Control plots showing the comparison between the data and the LEPTO-MEPS sample for the jet variables in the laboratory and Breit frames 101
4.10 Uncorrected (visible) inclusive jet cross sections. The data are compared with the predictions given by the ARIADNE Monte Carlo sample for all the distributions under study 102

4.11 Uncorrected (visible) inclusive jet cross sections. The data are compared with the predictions given by the LEPTO-MEPS Monte Carlo sample for all the distributions under study 102

4.12 Correction factor to apply to the data to correct for QED effects 104

4.13 Inclusive jet cross sections corrected for detector and QED effects by using the ARIADNE simulations. The data points are compared with ARIADNE Monte Carlo predictions normalised to the data in each plot 105

4.14 Inclusive jet cross sections corrected for detector and QED effects by using the ARIADNE simulations. The data points are compared with LEPTO-MEPS Monte Carlo predictions normalised to the data in each plot 106

4.15 Values of the correction factor to be applied to the mean subjet multiplicity measured in the data to correct for detector effects obtained with the ARIADNE sample. 108

4.16 Values of the correction factor to be applied to the mean subjet multiplicity measured in the data to correct for detector effects obtained with the LEPTO-MEPS sample. 109

4.17 Control plots showing the comparison between the data and the ARIADNE sample for the jet and the positron variables reconstructed with the detector . . 110

4.18 Control plots showing the comparison between the data and the LEPTO-MEPS sample for the jet and the positron variables reconstructed with the detector . . 111

4.19 Uncorrected distributions of the mean subjet multiplicity compared with the predictions given by the ARIADNE and LEPTO-MEPS Monte Carlo sample . . 111

4.20 Distribution of the number of subjets in the data for different values of y_{cut} (black dots). The predictions of ARIADNE (histograms), normalised to the data, are also shown. 112

4.21 Distributions of the number of subjets in the data for $y_{cut} = 10^{-2}$ and different regions in $E_{T,jet}$ (black dots). The predictions of ARIADNE (histogram), normalised to the data, are also shown. 113

4.22 Distribution of the number of subjets in the data for different values of y_{cut} (black dots). The predictions of LEPTO-MEPS (histograms), normalised to the data, are also shown. 114

4.23 Distributions of the number of subjets in the data for $y_{cut} = 10^{-2}$ and different regions in $E_{T,jet}$ (black dots). The predictions of LEPTO-MEPS (histogram), normalised to the data, are also shown. 115

4.24 Corrected mean subjet multiplicity as a function of y_{cut} 117

4.25 Corrected mean subjet multiplicity as a function of η_{jet} for $y_{cut} = 10^{-2}$ 117

4.26 Corrected mean subjet multiplicity as a function of $E_{T,jet}$ for $y_{cut} = 10^{-2}$ 118

5.1 Ratio of the NLO QCD predictions obtained with DISASTER and DISENT for the two analyses 121

5.2 NLO QCD predictions for the inclusive jet cross sections in the Breit frame obtained with DISENT using MRST99 central as the set of proton PDFs 124

5.3 NLO QCD predictions for $\langle n_{sbj} \rangle$ as a function of y_{cut} (top left), η_{jet} (top right) and $E_{T,jet}$ (bottom) obtained with DISENT 126

5.4 Predicted cross sections at parton level by using the Monte Carlo program LEPTO with and without Z° exchange 128

5.5 Parton-to-hadron correction predicted by the different Monte Carlo programs for the distributions under study 129

5.6 The differential cross-section $\mathrm{d}\sigma/\mathrm{d}Q^2$ for inclusive jet production 132

5.7 The differential cross-section $\mathrm{d}\sigma/\mathrm{d}E^B_{T,jet}$ for inclusive jet production 132

5.8 The differential cross-section $\mathrm{d}\sigma/\mathrm{d}\eta^B_{jet}$ for inclusive jet production 133

5.9 The normalized differential cross-section $(1/\sigma)\mathrm{d}/\mathrm{d}\phi^B_{jet}$ for inclusive jet production 133

5.10 The differential cross-sections $\mathrm{d}\sigma/\mathrm{d}E^B_{T,jet}$ for inclusive jet production 134

5.11 Ratios between the differential cross-sections $\mathrm{d}\sigma/\mathrm{d}E^B_{T,jet}$ and NLO QCD calculations 134

5.12 Parton-to-hadron correction factor as estimated by using ARIADNE (solid lines), LEPTO-MEPS (dashed lines) and HERWIG (dotted line) as a function of y_{cut} (left) and $E_{T,jet}$ (right). 136

5.13 The measured mean subjet multiplicity corrected to the hadron level $\langle n_{sbj} \rangle$ as a function of y_{cut} for inclusive jet production in NC DIS 137

5.14 The measured mean subjet multiplicity corrected to the hadron level $\langle n_{sbj} \rangle$ as a function of $E_{T,jet}$ at $y_{cut} = 10^{-2}$ for inclusive jet production in NC DIS 138

5.15 NLO QCD calculations of $\langle n_{sbj} \rangle$ for different values of $\alpha_s(M_Z)$ in various $E_{T,jet}$ regions 140

5.16 Values of the strong coupling contant extracted from the $\mathrm{d}\sigma/\mathrm{d}Q^2$ distribution . 142

5.17 Values of the strong coupling contant extracted from the $\mathrm{d}\sigma/\mathrm{d}E^B_{T,jet}$ distribution 143

5.18 Schematic representation of the different contributions to the total uncertainty in the extracted value of $\alpha_s(M_Z)$ from the $\mathrm{d}\sigma/\mathrm{d}Q^2$ distribution for $Q^2 > 500$ GeV^2 143

5.19 The $\alpha_s(M_Z)$ values determined from the QCD fit of the measured mean subjet multiplicity $\langle n_{sbj} \rangle$ at $y_{cut} = 10^{-2}$ in the different $E_{T,jet}$ regions 144

5.20 Schematic representation of the different contributions to the uncertainty in the extracted value of $\alpha_s(M_Z)$ from the subjet multiplicities for jets with $E_{T,jet} >$ 25 GeV 146

List of Tables

1.1 Quantum numbers for the three quarks as introduced in the original SU(3) Quark model 6

1.2 Quantum numbers and masses for all the fundamental fermions in the Standard Model 12

1.3 Bosons associated to the fundamental interactions in the Standard Model 13

2.1 CAL sections and the angular ranges covered by them 58

2.2 Luminosity collected by ZEUS in 1993-2000 63

Chapter 1

Theoretical introduction

At present the most successful way to describe the measurements in high energy experiments is summarised in the Standard Model. It describes the interactions between the fundamental particles in terms of three kind of forces: the electromagnetic, the weak and the strong interaction. They are introduced as coming from fundamental gauge symmetries $U(1)_Y$ x $SU(2)_L$ x $SU(3)_C$ based on the solid grounds of Quantum Field Theory. It developed through the 1960's and 1970's by a fruitful combination of experimental and theoretical discoveries.

In this chapter a discussion about the Standard Model is presented. It includes how this model describes the formation of hadronic jets and its internal structure, which is the relevant part for the analyses presented in this thesis.

1.1 The Standard Model of particle interactions

The Standard Model is, together with General Relativity, the last step in the developments done to understand the phenomena which we observe in the Universe. It can be considered the great thriumph of the discoveries made during the 20th Century in trying to explain the experimental results which were not described by the classical mechanics (developed in 16th and 17th Centuries) and electrodynamics (developed during 18th and 19th Centuries).

In the following sections we will describe how the different results were interpreted and related to complete a model which has been able to describe most of the experiments done during the last 25 years.

1.1.1 The internal structure of atoms

At the beginning of the 20th Century only two types of interaction were known: the electromagnetic interaction, which was needed to describe the forces between electrically charged particles and the gravitation force, which was associated to the mass. The matter was understood by Dalton's picture that fundamental particles (atoms) exist and their combinations form everything we observe in Nature.

Different experimental results of those years were demonstrating that this simple picture had to be corrected; the atoms seemed not to be fundamental particles since some elements change into others and even one fundamental particle has been found inside the atom: the electron.

On the interaction side, although Faraday and Maxwell's vision of the electromagnetic fields looked successful, the energy and especially the electromagnetic one, displayed a behaviour easier to explain assuming that the energy presents not only wave- but also particle-like behaviours.

After different experiments and models, a new theory was developed, Quantum Mechanics, and it turned very useful to describe the experiments designed to study the internal structure of the atoms. During the first three decades of the 20th Century, the theoretical and experimental progresses concluded with the following picture:

- At very small scales (atom size) matter cannot be described as fundamental particles in a classical way. Particles display wave-like behaviours and have to be described using Quantum Mechanics.
- Matter and Energy cannot be understood in a separate way: the Theory of Relativity shows that energy can be converted into matter and viceversa. On the other hand, Quantum Mechanics shows that particles (matter) has to be described by fields and the interactions (energy) need to be described using *quanta of energy*, that is particles.
- The electrically neutral atom is formed by a nucleus which has a positive electric charge which define the chemical properties of the element. To compensate this charge the nucleus is surrounded by electrons. The structure of the electron cloud around the nucleus is described with Quantum Mechanics.
- The nucleus contains the majority of the mass of the atom. It contains a given number of protons and neutrons, which are packed together to form the nucleus.

This picture of energy and matter is still today correct, although it was clear that it has to be completed because there must be some additional force to pack together protons and neutrons in the nucleus. At this point, two ways of study were followed: the first one tried to understand the interactions between electrons and the electromagnetic field. The second looked inside the nucleus to understand its internal structure.

1.1.2 The electromagnetic interaction and QED

Although Quantum Mechanics was very successful to describe the structure of the atoms, it was very clear that it was not enough, since it doesn't include the relativistic effects which are needed for high energy processes. In this case high energy means in comparison with the electron mass or the bounding energy of the electrons to the atom.

The first attempts to include the relativistic principles in the description of the particle behaviour were not very successful because strange solutions appeared. One had to wait till Dirac's equation to describe the free electron. This equation can be written in the covariant form [6]

$$(i\gamma^\mu \partial_\mu - m)\psi = 0, \tag{1.1}$$

where m is the mass of the particle, ψ is the wave function to describe the quantum state where the particle is, and γ^μ are the four Dirac γ-matrices needed to recover the relativistic Klein-Gordon equation. For an electron, the γ-matrices has to be at least 4x4 matrices, so ψ is a four-component spinor[1]. Two of then were related to the two components of a "standard" electron

[1] An spinor is a mathematical vector but with a specific set of transformation properties.

of spin $\frac{1}{2}$ and the other two, associated to negative energy states, were interpreted as the two components of a 1/2-spin particle with the same mass as the electron but positively charged (the positron). It should be noted that the spin is naturally introduced in the relativistic-quantum description of the electron.

The discovery of the positron was a sucess of Dirac's description of the relativistic free electron, so there were some attempts to modify the equation to include interactions. The inclusion of the interaction of the electron with a nucleus was very succesful when making the approximation to the non-relativistic regime. Some corrections predicted by Dirac's theory (for example related to the spin of the electron coupled to the magnetic field of the nucleus) has been observed experimentally [7].

On the other hand for a complete relativistic quantum description of the electron coupled to the electromagnetic field it was necessary to describe the electromagnetic field within the quantum mechanics framework. In the first attempts it was realised that many complications appear, mostly due to divergences in observables which were experimentally finite. It was needed to wait till the 40's and 50's to find the solution to all these problems.

The solution was the renormalisation procedure: the divergences which appear in the calculation of observables are absorbed in some non-observable quantities which are present in the theoretical basis, i.e. contained in the Lagrangian. With this kind of mathematical treatments, one is able to use Quantum Field Theory to obtain predictions and these ideas were successfully applied to Quantum ElectroDynamics (QED). In this theory the electromagnetic interaction is described by two quantum fields: one for the charged particles (the electron-positron field) and one for the electromagnetic (or photon) field. They are coupled in such a way that the variations in one field induce changes in the other.

This leads, in the classical limit, to Faraday's picture of interactions by means of fields created by the particles.

The validity of QED to describe the electromagnetic interaction has been confirmed during more than 50 years and at present this theory is among the best established ones in Physics. Its success confirms the validity of the Theory of Relativity and of Quantum Mechanics, which can be considered as the two great developments in Physics during the 20th Century.

1.1.3 The strong and weak interactions

After the discovery of the proton one question arose: how can the protons be packed together in the nucleus? The gravitational force was not strong enough to compensate the electrical forces which tends to push away particles with the same electric charge. The discovery of the neutron as a fundamental piece to build the atomic nucleus[2] showed that new forces are present in Nature and the atomic nucleus was the place where to study them. The stability of the neutron within the nucleus suggests that a new interaction is present between protons and neutrons. This force, called *the strong force* due to the fact that it was stronger than the electromagnetic one, was present only when particles were very close.

With the development of new experimental devices, new particles were discovered and the analysis of their behaviour revealed that two different kinds of particles appear in Nature:

[2]The only nucleus that does not contain any neutron is the hydrogen nucleus, but it consists of only one proton... so it is not a "nucleus" but a proton.

- Leptons: these are particles which don't interact through the strong force. The electron is a lepton.

- Hadrons: these are particles which interact trough the strong force. The group is divided into mesons (which are bosons) and baryons (which are fermions). The proton is a hadron.

In both groups appear particles with and without electric charge so they are able to interact with the electromagnetic field. The study of some decays led to the introduction of a new interaction: *the weak interaction*. It was named this way because its main property was that its effects were weaker than the effects induced by the electromagnetic interaction.

Although some principles were accepted (conservation laws, the existence of an antiparticle for each particle,...) no one knew how to describe the new interactions in a fundamental way. It took more than 35 years to understand the nature of these new forces; it concluded with the development of the Standard Model during the seventies.

1.1.4 Hadron spectroscopy and the Quark-Parton Model

After the discovery of the first hadrons, a new branch in fundamental physics appeared. It is *hadron spectroscopy* and its aim is to study the different kinds of hadrons and understand the different relations between them.

The first step in this new branch was the introduction by Heisenberg of the *isospin quantum number*. This quantum number sets the differences between a neutron and a proton, which seems otherwise to be identical particles regarding the nuclear interaction. Formally, a proton and a neutron can be considered as the same particle (a nucleon) but with different isospin quantum numbers.

The discovery of additional hadrons led to use the isospin to classify them. In fact, it is noted that hadrons are classified in isospin families in such a way that the members are very similar.

The second classification of hadrons was made taking into account the spin-statistics connection for particles. In this way, hadrons can be fermions or bosons and they can have spin from 0 to 3/2. To differentiate baryons from mesons a new quantum number is introduced, the baryon number (B). It takes value 1 for baryons (which are hadrons following Fermi-Dirac statistical rules), -1 for antibaryons and 0 for mesons (which are hadrons following Bose-Einstein statistical rules). The conservation of the baryon number in Nature is the only explanation to avoid proton decay. The proton would be stable since is the baryon with smallest mass.

The discovery of new relations between hadrons needed the introdution of a new quantum number, the *strangeness* (S). It is needed to explain why some particles are only created in pairs when strong and electromagnetic interactions are present. The weak interaction does not conserve this quantum number, and that explains why the created pairs can decay to particles with S=0 via the weak interaction although the creation was done via the strong or electromagnetic force.

Using the strangeness and the baryon number, a new quantum number can be constructed which turns out to be more useful for the classification of hadrons. It is the "hypercharge" and it is defined by

$$\mathrm{Y} = \mathrm{B} + \mathrm{S}\,,$$

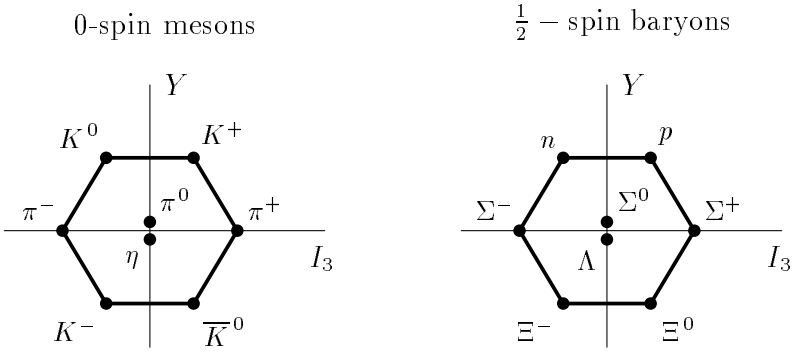

Figure 1.1: Two examples of the 'Eightfold Way' classification of hadrons. On the left some of the 0-spin ground-state mesons and on the right the 1/2-spin ground-state baryons. The particles belonging to these groups are distributed in octets of SU(3). The plane containing these octets is defined, as mentioned in the text, by the hypercharge $Y\,(=B+S)$ and the third component of the isospin $I_3\,(=Q-Y/2)$.

which leads to another important relation involving the electric charge (in units of the proton charge):

$$\mathrm{Q} \;=\; \mathrm{I_3} \;+\; \frac{\mathrm{Y}}{2},$$

where $\mathrm{I_3}$ is the value of the third component of isospin, which differentiates the particles belonging to the same isospin family.

The next important step in the studies on hadron spectroscopy was the introduction of the 'Eightfold Way', proposed independently by Ne'eman and Gell-Mann [8]. It consists of a classification scheme to group the observed baryons and mesons with the same spin according to their third isospin component (that is, the charge) and hypercharge (that is, the strangeness) using the SU(3) group symmetry. As shown in figure 1.1, these representations are very simmetric and the distribution of all the hadrons in this kind of schemes suggests that the origin of the hadronic structure is common to all these particles. In a similar way as with Mendeleev's table for chemical elements, some hadrons were not yet discovered when the 'Eightfold Way' appeared. The discovery of a predicted particle with Q=−1 and S=−3 in 1964 led to a wide acceptance of the 'Eightfold Way' for the classification of hadrons.

The nice way the hadrons are distributed in representations of the SU(3) group can be used as a hint to analyse its internal structure, at least in a formal way. It should be mentioned that it was already known that hadrons were not point-like particles. The first indication of this came from the magnetic moment of the neutron: it is simpler to consider the neutron as a non-elementary particle than to explain how a neutral particle has a magnetic moment.

The second indication came from the *g factor* for the neutron and the proton. Although QED introduce corrections to the value of 2 predicted by Dirac's theory, the proton and the neutron have values too far away of 2, which is the expected value for 1/2-spin point-like particles, as the electron.

In 1964, Gell-Mann and Zweig independently proposed that hadrons are composed of elementary constituents, called *quarks* [9], providing the basis for the 'Eightfold Way'. The quarks, coming in three flavours, up (u), down (d) and strange (s) and carrying spin $\frac{1}{2}$ were assigned fractional charges: $+\frac{2}{3}$ for the u and $-\frac{1}{3}$ for the d and s, in units of the proton's charge.

Quark	Q	B	S	Y	I_3
d	$-\frac{1}{3}$	$\frac{1}{3}$	0	$\frac{1}{3}$	$-\frac{1}{2}$
u	$\frac{2}{3}$	$\frac{1}{3}$	0	$\frac{1}{3}$	$\frac{1}{2}$
s	$-\frac{1}{3}$	$\frac{1}{3}$	-1	$-\frac{2}{3}$	0

Table 1.1: Quantum numbers for the three quarks as introduced in the original SU(3) Quark model. The corresponding antiquarks have the same numbers but with opposite sign. As described in the text, the hypercharge is defined as $Y = B + S$ and the isospin is defined in terms of the electric charge $I_3 = Q - Y/2$.

The quantum numbers of the three quarks (shown in table 1.1) are chosen in such a way that the quarks and the corresponding antiquarks are distributed in a fundamental multiplet of SU(3) (see figure 1.2). Combining the quarks, it is posible to reproduce the various representations of SU(3) which configures the 'Eightfold Way'. To do that, it is necessary to describe the baryons as formed by three quarks, the antibaryons by three antiquarks and the mesons by one quark and one antiquark. This quark model of the hadron internal structure simplifies the studies on hadron spectroscopy, where its use would be justified even in the case that quarks were not real particles[3].

Two strong points were against the quark model. The first one was that quarks had not been observed, and with a fractional electric charge its detection would have been very simple.

The second one was that the model needs an additional quantum number to explain some of the quark states. Some hadrons contain three quarks of the same flavour and the same spin component and since they are fermions, there must be another quantum number to be consistent with the Pauli Exclusion principle. This new quantum number was called *colour* [10] since it was used to construct a mnemonic rule for the particularly reduced quark association: *with three colours (or anticolours) or one colour and its relative anticolour it is posible to form colourless particles*. That means that colour is related to the quark world, although the observable hadrons are colourless... and only combination of three (anti)quarks or one quark and one antiquark are possible observable states.

The discovery in the last years of the 1960's that the structure functions of the nucleon scale with energy (see section 1.2.2 for a complete description) and that this result could be explained considering that the nucleon is formed by point-like particles with spin $\frac{1}{2}$ leads to reconsider the validity of the quark model as a good description of the internal structure of the hadrons. This was the origin of the Quark-Parton Model which describes the proton as formed by free particles (the partons). This model does not contain interactions between the partons, which in fact are needed to explain the confinement of the quarks inside the colourless hadrons.

The different studies done during the begining of the seventies conclude with a model where the proton was formed by additional partons apart from the three quarks predicted in the quark model as used in hadron spectroscopy. In the nucleon there were additional neutral partons, which were called gluons, and from the interactions between the gluons and the quarks, new quarks appear. This leads to a separation of the partons inside the hadrons into three groups:

[3] "Such particles [quarks] presumably are not real but we may use them in our field theory anyway" (Gell-Mann, 1964).

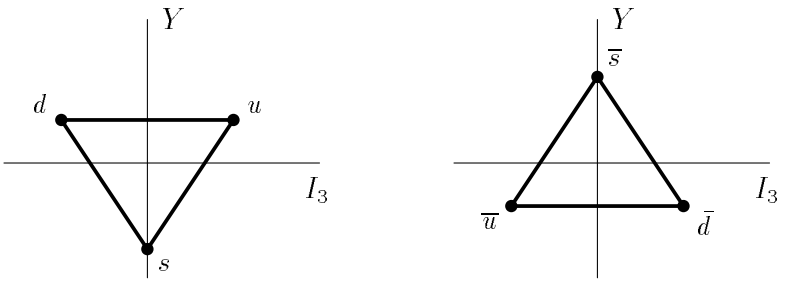

Figure 1.2: The multiplets for the quarks and the antiquarks as introduced in the original Quark model. With successive combinations of these particles, it is possible to reconstruct the various hadrons belonging to the different SU(3) multiplets.

- **The valence quarks**: they are the original quarks of the Quark model
- **The gluons**: the valence quarks can radiate gluons as a consequence of the strong force which keeps the partons together within the hadron. This gluon content makes no contribution to the quantum numbers of the hadron and does not affect the espectroscopic values of the original quark model.
- **The sea quarks**: the gluons can split into quark-antiquark ($q\bar{q}$) pairs. These pairs don't contribute to the quantum numbers of the hadron since those of the quark are compensated by those of the antiquark.

All these contributions configure the complete internal structure of the hadron, which is far from simple and determined by the interaction between the partons. The strong interaction between hadrons is related to the interactions between quarks and gluons. This means that the interaction between hadrons is not a fundamental interaction. It is only the indirect consequence of the interactions between the partons from the different hadrons. This explains why the interactions between hadrons (as the nuclear interaction) is only present at short distances: it is needed that the partons in one hadron "detect" the existence of the colour fields produced by the partons in the second hadron, and since the hadron is colour neutral, only contributions resolving the internal structure of the hadron can take part in the hadron-hadron interaction.

Since the discovery of the c-quark (charm), the quark model has been considered as the best description of the internal structure of hadrons, at least from the point of view of hadron spectroscopy. During this time, quarks and gluons have become a fundamental part of the present knowledge on fundamental physics.

1.1.5 Quantum Chromodynamics

Following the way opened by QED and Yang-Mills theories, Quantum ChromoDynamics (QCD) was developed in the context of Quantum Field Theory starting with a global symmetry. This symmetry is based in the colour group $SU(3)_C$ and when the free-quark Lagrangian is imposed to preserve this symmetry locally, then a local non-abelian gauge theory of quarks and massless gluons appears. This theory can be described by the Lagrangian

$$\mathcal{L} = -\frac{1}{4} F^A_{\alpha\beta} F_A^{\alpha\beta} + \sum_{flavours} \bar{q}_a \left[\gamma^\mu D_\mu - m\right]_{ab} q_b \,, \tag{1.2}$$

where $F^A_{\alpha\beta}$ is the field strength tensor defined in terms of the gluon field A^A_α by

$$F^A_{\alpha\beta} = \left[\partial_\alpha A^A_\beta - \partial_\beta A^A_\alpha - g f^{ABC} A^B_\alpha A^C_\beta\right] ,$$

where indexes A, B, C run over the eight colour degrees of freedom of the gluon field. The last term in the expression for $F^A_{\alpha\beta}$ distinguishes QCD from QED since it gives rise to cubic and quartic gluon self-interactions; g is the coupling charge which determines the strength of the interaction and f^{ABC} are the structure constants of the $SU(3)_C$ group.

The sum in the lagrangian runs over the different flavours of quarks. The quarks fields (q_a) are in the triplet representation of the group (a=1, 2, 3). The covariant derivative D_μ takes the form

$$\left(D_\mu\right)_{ab} = \delta_{ab}\partial_\alpha + ig\left(t^C A^C_\alpha\right)_{ab} , \tag{1.3}$$

where δ_{ab} is Kronecker's delta, and $\{t\}$ are matrices in the fundamental representations of SU(3). By convention, the normalisation of the SU(N) matrices is chosen to be

$$Trace\{t^A t^B\} = \frac{1}{2}\delta^{AB} .$$

With this choice, the colour matrices obey the following relations:

$$\sum_A t^A_{ab} t^A_{ba} = C_F \delta_{ab} , \qquad C_F = \frac{N^2-1}{2N} ,$$

$$Trace\{T^C T^D\} = \sum_{A,B} f^{ABC} f^{ABD} = C_A \delta_{CD} , \qquad C_A = N ,$$

where $\{T\}$ are matrices in the adjoint representation of SU(N). For the SU(3) group, these are the eight Gell-Mann matrices.

With all theses tools it is possible to describe the interactions between quarks and gluons. Using the perturbative approach, the theory is able to make predictions for those processes in which the strong coupling constant $\alpha_s = g^2/4\pi$ is small.

The validity of QCD to describe the strong force was experimentally confirmed with the discovery of the scaling violations of the structure functions and when the existence of the gluon was confirmed experimentally with the observation of three-jet events in e^+e^- annihilation. In this way, the colour interaction has been able to describe the results related to the strong interaction for more than 20 years and is at present one of the fundamental interactions included in the Standard Model.

1.1.6 The electroweak unification

If the understanding of the strong interactions needed a very hard work to explain the hadron spectroscopy and the experimental results, even harder was the long way needed to complete a theory which included the weak interaction.

After the first steps introducing a new, undetected particle (the *neutrino*) and some rules for the calculation of cross sections and decay processes (known as *Fermi theory of the weak*

interaction), it was demostrated in 1956 that the weak interaction violates parity and charge-conjugation symmetry. That is, the experiments would provide different results if all the particles are changed by their antiparticles. The same occurs if the space is mirror-reflected.

In the new theory to describe this property, the neutrino was introduced to have a well-defined and fixed helicity, which is only possible if these particles are massless. This characteristic of neutrinos obviously violates parity symmetry, since right-handed neutrino would be forbidden in Nature[4].

On the hadronic sector, interesting features were discovered in parallel. With the quark model description in hand, the weak interaction was shown to change the flavour of the quarks, similarly to the transformation of electrons into neutrinos and of neutrons into protons. Additionally, the weak interaction couples to quark states which are not the flavour-defined states. The interaction couples linear combinations of the physical quarks[5]. This mixing, which is understood as a rotation in the space containing the quark states, was first described by the Cabibbo angle. After the discovery of the third family of quarks, the 3x3 CKM matrix (Cabibbo, Kobayashi, Maskawa) describes the mixing in the quark sector [11].

The first successful description of the weak interaction based on a symmetry group was done by Glashow in 1961 [12]. The fundamental group was the SU(2) associated to the left-handed helicity of the particles. From the point of view of this group the particles are divided into left-handed doublets and right-handed singlets. For example, for the leptons of the first generation, the left-handed electron is associated to the neutrino in a doublet. The right-handed electron forms a singlet which does not couple to this interaction.

Of course, for a consistent description of this interaction the masses have to be neglected since $SU(2)_L$ cannot be a symmetry in nature if particles have mass. This is one of the difficulties of the theory.

Since an interaction based in $SU(2)_L$ is divided into a "charged part" (that is, exchanging the components of the doublet) and a "neutral part" (that is, leaving the doublets as they are), the description seemed to be inexact since neutral-current weak interactions had not been observed at that time. The discovery of this kind of interactions in 1973 confirmed the validity of this model.

In fact the complete model has to be slightly more complex since the observed neutral-current weak interaction displays a right-handed component, so there must be something else in the theory. At present, the Standard Electroweak Model or GWS Model (Glashow, Salam and Weinberg) [12, 13] is based on the group $SU(2)_L$ x $U(1)_Y$. The first group, related to the left-handed particles, is described by introducing a new quantum number, the *weak isospin*. The second group is related to the *weak hypercharge*. The matrices $\{T\}$ are the representation of the $SU(2)_L$ algebra, while Y is the gauge charge associated to the $U(1)_Y$ group.

The weak isospin is formally similar to the hadronic isospin we described in section 1.1.4. It is associated to spin-like multiplets, in this case associated to $SU(2)_L$. The fermions are set in doublets (i.e., weak isospin $T=\frac{1}{2}$) in case of left-handed components, or singlets (i.e. $T = 0$) for the right-handed ones. The third component of the weak isospin (T^3) allows to differentiate

[4] In fact, it is not forbidden that a right-handed neutrino exists. The theory only forbids this neutrino to interact with matter through the usual weak interaction.

[5] "Physical quarks" is meant for the particles with defined mass, which in the case of quarks are the ones with a given flavour.

the two components of the doublet. The weak hypercharge is then defined for each particle as [6]

$$Q = T^3 + \frac{Y}{2} , \tag{1.4}$$

where Q is, as usual, the electric charge of the particle in units of the proton charge.

For this model, using Yang-Mills fields and local gauge invariance, the following Lagrangian is defined

$$\mathcal{L} = -\frac{1}{4} W_i^{\mu\nu} W^i_{\mu\nu} - \frac{1}{4} B^{\mu\nu} B_{\mu\nu} + \bar{f}\big(i\gamma_\mu D^\mu\big) f , \tag{1.5}$$

where f represent the fermionic fields and

$$W^i_{\mu\nu} = \partial_\mu W^i_\nu - \partial_\nu W^i_\mu - g_W \epsilon^{ijk} W^i_\mu W^k_\nu ,$$

$$B_{\mu\nu} = \partial_\mu B_\nu - \partial_\nu B_\mu ,$$

$$D^\mu = \delta_{ij}\partial^\mu + i g_W \left(T \cdot W^\mu\right)_{ij} + iY\delta_{ij} g_Y B^\mu .$$

The antisymmetric (Levi-Cività) tensor ϵ^{ijk} appears in the expressions because its components are the structure constants of SU(2) [14].

The Lagrangian constructed in this way evidently describes four massless vector bosons forming a singlet (B) and a triplet ($W^\pm, W^0$) under weak isospin transformations. The model cannot yet describe the real world because there is only one massless vector boson observed in Nature which can be considered as a candidate, the photon. The direct addition of explicit mass terms for three of the bosons would violate local gauge invariance and spoil the renormalisability of the theory.

On the other hand, since the weak isospin is only well-defined for fermions of a fixed helicity, mass terms for the fermionic field would break the symmetry and the local gauge invariance would be lost. However, in Nature, the fermions are observed to have a mass which is only negligible for high energy processes, so the model has to be completed to include mass terms in a natural way while preserving the properties of the theory.

This is done using the Higgs mechanism [15], based on the idea of "spontaneous symmetry breaking". A rough description of this idea is that the need to select between several identical options leads to a symmetry breaking. Of course, the way this selection is done can be completely at random, and in principle any other choice would be equally valid; it is the need to make this choice which leads to symmetry breaking, and not the choice itself.

In the Standard Model, a single complex doublet of scalar fields is introduced. These fields transform as a doublet under $\mathrm{SU}(2)_L$. By assigning them a weak hypercharge of $\frac{1}{2}$ we fix their transformation properties under $\mathrm{U}(1)_Y$. The inclusion of these fields in the Lagrangian after coupling them to the vector bosons makes a mass term for the scalar field to appear, but it is an imaginary mass. A real mass is made to appear by transforming the fields into physical fields, but this transformation is not unique and a choice of parameters is needed. Here is where the "spontaneous symmetry breaking" takes place, because the transformation to the physical fields is not invariant under $\mathrm{SU}(2)_L$ x $\mathrm{U}(1)_Y$. A deeper study yields that three of the symmetries are spontaneously broken, and three of the massless bosons get a finite mass by means of the Goldstone theorem [16] applied to this case.

One symmetry is preserved, which is related to the standard $U(1)_{em}$ group, and the photon is kept massless. The neutral currents of the original groups are now mixed and two new fields appear:

$$Z_\mu = W_\mu^0 \cos\theta_W - B_\mu \sin\theta_W \ ,$$

$$A_\mu = W_\mu^0 \sin\theta_W + B_\mu \cos\theta_W \ ,$$

where the second one is the standard electromagnetic field and θ_W is the *weak angle* which dictates the mixing of the high-energy fields (given in the GSW symmetry group) with the low-energy ones (where the electromagnetic and the weak fields are separated).

The mass scale for this symmetry breaking is set by the mass of the weak bosons, which is of the order of 100 GeV. For energies well above this scale, the electromagnetic and the weak interactions are unified and the description of the electroweak force is done in terms of the weak isospin and hypercharge interactions. For energies close to that scale and smaller, the weak interaction separates from the electromagnetic one and massive bosons are needed to describe this low energy region. Since the degrees of freedom have to be conserved when going from high energy to low energy, the remaining degree of freedom of the Higgs complex fields has to be observed at low energies as a scalar field, since the other three degrees of freedom have been absorbed by the longitudinal helicity components of the massive fields.

This particle has not been yet observed[6], but it has to be included in the Standard Model to allow the gauge bosons to acquire a mass. Furthermore, the coupling between fermions and the Higgs field is the origin of the fermionic mass, as an additional consequence of the Higgs mechanism.

For a more complete description of the electroweak unification, the GSW model and the Higgs mechanism, see [6, 14].

1.1.7 Summary: the Standard Model and beyond

With the artificial unification of the electroweak and strong interactions, we are left with the symmetry group $SU(3)_C$ x $SU(2)_L$ x $U(1)_Y$, which contains the description of all these fundamental forces. These forces are present in the interactions between the fundamental particles and the Standard Model is completely defined.

In the so-called matter sector, the particles are divided into three families or generations, which are formally identical. The only difference between generations is the mass of the particles. The first generation is the lightest one and contains the components of ordinary matter (i.e. the atoms). The formal structure of this generation is

$$\begin{pmatrix} \nu_e \\ e_L^- \end{pmatrix} \ , \ e_R^- \ , \ \begin{pmatrix} u_L \\ d_L \end{pmatrix} \ , \ u_R \ , \ d_R \ .$$

In fact, the quark states with well-defined mass are not the same states that enter into the doublets and singlets of the $SU(2)_L$ group, as we described above. However, this is usually

[6] Although some events from the LEP experiments in autumn 2000 suggest the presence of the Higgs boson at a mass around 115 GeV, the results have not been considered as the discovery of this particle. Further experimental evidence is needed to confirm or rule out these results.

	Generations			Quantum numbers				
	1^{st}	2^{nd}	3^{rd}	Q	T	T_3	Y	colour
Quarks	u u_L (1-5 MeV) u_R	c c_L (1.5 GeV) c_R	t t_L (175 GeV) t_R	$\frac{2}{3}$	$\frac{1}{2}$ 0	$\frac{1}{2}$ 0	$\frac{1}{3}$ $\frac{4}{3}$	Yes
	d d_L (3-9 MeV) d_R	s s_L (75-170 MeV) s_R	b b_L (4-5 GeV) b_R	$-\frac{1}{3}$	$\frac{1}{2}$ 0	$-\frac{1}{2}$ 0	$\frac{1}{3}$ $-\frac{2}{3}$	Yes
Leptons	ν_e (L) (< 1 eV) $-$	ν_μ (L) (< 0.2 MeV) $-$	ν_τ (L) (< 18.2 MeV) $-$	0	$\frac{1}{2}$	$\frac{1}{2}$	-1	No
	e^- e_L (0.51 MeV) e_R	μ^- μ_L (106 MeV) μ_R	τ^- τ_L (1.8 GeV) τ_R	-1	$\frac{1}{2}$ 0	$-\frac{1}{2}$ 0	-1 -2	No

Table 1.2: Quantum numbers and masses for all the fundamental fermions in the Standard Model. The only couplings which have been left out are the ones related to the weak neutral current. These are obtained as $C_V = T_3 - 2\sin^2 Q$ and $C_A = T_3$ for the vector and the axial part, respectively.

neglected in the presentation of the formal struture of the generations[7]. Additionally, all the antiparticles are included in the corresponding structure. It should be mentioned that the left-symmetry of the particles is translated into a right-symmetry of the antiparticles, due to the standard convention to define helicity states.

The second generation is identical to the first but with the muon and the muonic neutrino in the lepton sector and the strange and charm quarks. For the third generation we are left with the tauon and its neutrino, the bottom and top quarks. No direct or indirect hint of additional generations has been found in the experimental analyses.

Table 1.2 shows the most important characteristics of the various particles. It should be noted that the colour charge is the same for all the quarks and for this reason is not included. Additionally, the antiparticles have the same quantum numbers as the particles but with the opposite sign.

On the interaction side, five different gauge bosons are present in the Standard Model. In principle, eight different gluons exists in Nature, but they can be simplified to one since colour charge is not observable. Table 1.3 shows the parameters associated to all the gauge bosons.

Since the Standard Model is founded on Quantum Field Theory, the processes it describes undergo quantum-mechanical effects. One example is that the neutral-current interaction via the exchange of a neutral boson proceeds through all the possible bosons which can couple to the interacting particles. When an electron, for example, is scattered by a hadron, contributions from the photon and the Z° boson are present. Since the two contributions are added to compute the amplitude of the process, then the final observable will have not only two separate contributions, but also the interference term. This contribution is experimentally

[7]Obviously, the problem is that the three generations cannot be completely separated since the quark sector is mixed.

	Particle	Mass	Interaction
gluon	g	0	strong/colour $\mathrm{SU}(3)_C$
photon	γ	0	electromagnetic $\mathrm{U}(1)_{em}$
weak bosons	Z°	91.19 GeV	weak, neutral
	$W^\pm$	80.42 GeV	weak, charged

electroweak: $B^0 \rightarrow \mathrm{U}(1)_Y$; $W^3 \rightarrow \mathrm{SU}(2)_L$

Table 1.3: Bosons associated to the fundamental interactions in the Standard Model. At very high energies the weak and the electromagnetic interactions are unified and in fact they are replaced by another two separate interactions, as described in the text.

negliglible at energies smaller than the mass of the Z° boson, but it becomes very important when approaching that energy scale.

Apart from all these particles, the Standard Model includes an additional scalar boson, the Higgs particle, as we described before. This is the only particle which is left to be discovered from the complete spectrum of the Standard Model.

The success of the Standard Model to describe the experimental results during the last two decades is a great thriumph of theoretical physics in describing the fundamental interactions. However we cannot forget that this model still presents some problems and that gravity has to be included in the description of the fundamental forces. Apart from this, new questions and even some of the old questions still remain to be answered, so it is clear that the Standard Model is only a step in the understanding of Nature.

Some experimental results during the last years have shown that the Standard Model has to be completed. Among these, the mixing between neutrinos is the most important one. These results imply that neutrinos are massive and that is at present not included in the Standard Model.

Some studies have been done to construct models beyond the Standard Model. The most interesting ones unify all the known interactions at very high energies. The mechanism for "spontaneous symmetry breaking" is then applied to separate the interactions into the ones we observe at low energy.

However, at present the Standard Model seems to be enough to describe the experimental results. The presence of a well-established theory is used in the experimental side to determine the parameters of the theory, in addition to the tests which are performed to confirm the validity of the predictions in unexplored regions.

1.2 Deep Inelastic Processes

One of the most useful experiments to study the internal structure of hadrons is the scattering of leptons on hadrons, usually protons or nuclei. When the momentum transfers are very large, the process is said to be in the deep inelastic scattering (DIS) regime. In this case the target loses its identity completely and the resulting final states are complicated multiparticle states whose study allows to gain insight into the internal structure of the initial target.

The following sections describe how the DIS processes have been used in the past as a fundamental tool to build the Standard Model. At the same time, the notation which will be used in the description of the analyses is introduced.

1.2.1 DIS processes

Usually, a DIS process is related to the scattering of a high-energetic lepton (l) on a hadron (h), which leads to the general reaction

$$l(k) + h(p) \rightarrow l'(k') + X(p') \ ,$$

where the initial state particles (l, h) are defined by the experiment and the final ones (l', X; where X means any state of particles) are given by the processes which have occured in the collision.

At HERA the initial state particles are electrons (or positrons) and protons, so we will concentrate on the related processes. Any other DIS process can be described in a very similar way.

When a positron is scattered on a proton, two major processes can occur depending on the boson which is exchanged in the collision (see figure 1.3). If the exchanged particle does not carry electric charge, the process is called *neutral current DIS*. If, on the other hand, it carries electric charge, then is called *charged current DIS*. To distinguish between the two processes, the only information we need is the type of the final-state lepton. If it's the same as the initial one, a neutral current event has happened. If not, the electric charge of the incoming lepton has been taken by the exchanged particle and the final-state particle cannot be the same as the initial one; the electron (positron) has transformed into a (anti-)neutrino via the exchange of a $W^{\pm}$ boson.

In the following, only neutral current processes will be considered, although most of the arguments can be applied to charged current studies.

At a given center-of-mass energy ($\sqrt{s}$) the kinematics of a DIS event are completely described by two variables among the following three Lorentz-invariant quantities:

$$Q^2 = -q^2 = -(k - k')^2 \ , \tag{1.6}$$

$$x = \frac{Q^2}{2\, p \cdot q} \ , \tag{1.7}$$

$$y = \frac{p \cdot q}{p \cdot k} = \frac{Q^2}{s\, x} \text{ (ignoring masses)} \ , \tag{1.8}$$

where the notation for the four-momenta is that of figure 1.3. Q^2 is the negative square of the momentum transfer and specifies the virtuality of the exchange boson. If $Q^2 > 0$ the exchange boson can have longitudinal as well as transverse polarisation. In this case Q^2 sets the energy scale of the process. If $Q^2 = 0$ then the process takes place in the photoproduction regime, in which the proton collides with a real photon. The photoproduction regime is studied in a slightly different way and we don't consider it further since the analyses described in this thesis are performed in the region where Q^2 is well above 1 GeV^2.

x is the scaling variable introduced by Bjorken. In the Quark-Parton Model it is interpreted as the fraction of the proton momentum carried by the struck quark (see section 1.2.2).

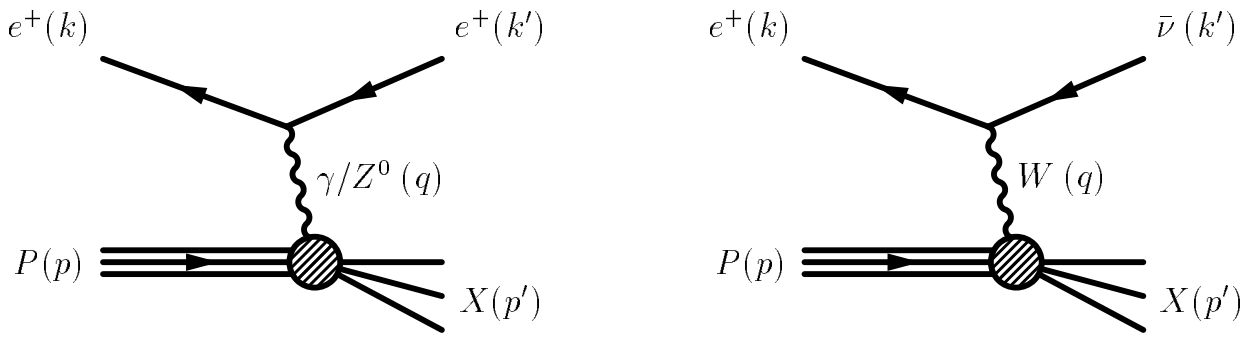

Figure 1.3: Feynman diagrams for the lowest order of neutral and charged current DIS interactions with a positron being scattered by a proton.

It can be shown (see [6], for example) that at fixed x, the exchanged boson probes smaller distances with increasing Q^2 since the wavelength of the boson is inversely proportional to $\sqrt{Q^2}$.

Finally, y corresponds to the fractional energy transfer from the lepton to the proton in the proton rest frame.

In the single-boson exchange approximation the cross section for deep inelastic ep scattering can be factorised into a leptonic tensor $L_{\mu\nu}$ and a hadronic tensor $W^{\mu\nu}$

$$d\sigma \sim L_{\mu\nu}\, W^{\mu\nu} \ .$$

The leptonic tensor,which is symmetric in μ and ν, can be calculated exactly using the Standard Model. The ignorance of the structure of the proton and hence the details of the interaction at the hadronic vertex are parametrised in terms of the hadronic tensor. The most general form of this tensor, taking Lorentz-invariance and the symmetry of the leptonic tensor into account is [6]

$$W^{\mu\nu} = -W_1 g^{\mu\nu} + W_2 \frac{p^\mu p^\nu}{M^2} + iW_3 \epsilon^{\mu\nu\rho\sigma} p_\rho q_\sigma + W_4 \frac{q^\mu q^\nu}{M^2} + W_5 \frac{p^\mu q^\nu + q^\mu p^\nu}{M^2} \ ,$$

where M is the mass of the hadronic target, in our case the proton.

Imposing the conservation of the four-vector current yields

$$W_5 = -\frac{p\cdot q}{q^2}\, W_2 \quad \text{and} \quad W_4 = -\frac{p\cdot q}{q^2}\, W_5 + W_1 \frac{M^2}{q^2} \ .$$

The three remaining functions depend on two independent Lorentz-invariant scalar variables, which can be chosen to be Bjorken x and Q^2. The dynamics of the strong interaction and related processes in the hadronic vertex are contained in these x and Q^2 dependencies. Nowadays, the notation given by the definitions

$$\begin{aligned} F_1(x,Q^2) &= M \cdot W_1(x,Q^2) \ , \\ F_2(x,Q^2) &= \frac{Q^2}{2M\,x} \cdot W_2(x,Q^2) \ , \quad \text{and} \\ xF_3(x,Q^2) &= \frac{Q^2}{2M} \cdot W_3(x,Q^2) \end{aligned}$$

is commonly preferred. The $\{F_i\}$ are the so-called *proton structure functions*. As $F_3(x,Q^2)$ describes the parity violation contribution this structure function is small for $Q^2 \ll {M_Z}^2$.

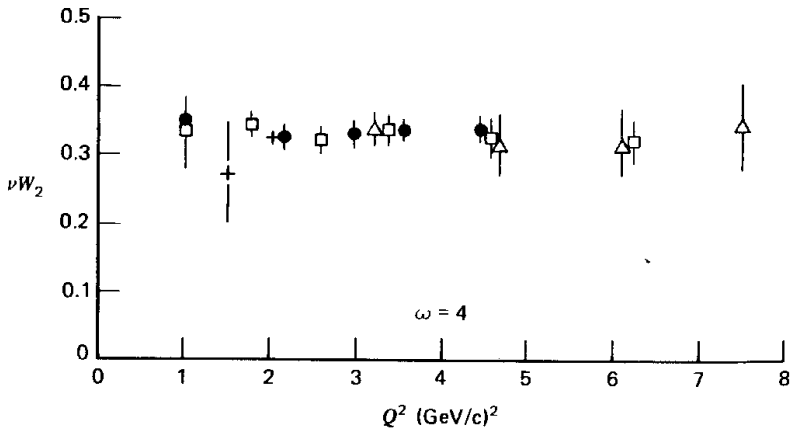

Figure 1.4: The structure function F_2 (here denoted νW_2 where $\nu = \frac{Q^2}{2M\,x}$ is the energy of the exchanged boson) is shown as a function of Q^2 for $\omega = \frac{1}{x} = 4$ as measured at SLAC. The scaling behaviour is evident.

Using these definitions, the deep-inelastic $ep \to e + X$ scattering cross section can be written as

$$\frac{d^2\sigma(e^{\pm}p)}{dx\,dQ^2} = \frac{4\pi\alpha^2}{xQ^4}\left[y^2xF_1(x,Q^2) + (1-y)F_2(x,Q^2) \mp y(1-\frac{y}{2})xF_3(x,Q^2)\right], \qquad (1.9)$$

or with the definition of $F_L = F_2 - 2xF_1$ as

$$\frac{d^2\sigma(e^{\pm}p)}{dx\,dQ^2} = \frac{4\pi\alpha^2}{xQ^4}\left[Y_+F_2(x,Q^2) - y^2F_L(x,Q^2) \mp Y_-xF_3(x,Q^2)\right], \qquad (1.10)$$

where $Y_\pm = 1 \pm (1-y)^2$.

In the single-photon exchange approximation (within QED), the structure function F_L is only related to the absorption cross section of longitudinally-polarised "virtual" photons. In the quark-parton model, this absorption process is forbidden and $F_L = 0$ (see section 1.2.2).

1.2.2 The Quark-Parton Model and Bjorken scaling

Already in 1968, Bjorken predicted that the structure functions would depend only on one dimensionless variable in the high energy limit $Q^2 \to \infty$ at finite x (the "Bjorken limit"). This behaviour, represented by

$$F_i(x,Q^2) \to F_i(x), \qquad (1.11)$$

is kwown as *scale invariance* or *Bjorken scaling* [17, 18]. As we mentioned earlier, the resolution power of the exchanged particle increases with Q^2. If the proton consists of point-like constituents, it turns out to be possible to observe Bjorken scaling using finite Q^2 since an increase in the resolution does not change the way a point is observed.

The experimental results from SLAC [19] showed the scaling behaviour very clearly (figure 1.4) for F_2.

According to Feynman's parton model [20], the proton is composed of free point-like constituents, called partons. In this model the deep-inelastic ep scattering cross section is the incoherent sum of quasi-elastic e-parton scattering processes, that is

$$\frac{d\sigma(e^{\pm}p)}{dx\,dQ^2} = \sum_i \frac{d\sigma}{dx\,dQ^2}\,(e^{\pm} - \text{parton-}i)\ . \tag{1.12}$$

In the proton's infinite momentum frame all transverse momenta are negliglible and the Bjorken scaling variable x receives a simple interpretation: x corresponds to the fractional longitudinal proton momentum carried by the struck parton, i.e. the parton which interacts with the boson. This can be verified neglecting the proton and parton mass. For the parton after colliding with the boson

$$(\xi p + q)^2 = m^2 \approx 0\ ,$$

where ξp is the four-momentum of the initial parton in the proton. Operating with this expression

$$\begin{aligned} 0 &= (\xi p)^2 - Q^2 + 2\xi(p\cdot q)\ ; \\ \text{thus: } \xi &= \frac{Q^2}{2\,p\cdot q}\ , \end{aligned}$$

which is equal to the definition given above for x (Eq. (1.7)).

Taking Eq. (1.12) into account, the structure functions $\{F_i\}$ correspond to the sum of the parton momentum distributions weighted with the square of the electric charge of the parton[8]:

$$\begin{aligned} F_1(x) &= \frac{1}{2}\sum_i {e_i}^2 f_i(x)\ , \\ F_2(x) &= \sum_i {e_i}^2 x f_i(x) = 2x\,F_1(x)\ , \end{aligned} \tag{1.13}$$

where the functions $\{xf_i(x)\}$ are called *parton distribution functions* or simply *parton densities*, and describe the probability of finding a parton of type i in the proton carrying a fraction x of the proton momentum.

The relation between F_1 and F_2 is known as the Callan-Gross relation [21]. It holds exactly only for 1/2-spin partons which cannot couple to longitudinally polarised photons. The experimental confimation of this relation allowed the identification of Feynman's partons with Gell-Mann's quarks and the model was called the Quark-Parton Model (QPM). It should be mentioned that the fractional charge of the partons was confirmed using neutrino-nucleon scattering and the postulated number of three valence quarks in the proton and neutron was experimentally confirmed using the Gross-Llewellyn-Smith sum rule[9]

$$\int_0^1 \frac{dx}{2}\,({F_3}^{\nu p}(x) + {F_3}^{\nu n}(x)) = \int_0^1 dx\Big[u_v(x) + d_v(x)\Big] = 3\ , \tag{1.14}$$

which experimentally was found to be 3.2 ± 0.6 [22].

If the proton consisted only of charged quarks, their momentum would be expected to add up to the proton momentum, but experimentally it was shown that half of the momentum of the proton is carried by neutral partons. Direct evidence for the existence of these partons, called gluons, was provided at DESY via the observation of three-jet events in e^+e^- annihilation [23].

[8]Note that in this discussion, the single-photon exchange approximation is considered in order to simplify the expressions.

[9]This relation counts the number of valence quarks in the nucleon.

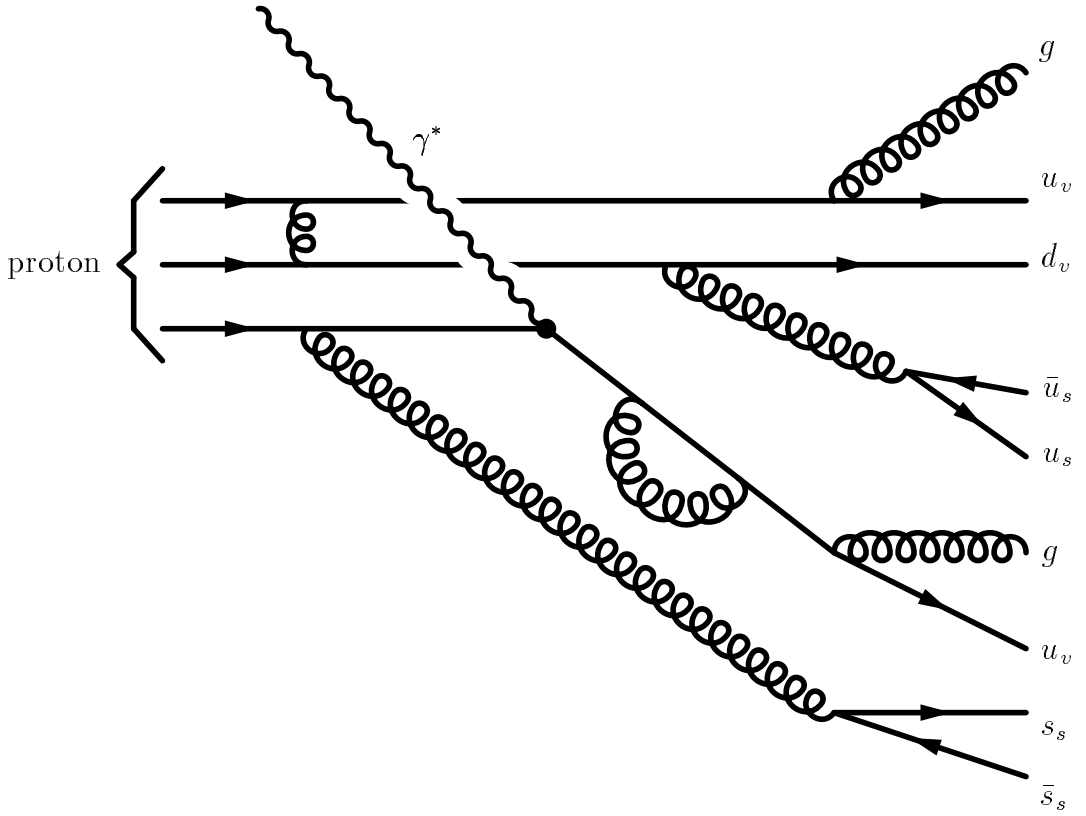

Figure 1.5: The structure of a proton interacting with a virtual photon. In addition to the three valence quarks defined in the quark model, the proton is made up of gluons and slow debris consisting of quark-antiquark pairs (the so-called sea quarks).

1.2.3 DIS and Quantum Chromodynamics

Although the Quark-Parton Model gives a good description of the experimental results for lepton-nucleon interactions at first order, it cannot explain how the partons are bound together to form the nucleon or other hadrons if the quark structure of hadrons introduced by Gell-Mann and Zweig is considered. It is necessary to add a force between the quarks/partons in such a way they are bound to form the hadrons.

Thus, the naive QPM has to be completed to get the QCD theory where the picture shows not only the three quarks which determine the quantum numbers of the proton (valence quarks). The proton is formed by quarks interacting through gluons, and radiating gluons which can split into quark-antiquark pairs (the so-called sea quarks) or more gluons (see figure 1.5).

In the 1970's QCD was developed as the field theory governing the strong interaction between quarks and gluons and therefore as the basis for the interaction between hadrons including the nuclear forces. QCD is a non-abelian gauge theory based on the SU(3) symmetry group. Each quark has three possible "charges" related to the colour quantum number and the strong interaction is mediated via the exchange of eight different coloured gauge particles, called gluons. The gluon always carry a combination of colour and anti-colour and the emission of one gluon change the colour number of the quark (anticolour for the antiquarks). Since the symmetry group of the colour quantum number ($SU(3)_C$) is non-abelian, the gluons also carry a net colour charge themselves and therefore couple to each other. This is the main difference

with QED[10], in which the photon is a neutral particle (and the group is the abelian $U(1)_{em}$).

The self-coupling of the gluon is the reason for the strong (QCD) coupling constant α_s to become large at small energies (large distances) and to decrease at high energies (small distances). This property of QCD is used to explain the observed behaviour of the strong interaction:

- **Asymptotic freedom**: at high energies (or small distances) the strong interaction proceeds via colour fields of reduced strength and the quarks and gluons behave as essentially free, non-interacting particles.

  This property is needed to explain why in deep-inelastic scattering the hard interaction between the boson and the parton can be calculated with non-interacting partons during the time scale in which the interaction takes place. That is, this property explains the success of the naive QPM approach even considering that partons are not free in time-scales longer than that of the hard-interaction in deep-inelastic scattering.

  As we will see in section 1.3, this property allows the application of perturbation theory to calculate scattering amplitudes.

- **Infrared slavery**: at low-energy (or large distances) the strength of the colour field is increasing (the potential behaves as $V(r) \sim \lambda r$) and in this way the quarks and gluons can never be observed as free particles. If two interacting partons are separated, the energy of the field increases so much that it creates new interacting particles and at the end (that is, at long time scales) we are left with colourless hadrons containing the partons. This is the way QCD explains the **confinement** of the partons, which are not observed as free particles at long time scales.

  It should be noted that the outgoing partons can be separated and observed as different objects, although each of these partons will be confined in a different hadron. What are not observed as free particles are coloured partons, although the partons, as well as their quantum numbers (except colour), can be studied experimentally.

This scale dependence of the strength of the interaction is translated into a dependence of α_s with energy, which is given by the so-called renormalisation group equation and the β function [14]

$$\mu^2 \frac{d\alpha_s}{d\mu^2} = \beta(\alpha_s) = -b{\alpha_s}^2 \left(1 + b_1 \alpha_s + \right), \tag{1.15}$$

where n_f is the number of active quark flavours (whose mass is smaller than the energy scale μ). The coefficients are calculated to be

$$b = \frac{33 - 2n_f}{12\pi},$$

$$b_1 = \frac{153 - 19n_f}{2\pi\,(33 - 2n_f)},$$

$$\dots$$

and α_s decreases with incresing the energy scale as long as $n_f < 17$. This is the first step for α_s to exhibit asymptotic freedom.

[10] In fact this is the only difference, since all the others are consequence of this non-abelian structure of QCD.

The solution of equation (1.15) to first order in an expansion in α_s is

$$\alpha_s(\mu) = \frac{\alpha_s(Q)}{1 + 2b\,\alpha_s(Q)\,\ln\left[\frac{\mu}{Q}\right]}\,, \tag{1.16}$$

which shows very clearly the asymptotic freedom property of QCD ($\alpha_s(\mu) \to 0$ for $\mu \to \infty$). Notice that the sign of b is crucial. With the opposite sign of b the coupling would increase with the scale μ, as it does in QED. The infrared slavery cannot be derived from this expression since it was obtained from a perturbative expansion valid when α_s is small enough, but it should be remarked that the coupling becomes large for smaller μ and perturbation theory breaks down. This could be an indication that the confinement of quarks and gluons inside hadrons is actually a consequence of the growth of the coupling at low scales [14].

It should be noted that the renormalisation group equation (1.15) tells us how is the dependence of the coupling contant with the scale, but not the absolute value itself. The latter has to be obtained from experiment. Thus we can choose as the fundamental parameter of the theory the value of the coupling constant at a given reference scale which is large enough to be in the perturbative domain. The common selection is the mass of the Z° boson. The value at any other large scale is completely defined by the evolution of the coupling constant with the scale.

An alternative approach, which was adopted historically and is still convenient for many purposes, is to introduce a dimensional parameter which is then considered as the fundamental parameter of QCD. This parameter (usually called Λ_{QCD}) is the energy scale at which α_s becomes large and the perturbative approach is no longer valid. It is formally defined by the expression [14]

$$\ln\frac{\mu}{\Lambda_{QCD}} = -\frac{1}{2}\int_{\alpha_s(\mu)}^{\infty}\frac{dx}{\beta(x)} = \int_{\alpha_s(\mu)}^{\infty}\frac{dx}{2bx^2\,(1 + b_1\,x + \cdots)}\,. \tag{1.17}$$

The introduction of Λ_{QCD} allows to write the asymptotic solution of the renormalisation group equation in terms of this parameter. In leading order (LO) we should retain only the b coefficient, and the integration yields:

$$\alpha_s(\mu) = \frac{1}{2\,b\,\ln(\mu/\Lambda_{QCD})} = \frac{12\pi}{2\,(33 - 2n_f)\,\ln\left[\frac{\mu}{\Lambda_{QCD}}\right]}\,, \tag{1.18}$$

which agrees with the expression in equation 1.16 for large scales.

Including the next-to-leading (NLO) contribution the definition of Λ_{QCD} leads to an implicit equation for the value of $\alpha_s(\mu)$:

$$\frac{1}{\alpha_s(\mu)} + b_1\,\ln\left[\frac{b_1\,\alpha_s(\mu)}{1 + b_1\,\alpha_s(\mu)}\right] = 2\,b\,\ln(\mu/\Lambda_{QCD})\,. \tag{1.19}$$

This equation could be solved numerically to obtain $\alpha_s(\mu)$ for a given value of Λ_{QCD}.

Alternatively, it is possible to obtain an approximate solution of this equation in terms of an expansion in inverse powers of $\ln(\mu/\Lambda_{QCD})$. This solution is [14]

$$\alpha_s(\mu) = \frac{1}{2\,b\ln(\mu/\Lambda_{QCD})}\left[1 - \frac{b_1}{b}\,\frac{\ln\left[2\ln(\mu/\Lambda_{QCD})\right]}{2\,\ln(\mu/\Lambda_{QCD})} + \cdots\right]\,, \tag{1.20}$$

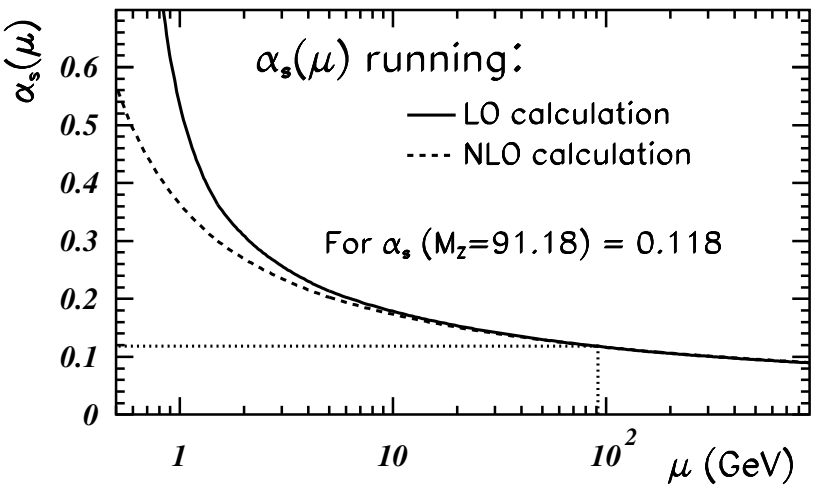

Figure 1.6: Running of the strong coupling constant with the scale, calculated at leading (LO, dashed line) and next-to-leading (NLO, solid line) orders of the perturbative expansion in QCD. The absoluted value of the constant was set to $\alpha_s(M_Z) = 0.118$ for both calculations. For the calculation the mass of the heavy quarks was set to 1.5 GeV, 5 GeV and 175 GeV for the c, b and t quarks, respectively.

where it should be noted that this expression corresponds to a different definition of Λ_{QCD} than the one before. The actual expansion related to the definition of Λ_{QCD} given in equation (1.17) would contain a term of order $1/\ln^2\left(\mu/\Lambda_{QCD}\right)$ which is missing. Equation (1.20) is then used as the definition of the corresponding Λ_{QCD}, which is most commonly preferred.

The use of Λ_{QCD} as the fundamental parameter of QCD presents several difficulties [14]. First, it can be multiply by a constant and the definition is equally acceptable since the change in α_s are one order higher in perturbation theory. Secondly, Λ_{QCD} depends on the renormalisation scheme. Finally, this parameter depends also on the number of active flavours. The presence of quarks with masses large enough can be taken into account with a scale-dependent number of active flavours. The usual approach is to define values of Λ_{QCD} for different number of flavours by imposing the continuity of α_s at the mass of the heavy quark.

For example, using the next-to-leading order solution obtained before, one can show that the continuity condition at the mass of the bottom quark (m_b), implies the following relation between the two Λ's (for four and five active flavours) [14]

$$\Lambda^{[4]}_{QCD} \approx \Lambda^{[5]}_{QCD} \left(\frac{m_b}{\Lambda^{[5]}_{QCD}}\right)^{\frac{2}{25}} \left[2\,\ln\left(m_b/\Lambda^{[5]}_{QCD}\right)\right]^{\frac{963}{14375}} \quad .$$

Figure 1.6 shows the dependence of the coupling on the scale for a value $\alpha_s(M_Z) = 0.118$. The dependence is displayed at leading and next-to-leading orders. It should be noted that the coupling constant decreases when increasing the scale (asymptotic freedom) while it increases very rapidly for $\mu \sim 1$ GeV, suggesting the presence of confinement.

Coming back to the structure functions of the proton, the inclusion of the gluon and the strong interaction dictated by QCD introduces some modifications to the conclusions derived in the previous section. The most obvious feature is that gluon radiation by the quarks results in a transverse momentum component on the partons. Consequently, quarks can couple to longitudinally polarised photons and the Callan-Gross relation is no longer satisfied exactly.

The longitudinal structure function is non-zero and, due to its origin, is largely dependent on the gluon content of the proton and is therefore considered to be a good measure of the latter [11].

A more important consequence of the gluon content of the proton are the so-called *scaling violations* of the structure functions, which exhibit a logarithmic dependence on Q^2 at fixed x. In QCD, this is interpreted as follows: at low Q^2 the resolution of the exchanged boson is rather broad, so that only just the quark substructure of the proton is "seen". At high Q^2, however, a finer resolution is achieved and quark-antiquark pairs originating from radiated gluons can be resolved. This means that the history of a quark before it interacts with the boson becomes very important. It could radiate a gluon and thus, although the quark which is struck has momentum fraction[12] x, the quark originally had a larger momentum fraction $z > x$ (this kind of process is known as the QCD Compton process). Alternatively it may be that a gluon with momentum fraction z produced a $q\bar{q}$ pair and one of these became the struck quark of momentum fraction x (this process is known as Boson Gluon Fusion, BGF).

Although the QPM description is not exact, the analytical tools described in section 1.2.2 are still useful. Specifically, the parton distribution functions can be kept including a dependence on the scale at which the proton substructure is resolved, $xf_i(x) \rightarrow xf(x, Q^2)$.

Considering all these modifications, now we should take into account that the quark and gluon distribution functions $zf(z, Q^2)$ for all momentum fractions z such that $x < z < 1$ contribute to the given reaction via QCD-Compton or BGF processes. At large x, where valence quarks dominate, the quark density and hence F_2 falls with Q^2 as a result of the gluon radiation, while at small x the amount of $q\bar{q}$ pairs which configures the partonic 'sea' increases, so that F_2 rises with Q^2. These scaling violations in conjunction with a strong rise at small x for fixed Q^2, which are clear predictions by QCD, have been observed experimentally, by the H1 and ZEUS experiments at HERA [25, 26], as can be seen in figure 1.7.

It should be noted that the presence of all these effects in the description of DIS processes is what allows the study of the strong interaction by using the multihadronic final states in *ep* collisions.

1.2.4 The Breit or brick-wall frame

The Breit frame [18, 27], also called the brick-wall frame, is defined as the frame where the exchanged boson and the proton collide face to face and no energy transfer occurs between the lepton and the hadronic side of the process.

In a mathemathical form, the general expression to define this frame is given by

$$2x\vec{p} + \vec{q} = 0\,, \tag{1.21}$$

where $\vec{p}$ and $\vec{q}$ are the three-momenta of the incoming proton and the exchanged boson, respectively.

It is very common to define the z-axis in the Breit frame by means of the three-momentum of the incoming proton, and if we define $Q \equiv \sqrt{Q^2}$, then the four-momentum of the exchanged boson, as seen in the Breit frame is fixed to

$$q = (0, 0, 0, -Q)\,. \tag{1.22}$$

[11] Unfortunately, the measurement of F_L is experimentally very difficult, particularly at HERA [24].

[12] It should be noted that x cannot longer be related to the fraction of the proton momentum carried by the parton, but it is still an useful kinematic variable.

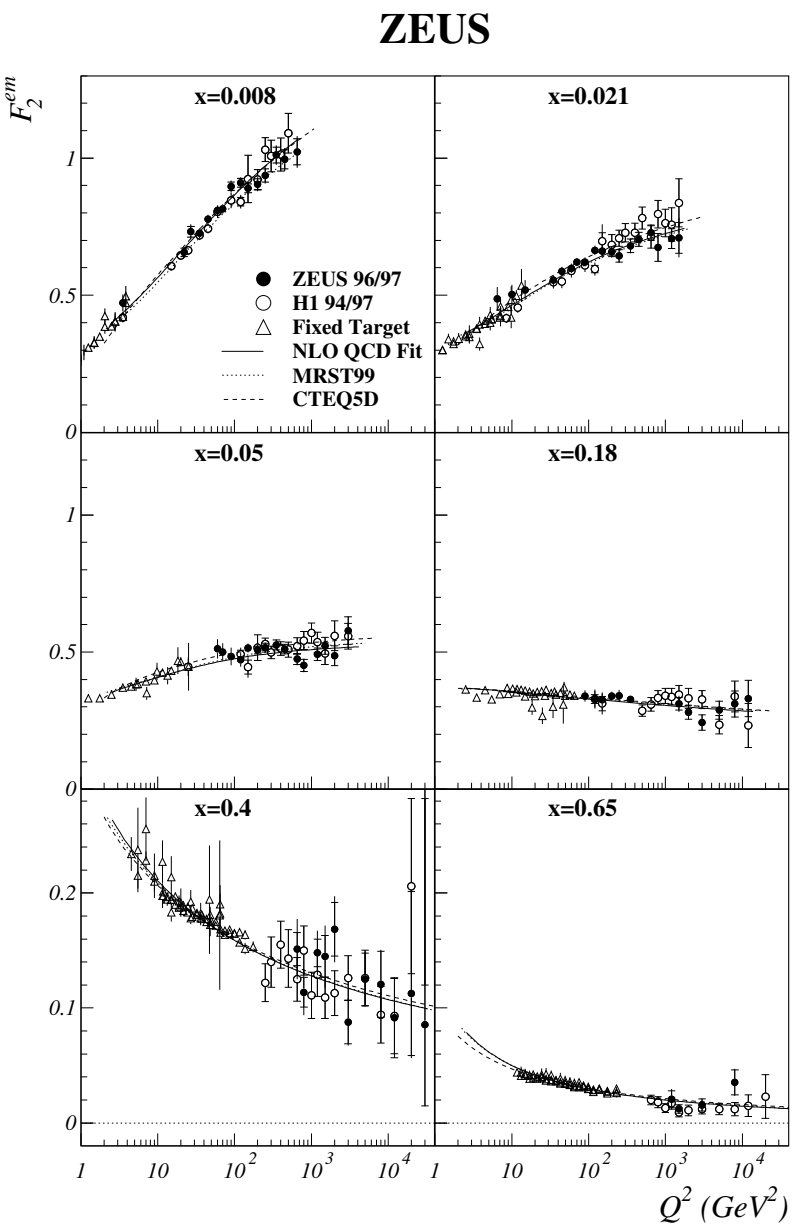

Figure 1.7: The results from ZEUS (solid points) for F_2^{em} versus Q^2, for six values of x, are compared with results from NMC, BCDMS, E665 (triangles) and H1 results (open symbols) [26]. A behaviour close to Bjorken scaling for intermediate x values and Q^2 not very small is observed. The scaling violations predicted by QCD are clearly observed for low x and high x values.

In the Quark-Parton model (see section 1.2.2), the initial quark collides face to face with the boson. The struck quark is then scattered back in the same axis, since no transverse component is provided by the boson. On the other hand, when contributions from QCD are present the situation is slightly different since with two or more partons, it is possible to have partons out of the z-axis without violating any conservation law.

All these situations are displayed in figure 1.8 for the lowest order processes. In the Born process, the struck quark is scattered back and with the same energy as the incoming quark[13].

[13]This is why this frame is also called the "brick-wall" frame.

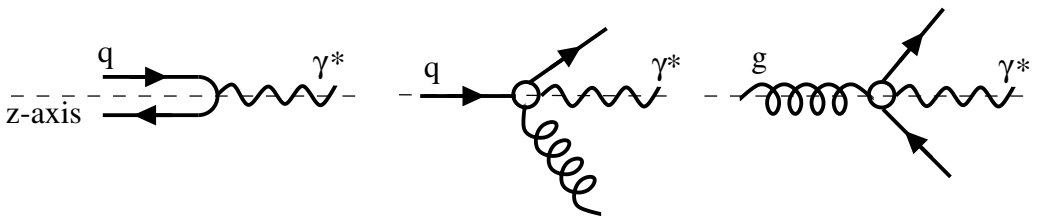

Figure 1.8: Schematic diagrams of the Born, QCD Compton and Boson-Gluon fusion processes in the Breit frame (from left to right). The processes with contributions from QCD allow the presence of partons which are not collinear to the colliding particles, while in the Quark-Parton model all the particles in the hadronic part of the event are contained in the z-axis.

In fact their four-momenta are fixed to be:

$$p_q = (Q/2, 0, 0, Q/2) \quad \text{and} \quad p_{q'} = (Q/2, 0, 0, -Q/2)\,, \tag{1.23}$$

after requiring the conditions mentioned previously.

In the two remaining plots in figure 1.8, the QCD Compton and Boson-Gluon Fusion processes are presented to show how with QCD contributions it is possible to have partons with transverse components (in the x-y plane).

This property results in the main advantage when using the Breit frame. The presence of transverse momentum in the Breit frame belonging to the hadronic system is always related to QCD processes, in the sense that they have to be described by including contributions from QCD.

1.3 The perturbative QCD framework

As was already discussed in the previous section, QCD gives a very successful description of the strong interaction, containing in a very natural way the properties of asymptotic freedom and confinement. However, these properties make especially difficult to obtain predictions for the soft limit, where hadrons live and are observed in the experimental setup. Nevertheless, the coupling constant can be kept small in some process and the usual perturbative approach can be applied giving rise to a predictive power never achieved before in hadron physics. This section gives a description of the way perturbative QCD (pQCD) is actually implemented in order to provide quantitative predictions.

1.3.1 The perturbative QCD approach

From the Lagrangian density for QCD different couplings appear in the theory. They can be related to the following processes:

- **A (anti)quark radiating a gluon**, which is dictated by the quark-gluon coupling which, in turn, is formally equal to the coupling between an electric charge and the electromagnetic field. The same coupling is related to the process in which a **gluon splits into a quark-antiquark pair**.

- **A gluon splitting into two or three gluons**, which is dictated by the self-interaction coupling of the gluon.

These processes are proportional to the strong coupling constant, so if the energy scale associated to the process is large enough, then the coupling is small and the interaction can be described by a perturbative expansion. This expansion allows the equations describing the processes to be solved in the limit where the strong coupling constant is small (*"hard processes"*). On the other hand, if the energy scales are small, i.e. the interacting partons become further apart, then the strong coupling constant becomes very large and the perturbative approach is no longer valid.

In order to be able to make predictions for the measurements performed in a collider, QCD should be studied in reactions in which the hard processes are dominant versus the non-perturbative ones. Usually the hard process occurs as a first step in the collision and afterwards, the soft, non-perturbative, process gives rise to the final-state hadrons (*hadronisation*) from the partons taking part in the hard process. Perturbative QCD is applied to obtain predictions for the partons dynamics, and the results can be considered reliable if the hadronisation process does not hide the properties of the partonic state; that is, if the experimental measurement can be related to the parton dynamics in some direct way.

Even in the region where perturbative QCD can be applied, additional difficulties are present in the calculations. In the same way as in QED, different types of divergences appear when the vacuum fluctuations (*UV divergences*) or radiation of partons with very small relative transverse momentum with respect to the original parton (*IR divergences*) are included. Both are dealt with by following the standard regularisation procedures. This mechanism is very often called *renormalisation* when it is applied to get rid of the UV divergences. To remove the IR divergences the regularisation is made selecting observables which are insensitive to these particular divergences. This type of observable is called *infrared-safe* and is usually constructed in such a way that the result doesn't change in case an IR-divergent process appears in the calculation.

The use of infrared-safe observables allows a complete separation of the hard process from the soft process in a formal way, and in this way perturbative QCD predictions can be obtained for those observables, which then avoid the divergences without any additional treatment.

When the interaction contains hadrons in the initial state, as in the case of deep-inelastic scattering, it is imposible to be fully insensitive to the soft phenomena (including IR divergences) occuring within the hadrons, or in the steps leading from the free, initial hadron to the hard interaction. In that case, a complete regularisation mechanism is needed to separate (factorise) the theoretical description into a calculable hard and a soft part. This mechanism is called *factorisation* and is very similar to the renormalisation procedure. We will describe both in the next sections.

1.3.2 Renormalisation

The UV divergences arising from loop integrals associated to vacuum fluctuations are dealt with by renormalising the bare parameters in the lagrangian, which are not observable, to the physical (observable) ones. The procedure is not unique, i.e. there is a renormalisation scheme choice which is chosen depending on the properties of the parameters which are needed in the calculation. Of course, the physical results cannot depend on this choice; however, a theoretical

dependence is usually obtained in pQCD since the perturbative expansion is performed only to a given order. The renormalisation scheme determines the values of the physical parameters when calculated to a given order in the pertubative approach. The $\overline{MS}$ renormalisation scheme is the most widely used[14].

In the renormalisation procedure a scale μ_R is needed to set the scale at which the renormalisation is performed. At a fixed order in perturbation theory, a dependence on this scale is introduced in the predicted value of an observable. Of course, any physical observable should be invariant under variations of this scale. This is formally expressed using the renormalisation group equation by

$$\mu_R{}^2 \frac{d}{d\mu_R{}^2} \mathbf{\Gamma} = 0 \ , \tag{1.24}$$

where $\mathbf{\Gamma}$ is the observable we are interested in. In the perturbative approach, this equation has to be applied to the perturbative expansion of the observable, and in pQCD we have

$$\mathbf{\Gamma} = \mathbf{\Gamma_0} + \alpha_s \, \mathbf{\Gamma_1} + \alpha_s{}^2 \, \mathbf{\Gamma_2} + \cdots$$

and the renormalisation group equation transforms into

$$\mu_R{}^2 \frac{d}{d\mu_R{}^2} \sum_{j=0}^{N} \alpha_s{}^j \mathbf{\Gamma_j} = \mathcal{O}(\alpha_s{}^{N+1}) \ , \tag{1.25}$$

that is the variation of the observable with the scale is given by terms which were not included in the perturbative expansion.

It is very common to use this relation to estimate the size of the theoretical uncertainty of the observable coming from the truncation of the perturbative expansion at order N in α_s. This estimation is obtained by analysing the variation of the pQCD theoretical prediction with the renormalisation scale; that is by computing the prediction for different choices of this scale one can estimate the size of the truncated orders in the series.

1.3.3 Factorisation

In order to separate the infrared-divergent phenomena within the hadrons in the initial state from the hard interaction calculable in pQCD, the soft processes are isolated and factorised out in the parton distribution functions (PDFs). The PDFs are not calculable in pQCD, but can be determined from the experimental results. The universality of the parton distribution functions allows to make predictions for a process after measuring the PDFs in another, so that the predictivity of the theory is not lost. The hard-scattering factorisation has been proved to hold for a different number of processes and it is summarised in the following expression for a cross section (it can be generalised to any obervable) for lepto-hadron scattering:

$$\sigma(P_1, P_h) = \sum_i \int d\xi \, f_i(\xi, \mu_F{}^2) \, \hat{\sigma}(P_1, \xi P_h, \alpha_s(\mu_R), \mu_R, \mu_F) \ , \tag{1.26}$$

[14] Another common choice is the DIS scheme which has the property that at any order in the perturbative expansion the structure functions are computed as linear combinations of the quark distribution functions, as shown in Eq. (1.13). This property is not preserved in other renormalisation schemes, including the $\overline{MS}$ scheme.

where P_1 is any parameter to characterise the final state; P_h is the four-momentum of the incoming hadron; the sum is over all the flavours; f_i are the parton distribution functions evaluated at the *factorisation scale* μ_F; and $\hat{\sigma}$ is the lepton-parton cross section which is calculable in pQCD.

Thus, the factorisation procedure introduces an additional scale and the prescription to be followed (factorisation scheme) is not unique; the physical results are independent on the scheme and on the factorisation scale. In a similar fashion to the renormalisation procedure, the parton distribution functions are regularised to bury infrared divergences coming from configurations where soft and collinear partons are emitted.

This factorisation scale is related to the scale that separates soft and hard processes occuring in the parton system which configures the initial-state hadron. In practice, this scale separates what occurs "inside" and "outside" the hadron, being the "outside" region where the hard process occurs and where the perturbative approach can be applied.

Perturbative QCD is not able to give the value of the parton distribution functions, but it is possible to obtain predictions about the variation with the scale that arises from the factorisation procedure using the evolution equations (see section 1.3.4). The equations provide resummations of terms from the perturbative expansion and introduce a known dependence of the $\{f_i\}$ on the scale.

For some observables, like the ones used in hadron production, the theoretical predictions are not completely infrared-safe since the process transforming the final-state partons into the observable hadrons (also known as *fragmentation*) is not free of new divergences. The kind of divergences that appear are the same as those removed using the factorisation mechanism, but now related to the final state processes. When this kind of observables is under study, a new regularisation procedure is needed, so as to absorbe all these divergences into *fragmentation functions*, which again factorise in the expression to compute the observable. These functions are the equivalent of the parton densities, but now giving the information on the probability for a parton to transform into a given hadron with the corresponding momentum fraction and energy scale. Since in the analyses in which the final state is studied by using jets this kind of regularisation is not needed and the observables are quite independent of the fragmentation functions[15], we don't go deeper into this aspect of the factorisation procedure.

The isolation of all divergences for any process in deep-inelastic scattering has left as inheritance the residual and non-physical dependence of the prediction on, at least, two scales. These dependencies characterise the precision of a calculation and if the changes produced by the scale variations are large, the next order(s) has to be calculated to gain accuracy in the theoretical predictions. In some cases, some terms which appear at all orders are identified and resummed, improving in this way the accuracy of the predictions. An example of this resummation are the evolution of the PDFs or the calculation of the running of the strong coupling constant.

1.3.4 Evolution equations

The interactions between partons inside the hadrons lead to a dependence of the predictions on the partons with momentum fraction of the hadron larger than x, as we described above (see

[15]In the studies of jets, the effects of fragmentation processes are estimated by studying the differences of applying the jet algorithm to the partons and to the hadrons. The differences are given by the various models of the hadronisation process, which indirectly include the fragmentation functions.

section 1.2.3). This dependence can be introduced in the following way: the parton density associated to one parton type is given by the processes which directly or indirectly generate partons of that type. For example, the gluon content is partly driven by the probability of the quarks to radiate a gluon.

As already mentioned, perturbative QCD is not able to predict the values for the parton distribution functions $\{f_i(x,\mu^2)\} = \{q_i(x,\mu^2), g(x,\mu^2)\}$, but it can give predictions for its evolution; that is, given all the parton densities at a given scale for all x, pQCD can predict the values for each parton density at other scales.

To do this, pQCD allows the construction of a set of integro-differential equations known as "Altarelli-Parisi equations" [28], which can be formally written as follows:

$$\begin{aligned}
\frac{dq_i(x,Q^2)}{d\ln Q^2} &= \frac{\alpha_s(Q^2)}{2\pi}\int_x^1 \frac{dy}{y}\left[q_i(y,Q^2)\mathcal{P}_{qq}(x/y) + g(y,Q^2)\mathcal{P}_{qg}(x/y)\right], \\
\frac{dg(x,Q^2)}{d\ln Q^2} &= \frac{\alpha_s(Q^2)}{2\pi}\int_x^1 \frac{dy}{y}\left[\sum_i \left(q_i(y,Q^2)\mathcal{P}_{gq}(x/y)\right) + g(y,Q^2)\mathcal{P}_{gg}(x/y)\right],
\end{aligned} \tag{1.27}$$

where the splitting function $\mathcal{P}_{kl}(z)$ represents the probability of a parton l emitting a parton k with momentum fraction z of the parent parton.

It is easy (see [6, 14]) to obtain the pQCD expressions for these splitting functions at first order in α_s by simply analysing the radiative process and the associated couplings for the radiative processes contributing to these evolution equations, which are shown in figure 1.9. The expressions associated to these diagrams lead to the results

$$\begin{aligned}
\mathcal{P}_{qq}(z) &= \frac{4}{3}\,\frac{1+z^2}{1-z}, \\
\mathcal{P}_{qg}(z) &= \frac{1}{2}\,\left[z^2+(1-z)^2\right], \\
\mathcal{P}_{gq}(z) &= \mathcal{P}_{qq}(1-z) = \frac{4}{3}\,\frac{1+(1-z)^2}{z}, \\
\mathcal{P}_{gg}(z) &= 6\,\left[\frac{z}{1-z} + \frac{1-z}{z} + z(1-z)\right].
\end{aligned} \tag{1.28}$$

In the context or perturbative QCD two types of terms can become large and hence important in the perturbative expansion in $\ln Q^2$ and in $\ln(1/x)$. Depending on which terms are considered on each case the evolution equations lead to different results and different regions of application.

DGLAP evolution

The equations describing the so-called DGLAP evolution (Dokshitzer, Gribov, Lipatov, Altarelli and Parisi) [28, 29] are formally derived in the leading logarithm approximation (LLA), where terms of the form ${\alpha_s}^n \cdot (\ln Q^2)^n$, which give the dominant contribution at large Q^2 and large x, are summed to all orders. In a field theory having asymptotic freedom such an approximation proves to be asymptotically exact. The amplitude for the inelastic ep scattering process can be obtained as the sum of ladder diagrams of consecutive gluon emissions (figure 1.10) thus losing, gradually, its longitudinal momentum. If the rungs of the gluon ladder are labelled 1 to n from

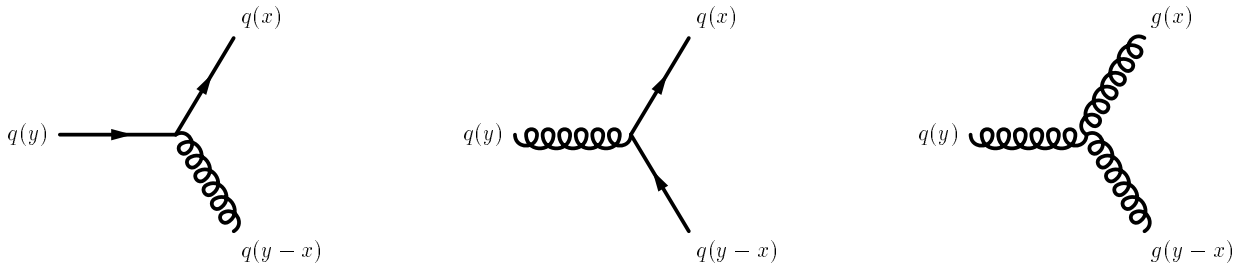

$\mathcal{P}_{qq}(\frac{x}{y}) = \mathcal{P}_{gq}(\frac{y-x}{y})$ $\mathcal{P}_{qg}(\frac{x}{y}) = \mathcal{P}_{qg}(\frac{y-x}{y})$ $\mathcal{P}_{gg}(\frac{x}{y}) = \mathcal{P}_{gg}(\frac{y-x}{y})$

Figure 1.9: The splitting functions at lowest order in α_s. The diagram on the left shows the gluon radiation by a (anti)quark and the two diagrams on the right show the gluon splitting into two partons.

the proton to the photon, the fraction of longitudinal momentum x_i carried by the rungs are ordered

$$x_1 > x_2 > x_3 > \ldots > x_n \ ,$$

while the transverse momenta of the emitted gluons increase strongly as going up the ladder

$${k_{t,1}}^2 \ll {k_{t,2}}^2 \ll \ldots \ll {k_{t,n}}^2 \ll Q^2 \ .$$

The solution of the DGLAP equations give the parton distributions as a function of x at any Q^2, provided their x dependence at an input scale ${Q_0}^2$ is known. The latter cannot at present be calculated and are determined experimentally.

At small x, the $\ln(1/x)$ terms entering the cross section become important. In the moderate region, where $\alpha_s(Q^2)\ln Q^2 \ll 1$ and $\alpha_s(Q^2)\ln(1/x) \ll 1$, but $\alpha_s(Q^2)\ln Q^2 \ln(1/x) \sim 1$, the so-called Double Leading Logarithm Approximation (DLLA) is used. In this approach leading terms in $\ln(1/x)$ are summed when they are accompanied by a leading $\ln Q^2$.

In the solution of these equations, the gluon density presents a very steeply rise at small x, a rise which is faster than any power of $\ln(1/x)$, but slower than any power of x. However, over a limited x, Q^2 range, as in the case of HERA, it may mimic a power behaviour.

BFKL and other evolution equations

The steep behaviour of the gluon density and hence of F_2 at low x has led to further developments in pQCD. In the low-x region the DLLA approach is not enough and it is appropriate to sum contributions which are leading in $\ln(1/x)$ independent of $\ln Q^2$. This calculation has been done by Balitzki, Fadin, Kuraev and Lipatov [30], resulting into the BFKL evolution equations. Summing $(\alpha_s \cdot \ln(1/x))^n$ terms involves the evolution of a gluon distribution which is not integrated over k_t and the gluon ladder does not have to be ordered in k_t anymore (rather it involves a 'random walk in k_t').

The solution to the BFKL equation to leading order in $\ln(1/x)$ and fixed α_s has a very steep power law behaviour, which would violate unitarity in the limit $x \to 0$. However, the current form of the equations does not incorporate the running of α_s with Q^2 and the kernel has only

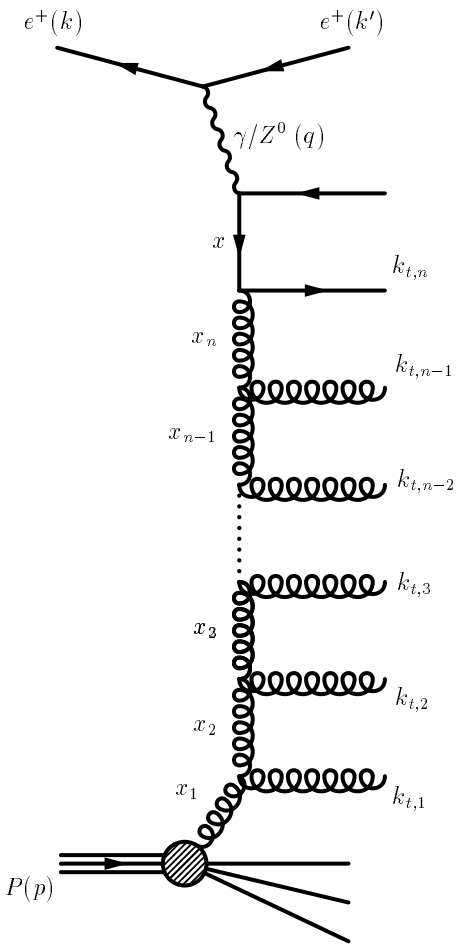

Figure 1.10: A ladder diagram initiated by a gluon in the proton. This kind of ladder illustrates how the parton evolution in the DGLAP equations is taken into account.

been calculated to first order in $\ln(1/x)$. Furthermore cut-offs have to be introduced in the integral in the infrared and ultraviolet limits.

Due to all these problems and the difficulties of BFKL to deal with Q^2 evolution, progress has been made to achieve an 'unified' treatment of the x and Q^2 dependencies of the parton distributions and structure functions throughout the kinematic plane. The most important is the development of the so-called CCFM equation (Catani, Ciafaloni, Fiorani and Marchesini) [31]. It is based on the idea of coherent gluon radiation, which leads to angular ordering of gluon emission in the gluon ladder. The maximum angle of gluon emission is specified by an additional scale, which can be taken to be the Q^2 of the probing photon.

At small x the CCFM equation reproduces the BFKL behaviour, while at moderate x it reproduces the DGLAP equation for the integrated gluon density $g(x, Q^2)$ [32]. It should be mentioned that technically the CCFM equation involves similar limitations as the BFKL equation such as the incorporation of the running of α_s and the UV and IR cut-offs.

Shadowing

The considerations so far have yielded a steeply rising gluon density at small x. If this were the asymptotic behaviour of the gluon density, the unitary bound would eventually be saturated or even violated.

On the other hand, all the evolution equations discussed above are linear integro-differential equations as they deal with the emission of gluon from quarks or the gluon splitting into quarks or additional gluons. However, as $x \to 0$ the gluon density becomes very large, and the self-coupling gluons may annihilate, or recombine into gluons. Such gluon *shadowing* or *screening process* may compete with the standard evolution and eventually saturates the gluon density.

A measurement at Q^2 probes a parton of transverse size $\sim 1/\sqrt{Q^2}$. Assuming a homogeneous distribution of gluons in the proton, the $xg(x,Q^2)$ gluons occupy a transverse area of order $xg(x,Q^2)\frac{\pi}{Q^2}$ which increases with decreasing x. If this area gets comparable to the transverse area of the proton, shadowing effects are expected to emerge.

For a proton radius of 1 fm and $Q^2 \sim 10$ GeV^2, this limit is reached at $xg(x,Q^2) \sim 250$, which is well above the values found at HERA. Other models (like the scenario of 'hot spots' [33]) quote the relevant area to be smaller. In any case, no evidence for such an effect has so far been seen at HERA.

In order to take the recombination of gluons $gg \to g$ into account, Gribov, Levin and Ryskin added a quadratic correction to the evolution of the gluon distribution, yielding the so-called GLR equation [34]. This equation can only be considered an approximation since possible interactions of gluons ladders before the recombination are not included and multi-ladder diagrams may also be important.

1.3.5 Modern parametrisations of parton densities

The measurement of structure functions serves two main purposes: to test QCD as the theory of the strong interactions and to extract the, as yet, uncalculable parton distribution functions and use them as input to obtain predictions for other processes. In this section the most recent parametrisations of the proton parton densities are introduced. Most of them are obtained using the DGLAP evolution equations to evolve the parton densities to the measured values of Q^2. The x dependence of the parton densities is parametrised from a starting scale ${Q_0}^2$. The parameters are determined by a χ^2 minimisation over data from structure functions in deep-inelastic e, μ or ν scattering, measurements of Drell-Yan production and W-asymmetry in $p\bar{p}$ collisions as well as prompt photon production $pN \to \gamma X$.

Martin-Roberts-Stirling (MRS)

The MRS parametrisation, obtained by using the next-to-leading order DGLAP equations, uses the following functional form for the quark and gluon distributions at the starting scale ${Q_0}^2$ in the $\overline{MS}$ renormalisation scheme:

$$xf_i(x,{Q_0}^2) = A_i \cdot x^{\delta_i}(1-x)^{\eta_i}(1+\epsilon_i\sqrt{x}+\gamma_i x)\ , \tag{1.29}$$

where f_i is a particular parton density and $\{A_i, \delta_i, \eta_i, \gamma_i\}$ are the parameters to be fitted. Not all the normalisation factors A_i are free parameters, but some are fixed from flavour or momentum sum rules. The charmed sea, assumed to be zero at the starting scale, is generated by gluon splitting as included in the DGLAP equations for massless partons.

One of the recent parametrisation of the parton densities coming from this group is the set denoted by MRST98 [35] and the corrected version MRST99 [36], which has been used in the analyses presented in this thesis. These parametrisations have been obtained by using very recent experimental measurements and the fits are done in different configurations, which allow

the studies of the dependence on the α_s value or the uncentainty due to that of the gluon density for the perturbative QCD predictions. This kind of study has been performed in the analysis presented here and is explained in section 5.1.

CTEQ Collaboration parametrisations

The 'Coordinated Theoretical-Experimental Project on QCD' (CTEQ Collaboration) uses a very similar approach to the MRS group. For the quark distributions the same functional form as in equation (1.29) is chosen, whereas the gluon density is parametrised as

$$xg(x, {Q_0}^2) = A_0 x^{A_1}(1-x)^{A_2}(1+A_3 x^{A_4}) \; . \tag{1.30}$$

CTEQ chooses a slightly different set of data for constraining the strange quark distribution. Furthermore, they do not suppress the charm distribution below the mass threshold but use the 'variable flavour technique'.

In 1996, the CTEQ Collaboration presented the set of distributions known as CTEQ4 [37]. This is one of the parametrisation sets used in the analyses for the pQCD predictions. There is a more recent parametrisation by this collaboration which is also used, named CTEQ5 [38]. Although it is more recent, this set is used only as a cross check of the results given by other parametrisations. This is because the CTEQ4 set has the advantage that parton densities are available for different values of α_s. These are needed for the determination of the strong coupling constant from the comparison of the measured values with the predictions, as it is described in section 5.4.

Glück-Reya-Vogt

Whereas the parton distributions of the MRS and CTEQ groups depend strongly on the input parametrisations at ${Q_0}^2$ this is, to a much lesser extent, the case for the GRV group [39]. Their basic idea was that at a very low starting scale (${Q_0}^2 = 0.34$ GeV^2) the nucleon only consists of constituent valence quarks. With increasing Q^2 the gluon and sea quarks would be generated dynamically from the valence quarks via the DGLAP evolution equations. As not all relevant data, in particular the prompt photon data, could be described adequately with this model, gluon and sea quarks had to be added at the starting scale. However, these distributions have a valence-like shape of the form

$$xg(x, {Q_0}^2) = A x^{\alpha}(1-x)^{\beta} \; . \tag{1.31}$$

Charm is treated as a heavy quark. In this approach, there is no such a concept as charm parton distribution. Its contribution to F_2 comes from gluon splitting and it is calculated via the DGLAP evolution with massive-quark coefficient functions. The DGLAP evolution from the very low starting scale ${Q_0}^2$ ensures that the behaviour of the gluon and sea quark densities at small x for $Q^2 \gtrsim 1$ GeV^2, as described by GRV, is nearly a parameter free prediction of perturbative QCD.

1.4 Jet physics

High-energy quarks and gluons are not directly observed due to the confinement of colour charge in QCD. Instead they are revealed through the appearance of *jets*, collimated flows of hadrons, that can be reconstructed from the observed particles, and thus relate the final jets of hadrons to

the original partons emerging from the interaction. To make a quantitative comparison between theory and experiment, one must go beyond a qualitative definition and use a precise algorithm for defining a jet. This algorithm has to be able to specify a jet configuration unambigously both in theoretical calculations and in the experiment.

1.4.1 Jet algorithms

Jet algorithms are not uniquely defined and the experimental results depend on the criteria used to define a jet. However, a well designed jet algorithm must have some basic properties: it must be easy to apply to the measured hadronic final state and infrared-safe so that the cross sections can be calculated order-by-order in perturbation theory. In perturbative QCD there is a collinear divergence when any of two massless partons are parallel. In the calculation of the total cross section this divergence is cancelled by the contribution from the virtual correction to the equivalent process, with the two partons replaced by their sum. However, for this cancellation to take place also in the jet calculation, it is necessary to ensure that a collinear pair of particles are treated identically as a single particle with their combined momenta. From the experimental point of view, the equivalent problem is the fact that parallel particles go into the same calorimeter cell and cannot be resolved. Likewise the requirement of infrared safety, i.e. insensitivity to emission of low energy particles, is necessary in perturbative calculations to avoid the soft divergence and in the experiment to avoid bias from the threshold trigger of the calorimeter cells and the background noise.

A clear difficulty in choosing a jet definition is that the latter most likely depends on the kind of high-energy scattering under consideration. Although the basic hard scattering processes studied in the different types of collisions can be described within the same theoretical framework, the overall event structure is quite different. In e^+e^- annihilation into hadrons, the initial state is purely leptonic and the entire final state can be thought of as arising from the virtual boson which creates a $q\bar{q}$ pair. Therefore, all the hadrons in the final state are associated with the hard scattering process. In contrast, in hadron (lepton)-hadron collisions, there are different contributions to the overall final state: only a fraction of the final-state hadrons are associated with the hard scattering process, and the remainder form part of the beam remnants or come from eventual $soft$ (i.e. small transverse momentum) interactions of the remaining partons in the incident hadrons. Moreover, since only a fraction of the initial energy of the incoming hadron takes part in the hard process, the angular distribution of the final-state particles could be affected by the boost in the longitudinal direction.

As a general rule, any jet definition should satisfy the conditions of being

i) collinear and infrared safe (see [40] for more details);

ii) easy to apply in experimental analysis to the hadronic final state and to the order-by-order calculations in pQCD to the partons in the final state;

iii) little sensitive to hadronisation corrections. Having small hadronisation corrections entails a closer correspondence between the measurements from final state hadrons and the parton dynamics.

In the case of hadron-hadron and lepto-hadron collisions, the jet definition should also fulfill the additional requirements of being

iv) able to factorise the collinear singularities arising from the initial state hadron into universal parton densities; that is, the algorithm has to conserve the factorisation properties of pQCD;

v) not strongly affected by contamination from hadron remnants or additional soft processes;

vi) longitudinally invariant. That is, the definition of distances to define a jet as a "collimated set of particles" has to be done in terms of quantities which are invariant under longitudinal boosts[16].

One of the first attempts to define jet cross sections in perturbation theory was made by Sterman and Weinberg for e^+e^- collisions [41]. They showed how to define cross sections free of singularities by integrating over finite ranges of energy and angle. The cross section for the process $e^+e^- \to q\bar{q}g$ has the form

$$\frac{1}{\sigma}\frac{d^2\sigma}{dx_1\,dx_2} = C_F\frac{\alpha_s}{2\pi}\frac{{x_1}^2+{x_2}^2}{(1-x_1)(1-x_2)}\,,$$

where x_1, x_2 are the energy fractions of the final-state quark and antiquark ($x_i = 2\cdot E_i/\sqrt{s}$). This cross section has a singularity when one or both x_i are close to one. This corresponds to the collinear and infrared singularities in the gluon emission. For this process, Sterman and Weinberg introduced the quantity $\sigma_2(s,\theta,c,\delta)$, which is the two-jet cross section, defined for all events where a fraction $(1-c)$ or more of the total energy $\sqrt{s}$ is emitted within two opposite cones of half-angle δ, making an angle θ with the beam axis (see figure 1.11). The total cross section for this process at first order in α_s can be written as an incoherent sum of two and three-jet cross section $\sigma = \sigma_2 + \sigma_3$. The fraction of two-jet events is then written as

$$\frac{\sigma_2}{\sigma} = 1 - 8\,C_F\,\frac{\alpha_s}{2\pi}\left[\left(\ln\frac{1}{\delta}\right)\left[\ln(\frac{1}{2c}-1) - \frac{3}{4} + 3c\right] + \frac{\pi^2}{12} - \frac{7}{16} - c + \frac{3}{2}c^2 + \mathcal{O}(\delta^2\ln c)\right]$$

which is free of any soft divergences as far as δ and c take reasonable and finite values.

At higher orders in perturbation theory, the final state can consists of more than three jets. It turned out that this algorithm is not well-suited to analyze these multijets events, and new algorithms were developed to improve the measurements of jet cross sections and the comparison with the theoretical calculations.

At present there are essentially two classes of algorithms in use: cone-type algorithms and cluster-type algorithms of the type first introduced by the JADE collaboration [42]. The cone-type algorithms are essentially modifications of the original Sterman-Weinberg algorithm to adapt it at the process under study and to partially avoid the difficulties of using this algorithm in multijet final states.

Generally, the cone-type algorithms define the jets using fixed geometrical structures which are positioned in the angular space occupied by the particles in such a way that the energy or the transverse energy is maximised. To specify an algorithm of this kind, the only requirements are the geometrical definition of the 'cone' (usually is a circle in the angular space with a given radius) and the criterion to be followed if two or more of these 'cones' overlap.

The cluster-type algorithms [42, 43] are characterised by successively finding pairs of particles that are 'nearby' in phase-space and merging them together to form new 'pseudoparticles'

[16] "Longitudinal" means along the initial hadron(s) direction.

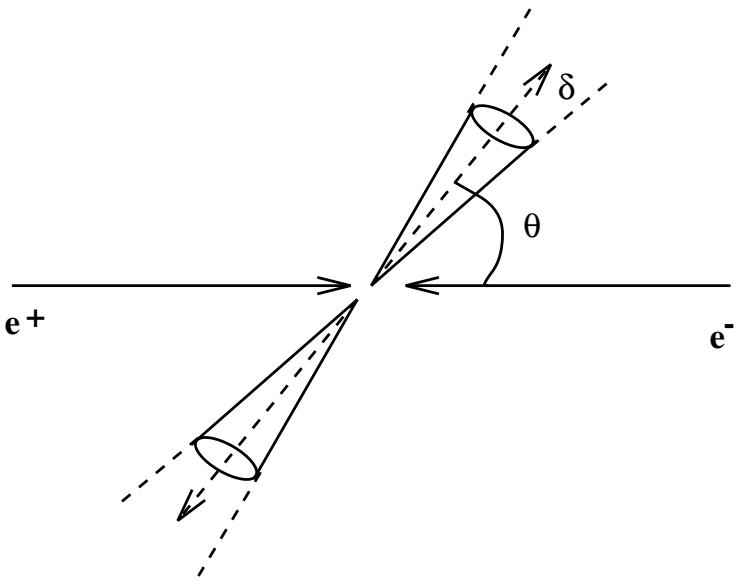

Figure 1.11: Sterman-Weinberg jet algorithm for e^+e^- interactions. The jets are studied by considering the energy distribution in the event adding up the energy within two opposite cones whose central axis forms an angle θ with the axis containing the incoming particles.

which are then considered in the next iteration (instead of the two original ones). To specify this kind of algorithm, a definition of distance is needed to decide what 'nearby' particles means in a quantitative way. As an additional requirement, usually some scale is needed to stop the iterative procedure and to define the final jets from the pseudoparticles.

It should be noted that in the discussion of jet algorithms, the word 'particles' is applied to any set of four-momenta. It could be the partons in the theoretical calculation, or the energy deposits detected in a calorimeter.

Several algorithms of the two types are at present available and currently used. Some of these algorithms, as used in e^+e^-, $p\bar{p}$ and ep at HERA are presented below.

The cone algorithm

In hadronic colliders it is still very common the use of cone-type algorithms. The most used is that developed for $p\bar{p}$ colliders by the UA1 collaboration [44] and modifications to it. In this algorithm, all the particles are characterised by their transverse energy ($E_T = E \cdot \sin\theta$, where θ is measured with respect to the direction of the beam hadrons, defined as the z-axis), azimuthal angle (ϕ) and pseudorapidity ($\eta = -\ln[\tan(\theta/2)]$)[17].

The particles with transverse energy above a certain threshold value are considered as *initiators*. For each of them a cone is defined taking a radius of R in the $\eta - \phi$ plane. All the particles whose distance to the cone axis is smaller than R

$$\sqrt{(\eta_{cone} - \eta_i)^2 + (\phi_{cone} - \phi_i)^2} < R \ ,$$

are included in the cone.

[17]The pseudorapidity is the "longitudinally invariant" polar angle. It is very easy to show that a Lorentz transformation along the z-axis only changes the pseudorapidity by an additive constant. As a consequence, differences in pseudorapidity are invariant under such a transformation. This makes this variable very useful to define jet algorithms for hadron colliders.

Then, the cone position is redefined using the particles included in the cone via the expressions

$$E_{T,cone} = \sum_i E_{T,i} \; ; \quad \eta_{cone} = \frac{1}{E_{T,cone}} \sum_i E_{T,i}\, \eta_i \; ; \quad \phi_{cone} = \frac{1}{E_{T,cone}} \sum_i E_{T,i}\, \phi_i \; ,$$

and the algorithm is repeated till the position of the cone converges. At that moment the jet is defined using the center of the cone.

Since two or more cones may overlap, a criterion is needed to decide if two cones should be merged into one or if the "overlapping" particles are distributed among the two different jets. After this criterion has been applied, we are left with a number of jets. An additional cut on E_T determines the final sample of jets.

It should be noted that this additional cut on E_T is needed to separate jets coming from the hard process and the hadrons coming from the remnants. At the same time, this cut allows the reduction of the dependence on the threshold to select the initiators.

As a final remark, the structure of this algorithm permits particles to be left unassigned. This means that the algorithm is "inclusive" and it is the main property for its use in hadron colliders: the particles which form the remnant must not be considered as parts of the jets and should not be taken into account.

The JADE algorithm

The JADE algorithm [42] was the first cluster-type algorithm. It is very common in studies of jets in e^+e^- colliders in its original form or via some of the modifications which have been developed since it was presented.

The jet reconstruction procedure starts by calculating the distance parameter m_{ij} for all pairs of particles according to the expression

$${m_{ij}}^2 = 2E_iE_j(1 - \cos\theta_{ij}) \; ,$$

where E_i (E_j) is the energy of particle i (j), and θ_{ij} is the angle between particles i and j. The variable m_{ij} is the invariant mass of one particle decaying into i and j under the approximation that both particles i and j are massless. The pair with the smallest m_{ij} is combined into a single cluster by the addition of their four-momenta. The procedure is repeated until all remaining pairs have an invariant mass exceeding a preselected cut-off value, ${m_{ij}}^2 > y_{cut}M^2$, determined by a resolution parameter y_{cut} and a reference mass M. The final clusters represent the jets of the event.

As a difference with respect to the cone algorithm described above, in this algorithm all the particles are assigned to the jets. This property is usually denoted as *exclusiveness*, and it should be noted that this type of algorithm is only useful when all the hadronic particles are coming from the hard interaction, i.e. no remnant is present.

The k_T-cluster algorithm

A two-step procedure, similar to that of the original JADE algorithm, is used in the k_T-cluster algorithm. Although it can be applied with slightly modifications to every kind of experiment, the DIS version [43] uses the first step to perform the preclustering of hadrons into a beam-jet and final state macro jets. The second step aims at resolving jet structures within the system of macro jets.

In the preclustering, a variable $k_{T,ij}$ is calculated for all pairs of particles i and j according to the expression

$$k^2_{T,ij} = 2\,(1 - cos\theta_{ij})\; min\left\{E_i^2, E_j^2\right\}\ ,$$

where θ_{ij} is the angle between the momenta vectors of particles i and j and E_i and E_j the corresponding energies. In addition, a parameter $k_{T,iP}$, related to the distance of particle i to the beam-jet, is calculated for each particle i according to

$$k^2_{T,iP} = 2\,(1 - cos\theta_{iP})\; E_i^2\ ,$$

where θ_{iP} is the angle between i and the incoming proton direction.

At this stage a scale E_T is introduced and the iterative procedure starts till the smallest of all the $\{k_{T,ij}, k_{T,iP}\}$ is greater than E_T. If this is not the case the two particles related to that smallest value are combined into a new cluster and a new iteration is performed. Any particle combined with the proton remnant (the smallest is $k_{T,iP}$) is considered as part of the spectator jet and is not included in the next iteration. If the two particles combined are "real", then a *recombination scheme* has to be introduced to define the four-momentum of the new cluster, which is considered in the following iterations.

In the second step, all the particles which where not assigned to the spectator jet are considered. The process is similar to that used in the first step, but now the scale can be selected to be smaller in such a way as to resolve more jets. This second parameter sets the scale to resolve the jets. The first one (E_T) is the scale which separates the hard process(es) with respect to the soft ones.

The longitudinally-invariant k_T-cluster algorithm

The original k_T-cluster algorithm can be modified to define a longitudinally invariant algorithm whose advantages for jet studies in DIS have made it to become the most extended algorithm in HERA physics. This algorithm is the one used in the analyses presented in this thesis and make use of the longitudinally invariants E_T, η and ϕ, which were defined in the description of the cone algorithm.

The algorithm proceeds according to the following steps [45]:

1. For every pair of particles i and j, define a closeness between the two particles according to

   $$d_{ij} = min\left\{E_{T,i}, E_{T,j}\right\}^2\ \left[(\eta_i - \eta_j)^2 + (\phi_i + \phi_j)^2\right]\ ,$$

   where it should be noted that for small distances in the $\eta - \phi$ plane, d_{ij} represents the relative transverse momentum squared between particles i and j.

2. For every particle i, define a closeness to the beam direction according to

   $$d_i = E^2_{T,i} \cdot R^2\ ,$$

   where R is a parameter of the algorithm which plays the rôle of a jet radius in the $\eta - \phi$ plane. It is usually set to one, which is the preferred value from the theoretical point of view as it treats initial and final state radiation on equal footing.

3. The smallest value of all $\{d_{ij}, d_i\}$ is considered. If this is one of the d_{ij} then the two particles are merged into a new one following the recombination scheme. If the minimum is one of the d_i, then that cluster is considered as a *protojet* and no longer considered for clustering.

4. The procedure is repeated till no remaining cluster is left and all the particles have been assigned to protojets. It should be noted that at each iteration, one particle is removed, so the number of iterations is always equal to the original final-state particles.

5. From the sample of protojets, the final jets are selecting imposing a cut on E_T which sets the scale to distinguish the hard and the soft processes.

Although the recombination scheme is not fixed by the algorithm, the most natural definition is to recombine the particles using the following expressions (where the two particles i, j are merged into a new one k):

$$E_{T,k} = E_{T,i} + E_{T,j} \;\;,\;\; \eta_k = \frac{1}{E_{T,k}}\Big(\eta_i\, E_{T,i} + \eta_j\, E_{T,j}\Big) \;\;,\;\; \phi_k = \frac{1}{E_{T,k}}\Big(\phi_i\, E_{T,i} + \phi_j\, E_{T,j}\Big)\;. \quad (1.32)$$

In this way the jet quantities are defined according to the Snowmass convention [46], in the same way as it was introduced above for the cone algorithm.

Although this algorithm does not impose a given geometry to the jets, the parameter R can be related to the radius of the cone algorithm. The definition of the k_T-cluster algorithm has the property that the jets are far away at least a distance in $\eta - \phi$ equal to R (if not, the algorithm would have merged them). On the other hand any particle in a radius R in the $\eta - \phi$ plane around the jet axis is included in the jet (since the protojets are only selected from clusters which have no other clusters at a distance smaller than R). That is the reason why the jets defined with this algorithm are phenomenologically similar to those defined by the standard cone algorithm described above.

However, the invariant k_T-cluster algorithm is less influenced by soft particles than the cone algorithm, which results in smaller hadronisation and detector corrections. Qualitatively one can say that the longitudinally invariant k_T-cluster algorithm pays more attention to the core of the jet and only merges neighbouring particles if they are close enough, whereas the cone algorithm, in order to maximise the jet transverse energy, pulls in as much neighbouring energy as possible.

1.4.2 Jet production in the Breit frame

As we have described in section 1.2.4, the generation of partons with transverse momentum in the Breit frame can directly be related to QCD processes. This is very important when studying jet production, because high-E_T jets are related to partons in the hard process: high-E_T jets in the Breit frame will be related to partons generated by hard QCD processes.

This property can be exploited for two purposes. First, it is possible to obtain theoretical predictions for hard QCD processes by means of the perturbative approach (see section 1.3). This implies that jet production in the Breit frame provides an useful way to test perturbative QCD predictions and the validity of QCD to describe the strong interaction.

Secondly, since jet production in the Breit frame is described in the perturbative approach by including QCD contributions, the cross section for producing jets in the Breit frame can be expressed as

$$\sigma = a_1 \cdot \alpha_s \;+\; a_2 \cdot \alpha_s^2 \;+ \mathcal{O}(\alpha_s^3)\,, \quad (1.33)$$

which means that this kind of observable is very sensitive to the value of the strong coupling constant.

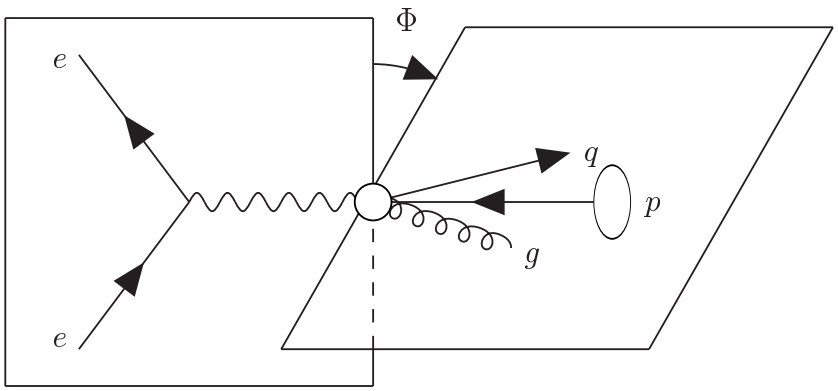

Figure 1.12: The first order QCD Compton process $\gamma^* q \rightarrow qg$, as viewed in the Breit frame. The lepton scattering plane and the parton plane are shown. Both planes contain the z-axis defined by the exchange boson and the proton. The angle between the two planes is the azimuthal angle in the Breit frame, with $\phi = 0$ defined by the scattered lepton.

From the theoretical point of view, there are additional reasons for preferring the Breit frame to perform a study of jet production in deep-inelastic scattering. It has been shown [47] that using the k_T-cluster algorithm in the Breit frame to define the jets, it is possible to factorise the beam fragmentation and the hard process. This property is very important since it assures that well-defined theoretical predictions can be obtained at parton level, where here well-defined means that all the infrared divergences are factorisable (absorbed) into the parton distribution functions.

1.4.3 The azimuthal asymmetry

Jet production in the Breit frame allows to investigate the non-trivial azimuthal distribution of the final-state partons predicted by the Standard Model [48]. In the definition of the Breit frame given in section 1.2.4, it remained an arbitrariness in the definition of the x-axis. This definition is usually done by noting that the initial lepton presents a transverse component which is absent in the hadronic system, which is contained in the z-axis.

In this way, the scattering plane of the lepton is usually defined to contain the x-axis, and in this way to be the reference for the azimuthal angle ($\phi = 0$ for the scattered lepton in the Breit frame).

As we have mentioned before, to produce jets in the Breit frame, we need to have at least two partons in the final state. This two partons are back to back in ϕ to conserve the transverse momentum in the hadronic system. In this way, the two partons define their own scattering plane which necessarily contains the z-axis.

The two scattering planes are shown in figure 1.12 for a QCD Compton process. Since both planes contains the z-axis, they form an angle which in fact is the azimuthal angle of the partons in the Breit frame. In fact, one of the partons will be at this azimuthal angle and the other parton at the same angle plus 180 degrees.

The jet production studied as a function of this azimuthal angle is predicted to be non uniform due to the values of the spin of the different particles present in the interaction. In fact, the

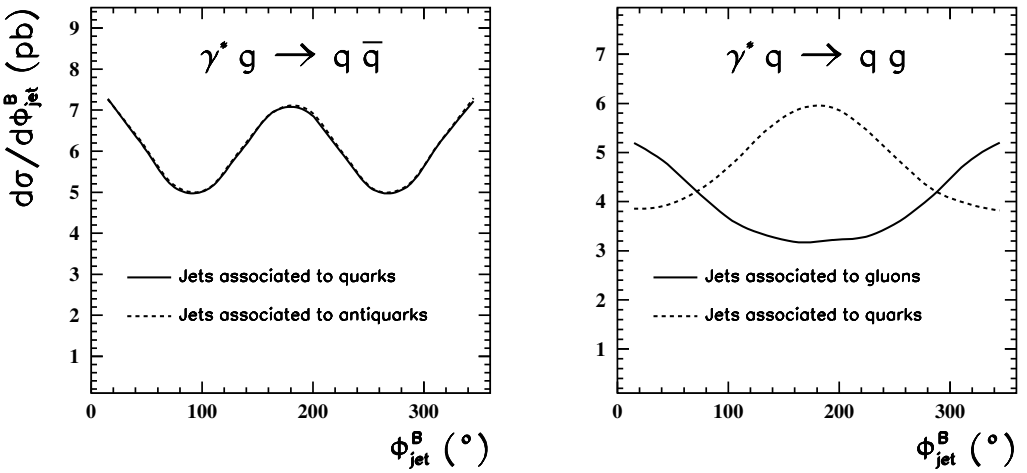

Figure 1.13: The first-order contribution to the azimuthal distribution for the two $\mathcal{O}(\alpha_s)$ processes: (left) Boson-Gluon Fusion and (right) QCD Compton. The expected distributions for the different partons are shown. It can be observed the clear differences coming from the different types of partons in the final state. It should be noted that adding the various contributions, an asymmetry is expected, which comes mainly from Boson-Gluon Fusion type of events.

theory predicts that, at order α_s, the cross section for neutral current DIS satisfies:

$$\frac{\mathrm{d}\sigma}{\mathrm{d}\phi^B_{jet}} = A + B\cos\phi^B_{jet} + +C\cos 2\phi^B_{jet}\,, \tag{1.34}$$

where the coefficients A, B and C depend on the type of jet and the type of proccess. The $\cos 2\phi^B_{jet}$ is coming from the interference of amplitudes related to the $+1$ and -1 helicity components of the transversely-polarised part of the exchanged boson, whereas the interference between the transverse and longitudinal parts give rise to the $\cos\phi^B_{jet}$.

Figure 1.13 shows the predicted distributions by the partons produced for the order-α_s contributions to the cross section. The plots were obtained by using HERWIG (see section 3.4) and imposing the cuts which were used in the corresponding analysis, described in section 4; the predictions for the different types of partons are shown. It can be seen that the azimuthal distribution shows a clear dependence on the type of process and the type of parton which initiates the jet. However, if one is interested in the azimuthal distribution for an inclusive sample of jets, and no flavour tagging is performed, the contribution to the asymmetry will be dominated by the $\cos 2\phi^B_{jet}$ term. In fact, for a completely inclusive and unbiased distribution, the $\cos\phi^B_{jet}$ term will cancel because we don't expect a difference between the two jets in the event and every time one jet appears at a given ϕ^B_{jet}, the other will appear with a difference of 180 degrees.

Measuring this distribution for high-E_T jets provide a very stringent test of the theory, since the prediction is dominated by the first-order contribution in the perturbative approach. However, to obtain this measurement without any bias, one should avoid to apply cuts in a different frame than the Breit frame. It is especially important to avoid the presence of cuts in the laboratory frame, otherwise the azimuthal distribution would be dominated by kinematic effects [49].

The azimuthal asymmetry, described here for jets, has been studied by the ZEUS Collaboration with the measurement of the azimuthal dependence of charged hadrons with high transverse momentum in neutral current DIS [50]. In this thesis one of the analysis will present the first observation of the azimuthal asymmetry by using jets.

1.4.4 Determination of α_s from jet production in the Breit frame

The direct dependence on α_s of the cross sections for producing high-E_T jets in the Breit frame (see section 1.4.2), provides a precise way to determine experimentally the value of that constant.

The method is the following: the measurements for the jet cross section are compared to the predictions of the theory, which has to assume a value for the strong coupling constant, since it is not predicted in the Standard Model. Afterwards, the dependence of the prediction on the value for α_s can be used to fit the theory to the data by adjusting the value of α_s to that which gives a better description of the data.

To make a sensible determination of the strong coupling constant, it is necessary to compare the measurements with a theoretical prediction which includes at least the first two orders in α_s for the perturbative description of the observable. At present, the calculation of these first two orders is available, and for this reason it will be possible to extract the value for the strong coupling constant from the inclusive jet production in the Breit frame, which is the first of the two analyses presented in this thesis.

1.4.5 The internal structure of jets

The internal structure of quark and gluon jets, which in the frame of pQCD is ascribed to the emission of additional partons according to the SU(3) colour factors (as discussed in sections 1.1.5 and 1.3.4), is an exclusive event property mainly ruled by the pattern of parton radiation in the process under study. Furthermore, the analysis of the internal structure gives insight into the process steering the transition from the partons to the observable hadrons. Thus, the comparison with the theoretical prediction is a stringent test of the validity of perturbative QCD as the theory describing the strong interaction.

In this section the physical observables which are commonly used to study the internal structure of the jets are presented. Especial stress is laid on the definition of the subjet multiplicity [51], which has been measured in the analysis presented here.

The most common way of resolving the internal jet structure, inspired by the cone-type algorithms, is to measure the energy distribution around the jet axis direction. The physical observable used is the so-called *jet shape* [52], which is related to the energy distribution around the jet axis. Close to this axis, the jet shape is dominated by collinear gluon emission, which can be calculated perturbatively. However, the cluster-type algorithms naturally suggest an alternative, additional way of analyzing the internal structure of a jet that is much closer to the partonic picture of how that structure arises: by resolving 'sub-objects' (called *subjets*) within a jet making use of a resolution variable. The physical meaning of the subjets would be related to the partons radiated inside the given jet, in the same way the jets themselves are related to the partons produced in the hard process. The physical observable most commonly used in this case is the so-called *subjet multiplicity*, which is the number of subjets within a given jet.

During the last years, the use of subjets to characterize the internal structure of the jets, particularly when the k_T-cluster algorithm is used to define the jets, has become more and more popular. This is due because it has been shown that it presents several advantages from the theoretical and experimental points of view.

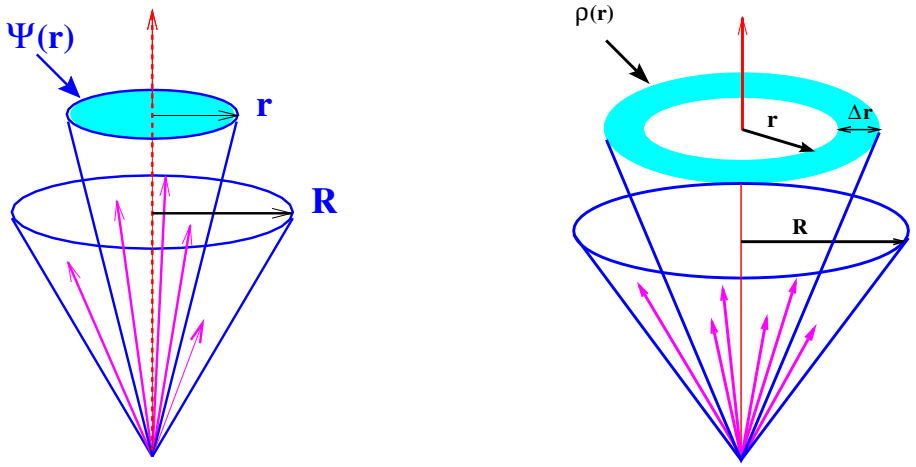

Figure 1.14: Schematic representation of the integrated (left) and differential (right) jet shape.

All the quantities related to the jet internal structure are usually studied in a statistical way and, therefore, the average values over a sample of jets are considered in the measurements.

The formal description of the quantities will be done as it is usually done in HERA physics. Definitions for other type of processes could be sligthly different although the underlying notions are the same.

The jet shape

The *integrated jet shape* $\psi(r, R)$ is defined as the average fraction of the jet's transverse energy that lies in an inner cone of radius r, in the $\eta - \phi$ plane, concentric with the jets axis (as shown in the drawing on the left-hand side of figure 1.14),

$$\psi(r, R) = \frac{1}{N_{jets}} \sum_{jets} \frac{E_{T,jet}(r)}{E_{T,jet}} ,$$

where $E_{T,jet}(r)$ is the jet's transverse energy within the inner cone of radius r, N_{jet} is the number of jets in the sample, and $E_{T,jet}$ is the entire transverse energy of the jet.

The jet shape can be also analysed in terms of the *differential jet shape*, i.e. the average fraction of the jet's transvers energy that lies in an angular annulus concentric with the jet axis (see drawing on the right-hand side of figure 1.14),

$$\rho(r) = \frac{d\psi}{dr}(r, R) = \frac{1}{N_{jets}} \sum_{jets} \frac{E_{T,jet}(r + \Delta r) - E_{T,jet}(r)}{E_{T,jet}} .$$

Narrower jets are characterised by larger values of $\psi(r, R)$, larger values of $\rho(r)$ at small r and smaller values of $\rho(r)$ at large r.

The subjet multiplicity

After identifying a jet of a given transverse energy $E_{T,jet}$, the longitudinally invariant k_T-cluster algorithm (see section 1.4.1) is rerun over only those particles that were assigned to the jet. This second clustering is stopped when all values of d_{ij} satisfy the condition:

$$d_{ij} > y_{cut} \cdot E^{2}_{T,jet} ,$$

that is when all the internal relative transverse momenta are greater than $\sqrt{y_{cut}} \cdot E_{T,jet}$ and the number of sub-structures inside the jet is counted (n_{sbj}). For a resolution scale $y_{cut} \sim 1$ the jet

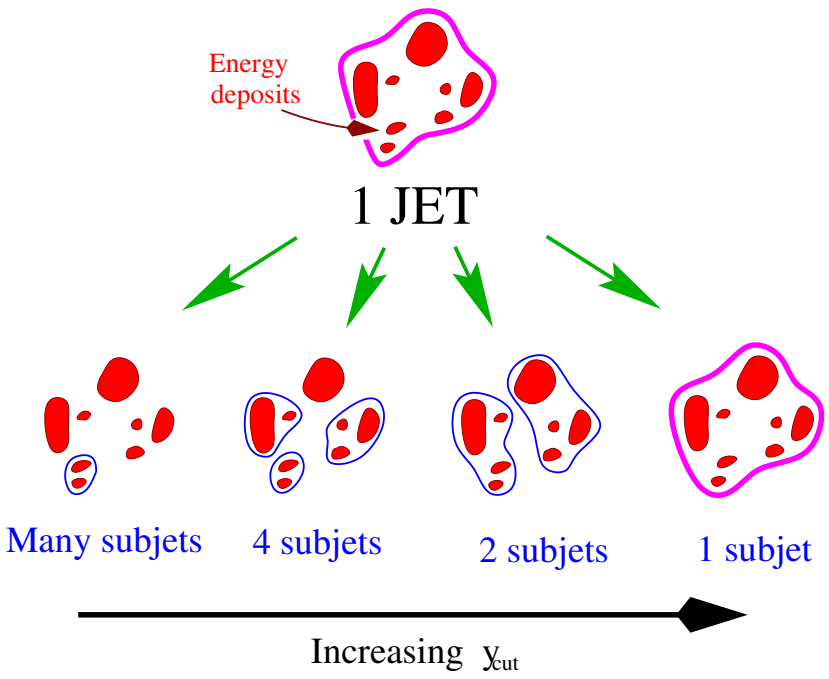

Figure 1.15: Schematic representation of the subjet structure within a jet. Depending on the value of the resolution scale (y_{cut}) the number of resolved subjets is different. For very small values, any energy deposit is defined as a subjet. In the limit where the resolution scale is close to 1, no internal structure is resolved.

always consists of only one subjet (i.e. the jet itself). This can be formally expressed as

$$\lim_{y_{cut}\to 1} n_{sbj} = 1.$$

When y_{cut} approaches zero every hadron is eventually considered as a separate subjet. Thus, varying the resolution scale y_{cut} allows a detailed study of the transition of the colour charged fields (partons) into colourless final-state hadrons[18].

Figure 1.15 shows a graphical representation of the meaning of subjet structure and how the definition presented above is related to the internal structure of the jets.

Since subjets are physical objets, at the same level as the original jets, they can be used to make very different kinds of analysis. The simplest way to study the internal structure of the jets using these subjets is by characterising that structure with the number of subjets resolved at the given resolution scale.

For statistical studies, the *mean subjet multiplicity* is defined as the average number of subjets in the sample of jets considered,

$$\langle n_{sbj} \rangle (y_{cut}) = \frac{1}{N_{jets}} \sum_{jets} n^{jet}_{sbj}(y_{cut}) \ ,$$

and this is the quantity used in the analysis described here.

[18]From the experimental point of view, very small values of y_{cut} cannot be considered since the detector effects would be very large. On the theoretical side, a very small resolution scale introduces large hadronisation corrections and the model dependence of the parton radiation and fragmentation becomes very large.

1.4.6 Quark- and gluon-initiated jets

In the frame of pQCD, the average number of hadrons in a jet initiated by a parton at a given scale can be calculated using the fragmentation functions and the evolution equations applied to that functions [40]. Since the sppliting functions are determined by the colour charge of the initial parton, it is clear that the multiplicity inside a jet will be dictated by the type of parton which initiates the jet.

To make a quantitative study of the differences between quarks and gluons, it is needed that pQCD gives a good description of the observable. For this, the scale should be relatively large and infrared-safe quantities have to be defined for a direct comparison of theory and measurements. The observables defined above, especially the mean subjet multiplicity, can be used to study these differences and to compare with the predictions of pQCD.

One of these predictions is that the asymptotic behaviour (i.e. at very large scales in comparison with that related to the fragmentation process) of the averaged multiplicity of any type of objet in quark and gluon-initiated jets can be expresssed as [14]

$$\left\langle n \right\rangle_{quarks} \sim \frac{C_F}{C_A} \left\langle n \right\rangle_{gluons} \propto \exp\left[\frac{1}{b} \sqrt{\frac{2C_A}{\pi \alpha_s(t)}} \right] . \tag{1.35}$$

This predicts that the multiplicity distribution should become larger for gluon-initiated jets than for quark jets by the factor C_A/C_F and the distribution of particles inside the jets should become wider by the square root of that factor.

These predictions are qualitatively correct, and it has been experimentally observed that gluon jets are broader than quark jets. However, the ratio of the two multiplicities is quite below the asymptotic value, although it is well described by the phenomenological models [53].

For the jet shape, a broader jet means that the distribution of energy is less concentrated in a small radius, so the qualitative prediction from QCD is

$$\psi_{quarks}(r, R) > \psi_{gluon}(r, R) ,$$

and the differential jet shape will be larger for quark jets at small radius and smaller at large radius than in gluon jets, as described earlier.

For the mean subjet multiplicity, it is expected that the expression (1.35) holds for $\left\langle n \right\rangle = \left\langle n_{sbj} \right\rangle$, so the gluon jets are predicted to display a larger $\left\langle n_{sbj} \right\rangle$ than in quark jets.

1.4.7 Determination of α_s from the internal structure of jets

When the non-perturbative effects are small, i.e. at large energy scales, the internal structure of the jets is expected to be dominated by "hard" parton radiation and perturbative QCD should be able to give predictions that can be compared to the measurements.

The calculations are done by applying the same definition for jets as for hadrons, and in this way, if a jet contains two or more partons, an internal structure can be resolved. This case is only posible when computing the perturbative expansion at least to the next order to the first one needed for the definition of jets.

The idea is that to define a jet we need an order in the perturbative expansion which contains at least one parton to be taken as a jet after imposing the selection cuts, for example on the

transverse energy. On the other hand, although one parton is enough to define the jets, the minimum requirement for the predictions of the internal structure is two partons in the same jet. This two-parton configuration represents the lowest order contribution to the internal structure. To compute the pQCD predictions to higher orders, configurations containing more partons are needed.

As for every prediction of pQCD, the internal structure will depend on the value of the strong coupling constant, which enters in the calculation at first order via the splitting of one parton into two which still belong to the same jet, but are resolved when the internal structure of the jet is taken into account.

For a meaningful determination of α_s from the measured values of the internal structure, at least two orders of the pQCD prediction are needed. This limits the kind of process where this determination can be done, since in most of them the calculation of those orders is still not available. This is the case in hadron-hadron collisions.

On the other hand, in deep inelastic scattering the production of jets in the laboratory frame is at first order described by the QPM diagram, which does not include any contribution from QCD. That is, the first order for describing jet production is given by order 0 in α_s. To describe the internal structure of the jets, the order α_s^2 is required, and these terms are known.

Thus, all the tools which are needed for the determination of α_s from the internal structure of jets are available for jets produced in deep inelastic scatering. Since neutral-current processes have larger cross sections than charged-current ones and the analysis has some advantages from the experimental and theoretical points of view, the most natural choice is to determine the strong coupling constant using jets produced in neutral-current deep-inelastic scattering events.

This is the goal of one of the analyses presented here, which uses the mean subjet multiplicity. A complete description of the next-to-leading order (NLO) QCD calculations is given in section 5.1.

Chapter 2

Experimental setup

In this chapter a brief description of the HERA *ep* collider and ZEUS detector is presented, specifically, the components that are more relevant for the analyses presented in this thesis.

2.1 The HERA collider

The Hadron Electron Ring Accelerator (HERA) [54] located at the DESY (Deutsches Elektronen-SYnchrotron) laboratory in Hamburg (Germany) is the first electron (positron)-proton collider in the world. The tunnel in which it resides was built 10 to 25 meters under the earth surface and it has a circumference of 6.3 Km. The storage ring consists of four circular arcs (with a radius of 779 m) and four straight segments (each 360 meters long) as can be seen in figure 2.1. Four interactions points (IP) are placed in the straight segments, where the experiments H1, ZEUS, HERMES and HERA-B are located.

One of the remarkable features of HERA, which distinguishes it from a 'classical' collider, is the asymmetry between the two beam energies. HERA was designed to collide electron (positron) and protons with nominal energies of 30 GeV and 820 GeV respectively, resulting in a center-of-mass energy of $\sqrt{s} \sim 300$ GeV.

Beam injection is performed by a procedure involving several preaccelerators (see figure 2.2). Electrons are initially accelerated up to 200 MeV in the electron linear accelerator LINAC II, and then in the DESY II synchrotron up to an energy of 7.5 GeV. Afterwards, the electrons are injected into PETRA[1], where their energy is increased up to 14 GeV, before they are finally transferred to HERA. The protons start as H^- ions in the proton LINAC and are accelerated up to 50 MeV. After acceleration in DESY III (to 7.5 GeV), the electrons are stripped off and the protons are injected in PETRA, where their energy increases up to 40 GeV, before injection into HERA.

While the high momentum of the proton beam requires superconducting magnets, the electrons are controlled using conventional magnets. The HERA proton ring consists of 422 main dipoles delivering a bending field of 4.68 Teslas and 244 main quadrupoles. Standard cells of 47 m length combining 4 dipoles, 4 quadrupoles, 4 sextupoles and correction magnets are installed in the arcs of the proton ring and are cooled down to 4.2 °K. The conventional electron ring consists of 456 main dipoles of 0.164 Teslas and 605 main dipoles grouped in 12 m long magnet modules

[1]PETRA (Positronen-Elektronen Tandem Ring Anlage) is a previously existing e^+e^- collider at DESY.

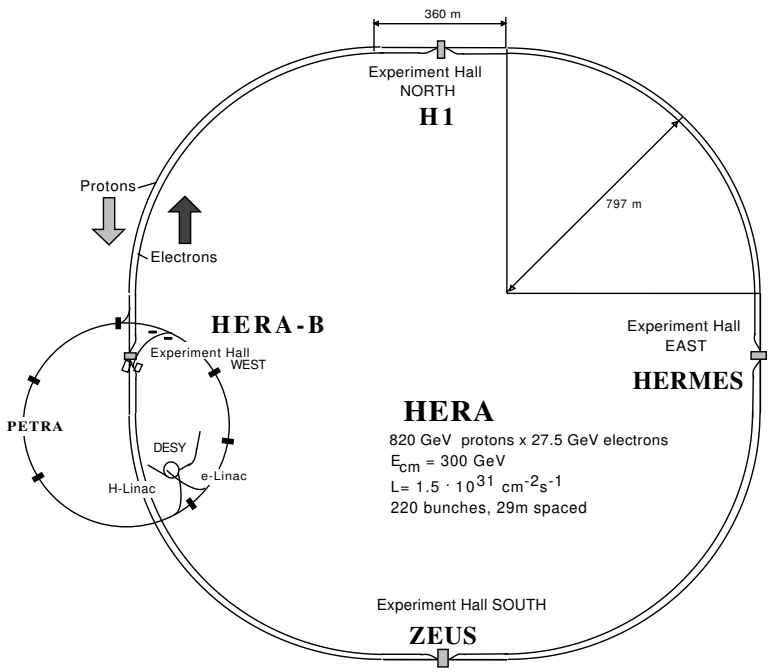

Figure 2.1: Layout of the HERA collider.

which contain one dipole, one quadrupole, one or two sextupoles and several correction dipoles. The energy loss due to synchrotron radiation is compensated by 500 MHz copper cavities installed in the straight segments of HERA. In addition, 16 superconducting 4-cell cavities with an electric field gradient of 5 MVolts/m are used to accelerate the electrons from 14 GeV (the energy they have when they are injected from PETRA to HERA) to the maximum energy. The electrons and protons are stored in separated bunches with a distance of 28.8 m between two successive bunches. This distance corresponds to a bunch crossing time of 96 ns (see figure 2.3). In order to maximise the luminosity, up to 210 bunches of particles can be stored for each beam. Unpaired bunches with only protons or electrons as well as completely empty bunches are used to estimate the number of background events coming from interactions with the residual beam gas in the storage ring, events produced by cosmics rays or other "non-*ep*" events.

Close to the interaction region, protons and electrons have to run in the same orbit in order to collide at zero angle. The distance of about 81 cm between the electron and the protons rings has to be traversed. A total of 123 guiding magnets are used to deflect the protons until they run in the same vacuum pipe as the electrons. After passing the interaction point they are brought back to the level of the proton ring.

From the '94 running period it was decided to accelerate positrons instead of electrons in order to achieve longer lepton-beam lifetimes. Interactions with almost stationary positive charged particles, most likely originated from the ion getter pumps of the HERA vacuum system, tend to defocus the electron beam. For a positron beam the pile-up of the ions is avoided due to the repulsive electromagnetic force between the positrons and the positively charged ions.

During some part of the '98 and '99 running periods the machine accelerated electrons. From that moment till September 2000, positrons were collided with protons. Since then, HERA and the experiments have been involved in a long shutdown to improve the performance and

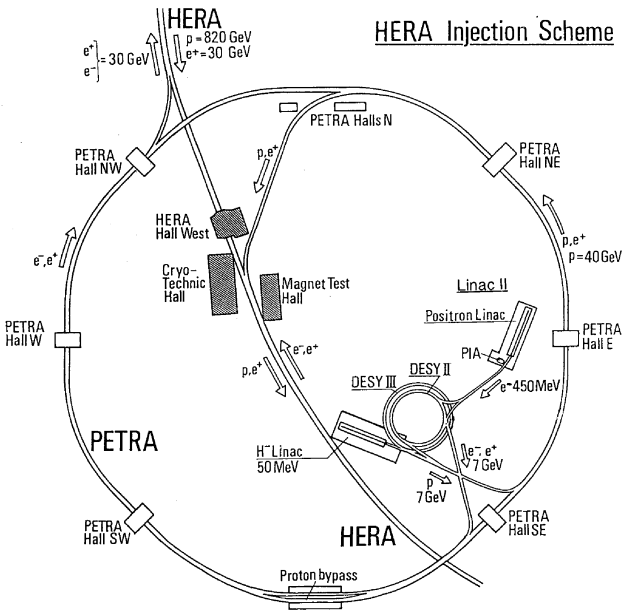

Figure 2.2: Scheme of the injection facilities at DESY.

increase the luminosity. From 1998 the proton beam has an energy of 920 GeV, which yields to an increase of 5% in the center-of-mass energy.

In addition to the available center-of-mass energy, another important quantity that characterises the performance of a collider is the luminosity. This quantity determines the rate at which interactions occur. From the luminosity (L) and the cross section for a given process (σ) the number of events observed is given by

$$N = L \cdot \sigma \ . \tag{2.1}$$

For an specific collider the luminosity L is controlled by the parameters of the collider: it depends of the number of bunches, the number of particles per bunch, the properties of the bunches and the crossing time.

Figure 2.4 shows the luminosity delivered by HERA during the several running periods from 1994 up to the end of the 2000 running.

2.2 The ZEUS detector

ZEUS[2] is one of the currently four experiments at the HERA collider. It is a large multipurpose detector designed to study the wide spectrum of HERA physics. The ZEUS Collaboration consists of around 450 physicists belonging to more than 50 institutes from 12 different nations. The detector is located 30 m underground in the South Hall of the HERA tunnel outside of the DESY site and has a size of 12 m x 11 m x 20 m and weighs 3600 tons. A detailed description of the ZEUS detector can be found in [55].

[2]ZEUS stands for the greek expression for Search to Elucidate Underlying Symmetry.

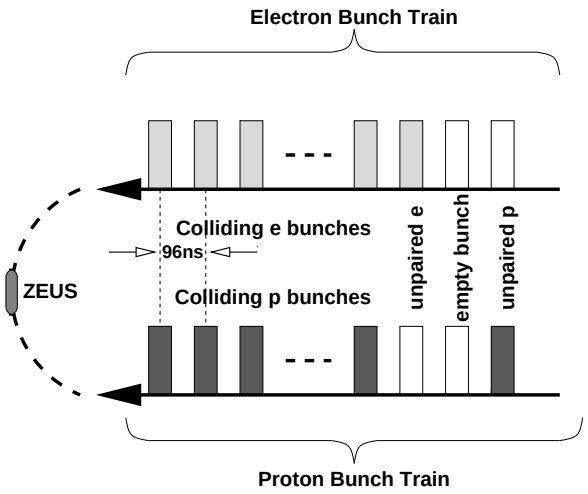

Figure 2.3: Bunch distribution for electrons and protons.

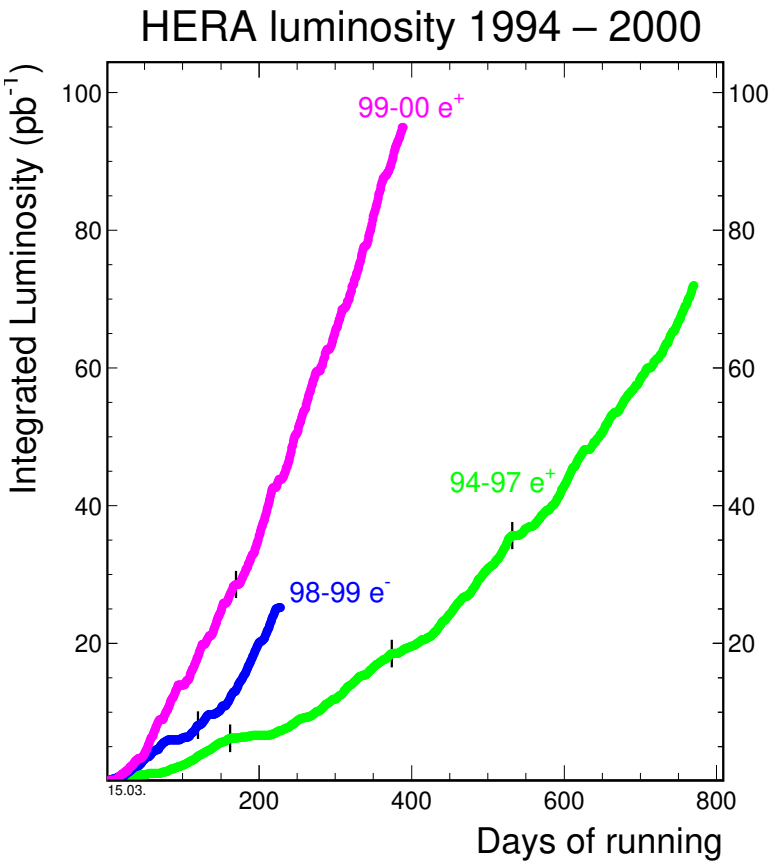

Figure 2.4: Accumulated luminosity delivered by HERA during RUN I divided in periods with equal lepton charge and proton beam energy.

Cross sections through the ZEUS detector are shown in figures 2.5 and 2.6. The ZEUS geometry is described by a right-handed coordinate system with its origin at the nominal interaction point. The z-axis is pointing along the incoming proton direction and the x-axis horizontally towards the center of HERA. A polar coordinate system (r, θ, ϕ) is very commonly used, where θ is the polar angle w.r.t. the positive z-axis and ϕ the azimuthal angle w.r.t. the x-axis.

Starting from the interaction point (see figure 2.5) ZEUS consists[3] of tracking detectors for charged particles. They are divided into central (CTD), forward (FTD) and rear (RTD) tracking detectors. The tracking chambers are surrounded by a high-resolution Uranium-Scintillator Calorimeter (UCAL). The UCAL is divided into three sections: the FCAL in the forward region, the RCAL in the rear region and the BCAL, a barrel section surrounding the central region. The small-angle rear track detector (SRTD) is situated behind the RTD and covers the face of the RCAL to a radius of $\sim$ 34 cm around the center of the beam-pipe hole. At a longitudinal depth of 3 radiation lengths in the RCAL the Hadron-Electron Separator (HES) is installed. It consists of 3x3 cm^2 silicon-diodes and provides a better discrimination power between electromagnetic and hadronic showers originating from low energetic particles (< 5 GeV). Between the UCAL and the CTD there is a superconducting solenoid. The coil has an overall length of 2.46 m and an inner diameter of 1.91 m, and produces a magnetic field of 1.43 Tesla. A high-field solenoid (5 Tesla) situated behind the RCAL compensates the effect of the main solenoid on the electron beam. The axial field produced by the solenoid is used to measure the momentum of the charged particles. A second low-resolution calorimeter (BAC) was constructed to measure the energy leakage out of the main calorimeter. The BAC is made of 7.3 cm thick iron plates and also serves as the return yoke for the magnetic flux from the solenoid. In order to detect muons and measure their momenta, muon chambers are located between the BAC and the CAL (inner muon chambers), as well as after the iron return yoke (outer muon chambers). The muon detector, as the UCAL, is divided into three parts, forward (FMUI, FMUO), rear (RMUI, RMUO), and barrel (BMUI, BMUO). In the rear part of the main detector, at 7.5 m upstream of the interaction point, an iron-scintillator VETOWALL is used to reject beam-related background. A small lead-scintillator counter, located around the beam pipe at $z = -3.15$ m, monitors the synchrotron radiation accompanying the beams and the timing and longitudinal structure of the proton and electron bunches. At $\sim$ 20-90 m downstream in the proton-beam direction the Leading-Proton Spectrometer (LPS) and the Forward-Neutron Calorimeter (FNC) detect protons and neutrons scattered through small angles, respectively. The Proton-Remnant Tagger (PRT) is a lead-scintillator counter located at $z = 5.1$ m around the beam pipe and covers the pseudorapity[4] range $4.3 < \eta < 5.8$. In the electron-beam direction, two small lead-scintillator calorimeters are installed at $z = -34$ m and $z = -104$ m for the measurement of outgoing electrons and photons, respectively, at low-scattering angles. They are used for the determination of the luminosity and also to detect $Q^2 \sim 0$ events (photoproduction regime) and radiative events. The short time interval of 96 ns between bunch crossing at HERA results in a nominal rate of 10 MHz. ZEUS uses a three-level trigger system to reduce the rate to a few hertzs (see section 2.2.6).

In the next sections a brief description is given of the components which were relevant to the analyses presented here.

[3]The description given here is the one related to the 96 and 97 running periods, which are the ones used in the analysis.

[4]The pseudorapidity is defined as $\eta = -\ln(\tan\theta/2)$, as described in section 1.4.1.

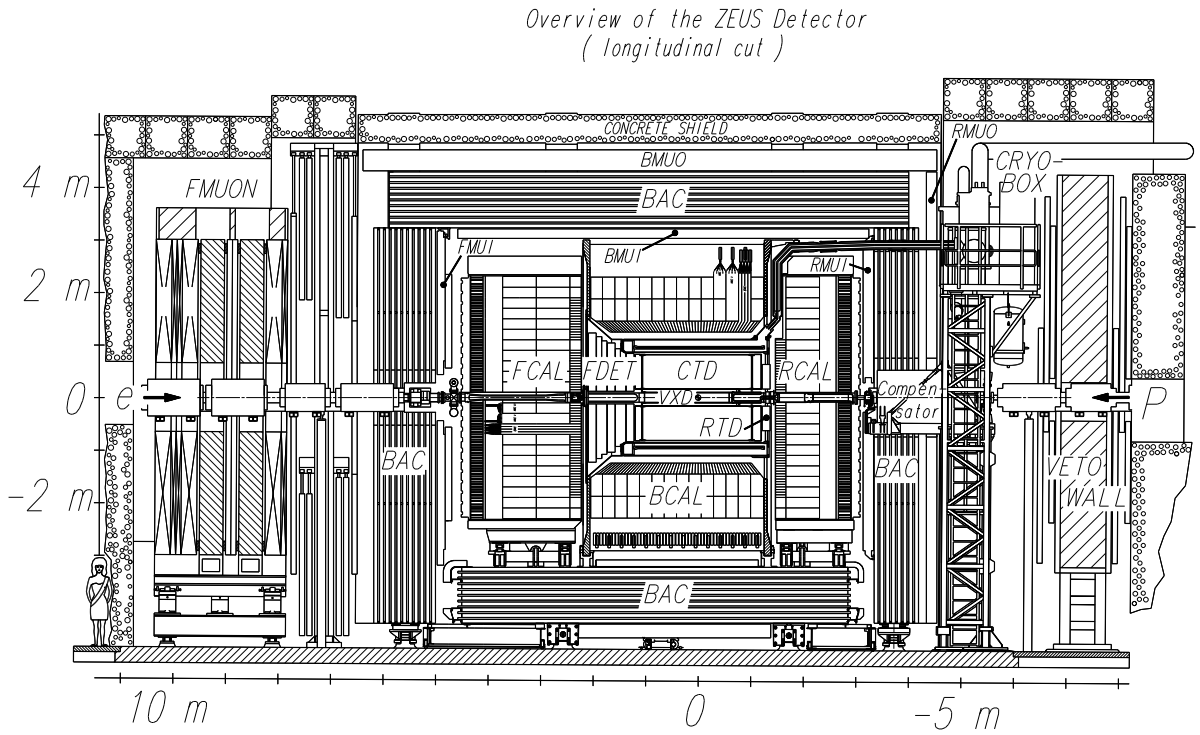

Figure 2.5: Longitudinal cut of the ZEUS detector. A person is drawn in the lower-left corner of the picture for reference of the dimensions. The vertex detector (VXD) was extracted before 1996 running. For a brief description of the most important components see section 2.2.

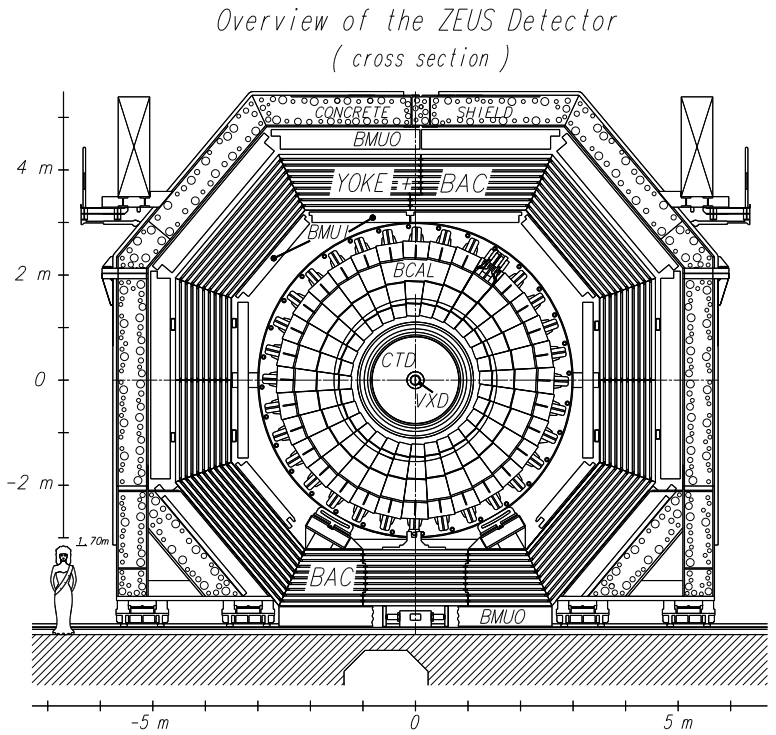

Figure 2.6: Cross section of the ZEUS detector perpendicular to the beam direction. Only the barrel components are shown in the picture.

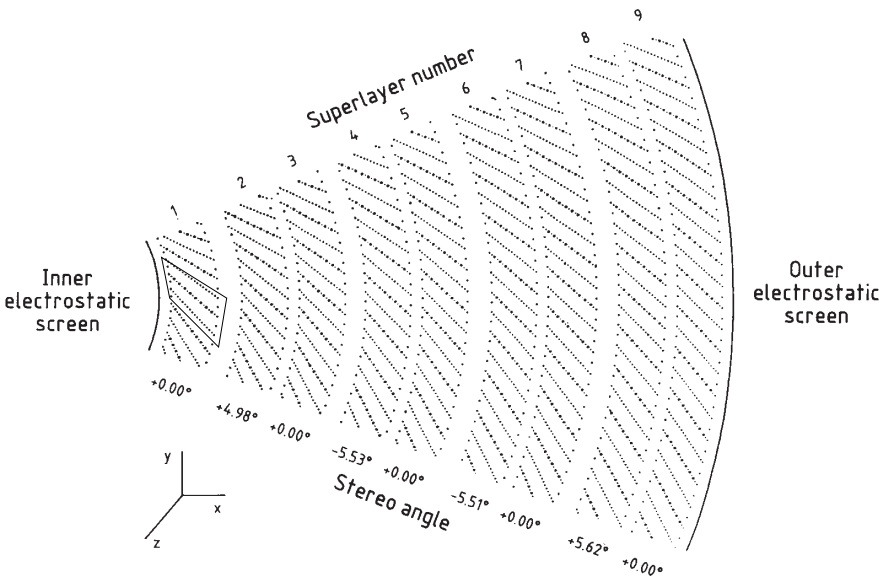

Figure 2.7: Layout of a CTD octant. The wires of the four superlayers with even numbers are slightly tilted with respect to the beam axis (stereo superlayers). The value of this angle is displayed below the corresponding superlayer in the figure.

2.2.1 The Central Tracking Detector (CTD)

The CTD [56] is a cylindrical wire chamber with nine superlayers of eight sense wire layers each, as shown in figure 2.7, covering the polar-angle range of $15° < \theta < 164°$. The inner radius of the chamber is 16.2 cm, whilst its outer radius is 85 cm. The longitudinal length is 241 cm. Five of the superlayers have wires parallel to the chamber axis and are called *axial superlayers*. The remaining four layers are *stereo superlayers* wich have wires with a small angle (5° or 6°) with respect to the beam, as displayed in figure 2.7, and are used to determine the z-coordinate of the hits.

The CTD is filled with a gas mixture of argon, carbon dioxide and ethane (in the ratio 83:5:12) which is bubbled through ethanol (see [57] for more details). This mixture has been chosen on the grounds of safety and detector lifetime [58], although a pure argon-ethane mixture (50:50) would provide a better resolution and less noise.

A charged particle, traversing the CTD, ionises the gas, creating electron-ion pairs along its trajectory. Under the action of the electric-field, the freed electrons drift towards the positive sense wires (with an approximately constant velocity of 50 μm/ns), whereas the positive ions are accelerated towards the negative field wires. In the field of the sense wires, avalanche-like multiplication of the electron occurs, being the amplification factor about 10^4. The produced sizable pulse is read out and digitised by 8-bit flash ADCs.

For trigger purposes, the three inner axial layers are additionally equipped with a z-by-timing system which determines the z-position of the hit from the difference in arrival times of a pulse at both ends of the chamber.

After the final offline reconstruction, the $r - \phi$ hit resolution is $\sim$200 μm (depending slightly on the polar angle θ). The resolution in z using the axial and stereo superlayers is $\sim$2 mm and

when using z-by-timing is 4 cm. The relative transverse-momentum resolution of the CTD is $\sigma(p_T)/p_T = 0.0058p_T \oplus 0.0065 \oplus 0.0014/p_T$ for particles transversing all 9 superlayers and with p_T in GeV. The actual numbers in this parametrisation have been obtained running the detector simulation (tuned with data) on generated tracks coming from the $D^* \to K\pi\pi$ channel [59]. The first term corresponds to the resolution of the hit positions, the second term to smearing from multiple scattering within the CTD and the last term to multiple scattering before the particle enters into the CTD [60].

In the forward region the acceptance of the CTD is extended by the FTD, a system of three planar drift chambers. Between the three FTD chambers, the modules of a Transition Radiation Detector (TRD), designed to enhance hadron-electron separation in the forward region, are positioned. FTD and TRD together form the Forward Detector FDET. In the rear direction, a single chamber (RTD) of identical design of those from the FTD extends the CTD acceptance to polar angles between 160° and 170°.

2.2.2 The Uranium-Scintillator Calorimeter (UCAL)

In high-energy experiments the energy of the particles and jets is measured with calorimeters, which are the central components of the large experiments at present storage rings. One of the essential properties of a calorimeter is its sensitivity to both charged and neutral particles.

2.2.2.1 Principles of Calorimetry

Before giving the description of the ZEUS Calorimeter, a brief introduction to some theoretical aspects of calorimetry is presented here.

Passage of radiation trough matter

Particle reactions which occur when radiation penetrates matter are the basis of particle detection devices. The interactions depend on the type of radiation, its energy and the penetrated material. A calorimeter absorbs an incident particle completely and transforms a part of its energy into a measurable signal. The penetrated detection material can suffer radiation damage which may produce a change of the detection characteristics. Therefore, the knowledge of the particle reactions and effects produced by these processes on the material is of fundamental importance when designing a detector.

The passage of particles through matter with kinetic energies from several keV upwards is mainly characterised by the following processes [61]:

- nuclear reactions,
- elastic or inelastic scattering from nuclei,
- inelastic collisions with the atomic electrons of the material,
- emission of Cherenkov radiation and
- bremsstrahlung.

Particle reactions resulting from the radiation passage through matter significantly depend on the type of radiation. In case of neutrons, for example, the most important type of interaction is collision with nuclei. Because of the short range of the associated force these elastic or inelastic reactions are much rarer than the Coulomb interactions of charged particles in matter. The main energy loss of heavy charged particles in matter (i.e. particles heavier than an electron) occurs in inelastic collisions with the atoms causing an ionisation or excitation of the latter. The energy transferred in each collision is a small fraction of the total kinetic energy of the particles. The energy deposition dE/dx can be described by the Bethe-Bloch formula [62]. During its passage through matter charged particles can also produce Cherenkov radiation, which arises when the velocity of the particle is larger than the speed of light in the same medium.

The energy loss of electrons (and positrons) is similar to that of heavy charged particles, but besides the collisional energy loss an additional effect appears; it is the electromagnetic radiation due to the electron being scattered in the electric field of the nucleus (bremsstrahlung). For kinetic energies of a few MeV or less the energy loss is dominated by ionisation. As the energy is increased up to a critical energy, the energy loss due to bremsstrahlung is comparable to ionisation loss. Above this energy, bremsstrahlung processes dominate the energy loss of electrons in matter.

The interaction of photons in matter, specially high energy ones (γ or X-rays), is mainly described by three types of processes: the photoelectric effect, Compton scattering and pair production. At higher photon energies, pair-production ($\gamma \rightarrow e^+ e^-$ in presence of a partner, usually an atom) dominates the energy loss in matter completely.

Electromagnetic and hadronic showers

During the passage in matter electrons (and positrons) of high energy mainly produce bremsstrahlung photons, which initiate pair production if their energy is bigger than[5] 1.022 MeV. The combined effect of bremsstrahlung emission by electrons and positrons and pair production by high energy photons forms a cascade of photons, electrons and positrons. This **electromagnetic shower** continues until the energy of the particles drops below the *critical energy* E_c defined as the energy at which the energy loss of an electron due to bremsstrahlung is equal to the energy loss through ionisation. Then collisional energy loss dominates the interactions and no further electron-positron pairs are produced. Thus, the propagation of the shower is halted [63]. The propagation of an electromagnetic shower converting bremsstrahlung into pair produced electrons/positrons and vice versa doubles the particle number N and bisects their average energy after each radiation length X_o. We can estimate the maximum number of particles produced in a shower using the relation

$$N \approx \frac{E_o}{E_c},$$

whereas the depth of the shower can be estimated as:

$$X_{max} \approx X_0 \, \log_2 N \approx X_0 \, \log_2 \frac{E_o}{E_c}. \tag{2.2}$$

An estimation of the depth D_{98} required to contain 98% of an electromagnetic shower produced by a 25 GeV electron leads to $D_{98} = 22X_0$ [64].

[5] 1.022 MeV is twice the mass of the electron, which is the particle with smaller mass which couples directly to the photon due to its electric charge.

The critical energy decreases with increasing atomic number of the absorbing material. Therefore, heavy materials such as lead or tungsten are preferred as absorbing materials inside calorimeters.

A **hadronic shower** in matter is initiated by interactions between the incident hadronic particles and nuclei of the absorbing material. Similar to an electromagnetic shower, but accompanied by a large variety of different interactions, a cascade of shower particles is produced. The hadronic shower propagation is dominated by inelastic scattering from nuclei with possible subsequent ejections of atomic particles. The nuclei are left in excited states which later may decay by emitting a photon or by means of other forms of emission as vaporisation, nucleus fission and neutral pions. Some of these particles and also the decay of π^0 into two photons produce electromagnetic showers inside the complete hadronic showers.

In practice, the energy deposition of a pure hadronic shower depends strongly on the energy of the incident hadron. A fraction of its energy is deposited due to ionisation. The rest is lost by nuclear interactions and production of neutrinos. The consideration of the absorption length encountered for shower products allows the simulation of hadronic cascades [65].

The length scale appropriate for hadronic showers is the nuclear interaction length λ_{int} [66] defined as $\lambda = A/\mathrm{N}_A\sigma_i$, where N_A is the Avogadro number and σ_i denotes the inelastic cross section. A good approximation of λ_{int} is given by [64]:

$$\lambda_{int} \propto 35 \cdot \frac{A^{\frac{1}{3}}}{\rho} \ \text{[cm]} \ ,$$

where A is the number of protons and neutrons in the nuclei and ρ the density of the material in units [g/cm^3].

As reference, the depth required to contain 95% of the hadronic shower energy is given by the parametrisation [67]

$$D_{95} \sim 0.2 \ln E + 2.5E^{0.3} + 0.7 \ .$$

Acording to this, a shower of a 300 GeV hadron can be contained in a calorimeter with a depth of 7.1 λ_{int}.

In conclusion, hadronic showers have much larger longitudinal and transverse dimensions than electromagnetic ones. As a reference, in a lead-based calorimeter the hadronic shower is roughly five times deeper and wider than the electromagnetic one. This difference is very commonly used to identify electrons, positrons and photons by using the calorimeters in present high-energy physics experiments.

Calorimeter design

A calorimeter based on scintillating materials is one of the prime devices for energy measurements in high energy physics. One important condition for a correct energy measurement is the complete energy absorption of incident particles within the calorimeter and a partial transformation of the energy into fluorescence light. The light is transformed into measurable electrical pulses by photo-detectors. Several posibilities exist to configure a calorimeter. A homogeneous calorimeter consists of one uniform material which is used for both energy dissipation and measurement (e.g. lead-glass calorimeter). A sampling calorimeter is based on alternating layers of passive absorbing material and active detector material. For the absorption of particles mostly a material is used with high density ρ and atomic number such as lead, tungsten or iron. Plastic scintillators, liquid argon or silicon diodes as active materials offer possibilities for detection.

Independently from any particular configuration a calorimeter has to fulfill some characteristics. It should be sensitive to both charged and neutral particles. The calorimeter has to absorb the total energy of the incident particles. The penetration depth of an incident particle into the absorbing material is proportional to the logarithm of the initial energy E_o. If the measurement uncertainties are dominated by statistical processes depending on the number of incident particles, the energy resolution σ/E decreases with increasing energy E like [68]

$$\frac{\sigma(E)}{E} \propto \frac{1}{\sqrt{E}} ,$$

while the depth D required to stop incoming particles increases only logarithmically with the particle energy (as in Eq. (2.2)).

In sampling calorimeters a significant fraction of energy remains in the absorbing material due to the production of fragments of nuclei and does not contribute to the measurable signal. At the same incident energy the ratio of the measurable energies of electromagnetic to hadronic showers, the so-called *sampling fraction* is larger than unity, i.e. $e/h > 1$.

In order to reduce the differences from the energy measurement of electromagnetic and hadronic showers, the energy of the latter which remains in the absorbing material has to be compensated. For this purpose the ZEUS calorimeter was constructed using depleted uranium (DU) as an absorbing material of a thickness of 3.3 mm (equivalent to one radiation length X_0 in that material) along with plastic scintillators as active material of 2.6 mm (equivalent to $0.006 \cdot X_0$) per plate. A hadronic shower traversing the DU plates produces fast neutrons whose kinetic energies are proportional to the energy loss due to nuclear reactions in the shower. These neutrons lose most of their energy by scattering elastically off the free protons of the scintillator and hardly due to any scattering off the heavy uranium nuclei. The deposited energy of the neutrons compensates the energy loss of the hadronic shower and achieves a sampling fraction close to 1 [69]. It should be mentioned that a compensating calorimeter can also be obtained with lead, provided that the layers of active material and passive material have the appropriate thickness relative to each other [70].

2.2.2.2 The ZEUS Calorimeter

The high-resolution ZEUS calorimeter is a sampling calorimeter with equal response to electrons (positrons and photons) and hadrons ($e/h = 1$) using absorber plates of depleted uranium and plastic scintillator layers as active plates. The depleted uranium plates have a composition of 98.1% U^{238}, 1.7% Nb and less than 0.2% U^{235}. The optical readout is performed via plastic wavelength shifters, lightguides and photomultipliers. In order to obtain equal calorimeter response to electron (positrons and photons) and hadrons, 3.3 mm thick uranium plates corresponding to one radiation length alternate with 2.6 mm thick scintillator plates. For a detailed description, see [71], [72] and [73]. The main features of the high-resolution calorimeter are:

- hermeticity over a large solid angle (99.7% of the solid angle is covered);
- energy resolution for hadrons of $\sigma(E)/E = 35\%/\sqrt{E} \oplus 2\%$;
- energy resolution for electrons of $\sigma(E)/E = 18\%/\sqrt{E} \oplus 2\%$;
- calibration of the absolute energy scale to 1%;

Part of the UCAL	Polar angle	Pseudorapidity
FCAL (forward)	$2.2^\circ < \theta < 36.7^\circ$	$4.0 > \eta > 1.1$
BCAL (barrel)	$36.7^\circ < \theta < 129.1^\circ$	$1.1 > \eta > -0.74$
RCAL (rear)	$129.1^\circ < \theta < 176.2^\circ$	$-0.74 > \eta > -3.4$

Table 2.1: CAL sections and the angular ranges covered by them. The polar angle and the pseudorapidity ranges are calculated with respect to the nominal interaction point. The regions of the FCAL and RCAL which are behind the BCAL are not considered.

- precise angular resolution for particles ($\leq 10\%$ mrad);
- longitudinal segmentation for hadron-electron separation;
- short signal-processing time at the nano-second level.

The solenoid and the tracking chambers are completely enclosed by the uranium calorimeter, except in the region around the beam-pipe. The UCAL is constructed in three main parts, the hollow cylindrical central part of BCAL with a polar angle acceptance of $36.7^\circ < \theta < 129.1^\circ$ and the two end caps FCAL and RCAL, which cover the polar angle of $2.2^\circ < \theta < 36.7^\circ$ and $129.1^\circ < \theta < 176.2^\circ$, respectively (see table 2.1 and figure 2.8). The inner radius of the BCAL is 134.5 cm, while the FCAL and RCAL face closer to the interaction point are located perpendicular to the z-axis at the position 234.4 cm and -160.2 cm, respectively, along that axis whose origin is in the nominal interaction point.

The total depth of the three different calorimeter sections takes into account the Lorentz boost and reflects the maximum energy deposition of scattered particles. The FCAL has a maximum depth of 7.1 interaction length (λ_{int}), while BCAL has $5.3\lambda_{int}$ and RCAL $4\lambda_{int}$. Each section is divided into modules and further subdivided into towers which provide granularity for position reconstruction.

The three calorimeter components have similar structures and are subdivided longitudinally into an electromagnetic calorimeter (FEMC, BEMC, REMC) with a depth of $1\lambda_{int}$, which is sufficient to fully contain the electromagnetic showers, and a hadronic calorimeter (HAC). In FCAL and BCAL the HAC section is divided into two subsections HAC1 and HAC2, while the RCAL has only one HAC section.

The whole calorimeter has a modular structure. The FCAL and RCAL calorimeters consist of 23 modules which follow the same construction principles, as shown in figure 2.9, where an isometric view of a FCAL module is presented. The FCAL and RCAL modules have the same width of 20 cm and have a height vaying from 2.2 m to 4.6 m so that roughly a clindrical structure with a radius of $\sim$2.3 m can be built. The depth varies from $7.1\,\lambda_{int}$ in the central region to $5.6\lambda_{int}$ in the outer horizontal regions for FCAL. For RCAL the depth is smaller ($\sim 4\,\lambda_{int}$) since momentum conservation does not allow very high energy particles going in the rear direction of the detector.

The centred module of the FCAL and RCAL calorimeter are split into a separate upper and lower part leaving a hole in between to allow the beam-pipe crossing through the detector. The horizontal segmentation is determined by the width of the modules. The transverse segmentation depends on the height of the wavelenght shifters which collect the scintillator light. Each longitudinal section (EMC, HAC1, HAC2) is read out in both sides by wavelegth shifters. For

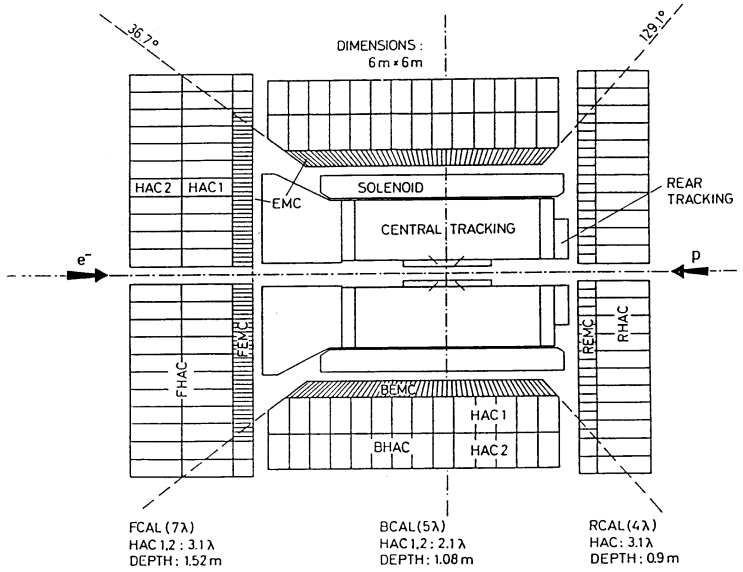

Figure 2.8: Layout of the ZEUS high resolution uranium-scintillator calorimeter. The picture shows the three sections of the UCAL and the polar-angle acceptance of each section.

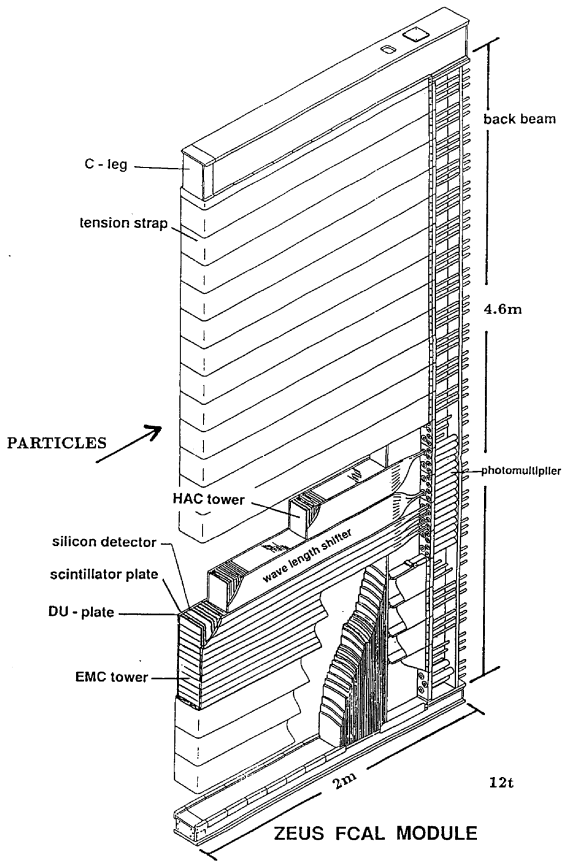

Figure 2.9: Internal structure of an FCAL module. The RCAL modules are very similar but they contain only two EMC cells instead of the four in FCAL and BCAL. One module in BCAL follows the same distribution as in FCAL but its geometry is adapted to the barrel requirements (see section 2.2.2.2).

FCAL the segmentation of the EMC section is 5x20 cm^2, and for RCAL 10x20 cm^2. These sections are called EMC cells. The hadronic cells of FCAL and RCAL have a segmentation of 20x20 cm^2.

The BCAL modules [55] present a similar distribution than of FCAL, but the geometrical design is slightly different to adapt to the barrel-shape requirements of this calorimeter part. Each module consists of 14 towers parallel to the z-axis. The 32 modules complete the circle around the z-axis containing the interaction point. In the BCAL, each tower is similar to one tower in FCAL except that the depth is around 5 λ_{int}. The first (last) tower in each module contains only 3 (2) electromagnetic cells. To increase the efficiency for detecting electromagnetic showers, the first and the last towers have their electromagnetic cells oriented towards the interaction point.

Due to the optical read out combined with photomultipliers a fast readout processing can be performed which allows the determination of the arrival times of incoming particles at the nanosecond level. The timing resolution for each calorimeter cell is $\sigma_t = 1.5/\sqrt{E} \oplus 0.5$ ns, where E (GeV) is the energy deposited in the cell [73]. The timing information from the calorimeter is useful to remove both beam-gas and cosmic ray related backgrounds. The time $t = 0$ ns is defined to be the time at which the particles originating from ep collisions at the interaction point arrive at the calorimeter.

When particles from beam-gas interactions which occur behind the RCAL, deposit energy in the RCAL, this time is negative. Therefore, a cut on the RCAL time can remove beam-gas events. In addition, the "up-down" time difference[6] should be zero for deposits related to an ep collision. However, for cosmic rays, this time difference is greater than 10 ns. Therefore, cosmic rays events can also be removed with the calorimeter time information. The vertex position along the the z-axis can also be measured using calorimeter time information. The time t at which energy is deposited in the FCAL near the beam-pipe from an ep collision will depend on the vertex position along the z-axis (z_{vtx}) according to the equation $t = -2z_{vtx}$, where c is the speed of light. The correlation between the z_{vtx} measured using the tracking detectors and the FCAL timing information can also be used to remove beam-gas interactions.

The readout of the calorimeter cells is fast enough to avoid mixing the information of two successive bunch crossings, but since the trigger decission about each event is slower (see section 2.2.6), the information has to be stored waiting for it. This is done by means of a pipelined readout of the calorimeter [74]. Each of the channels stores the information in a system of capacitors which delays the transmission of the read values during the time the trigger system takes a decision about the event. This system can store up to a maximum of 58 events, which means that the information is kept ~ 5.6 μs after the event occurs. This time delay is enough for taking a fairly good decision about the usefulness of the event.

The calibration of the calorimeter is performed using several redundant tools, which are described in [72]. The main calibration source is the use of the natural uranium radioactivity, the so-called uranium noise (UNO), which produces a low background current in the photomultiplier. This current is statistically very stable and the deviations from the expected value allow the detection of problems in the operation of the photomultiplier. On the other hand, to calibrate the electronic system reading the information for each channel, injectors of charge are used to simulate the signal coming from the photomultiplier. Since the quantity of charge is known, the returned value given by the complete readout system is used to calibrate the effects

[6]Defined as the difference between the time at which energy is deposited in cells at the top and at the bottom of the BCAL.

of the electronics, after substraction of the noise contribution. All these tools provides a stable diagnostic tool for monitoring and calibration of the calorimeter.

2.2.3 The Backing Calorimeter and the Muon Chambers

The main purpose of the Backing Calorimeter (BAC) is to measure the energy leakage out of the main calorimeter. In addition, it is used to detect muons from *ep* interactions and cosmics. The BAC totally covers the UCAL using as absorber material the 7.3 cm thick plates of the iron yoke. The iron yoke for the return of the magnetic field has the shape of an octogonal prism which is closed by endcaps on both sides. The yoke can be magnetised by copper coils, in order to create a magnetic field for an independent measurement of the momentum of muons in the barrel muon chambers. It consists of slabs of iron separated by 3.7 cm gaps instrumented with proportional tubes.

The Muon Chambers are located inside and outside of the iron yoke, and measures tracks penetrating the calorimeter and cosmics rays. This detector is constructed in three main modules: the forward (FMUON), barrel (BMUON) and the rear region (RMUON); more components are placed in the forward region in order to cover the higher particle flux. By measuring the momenta of reconstructed track segments, and comparing this measurement with track segments in the CTD, prompt muons can be detected. Each barrel chamber consists of two double layers of limited streamer tubes, with wires oriented along the beam axis. The position resolution is better than 1 mm. The barrel muon chambers accept muon tracks at $\theta > 34^\circ$. In order to reach the muon chamber, muons must transverse the UCAL and BAC. As a minimum ionising particle, the muon typically deposits $\sim$2 GeV in the UCAL and this is the energy needed for the muon to be detected in the inner muon chambers. In crossing the iron yoke between the inner and the outer muon chambers, the muon loses approximately 1 GeV of energy.

The forward direction is equipped with special muon chambers, which give an independent measurement of the muon momentum up to 100 GeV and down to very small angles. The detector consists of a toroidally magnetised iron region, interleaved with sections of drift chambers, limited streamer tubes and time-of-flight counters. The outer diameter of the toroids is 6 m and the average magnetic field inside is 1.7 T.

2.2.4 Luminosity measurement

Any process that is to be used to monitor the luminosity seen by an experiment must fulfil the requeriments that its cross section must be fairly large, so that a short measurement time is needed for a reasonably accurate estimate of the instantaneous luminosity, and that its cross section must be very well known, i.e. calculable and be short of uncertainties.

For HERA, the ep-bremsstrahlung process

$$e \; + \; p \; \rightarrow \; e' \; + \gamma \; + \; p$$

is used for the luminosity measurement. For the experimental measurement of this process, the outgoing electron and photon could be measured in coincidence in the so-called luminosity monitor (LUMI), with $E_{e'} + E_\gamma = E_e$, i.e. the scattered electron and photon energies must add

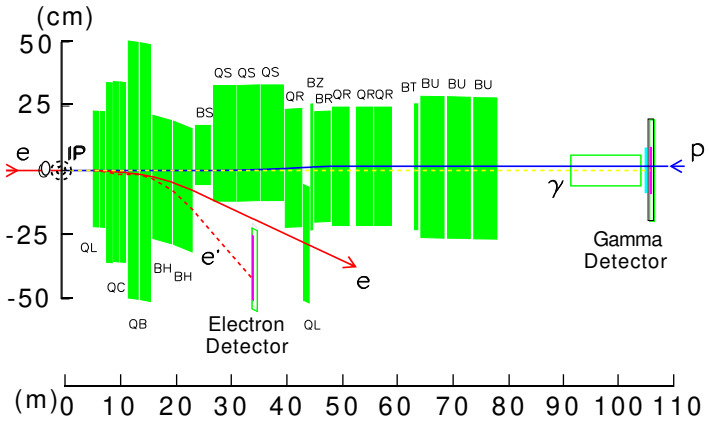

Figure 2.10: Layout of the ZEUS luminosity monitor.

up to the electron beam energy. The cross section for this processes is given semi-classically by the Bethe-Heitler formula [75]:

$$\frac{d\sigma_{bh}}{dE_\gamma} = 4\alpha r_c^2 \frac{E'_e}{E_\gamma\, E_e}\left(\frac{E_e}{E'_e} + \frac{E'_e}{E_e} - \frac{2}{3}\right)\left(\ln\frac{4E_p\, E_e\, E'_e}{M\, m\, E_\gamma} - \frac{1}{2}\right), \tag{2.3}$$

where E_γ is the photon energy, E_e, E'_e are the energies of the initial and final electrons, E_p is the proton energy, M (m) is the proton (electron) mass, α is the fine structure constant and r_c is the classical electron radius.

It has been shown that, within the experimental conditions, this cross section agrees excellently with QED calculations [76]. The radiative corrections to this process have been calculated and amount to -0.3% within the measurable area of phase space. The ZEUS luminosity monitor [77] consists of two separate detectors, one for the photon branch and one for the electron branch. The layout of the luminosity monitor components is shown in figure 2.10.

Photons emerging from the bremsstrahlung process at scattering angles $\theta_\gamma \leq 0.5$ mrad leave the beam pipe through a window located at a distance of 92.5 m from the interaction point, and are measured in a lead-scintillator electromagnetic calorimeter at 107 m from the interaction point. In front of the photon calorimeter, a 2 radiation length carbon filter absorbs the large flux of synchrotron radiation photons, which typically have low energy ($\sim$ keV), whereas the ep-bremsstrahlung photons used for the luminosity measurement have energies well above 1 GeV. A Cerenkov counter placed between the filter and the calorimeter detects events in which the photon has been converted in the filter in an e^+e^- pair. The energy resolution of this calorimeter under test beam conditions is $18\%/\sqrt{E(\mathrm{GeV})}$, although in practice is slightly worse $\left(25\%/\sqrt{E(\mathrm{GeV})}\right)$ due to the filter. The acceptance for bremsstrahlung photons is about 98%, independent of energy.

Electrons scattered at angles $\theta_{e'} \leq 6$ mrad, and with energies $0.2E_e \leq E_{e'} \leq 0.9E_e$ are deflected by the beam magnets away from the nominal electron beam orbit. They leave the electron beam line through a window at 27.5 m from the interaction point, and hit the electron calorimeter located at 34.7 m from the interaction point. The acceptance is measured to be above 70% and flat for scattered electrons with energies in the range $0.35E_e \leq E_{e'} \leq 0.65E_e$. This is the region used in the luminosity measurement. In addition, the electron calorimeter of the LUMI can be used to tag electrons scattered at very small angles. In this case, no coincidence with the

Period	HERA delivered (pb^{-1})	ZEUS on-tape(pb^{-1})	ZEUS physics (pb^{-1})	ZEUS physics (10^6events)
e^- 93-94	2.17	0.99	0.82 ($\pm$1.5%)	8.34
e^+ 94-95	17.42	10.57	9.64 ($\pm$1.2%)	29.98
e^+ 96-97	53.51	40.54	38.62 ($\pm$1.6%)	50.58
e^- 98-99	25.2	17.78	16.67($\pm$1.8%)	23.57
e^+ 99-00	94.95	73.37	66.04($\pm$2.25%)	66.76

Table 2.2: Luminosity collected by ZEUS in 1993-2000. The difference between "on-tape" and "physics" comes from the rejection of data considered not useful for analysis by the offline data quality monitoring.

photon calorimeter is required. This electron-tagger mode covers the Q^2 range between 10^{-7} and $2 \cdot 10^{-2}$ GeV^2, although the location of this calorimeter is such that only a fraction of the electrons are tagged in this region of Q^2.

The luminosity value is easily obtained from the observed ep-bremsstrahlung rate R_{ep} by $L = R_{ep}/\sigma_{obs}$, where σ_{obs} is the ep-bremsstrahlung cross section corrected for detector inefficiencies and acceptances. The uncertainty in σ_{obs} is small and, therefore, the error in the luminosity measurement is largely dominated by the uncertainty in R_{ep}. The luminosity measurement suffers from a number of background processes. By requiring a coincidence between a high-energy electron and photon, this background is dominated by interactions of electrons with the remaining gas in the beam pipe. The most problematic contribution is the beam-gas bremsstrahlung process in which the positron interacts with a nucleus (Z),

$$e\,Z \;\rightarrow e'\,Z\,\gamma\;,$$

which is impossible to distinguish from the process we want to measure and its contribution to the total counting rate of the luminosity monitor has to be estimated by using the pilot electron bunches. Let the fully measured counting rate of the luminosity detector be R_{tot}, the rate of the pilot bunches be R_{pilot}, the total current in the electron ring be I_{tot}, and the current in the pilot bunches be I_{pilot}; the actual *ep*-bremsstrahlung rate for the luminosity measurement can be estimated as:

$$R_{ep} = R_{tot} - R_{pilot} \cdot \frac{I_{tot}}{I_{pilot}}\;,$$

from where the luminosity can be extracted using the Bethe-Heitler expression corrected for the acceptance of the LUMI detector. For the determination of the luminosity photons with energies in the range 10-16 GeV are used. However, these cut values are varied for systematic checks.

The ZEUS integrated luminosity available for physics analysis is listed in table 2.2 for the 1993-2000 running periods. In these years the average ZEUS efficiency was around 70%.

2.2.5 Other components

Veto Wall

The veto wall (VETO) is an iron wall equipped with two layers of scintillator on both sides and placed 7 m away from the interaction point in the electron direction. Its dimensions are

800 cm x 760 cm x 87 cm, with a square hole of 95x95 cm^2 in the center for the beam pipe and magnets. Its main purpose is to shield the detector against particles from the proton beam halo and to give a veto signal for the main detector components.

C5 Counter
The C5 Counter is an scintillator counter which is located near the collimator C5, about 3 m away from the interaction point in the electron direction and very close to the beam (4 cm - 10 cm). Its main purpose is to provide an accurate time measurement for the backgroud in order to veto events which are not in the time window of the crossing of electron and proton bunches. From this timing information it is possible to reduce the background rate by an order of magnitude.

The Small-angle Rear Track Detector
The SRTD is installed in the region around the RCAL beam pipe [78]. The active part of the SRTD consists of arrays of scintillator strips grouped in 4 quadrants, 24x24 cm^2. Each quadrant contains two layers of scintillator strips arranged in orthogonal directions. The SRTD improves the measurement of charged particles, mainly small-angle scattered electrons, which is essential for an accurate reconstruction of the event kinematics at low Q^2.

2.2.6 Trigger and Data Acquisition Systems

At HERA one of the challenges for the data acquisition system is the bunch crossing time of 96 ns, clearly too short to perform a full data readout or to make a trigger decision. The purpose of the ZEUS trigger system is to distinguish interesting physics events from the background events. The total interaction rate, which is dominated by background from upstream interactions of the proton beam with residual gas in the beam pipe, is of the order of 10-100 kHZ while the rate of *ep* physics events in the detector is of the order of 3-5 Hz. In addition, other background sources like electron-gas collisions, halo muons and cosmic rays are also present. Background suppression is achieved by a sophisticated three-level trigger system [79], where each successive level has more time available to take more complicated trigger decissions. A schematic diagram of the ZEUS trigger and data acquisition systems is presented in figure 2.11.

The *First Level Trigger* (FLT) is a hardware trigger, designed to reduce the input rate below 1 kHz. Each component of the ZEUS detector has its own FLT, which stores the data in a pipeline and makes a trigger decision within 2 μs after the bunch crossing. The decisions from all the FLT parts are collected by the Global First Level Trigger (GFLT), which decides whether to accept or reject the event, and returns this decision to the readouts of the different components within 4.6 μs, corresponding to 46 bunch crossings. The FLT operates only on a small subset of detector data in order to achieve such rate in the decision. At this level most of the beam-gas and beam-halo events are rejected.

If the event is accepted by the FLT, the data are transferred to the *Second Level Trigger* (SLT), which is software-based and runs on a network of transputers. It is designed to reduce the rate below 100 Hz. For the SLT almost all the event information and the full dynamic range are used. The Global Second Level Trigger (GSLT) receives all of the SLT information from the individual components as well as the trigger information from the GFLT. The SLT produces a decision within 3 ms after the corresponding *ep* interaction. If the event is accepted by the GSLT, all the detector components send their data to the Event Builder, which collects the information to reconstruct a complete event. The event is then passed to the *Third Level Trigger* (TLT) which is software-based and runs a reduced version of the offline data analysis

code. It is designed to reduce the rate to a few Hz. Events accepted by the TLT are written to tape for further analysis.

2.2.7 Offline and detector simulation

The data previously stored on tape is reconstructed with the ZEPHYR package. During the reconstruction a preselection logic based on very soft, process oriented, requirements is performed. The results of this preselection are DST bits, which are stored in the header of the event file. Only the header is read for events which do not fulfill the required DST bit logic. This allows to run more efficiently over large amounts of data.

During the reconstruction procedure the information of the different components is reanalysed by applying corrections given by the data quality monitoring and by the calibration of the different channels on each component. At that point the whole detector information is available and can be used for the reconstruction of information which is obtained indirectly from the detector. For example the tracking reconstruction using the different hits in the tracking chambers or the reconstruction of the vertex position using the reconstructed tracks.

After this point the data are written on disk and is available for the final physics analyses [80].

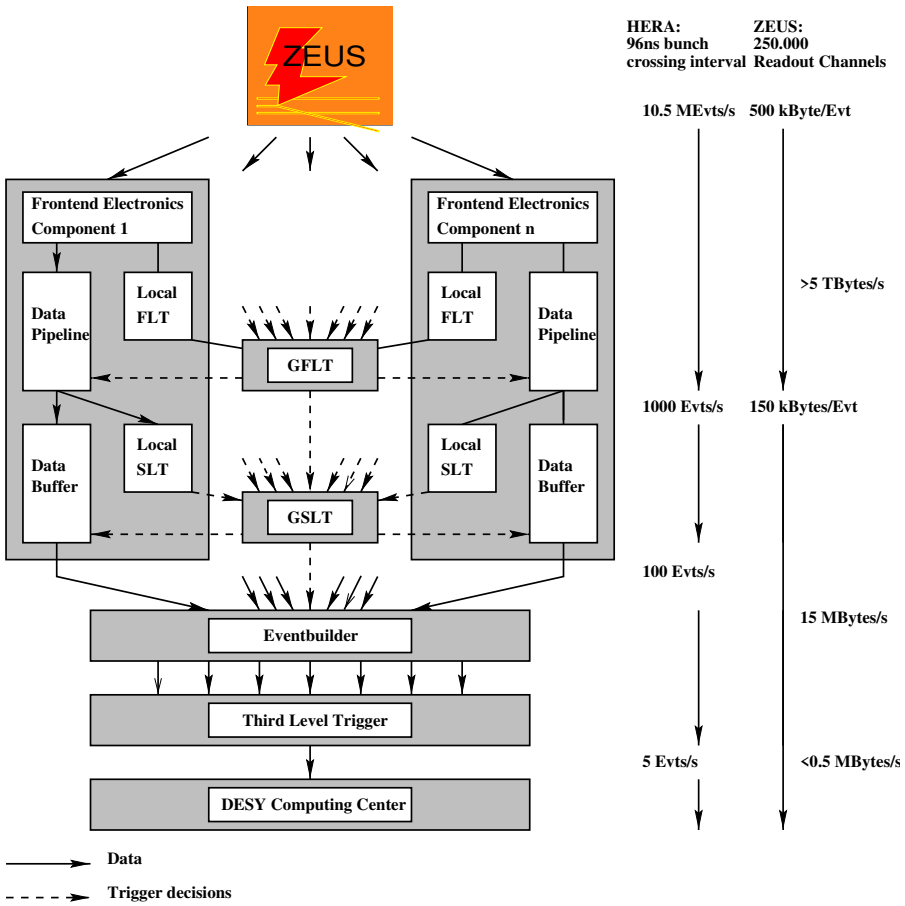

Figure 2.11: Scheme of the ZEUS data adquisition system. The effects of the trigger selection on lowering the rate (in events per second and in data size) is shown in the lines parallel to the decision diagram.

The Monte Carlo (MC) detector simulation is performed with the MOZART program (based in GEANT [81]). It allows the application of the detector response to simulated final states. After passing through the simulation the MC samples supply the detector information in the same format as for the data. This information is input for the trigger simulation (ZGANA) and afterwards the simulated events are reconstructed using ZEPHYR as for the real data.

2.3 Reconstruction of the kinematic variables

A precise reconstruction of x and Q^2 from the final state is of vital importance for the description of DIS events. The kinematic reconstruction based on quantities measurable in the ZEUS detector using several methods is described in this section. In deep inelastic scattering, the kinematics of the event must be reconstructed from the measured final state. At first order, the final state in a neutral current DIS event consists of the scattered lepton and the scattered quark

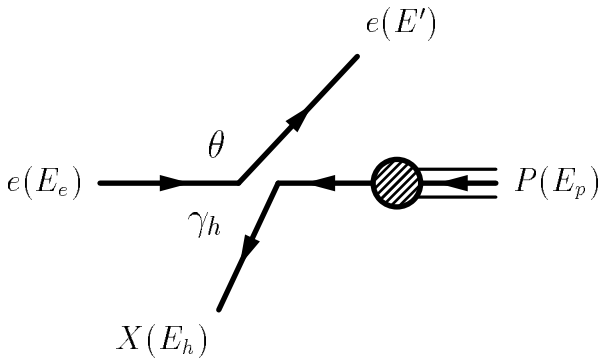

where E_e, E' and θ are the initial energy, final energy and scattered angle of the lepton, respectively. E_p, E_h and γ_h are the beam proton energy, the final hadronic energy and the polar angle of the final hadronic system, respectively. The kinematics of the event can be completely known from any pair of the variables E', E_h, θ and γ_h. In the following, some methods are considered and classified depending on the information that was used: either the electron variables, the hadronic final state information or a combination of the scattered lepton and hadronic system variables.

2.3.1 Reconstruction using the scattered electron variables

In neutral-current DIS there is an electron in the final state. In fixed target experiments, x and Q^2 are reconstructed from the angle and energy of the final-state electron. Using the definition of the kinematic variables given in the previous chapter, the following expressions are obtained:

$$\begin{aligned} Q^2_{ele} &= 2E_e E' \left(1 + \cos\theta\right) ; \\ y_{ele} &= 1 - \frac{E'}{2E_e} \left(1 - \cos\theta\right) ; \\ x_{ele} &= \frac{Q^2_{ele}}{s\, y_{ele}} . \end{aligned} \tag{2.4}$$

It is noted that the following relation holds

$$Q^2_{ele} = \frac{(p_{T,ele})^2}{1 - y_{ele}} \, , \tag{2.5}$$

where $p_{T,ele} = E' \sin\theta$ (in the massless aproximation) is the transverse momentum of the scattered electron. The contours of constant energy or scattering angle in the (x, Q^2) plane accesible to HERA are displayed in figure 2.12. It is seen that at low values of Q^2 the electron scattering angle is large (measured with respect to the proton direction) and hits the rear part of the UCAL. Occassionally the electron is deflected to the forward part of the detector. The scattering angle increases with Q^2, and is largely independent of x, except at high values of y.

The very low-Q^2 region, which is not covered by the nominal vertex data due to the beam hole in the ZEUS calorimeter, is indicated by the grey-shading in the right-plot of figure 2.12.

From the expressions:

$$\begin{aligned}
(\Delta Q^2/Q^2)_{E'} &= \Delta E'/E' \, , \\
(\Delta Q^2/Q^2)_{\theta} &= \tan(\theta/2)\, \Delta\theta \, , \\
(\Delta x/x)_{E'} &= \frac{1}{y}\, \Delta E'/E' \, , \\
(\Delta x/x)_{\theta} &= (x\frac{E_p}{E'_e} - 1) \tan(\theta/2)\, \Delta\theta \, ,
\end{aligned}$$

it is seen that the resolution in Q^2 as obtained by the electron variables is very good (except for very small scattering angles, that is, high Q^2 values). However, the resolution in x becomes very poor at low y due to the limited energy resolution.

2.3.2 Reconstruction using the hadronic system

Since ZEUS is an almost 4π detector, it is possible to use a completely independent reconstruction method based on the hadronic final state. This method is mainly used when the electron variables are not reconstructed due to the final lepton not being detected. For neutral-current DIS events this method allows to extend the measurable region in the (x, Q^2) plane to that in which the electron escapes through the beam pipe hole. For charged-current DIS events, where the final-state neutrino leaves the detector unobserved, this method provides the only way to reconstruct the kinematics.

From the scattered-quark energy E_h and angle with respect to the proton direction γ_h, the kinematics can be reconstructed using the following expressions:

$$\begin{aligned}
y &= E_h \, \frac{1 - \cos\gamma_h}{2\, E_p} \, ; \\
Q^2 &= {E_h}^2 \, \frac{\sin^2\gamma_h}{1 - y} \, ; \\
x &= \frac{Q^2}{s\, y} \, .
\end{aligned} \tag{2.6}$$

However, it is not possible to measure directly E_h and γ_h. One possibility could be to look for jets in the final state and associate one (or more) of them with the struck quark. Since jets could originate from soft and hard QCD processes, their use obscures the direct use of E_h and γ_h. Instead, the hadronic energy flow as measured in the cells of a segmented calorimeter can

be used without explicit jet finding. Jacquet and Blondel [82] proposed such a method, based on an appropriate weighting of the energy deposits in the cells. The idea is that the hadronic final state consists of a component that has taken part in the hard scattering (which therefore contains the information on E_h and γ_h) and a component that was only an spectator during the interaction (the target remnant). The kinematics can be accurately reconstructed from the hadronic energy flow if the latter is suppressed. The spectator component is characterised by a boost in the incoming proton direction. The Jacquet-Blondel method uses the following expressions:

$$\begin{aligned} y_{JB} &= \frac{1}{2\,E_e} \sum_i (E_i - p_{z,i}) \; ; \\ {Q^2}_{JB} &= \frac{1}{1-y_{JB}} \left[\Big(\sum_i p_{x,i} \Big)^2 + \Big(\sum_i p_{y,i} \Big)^2 \right] \; ; \\ x_{JB} &= \frac{{Q^2}_{JB}}{s\, y_{JB}} \; , \end{aligned} \tag{2.7}$$

where the sums run over the hadronic particles (or energy deposits) in the final state. The influence of the target remnant and any hadron lost in the forward beam-pipe hole, characterised by low p_T and low $E - p_z$, is suppressed in the above expressions. The problem with the use of the hadronic energy flow lies in the limited hadronic energy resolution of a calorimeter.

Figure 2.13 shows the contours of constant current-jet energy and angle in the (x, Q^2) plane. In contrast to the electron method, the effect on the resolution in x from the measurement errors of the jet energy is small at high x. However, the forward beam-pipe hole at $\lesssim 2.2^\circ$ limits the reach of this reconstruction method to $y > 10^{-3}$. At very low x and high y a similar limit is set by the rear beam hole (see the grey-shaded regions in the right-plot of figure 2.13).

2.3.3 Reconstruction from mixed variables

The methods which combine information from the electron and the hadronic final state are known as *mixed methods*. Taking into account the advantages of both the electron and the Jacquet-Blodel methods, it is straightforward to design the following expressions:

$$y_{mix} = y_{JB} \; ; \qquad {Q^2}_{mix} = {Q^2}_{ele} \; ; \qquad x_{mix} = \frac{{Q^2}_{mix}}{s\, y_{mix}} \; .$$

The Double Angle method

In addition, it has been proved useful to use θ and γ_h in the event kinematics reconstruction (the "Double Angle" (DA) method) [83], which exploits the advantage that angles are measured with better accuracy than energies, and do not suffer (to first order) from calorimeter energy calibration uncertainties. The expressions to reconstruct the kinematic variables in terms of these two angles are the following:

$$\begin{aligned} y_{DA} &= \frac{\sin\theta\,(1-\cos\gamma_h)}{\sin\gamma_h + \sin\theta - \sin(\gamma_h+\theta)} \; . \\ {Q^2}_{DA} &= 4{E_e}^2\, \frac{\sin\gamma_h\,(1+cos\theta)}{\sin\gamma_h + \sin\theta - \sin(\gamma_h+\theta)} \; . \\ x_{DA} &= \frac{{Q^2}_{DA}}{s\, y_{DA}} = \frac{E_e}{E_p}\; \frac{\sin\gamma_h + \sin\theta + \sin(\gamma_h+\theta)}{\sin\gamma_h + \sin\theta - \sin(\gamma_h+\theta)} \; . \end{aligned} \tag{2.8}$$

The difficulty in the DA method appears in the determination of γ_h. It has been suggested to determine γ_h from the Jacquet-Blondel variables,

$$\cos\gamma_h = 1 - \frac{8\, y_{JB}^2 {E_e}^2}{{Q^2}_{JB}(1-y_{JB}) + 4\, y_{JB}^2 {E_e}^2} \ ,$$

which is completely equivalent to (in terms of the four-momentum of the final particles or energy deposits)

$$\cos\gamma_h = \frac{(\sum p_x)^2 + (\sum p_y)^2 - (\sum E - p_z)^2}{(\sum p_x)^2 + (\sum p_y)^2 + (\sum E - p_z)^2} \ , \tag{2.9}$$

where the sums run over all the particles (energy deposits) associated to the hadronic final state. It should be noted that when the transverse momentum of the spectator jet and the jet masses are neglected, this expression is equivalent to the angle of the current jet defined as

$$\cos\gamma_h = \frac{\sum E_i \ \cos\gamma_{h,i}}{\sum E_i} \ ,$$

where the sum now runs over all the particles in the jet.

The Σ method

The Σ method [84] combines the measurements of energies and angles of the electron and hadronic system. Making use of the relation

$$\sum_i (E_{h,i} - p_{z,i}) + E'(1-\cos\theta) = 2E_e \ ,$$

which holds exactly for a hermetic and ideal detector, a new expression for y can be derived

$$y_\Sigma = \frac{\sum_i (E_{h,i} - p_{z,i})}{\sum_i (E_{h,i} - p_{z,i}) + E'(1-\cos\theta)} \ ,$$

which gives y at the hard interaction vertex even if an initial state radiation (ISR) photon has been emitted. Using the expression

$${Q^2}_\Sigma = \frac{(E'\sin\theta)^2}{1-y_\Sigma} \ ,$$

it is possible to determine Q^2 independently of ISR assuming that the initial-state radiated photon is collinear to the beam line and does not carry transverse momentum. The value of x_Σ is calculated from the last two expressions using the usual relation:

$$x_\Sigma = {Q^2}_\Sigma/(s\, y_\Sigma) \ .$$

The e-Σ method

Considering the good resolution for ${Q^2}_{ele}$ it is possible to use it in combination with y_Σ to make a kinematics reconstruction which is less sensitive to ISR photons. The variable x is reconstructed from these two variables using the usual relation:

$$x_\Sigma = {Q^2}_{ele}/(s\, y_\Sigma) \ .$$

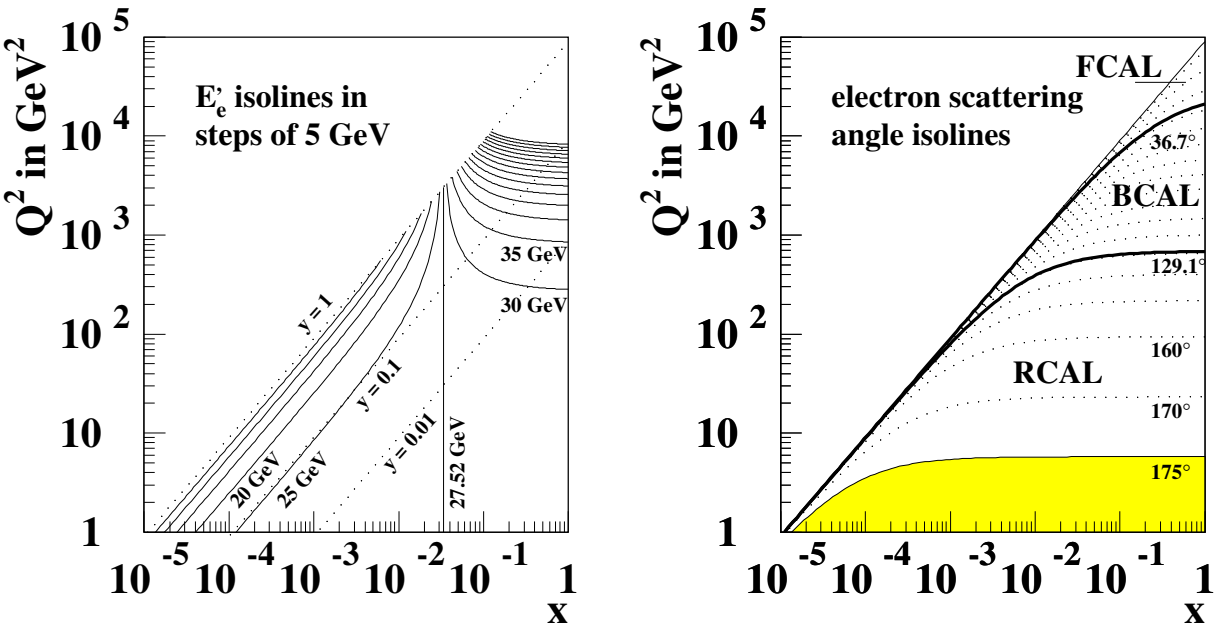

Figure 2.12: Contours of constant electron energy (left) and scattering angle (right) in the (x, Q^2) plane. The shaded region shows the angles for which the scattered electron escapes through the rear beam-pipe hole.

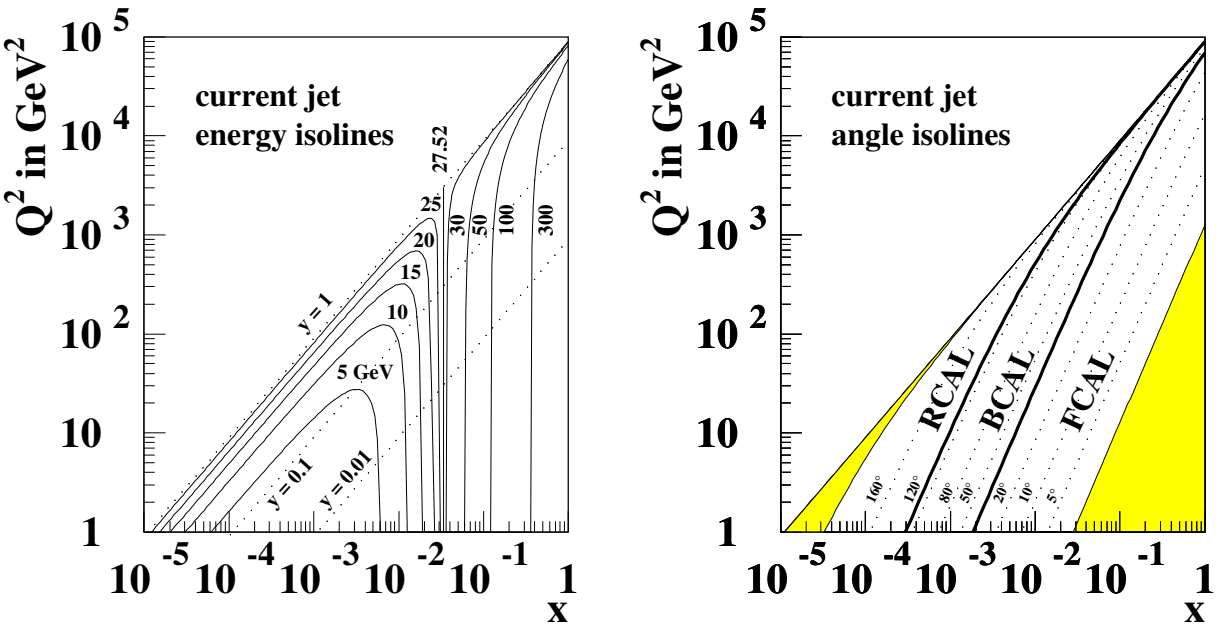

Figure 2.13: Contours of constant current jet energy (left) and hadronic angle (right) obtained in the QPM approach in the (x, Q^2) plane. The shaded regions show the angular ranges in which the scattered quark escapes through the forward or rear beam-pipe holes.

Chapter 3

Event simulation

In order to understand how the detector effects modify the observation of the final state in a high energy process is necessary to study these effects by means of a detector simulation. This simulation is applied to final state particles which have been generated according to the physical process under study. The generation of *Monte Carlo (MC) events* has become a fundamental tool in high energy experiments for the understanding of the complicated detector effects.

On the other hand, since the measurements are done for hadrons but pQCD only gives predictions for partons, it is necessary to incorporate some phenomenological models to transform the partons into hadrons. These models are not only useful to obtain the simulated events at hadron level which are passed through the detector simulation. They can also be used to estimate the corrections in going from partons to hadrons; these corrections are needed to make a direct comparison with the theory. Furthermore, the comparison of different models allows an estimation of the uncertainty for these corrections.

In this chapter, a description of the most important aspects of Monte Carlo event generation is presented, particularly for the models and generators which were used in the analysis

3.1 Global description

As already mentioned in section 2.2.7, generated events are passed through the detector and trigger simulation to study the response of the detector. The output of this simulation has the same format as the real data, but it also contains the information about the generated event. This information consists of tables containing the list of particles which are created in the process under study with a Monte Carlo event generator.

In the case of *ep* scattering the generation of simulated events relies in phenomenological approaches to QCD to describe the different processes which appear at the partonic level. The theoretical justification of the way the MC event generators apply the different steps in the simulation lies in the factorisation theorem for hard processes [85]. That is the event generators utilise the fact that a scattering process with a hard scale can be factorised into separate stages (see figure 3.1):

1. **hard sub-process**: it involves a hard scale and can therefore be calculated in a fixed-order perturbative expansion. The nature of the interaction determines the main characteristics of the event.

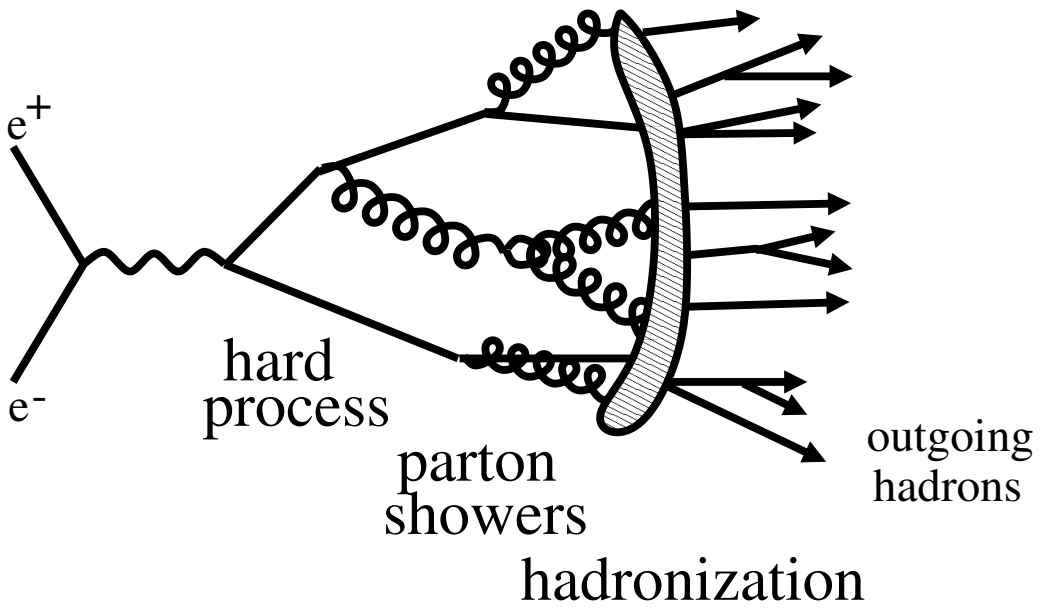

Figure 3.1: Representation of the different steps in the generation of an $e^+e^- \rightarrow$ hadrons event. The hard scattering is followed by the parton showering and the hadronisation processes. It should be noted that the different steps are artificially separated in the generation.

2. **initial- and final-state radiation**: in every process that contains coloured and/or charged objets in the initial or final state, additional partons and/or photons may be radiated, which can give rise to large corrections to the overall topology of the event. A very common approach to the modelling of these radiation processes is the use of an arbitrary number of branchings of one particle into two by using the corresponding splitting functions (see figure 1.9 for the case of QCD radiation). This generates a shower of particles which configures the partonic final state in the case of QCD radiation. This parton radiation tends to simulate the higher-orders contribution to the cross section and the inclusion of partly-known higher-order terms is standard. It is done in a similar way as described for the evolution equations, although the parton radiation is clearly dominated by the approximation considered.

   In the case of QED radiation, the showers generate a set of particles which will appear in the final state and may have an important contribution to the global properties of the event, although it does not affect the processes which tranform partons into hadrons.

   Note that initial-state QCD radiation leads to the evolution of the parton distribution functions, as it was described in section 1.3.

3. **hadronisation (fragmentation)**: it is the process by which the coloured partons are transformed into colourless hadrons. This non-perturbative process has yet to be understood from first principles and, at present, only phenomenological models are available to generate the hadronic final state starting from the partons.

4. **beam remnant fragmentation**: in the scattering process, the algorithm of initial-state radiation reconstructs in each beam particle the shower initiator by backward evolution from the hard sub-process. This shower initiator takes only some fraction of the total beam energy, leaving behind a beam remnant that takes the rest. If the shower initiator

is coloured, so is the remnant. Being colour-connected to the hard interaction, the beam remnant forms part of the same fragmenting system and needs to be reconstructed and connected to the rest of the event. In addition, in collisions where the two incoming beam particles have a composite nature (e.g. hadron-hadron interaction) there is the additional posibility that several parton pairs undergo separate hard or semihard scattering, usually referrerd to as 'multipartonic interactions'. At present there is very little understanding of these mechanisms and the event generators have to resort to phenomenological models and parametrisations from existing data to simulate these effects.

Following the scheme above, it should be clear that for the generation of simulated events, the two most important steps from the point of view of modellisation are parton radiation and hadronisation. The radiation of photons does not present the difficulties of parton radiation, mostly because it is easier to simulate than the complicated and unobservable processes which transform the hard partons into observable hadrons.

For this reason, in the following we will concentrate on the simulation of parton radiation and on the models to generate the hadrons from a given set of partons.

3.2 Multipartonic production

The description of the hadronic final state in high energy processes requires the calculation of multiple-parton emissions in QCD. For these higher-order QCD processes it is usually not possible to perform exact matrix element calculations (i.e. to obtain pQCD predictions) and one has to use aproximation schemes. Two different approaches will be described here and used in the analysis: the Parton Shower (PS) approach [86], based on the QCD parton-branching processes, and the Colour Dipole Model (CDM) [87], in which the gluons are radiated from colour dipoles between the separated quarks, antiquarks and gluons originating from the initial hard process. Both models are able to describe the measurements in e^+e^- annihilation into hadrons [88]. However, the situation in deep inelastic scattering is more complicated, as mentioned before. In the following sections, a brief description of each model applied to DIS processes is presented.

3.2.1 The Parton Shower approach

In DIS, the quark struck by the electroweak boson can emit partons both before and after the interaction giving rise to initial- and final-state parton showers, respectively; it is schematically represented in figure 3.2.

A parton close to the mass-shell in the incoming nucleon can initiate a parton cascade where in each branching one parton becomes increasingly off-shell with a space-like virtuality ($m^2 < 0$) and the other is on-shell or has a time-like virtuality ($m^2 > 0$). This initial-state space-like shower results in a space-like quark which finally interacts with the electroweak boson that turns it into an outgoing quark which is either on shell or has a time-like virtuality. After the interaction, the different partons with time-like virtualities generate a parton shower where the off-shell mass is reduced by branching into daughter partons with decreasing virtualities and decreasing opening angles. This shower continues until all partons are essentially on-shell.

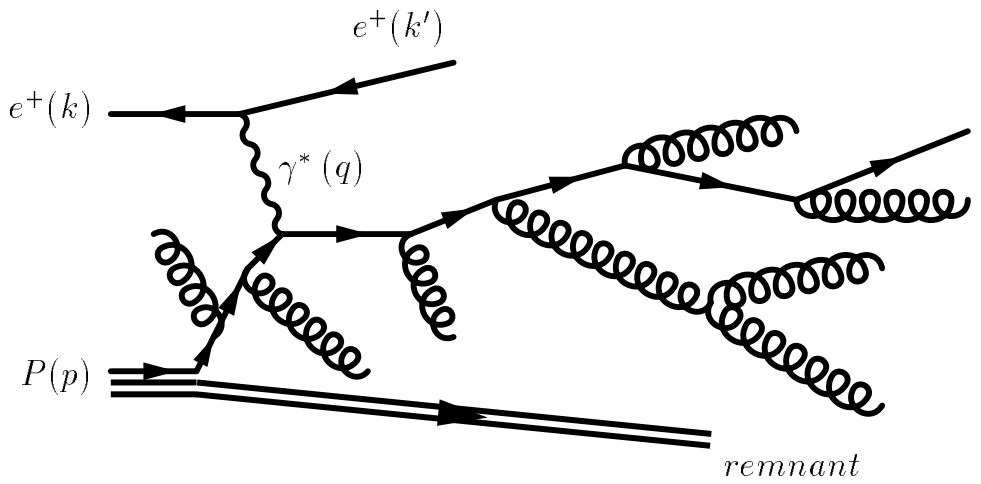

Figure 3.2: Schematic representation of the parton shower approach to the simulation of the parton cascade. The partons are generated by succesive splitting processes.

The general behaviour of initial- and final-state showers are similar since they are both based on the branching processes as described by the DGLAP evolution equations (see section 1.3.4) in the leading-logarithm approximation of perturbative QCD.

The final-state radiation is analogous to parton radiation in $e^+e^- \to q\bar{q}$. The evolution is based on the Sudakov form factor [89], which expresses the probability that a parton does not branch between some initial maximum virtuality and some minimum value. From this, one can find the mass of the decaying parton, the energy fraction in the branching and the flavour of the daughter partons. The process is iterated with a reduced virtuality until all parton vitualities are below some cut-off m_0^2 (around 1 GeV^2). Coherence in soft gluon emission is taken into account through angular ordering by decreasing opening angles in subsequent branches [90].

Initial-state radiation is handled with the backward-evolution scheme, where the shower is constructed from the hard electroweak interaction backwards with decreasing virtualities down to the on-shell partons in the incoming nucleon. This is a more complicated process since the nucleon parton densities must be taken into account. When combining the initial- and final-state radiation to construct the complete event, special precautions have to be taken in order to preserve energy-momentum conservation and to keep the definition of the kinematic variables, in particular that of Bjorken x.

The amount and hardness of the initial- and final-state radiation depends on the degree of off-shellness of the struck quark just before and after the interaction with the electroweak gauge boson. These virtualities are chosen, based on a Sudakov form factor, between m_0^2 and a maximum to be set by the energy or momentum transfer scale in the process.

The parton-shower approach has some shortcomings due to its approximate nature. The separation of initial- and final-state parton emission implies the neglect of interference terms between the two and it is not gauge invariant. The use of a leading-order approximation means that the emission of partons that are soft or close to the direction of the emitting partons should be well described, while the emission of hard partons at large angles could be mistreated. Therefore, the rate of events with additional hard partons that give rise to separate jets will not be well described. These problems were partially solved in e^+e^- by correcting ths first emission in the parton shower to agree with the result from exact pQCD first-order calculations. In DIS, this

matching is more difficult due to the more complicated matrix elements. Starting with the matrix elements, the hard emission is generated and extra, but softer emissions are then added using the parton-shower approach. The singular region of the matrix elements is avoided by a cut-off in the invariant mass of every parton pair.

3.2.2 The Colour Dipole Model

The Colour Dipole Model (CDM) is based on the property that a gluon emitted from a $q\bar{q}$ pair in an e^+e^- collision can be treated as a radiation from the colour dipole between the q and the $\bar{q}$, and that to a good approximation the emission of a second softer gluon can be treated as a radiation from two independent dipoles, one between the q and the first gluon and another between the same gluon and the $\bar{q}$. This approach can be generalised and the emission of a third gluon is given by three independent dipoles, and so on (see figure 3.3).

For DIS, the CDM does not divide the parton radiation process into an initial- and final-state ones, as is made in the Parton Shower approach discussed above. Instead it is assumed that all the radiation can be described by the colour dipole formed between the struck quark and the proton remnant. In $e^+e^- \rightarrow q\bar{q}$ both the q and the $\bar{q}$ are treated as point-like particles, but in DIS only the struck quark can be considered point-like while the proton remnant is an extended object. It is a well known fact that emission of small wavelengths from an extended antenna is suppressed and that for an antenna with a certain transverse size, effectively only a part proportional to the transverse wavelength $\lambda \propto 1/p_T$ is actually participating in the emission. In the model, this feature is implemented so that only a fraction

$$a = (\mu/p_T)^\alpha$$

of the proton remnant takes part in the emission of a gluon with transverse momentum p_T, where μ describes the size and α the dimension of the proton remnant. In this way, parton radiation is only dependent of the energy associated to the hadronic system in the hard interaction.

The CDM model correctly takes into account the QCD coherence effects included in the parton-shower approach by imposing angular ordering in the final-state emissions. The colour coherence

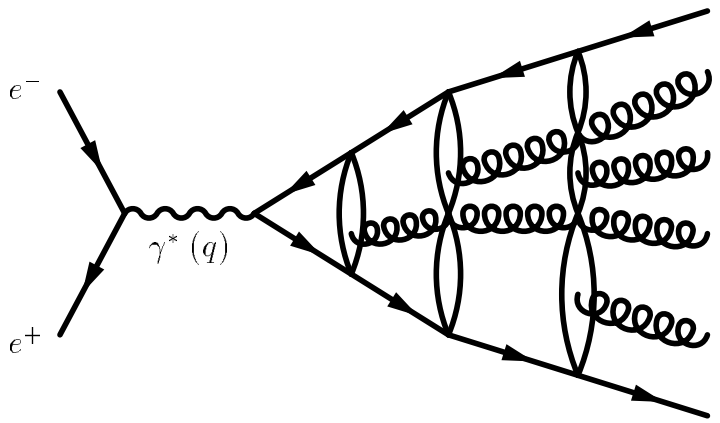

Figure 3.3: Schematic representation of the Colour Dipole Model for the simulation of the parton cascade in an $e^+e^- \rightarrow q\,\bar{q}$ event. The parton radiation is generated by colour dipoles defined between the partons present in each step.

effects due to the extension of the proton remnant included in the CDM has however no correspondence in the Parton Shower approach, where the remnant is considered as a non-radiating spectator.

The emission of partons from dipoles only describes the transverse momentum and rapidity distributions of the emitted parton in the rest frame of the emitting dipole. To describe completely an emission, there are two more degrees of freedom to fix. One is the azimuthal angle. The other describes the distribution of transverse recoil among the emitting partons. This is also different in DIS as compared to $e^+e^- \rightarrow hadrons$. Since only a fraction of the hadron remnant takes part in the emission, only that part should be allowed to recoil. This is realised by introducing an extra "recoil" gluon taking a fraction a of the remnant energy. The recoil is then distributed between the recoil gluon and the other emitting parton.

Although gluon emission in the CDM is close to the form of the exact matrix element, the processes initiated by gluons (i.e. the Boson Gluon Fusion process) are not included at all. Therefore, a matching procedure has been introduced for the first emission in a DIS event. In this procedure, the initial dipole between the struck quark and the hadron remnant can either emit a gluon according to the $\mathcal{O}(\alpha_s)$ matrix element or emit the antipartner of the struck quark according to the BGF matrix element. The selection of the process is, as usual, made by the Sudakov form-factor prescription. In the case of BGF, there are then two dipoles, connecting each of the struck quarks with the hadron remnant, which continue radiating independently.

3.3 Hadronisation models

After the parton shower has finished, the final state consists of a set of partons with virtualities of the order of the cut-off scale m_0^2. From this point, the low momentum-transfer (long-distance) regime, in which non-perturbative effects cannot be neglected, has to be considered to simulate the hadronisation step.

One general approach to hadronisation, based on the observation that perturbation theory seems to work well to rather low scales, is the hypothesis of *local parton-hadron duality*, where it is supposed that the flow of momentum and quantum numbers at the hadron level is established at the parton level. Hence, the flavour of the quark initiating a jet should be found in a hadron near the jet axis. The extent to which the hadron flow deviates from the parton flow reflects the smearing due to hadron formation. This smearing is related to energy scales of order Λ_{QCD} so its effects will be negligible if the energy scale associated to the partonic interaction is very large in comparison with Λ_{QCD}, which is of the order of 200-300 MeV.

Several phenomenological models have been constructed to simulate the formation of hadrons. Here three different models will be described: the independent fragmentation model, the string or Lund model and the cluster fragmentation model.

3.3.1 The independent fragmentation model

The simplest scheme, suggested by Field and Feynman [91], for generating distributions of hadrons from those of partons is to assume that each parton fragments independently. The fragmentating quark q creates a colour field in which a new light $q'\bar{q}'$ pair is produced. A meson $q\bar{q}'$ is formed with a fraction z of the energy of the quark q. The leftover quark q', with

energy fraction $(1-z)$, is fragmented in the same way, and so on until the leftover energy falls below some cut-off. For gluon fragmentation, the gluon is first split into a quark-antiquark pair, either assigning all the gluon's momentum to one or the other with equal probability, so that the gluon behaves as a quark of random flavour, or using the $g \to q\bar{q}$ splitting function.

Such a prescription contains an arbitrary function $f(z)$ plus other input parameters for the flavour/spin/mass options at each step. These parameters must be determined from the comparison with experimental data. The details of the procedure are, however, not fixed. One can identify z with the energy fraction or with the $E + p_L$ fraction instead. Alternatively, for example, the $q\bar{q}'$ pairs formed can be identified with low-mass hadronic clusters instead of single mesons.

3.3.2 The string model

The assumption of linear confinement provides the starting point for the string model [92]. As a q and $\bar{q}$ move apart from their common vertex, the physical picture is that of a colour vortex line being stretched between both partons. The transverse dimensions of the tube are of the order of the hadronic scale (~ 1 fm). If the tube is assumed to be uniform along its length, this produces a confinement picture with a linearly rising potential. In order to obtain a Lorentz covariant and causal description of the energy flow due to this linear confinement, a massless relativistic string with no transverse degree of freedom is needed. From hadron spectroscopy, the string constant, i.e. the amount of energy per unit length, is of the order of $k \sim 1$ GeV/fm. As q and $\bar{q}$ move apart the potential energy stored inside the string increases, and the string may break by the production of a new $q'\bar{q}'$ pair, so that the system splits into two colour singlet systems $q\bar{q}'$ and $q'\bar{q}$, each of them with a string evolving in an independent way (see drawing on the right of figure 3.4). If the invariant mass of either of these strings is large enough, further breakings may occur.

In the Lund string model [93], the string break-up process is assumed to proceed until only on-mass-shell hadrons remain, each hadron corresponding to a small piece of the string. In order to generate the quark-antiquark pairs, the Lund model invokes the idea of quantum mechanical tunnelling. This leads to a flavour independent gaussian spectrum of the p_T of the pairs and a suppression of heavy-quark production. A tunnelling mechanism can also be used to explain the production of baryons. In the simplest approach a diquark in a colour antitriplet state is just treated like an ordinary antiquark, such that a string can break either into a quark-antiquark or into an antidiquark-diquark pair.

If several partons are moving apart from a common origin, the string structure between them becomes more complicated. For a $q\bar{q}g$ event in e^+e^- collisions, a string is stretched from the q end to the $\bar{q}$ end via the gluon. The string will fragment along its length. To first approximation there is one fragmenting string piece between the quark and the gluon and a second one between the gluon and the antiquark. When considered in detail, the string motion and fragmentation is more complicated, with the appearance of additional string regions during the time evolution of the system. These corrections are specially important for soft and collinear gluons, since they have to provide a smooth transition between events where such radiation took place and events in which it did not. In this way, the string fragmentation model is *infrared safe* with respect to soft or collinear gluon emission.

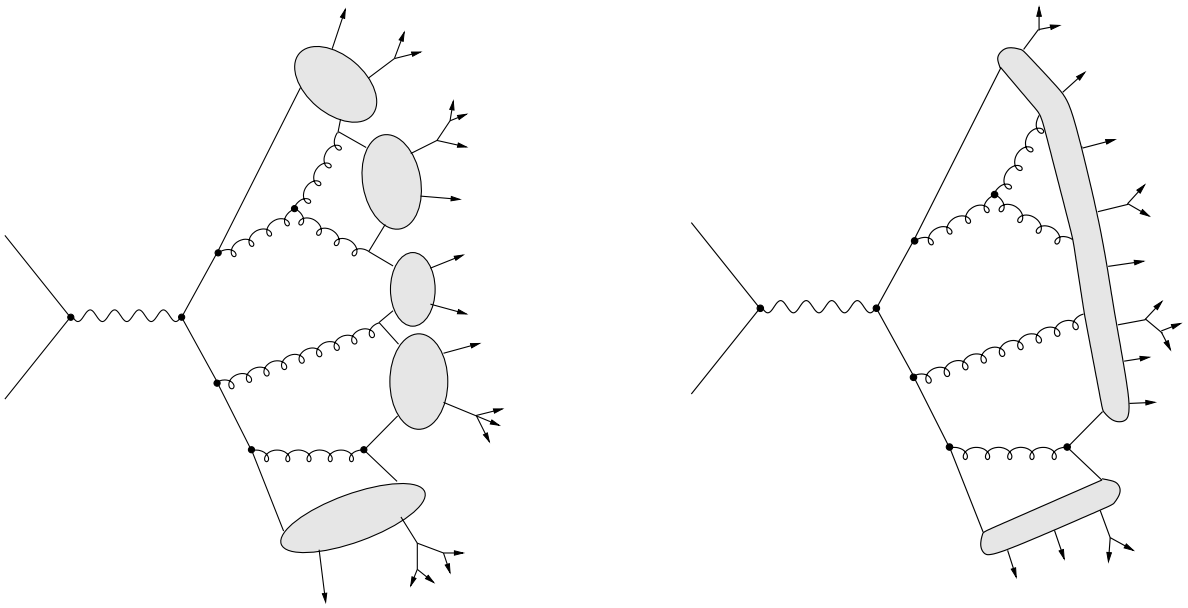

Figure 3.4: Schematic picture showing a parton shower followed by cluster hadronisation (left) and Lund-string hadronisation (right) for $e^+e^- \rightarrow$ hadrons.

3.3.3 The cluster fragmentation model

An important property of the branching process is the preconfinement of colour [94]. This suggests a class of *cluster hadronisation models* in which colour-singlet cluster of partons form after the perturbative phase of jet development and then decay into the observed hadrons (see drawing on the left of figure 3.4). The simplest way for colour-singlet clusters to form after parton branching is made via non-perturbative splitting of gluons into $q\bar{q}$ pairs [95].

Neighbouring quarks and antiquarks can then combine into singlets. The mass of the resulting clusters is typically two or three times m_0. If a low value of m_0 is used (of the order of 1 GeV) most clusters have masses of up to a few GeV and it is reasonable to consider them as superpositions of resonances. The hadronic energy and transverse momentum distributions for final states in $e^+e^- \rightarrow$ *hadrons* are quite well described without including additional adjustable fragmentation functions.

3.4 Event generators for neutral current DIS

In this section the main programs that are used for the simulation of events in neutral current deep inelastic scattering are presented. Obviously the event generator used in each case depends on the kind of events which are under study. Since the complete list of generators is large, we concentrate here on those most commonly used for inclusive studies in DIS. These generators are those used in the analyses presented later on.

The LEPTO Monte Carlo generator

The first step of the event generation is, as mentioned above, the simulation of the hard scattering process. This can be done using the LEPTO program [96], which is based on the

leading-order electroweak cross sections for the underlying parton level scattering, and includes QCD corrections using exact first-order matrix elements.

Since LEPTO is able to calculate lepton-hadron scattering at the parton level, a set of PDF's has to be provided for the calculation. This is done using the standard library PDFLIB [97], which contains the information for most parametrisations of the proton parton densities.

In addition, since LEPTO does not provide radiative corrections, the events are generated using this program interfaced to HERACLES [98] via DJANGO [99]. The HERACLES program includes first-order electroweak corrections; the generation of events using this interface allows the calculation of the radiative corrections. Furthermore, since these radiative corrections are present in the real data, the addition of them to the calculation should improve the similarity between the real events and the simulated events. This improvement is very important to understand some detector effects.

After the hard scattering process has been computed, the final products are considered as the input for the generation of the parton cascade. In LEPTO it is possible to select between the Parton Shower approach (in the Matrix-Element plus Parton Shower (MEPS) option of the program) and the Colour Dipole Model, as it is described below.

Once the parton radiation is completed, the hadronisation is performed with the Lund hadronisation model [92] as implemented in JETSET [100]. This program allows the selection of the independent hadronisation model, but its use is not recommended with LEPTO since it does not provide a smooth transition from configurations with radiation of soft partons and those without it [96]. After the fragmentation process, the final-state hadrons are provided and the simulated event is ready to be used for the extraction of predictions to be compared to the data, or for the detector simulation.

The MEPS and ARIADNE options for parton radiation

The parton cascade can be simulated following different phenomenological models, as it is mentioned in section 3.2. The most standard ones can be used to evolve the hard partons provided by the first step of the LEPTO program, as mentioned in the previous section.

The parton model approach is included in LEPTO as the MEPS option, which allows to calculate the predictions at parton level using the exact matrix element for the lowest orders and including higher orders in the leading logarithm parton shower approach, i.e. using the DGLAP equations. The simulation of the initial- and final-state parton radiation is done in the standard way described in section 3.2.1. However, it should be noted that the calculations to first order in α_s are done using the exact matrix element and this implies that the hard parton emission is better implemented than in a model where all the parton radiation is calculated using the Parton Shower approach, which is only a good model for soft radiative processes.

A switch allows the user to implement the parton radiation using the Colour Dipole Model and including the boson-gluon fusion process, as implemented in the ARIADNE program [101]. This program is not a complete event generator, and only generates the QCD cascade. It has to be interfaced to other programs which handle the hard interaction (as LEPTO) and the subsequent hadronisation and particle decays.

Since the two models can be used with the same program for the calculation of the hard process, the comparison of two samples only differing on the choice of parton cascade allows the extraction of the differences between the models. This is often used to estimate the uncertainty in the prediction for the parton cascade.

The HERWIG Monte Carlo generator

The program HERWIG[1] [102] is a general multipurpose particle physics event generator including the simulation of a complete set of interaction processes in one package. Among the different kind of interactions, it is possible to select the simulation of neutral current DIS events. This can be done by selecting the lowest order (QPM process) or the order-α_s processes. In both cases the higher orders are approximated with a parton cascade generated using the parton shower approach.

After the parton radiation, the fragmentation process is simulated using the cluster fragmentation model, which is performed in different steps:

- All the outgoing gluons are split non-perturbatively into quark-antiquark pairs (and optionally diquark-antidiquark pairs).
- For the quark and diquark states, a colour line can be followed, in the planar approximation, from each quark to an antiquark or diquark with which it can form a colour-singlet cluster.
- These clusters satisfy the preconfinement property and are then fragmented into hadrons with a mechanism which is globally like the one described in section 3.3.3. Special actions are taken when the cluster has small mass.

The philosophy of this program is to describe the perturbative-calculable parts in as much detail as possible, so it assumes that the observable will be dominated by the perturbative part of the calculations. Following this approach, simple models are taken to describe the non-perturbative hadronisation and beam remnant components, which results into a very few tunable parameters and a high predictive power.

On the other hand, the cluster fragmentation model usually gives a poorer description of the data than the Lund string model. This feature makes it not so useful for obtaining the detector effects to the hadron level by using the detector simulation. HERWIG is still very commonly used in different analysis of DIS at HERA because it allows the estimation of the uncertainty coming from the hadronisation process by comparing the predictions of two different phenomenological models.

[1] HERWIG stands for Hadron Emission Reactions With Interfering Gluons.

Chapter 4

Description of the analyses

The analyses were performed using the data taken with the ZEUS detector in the 96 and 97 running periods. During those years HERA collided protons of energy $E_p = 820$ GeV and positrons of energy $E_e = 27.5$ GeV. The integrated luminosity available for physics analyses is 38.6 ± 0.6 pb^{-1}.

In this chapter, the complete experimental analyses are described. It shows the requirements used to select the events in the data and simulated events.

4.1 Event selection

The first step in the analysis consists of selecting the events which are under study. The initial sample include all the events taken with the detector and trigger after the data have been processed. Depending of the kind of analysis, the selection requires different event properties.

In the case of the analyses described here, a similar selection of the events is needed for both analyses because we are interesting in a sample of neutral current DIS events. For this reason, the requirements for the global properties of the event are the same in the two cases. Those are described in the first parts of this section.

After the event selection has been done, the jet search is performed, which is different for each analysis. The particular selection is described in the corresponding part of this section.

4.1.1 Identification of the scattered positron

The main signature of neutral current DIS events is the presence of the scattered positron in the final state. A correct and efficient identification of the positron and a precise reconstruction of its position and energy are of vital importance for the analysis of this type of events. The different topology of electromagnetic and hadronic showers is the property used to identify the positron in the UCAL. In fact, using this property, it is possible to identify an electromagnetic shower as the one associated to the scattered positron provided that it has sufficiently large energy and is well isolated.

In the kinematic regions where the positron is expected to have small energy, the identification of the electromagnetic shower is difficult because it can be similar to a hadronic shower of similar energy.

If the hadronic final state deposits energy close to the positron, it is difficult to recognise the energy deposit as coming from an electromagnetic shower since the deposit is bigger than the shower initiated by the positron alone. The additional hadronic shower masks the positron deposit which no longer looks like an electromagnetic one.

Apart from the difficulties mentioned above, others come from particles falsely identified positrons. Photons in the final state produce energy deposits which are very similar to those of positrons and, thus, if no further information (e.g. tracking) is used, photons can be wrongly selected as positron candidates. Neutral pions are often identified as positrons because their very fast decay into two photons ($\pi^0 \rightarrow \gamma\gamma$) is detected in the calorimeter as only one electromagnetic shower if the pion has sufficiently large energy. Other particles (e.g. η) also decay to photons, but they are not so frequent due to their larger masses. In any case, all these fake positron signals in the calorimeter give rise to background, which has to be suppressed.

There are several parameters which can be combined to extract the information to identify positron candidates.

The complexity of the possible ways to obtain a combined, but simple answer made the problem appropriate for being solved by a neural network. In the analyses the neural network SINISTRA [103] is used for the identification of the scattered positron. SINISTRA is based on islands of calorimeter cells, where an island is a group of cells which are merged following a predefined criterion: each cell is merged with the cell with the highest energy of all cells which are contiguous to it. The procedure is made in such a way that the biggest islands are formed by 3x3 calorimeter towers.

The input variables are the energies registered in the corresponding cells of the island and the neural network projects the information into one output variable $\mathcal{P}$, which is interpreted as the probability that the island is the scattered positron ($\mathcal{P} \sim 1$) or of hadronic origin ($\mathcal{P} \sim 0$).

Furthermore, it is possible to find a position for each island, using the different cells and weighting their respective positions with the cell energy deposit. Using the energy and position, the four-momentum of the island is reconstructed. This four-momentum is that associated to the positron candidate if the island is accepted as the final candidate.

In the end, the different islands have an associated probability of being the scattered positron. The ones with largest probability are taken as good candidates. Efficiency and purity studies of the positron candidates have shown that a good selection of candidates is made by considering only candidates with $\mathcal{P} > 0.9$ and that the probability given by SINISTRA is reliable if the island has an energy larger than 10 GeV.

This sets the standard way to select the positron candidate to the following selection method, which is the one used in the analysis:

i) The candidate with largest probability is taken.

ii) If the candidate energy as measured in the calorimeter is larger than 10 GeV and the probability $\mathcal{P}$ is larger than 0.9, it is considered as a good candidate for the scattered positron.

iii) If the candidate does not fulfill the requirements in ii), then the candidate is rejected and the event is discarded, i.e. no longer considered as a neutral current DIS event.

iv) If the value of y_{ele} (see Eq. (2.4) in section 2.3.1) associated to the candidate is larger than 0.95, the event is discarded. This requirement reduces the background due to photoproduction events.

To improve the purity and efficiency of the positron identification, two additional cuts are imposed **only if the candidate has a polar angle in the region** $\theta_e < 140°$. They are related to the size of the electromagnetic shower and to the isolation of the candidate. These cuts reduce the chance that a hadronic jet or part of a jet is misidentified as an electromagnetic deposit and associated to the positron candidate.

v) The energy distribution of the positron is studied as a function of the distance in the $\eta - \phi$ plane to the candidate's direction, given by the four-momentum:

$$\Delta_{ele} = \sqrt{(\eta - \eta_e)^2 + (\phi - \phi_e)^2} \, .$$

If the summed energy inside a cone of 0.3 in this plane (i.e. $\Delta_{ele} < 0.3$) is less than 90% of the total energy of the candidate, the candidate is rejected and the event discarded. The requirement is raised to 98% in the region $\theta_e < 30°$.

This cut rejects candidates whose shower is bigger than the expected for a real positron.

vi) The same kind of study is done for the energy not associated to the candidate. In this case, if the summed energy not associated to the candidate in a cone of 0.7 around the candidate's direction is larger than 10% of the candidate's energy, the candidate is rejected and the event discarded. This is required only if the candidate has a polar angle $\theta_e > 20°$ since in the forward region this requirement is not good enough.

This cut allows to reject candidates which are not well isolated; they are frequently fake candidates (fake positrons[1]).

In some analyses, the positron candidate is required to have an associated track if the polar angle of the candidate is in the central region of the detector. This requirement has not been considered for the analyses described here, except as a cross-check [104, 105].

4.1.2 Selection of the neutral current DIS event sample

After the positron candidate has been accepted, the event is a good candidate to be a neutral current DIS event. Additional requirements are imposed, some of them to override the trigger requirements since it is obvious that at the first and second trigger level it is not possible to perform a sophisticated identification of the scatttered positron as that provided offline by an electron finder like SINISTRA.

The complete set of cuts used in the analysis to select the final sample of events is listed below. The cuts are grouped for a clearer description.

[1]Note that "fake positron" may refer to a real positron but not the scattered one. For example, an electron/positron coming from the semileptonic decay of a heavy quark. This kind of candidates are usually close to a hadronic deposit and will be not isolated at all.

Selection of events, energy scale and noise

The first step in the selection of the sample consists of removing the events which are not "good enough" for physics analysis by applying a cut on the events for which the detector conditions are considered as "bad". In this analysis, the standard selection used in ZEUS analyses is done. Since this selection only depends on detector conditions, it is only applied to the real data.

During the data selection, the energies of the calorimeter cells are scaled to improve the accuracy of the energy scale. These scale factors have been calculated by comparison of real and simulated events and yield a better comparison between the real data and simulated events. The factors applied in this analysis are the following [106]:

- For the FCAL, a factor of 1.04 (0.95) is applied to the EMC (HAC) cells.
- In the BCAL, a factor of 1.04 (1.08) is applied to the EMC (HAC) cells.
- In the RCAL, a global factor of 1.025 is applied to all cells.

These factors are only applied to the data.

The noise per calorimeter cell due to the natural radiactivity of the uranium has to be suppressed for a better reconstruction of the event. For this reason a suppression cut of 60 (110) MeV for EMC (HAC) cells is applied to the whole calorimeter. Furthermore, a cut of 100 (150) MeV is applied to isolated EMC (HAC) cells. All these cuts are applied also to simulated events; it should be noted that the detector simulation includes that of the noise due to the uranium radioactivity.

Some calorimeter cells are identified as "noisy" during certain running periods, i.e. they have a significantly higher mean energy or "firing" frequency compared to other cells. This is usually due to malfunctions in the electronics which reads the information of the photomultiplier. A list of noisy cells is made for each year and cells identified as "noisy" are not included in the final reconstruction if their energy is less than three sigma above the noise level.

To avoid the presence of "crazy photomultiplier signals" an additional cut on the imbalance is impossed: any cell with an imbalance between the two photomultipliers satisfying

$$\left|\frac{E_l - E_r}{E_l + E_r}\right| > 0.9 \,,$$

is not considered, where E_l (E_r) is the energy on the left-(right-)side photomultiplier. This kind of energy deposits are usually related to a *spark* in one of the photomultipliers, which makes the signal very large.

This scaling of the UCAL energy and the selection of cells above given threholds is done as the first step of the offline analysis. This means that all the quantities which are calculated in the following have been performed after this selection has been done. The only exception is the calculation of variables in the trigger.

Trigger requirements

Since the real data is selected using a complicated trigger system (see section 2.2.6), it is necessary to require which triggers should have been fired. In this way, it is possible to correct for trigger inefficiencies by applying the same trigger chain to data and Monte Carlo samples.

The trigger chain has to be completely defined to avoid biases coming from additional slots. In the present analysis, the required trigger chain was the following one:

- At the FLT, at least one of the slots numbered 40, 41, 42 and 43 has to be fired for the event. These slots are set by energy deposits in the calorimeter and if some vetoes related non-*ep* events were not fired for the event.

  The cuts applied at the FLT for the slots mentioned above are the following:

  $$E_{EMC}^{FLT} > 10 \text{ GeV} \text{ or}$$

  $$E^{FLT} > 15 \text{ GeV} \text{ or}$$

  $$E_{BEMC}^{FLT} > 3.4 \text{ GeV or}$$

  $$E_{REMC}^{FLT} > 2 \text{ GeV} \text{ or}$$

  $${E_T}^{FLT} > 11.6 \text{ GeV},$$

  where the superscript FLT indicates that the energy is that available from the calorimeter (of the indicated section) at the FLT level, where no correction was applied.

  Furthermore, for the determination of calorimeter energy sums at the FLT, the three inner rings around the FCAL beampipe and the inner ring around the RCAL beampipe are excluded. In the case of transverse energies, only the two inner EMC rings around the FCAL beampipe are excluded.

- As an additional cut, it is required that the FLT slot 49 was fired for the event. This slot requires that the event contains at least one "good track", where "good tracks" are defined as tracks for which the z position in the first superlayer of the CTD is between -50 cm and 80 cm.

- At the SLT, the analysis requires the events to pass through the SLT branch called SLT-HPP01. That is, the events are required to satisfy all the following conditions:

  - A reconstructed vertex with $-60 < z_{vtx} < 60$ cm.
  - $E - p_z > 8.0$ GeV, where E and p_z are the energy and the longitudinal momentum of the event, determined from the energy deposits in the calorimeter. For an ideal 4π detector this quantity is expected to be $2E_e \simeq 55$, as it was described in section 2.3.3. In a NC DIS event, this value will be very close to the expected one, so events with low values of $E - p_z$ are usually associated to proton beam gas or photoproduction events.
  - $E_T^{cone} > 8.0$ GeV, where E_T^{cone} is the sum of transverse energy in all calorimeter cells outside a cone of 10° around the FCAL beampipe.
  - $E - p_z > 12$ GeV or $p_z/E < 0.95$ [2].
  - This SLT branch is only fired if one of the FLT slots 40, 41, 42 and 43 is fired and if the FLT slot 49 is fired. These are the FLT slots described above.

  The quantities quoted above are computed with the information available at the SLT and not with the values after the event reconstruction.

  In addition, some vetoes are applied at the SLT to reject non-*ep* events.

[2]Since proton beam gas are characterised by $p_z \simeq E$, this requirement allows to make a softer cut on $E - p_z$ without losing ability in discarding background events, which is very important if the rate has to be drastically reduced.

- At the TLT more time is available to perform operations on the event information and, in particular, the software trigger allows the application of jet algorithms. In the analysis, the events are required to pass through one of the four TLT branches called TLT-HPP01, TLT-HPP02, TLT-HPP14 and TLT-HPP15.

  All these have the following set of common cuts:

  – A reconstructed vertex is found with $-60 < z_{vtx} < 60$ cm.

  – The number of "bad tracks" has to be smaller than 6. "Bad track" is defined as a track which is long enough for a good reconstruction (i.e. it has more than 5 hits in axial superlayers and more than 5 hits in stereo superlayers, and more than 20 hits in total) and is pointing to a very backward vertex ($z_{vtx} < -75$ cm). As an additional requirement for a "bad track", cuts on transverse momentum ($p_T \geq 200$ MeV) and pseudorapidity ($0.35 < \eta < 3.13$) are applied.

    This cut on the number of "bad tracks" suppreses proton beam gas background events, which usually contain forward-going tracks coming from the backward region. It should be noted that good events in coincidence with a proton beam gas event are also rejected.

  – They required a bit logic involving s everal SLT branches. This requirement is always fulfilled if the SLT-HPP01 branch is on, which was the required SLT logic for the analysis.

  In addition to the common requirements, each branch has its particular set of cuts, which are listed below. Cuts on jet variables refer to jets reconstructed using a cone-type algorithm (EUCELL) applied to the cells in the laboratory frame.

  - TLT-HPP01 requires the same cuts on $E - p_z$ and p_z/E than those described in the SLT-HPP01. In addition, it requires $E_T^{cone} > 25$ GeV.
  - TLT-HPP02 requires that the event contains at least one jet with $E_{T,jet} > 10$ GeV and $\eta_{jet} < 2.5$.
  - TLT-HPP14 requires $p_z/E < 1.0$ and that the event contains two or more jets with $E_{T,jet} > 4$ GeV and $\eta_{jet} < 2.5$.
  - TLT-HPP15 requires $p_z/E < 1.0$ and that the event contains either two (or more) jets with $E_{T,jet} > 6$ GeV and $\eta_{jet} < 2.5$ or two (or more) jets with $E_{T,jet} > 4$ GeV and $\eta_{jet} < 1.5$.

  It should be noted that the jet algorithm is applied to the whole calorimeter, including the cells belonging to the positron candidate. This procedure identifies the positron's energy deposit as a jet. For high Q^2, this procedure makes this trigger very efficient for neutral current DIS events containing jets, in spite of the fact that a positron candidate is not requested.

- As mentioned in section 2.2.7, during the offline reconstruction of the events some additional requirements are imposed and stored in a bit structure (DST bits). This works formally as a fourth trigger although the quantities calculated are based on the offline reconstruction information, i.e. closer to the final values.

  For the analysis presented here, at least one of the following DST bits has to be set: DST-b64, DST-b65, DST-b77 and DST-b78. Each of them is set on if the associated

TLT branch is set on. The corresponding TLT branchs are TLT-HPP01, TLT-HPP02, TLT-HPP14 and TLT-HPP15, respectively.

Cuts to remove non-ep background events

After the positron and trigger selection some non-*ep* events are still present in the sample. These events are removed by applying further cuts. In the analysis these cuts are applied using the information from the final reconstruction and are listed below:

- $\not{p}_T/\sqrt{E_T} < 2.5$ GeV$^{1/2}$, where $\not{p}_T$ is the total transverse momentum and E_T the total transverse energy of the calorimeter. These quantities are computed as

$$\not{p}_T = \sqrt{\left[\sum_{cells} E_i \sin\theta_i \cos\phi_i\right]^2 + \left[\sum_{cells} E_i \sin\theta_i \sin\phi_i\right]^2} \quad \text{and} \quad E_T = \sum_{cells} E_i \sin\theta_i \ .$$

  It is expected that $\not{p}_T \sim 0$ for a NC DIS event, while E_T can reach large values. In a sampling calorimeter, the energy measurement displays fluctuations and considering that these are of the order of $\sqrt{E_T}$ for the measurement of E_T, then the quantity $\not{p}_T/\sqrt{E_T}$ will be usually smaller than 1.

  On the other hand, for events originated by cosmic or halo muons, this quantity can be very large since the muon can leave more energy in one side of the detector giving rise to an imbalance.

- The number of "bad tracks" is required to be smaller than 5. This requirement is needed to override the trigger cut on "bad tracks".

  In the offline selection, the requirements for a track to be considered as a "bad track" are the same as those described for the trigger.

Additional cuts

Some final cuts are applied to override the trigger conditions, to remove background events and to reject events whose reconstruction is not reliable. These requirements are listed below:

- $38.0 \leqslant E - p_z \leqslant 65$ GeV, which removes background events coming from photoproduction processes and non-*ep* events. Furthermore, it removes NC DIS events with very low $E-p_z$; the kinematics of these events is not well reconstructed because of the initial-state QED radiation which escapes through the RCAL beam-pipe hole.

- The event must contain a vertex reconstructed using the CTD tracks. At least two tracks have to be associated to the vertex and the χ^2/ndf related to the fitted vertex must be smaller than 10. If such a vertex exists, it has to fulfill the conditions of being centred in the detector, i.e. $-38 \leqslant z_{vtx} \leqslant 32$ cm. This cut on z_{vtx} overrides the trigger requirements on the vertex. It is better not to include events far from the nominal interaction point in the final selection since the detector looks very different in comparison with the "centred" events, mainly regarding the angular position of the components. It should be mentioned that the x and y axis positions of the vertex were taken equal to zero in the two analyses.

- The identification of a second positron candidate makes possible to reject background events coming from elastic Compton processes ($ep \rightarrow ep\gamma$) in which two electromagnetic deposits are the only signals in the calorimeter[3]. To apply this cut, the second candidate is selected using SINISTRA (see section 4.1.1) as the one with next-to-largest probability. In case that two or more candidates display the same probability, the one with highest energy is taken.

  To improve the efficiency of selecting this second candidate, we apply the same cuts in the energy and isolation as for the first candidate. For the probability cut the value was raised to 0.99. The cut on the shower size is 0.9 for $20^\circ < \theta_{e(2)} < 140^\circ$ and is not applied if the candidate has $\theta_{e(2)} < 20^\circ$.

  It should be noted that no cut on y_{ele} is applied because this quantity is not adequate for a candidate which is not necessarily the scattered positron.

  If the second candidate is accepted as a good candidate, the cut to remove elastic Compton events is applied by requiring that the energy in the whole calorimeter not belonging to the two candidates is less than 4 GeV. In this case, the event is discarded. If the second candidate is not accepted this cut is not applied.

All the above cuts are applied to the simulated events in the same way as for the data. The only selection requirements which are different for data and simulated events is the cut on events in which the detector was in a "bad condition" and the scaling of the cell energies, as mentioned above.

Reconstruction and selection of the kinematic region

After all the above cuts and selection criteria have been applied, the kinematic reconstruction is performed. In both analyses, the Double Angle method is used for the kinematic reconstruction from the calorimeter information since it is the most convenient for the kinematic region we are interested in.

In the first analysis, the kinematic region is selecting by requiring the following cuts:

$$Q^2{}_{DA} \geqslant 125 \text{ GeV}^2 \quad \text{and}$$

$$-0.7 \leqslant \cos\gamma_h \leqslant 0.5 \ ,$$

where γ_h is the polar angle associated to the hadronic system, which is identified as the polar angle of the struck quark in the Quark-Parton Model. The way this variable is calculated is given in equation (2.9). This cut in $\cos\gamma_h$ is needed to assure a good reconstruction of the jets in the Breit frame (see [104, 107] for more details). Figure 4.1 shows the distribution in the kinematic plane (the $x - Q^2$ plane) of the events selected by the analysis of jets in the Breit frame. The events were selected with the complete set of cuts applied, including those described in section 4.1.4.

In the analysis of the subjet multiplicity, the following requirement is imposed to the virtuality of the exchanged boson:

$$Q^2{}_{DA} \geqslant 125 \text{ GeV}^2 \ .$$

[3]Since this cut only uses the calorimeter information, events consisting of an e^+e^- pair are also removed.

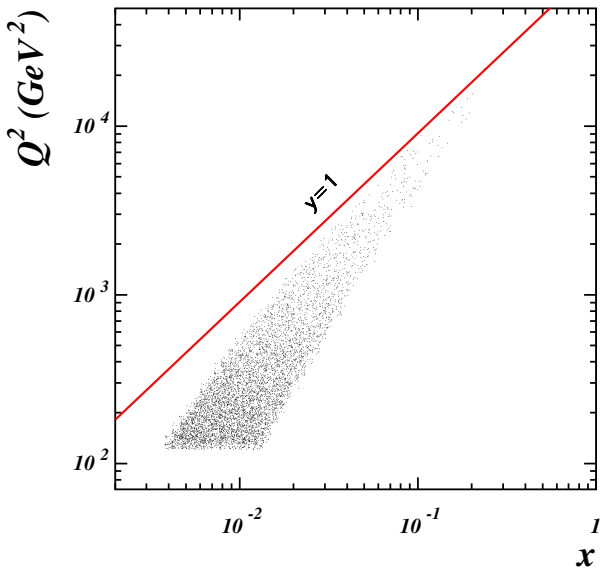

Figure 4.1: Distribution in the $x-Q^2$ plane of the selected events for the analysis of jets in the Breit frame. The line shows the kinematic limit $y = 1$.

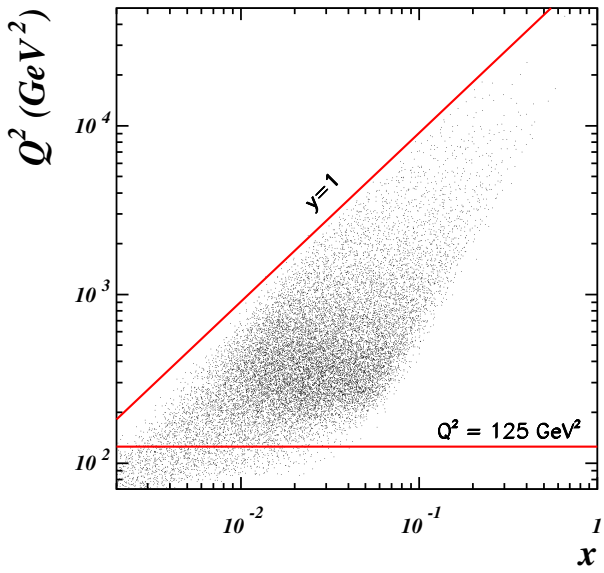

Figure 4.2: Distribution in the $x-Q^2$ plane of the selected events for the analysis of the subjet multiplicity. The lines shows Q^2 cut applied ($Q^2 = 125$ GeV^2) and the kinematic limit $y = 1$.

In this analysis the jets are reconstructed in the laboratory frame and, thus, the cut on $\cos\gamma_h$ is not needed. Figure 4.2 shows the distribution of the events in the kinematic plane (the $x - Q^2$ plane). The events were selected with the complete set of cuts applied in the analysis (including those described in section 4.1.3) except that on ${Q^2}_{DA}$, which is shown as an horizontal line in the plot.

4.1.3 Final selection of the jets in the laboratory frame

After the neutral current DIS events have been selected, the reconstruction of the jets is performed. Jets are reconstructed from the energies measured in the calorimeter cells. Only those cells passing the cuts described above are considered. Furthermore, all the cells belonging to the island identified as the positron candidate are not considered.

For each selected cell, its energy and the angular position with respect to the reconstructed vertex in the event allow the construction of a four-momentum, being by definition massless and having as energy that of the cell. The direction is reconstructed using the geometrical center of the cell.

After the application of the algorithm, the set of variables $\{E_{T,jet},\ \eta_{jet},\ \phi_{jet}\}$ contains all the information for the reconstructed jets.

The jets are preselected with a cut of $E_{T,jet} \geqslant 10$ GeV. The energy of the jets **in the data only** is then scaled by a factor which depends on the pseudorapidity of the jet and of the Monte Carlo sample which will be used to correct the data for detector effects. The reason of applying these factors is to decrease the uncertainty in the jet energy scale. They were obtained in a dedicated comparison between data and the predictions from the simulated events for quantities which are sensitive to differences in the jet energy scale [105].

The multiplicative factors obtained from the comparison between data and ARIADNE (LEPTO-MEPS) are the following:

- 1.0101 (0.9895) for jets with $-2 < \eta_{jet} < 0$;
- 1.0081 (0.9938) for jets with $0 < \eta_{jet} < 1$;
- 1.0168 (1.0056) for jets with $1 < \eta_{jet} < 1.5$;
- 0.9936 (0.9874) for jets with $1.5 < \eta_{jet} < 2$;
- 0.9916 (0.9873) for jets with $\eta_{jet} > 2$.

With the application of these factors, the differences in the jet energy scale between the data and the simulation is reduced; the uncertainty is estimated to be 1% for the jets used in the analysis.

The jet energies are then corrected for energy losses in the detector using theMonte Carlo simulations, as described in section 4.1.6. After this energy correction has been done, the final cuts are applied to the jets and only those satisfying the conditions

$$E_{T,jet} \geqslant 15 \text{ GeV} \quad \text{and} \quad -1 \leqslant \eta_{jet} \leqslant 2$$

are kept in the final sample.

As a final cut to improve the purity of the sample, the whole event is discarded if one of the final jets is close to the positron candidate by less than 1 unit in the $\eta - \phi$ plane. This cut removes events in which the positron is probably a fake candidate. Even being a real positron, the closeness to a jet indicates that probably it is the product of a semileptonic decay of a heavy quark, for example $b \to c\, e^- \bar{\nu}$.

After all these cuts, the final sample consists of 38779 events. Out of them, 37933 (97.8%), 821 (2.1%) and 25 (0.1%) events containing one, two and three jets are found, respectively. The total number of jets is therefore 39650.

For the selected jets, the subjet structure is resolved by using the algorithm described in section 1.4.5. The k_T-cluster algorithm is re-applied over the cells belonging to each jet and the number of subjets found at each resolution scale is considered in the calculation of the mean subjet multiplicity.

One of the selected events is shown in figure 4.3 as seen with the ZEUS detector. The distribution of transverse energy in the $\eta - \phi$ plane is also shown. The clear scattered positron candidate allows to classify the event as a neutral current DIS event candidate. In addition to the positron, the event contains one jet which, when looked in more detail, contains two subjets at $y_{cut} = 10^{-2}$.

4.1.4 Final selection of the jets in the Breit frame

In the analysis of jet production in the Breit frame, the cell information is reconstructed as described in section 4.1.3 and the four-momenta associated to the cells are transformed into the Breit frame. The kinematic variables reconstructed previously (see section 4.1.2) are used to calculate the matrix for the Lorentz transformation (see appendix A).

After boosting the cells into the Breit frame, the longitudinaly-invariant k_T-cluster algorithm is applied over the four-momenta in the way described in section 1.4.1. Upon the application of this algorithm, the set of variables for the jets in the Breit frame are obtained ($\{E^B_{T,jet}$, η^B_{jet}, $\phi^B_{jet}\}$).

The jets are preselected with a cut of $E^B_{T,jet} \geqslant 3$ GeV. Tn order to perform additional cuts to improve the purity of the sample the jet variables in the laboratory frame are calculated. In this case, the corresponding Lorentz transformation is applied to the four-momenta of the jets in the Breit frame, which are considered to be massless. The four-momenta of the jets in the laboratory are used to calculate the set of variables $\{E^L_{T,jet}$, η^L_{jet}, $\phi^L_{jet}\}$. This information is then used to perform the following cuts:

- If any of the jets in the event have $E^B_{T,jet} > 5$ GeV and $\eta^L_{jet} < -2$, the whole event is discarded and no longer considered.

  Very backward jets are likely to be photons radiated by the positron and detected in the backward region of the calorimeter. The presence of these photons introduces very serious biases in the reconstruction of the Breit frame. In fact, the Breit frame is so wrongly reconstructed that this photon is reconstructed as a "high-E_T jet". As it has been shown [107], it is more convenient to discard the whole event than to correct for its effects.

- If any of the jets in the event have $E^B_{T,jet} > 5$ GeV and is close to the positron candidate by less than 1 unit in the $\eta - \phi$ plane of the laboratory frame, the whole event is discarded. This cut removes events in which the positron is probably a fake candidate or the jet a photon radiated by the positron. This kind of events has to be discarded to improve the quality of the Breit frame reconstruction.

After these cleaning cuts have been applied, the energy of the jets **in the data only** is corrected as described in section 4.1.3 to reduce the differences between data and simulated events and the uncertainty in the jet energy scale [104].

With the application of these factors, the differences in the jet energy scale between the data and the simulation is reduced and the related uncertainty is estimated to be 1% for jets with $E^L_{T,jet} > 10$ GeV and 3% for lower $E^L_{T,jet}$ values [104].

The energy of the jets is then corrected for energy losses in the detector by using the simulations. This energy correction is performed in the laboratory frame as described in section 4.1.6; the correction to the jet transverse energy in the Breit frame is derived from that in the laboratory frame.

After the correction of the energy, the final sample of jets consists of every jet in the selected events satisfying

$$E^B_{T,jet} \geqslant 8 \text{ GeV} , \qquad -2 \leqslant \eta^B_{jet} \leqslant 1.8 \quad \text{and} \quad E^L_{T,jet} \geqslant 2.5 \text{ GeV} .$$

This sample of jets amounts to 12167 jets belonging to 8523 events.

Two of these events are shown in figures 4.4 and 4.5 as seen with the ZEUS detector. In both, the small-transverse-size energy deposit is associated to the scattered positron. In addition, two clusters of large transverse energy are present, which are the two jets. The energy deposits in the forward calorimeter are part of a jet due to the proton remnant.

4.1.5 Event selection at the hadron level in the MC samples

In simulated events, the same cuts are applied to select the events and the jets at the detector level as to the data. At the hadron level, a completely independent analysis is performed in order to obtain the information about the event before the detector simulation.

To select the events at the hadron level, cuts are applied which are described in the following paragraphs.

Reconstruction of the kinematic variables

At hadron level, all the information is exactly known. To obtain the kinematics, the exact theoretical expressions are used. For example, the value of Q^2 is obtained by squaring the four-momentum of the exchanged boson in the event, which is denoted by q_μ (for $\mu = 0, 1, 2, 3$), being the $\mu = 0$ the time-component (energy).

On the other hand, to obtain the expression for $\cos\gamma_h$ at the hadron level, the definition given in the Quark-Parton Model was used to avoid biases in the radiative events, in which y is not very useful because it is strongly affected by the radiation of photons by the positron.

The expression used is then

$$\cos\gamma_h = \frac{x\,E_p + q_3}{x\,E_p + q_0}\ , \tag{4.1}$$

being x Bjorken's x (see section 1.2.1) and E_p the energy of the initial proton. For this equation to make sense, the four-momentum of the boson is defined as going from the positron to the quark so that the above equation gives the polar angle of the struck quark.

To select the kinematic region we are interested in, the following cuts are applied in the first analysis:

$$Q^2 = -q_\mu\, q^\mu \geqslant 125\ \text{GeV}^2\ ,$$
$$-0.7 \leqslant \cos\gamma_h \leqslant 0.5\ .$$

In the analysis of the subjet multiplicity, the following cut is applied:

$$Q^2 = -q_\mu\, q^\mu \geqslant 125\ \text{GeV}^2\ .$$

Jet search and selection at hadron level

To obtain the jets at hadron level the same algorithm is applied to the final-state hadrons as to the calorimeter cells. The only difference is that the hadrons are not massless and their three-momenta are scaled so as to make the mass equal to zero just before the k_T-cluster algorithm is applied. This procedure sets the definition of transverse energy that is used in the analysis.

It should be noted that the hadrons are kept massive for the transformation to the Breit frame in the case of the first analysis.

After applying the algorithm to the "massless" hadrons in the same way as it was done for the cells, the following selections (depending on the analysis) were imposed:

- In the analysis of jets in the Breit frame, the jet search is done in the Breit frame and the selected jets must satisfy the cuts:

  $$E^B_{T,jet} \geqslant 8\ \text{GeV} \qquad \text{and} \qquad -2 \leqslant \eta^B_{jet} \leqslant 1.8\ ,$$

  where one should notice that no cut is applied in any frame other than the Breit at this level.

- In the analysis of the subjet multiplicity, the jet search is done in the laboratory frame and the selected jets must satisfy the cuts:

$$E_{T,jet} \geqslant 15 \text{ GeV} \qquad \text{and} \qquad -1 \leqslant \eta_{jet} \leqslant 2 \; .$$

  As for the detector level, the subjet structure is resolved by re-applying the corresponding algorithm, in this case over the hadrons assigned to each jet.

One of the major issues is the definition of the hadron level. Since for a Monte Carlo generated event all the information is available, the scattered positron and the possible radiated photons off the positron are removed from the list of final-state particles. These radiated photons are assigned to the leptonic part of the event and are not included in the hadronic final state. We are then left with the hadrons obtained after fragmentation. In principle, these hadrons can be considered as the hadronic final state, but a definition based on the lifetimes of the different particles is mandatory and described here.

Definition of the hadronic final state

The idea is as follows: although the fragmentation process is considered to take place very close to the interaction, the generated hadrons show a time evolution dictated by the different particle decays. This suggests that a precise way to define the final state, which is more independent of the fragmentation process, is the one based on the lifetime of the particles.

The selection of the hadrons which are considered as *stable* in the final state and used for the jet algorithm is done in terms of a *critical lifetime* τ_c: every particle belonging to the hadronic final state whose lifetime is longer than τ_c is considered as *stable*. If a particle belonging to the hadronic final state has a lifetime smaller than τ_c, then its decay products are considered. This leads to an iterative procedure which is stopped when all the particles generated by the fragmentation mechanism have been considered and they or their decay products form the list of particles (four-momenta) to be used in the jet search algorithm.

The lifetimes of the particles are distributed in such a way that two good choices for the critical lifetime can be made. These two values are the following:

$$\tau_c = 10^{-10} \text{ s} \qquad \text{or} \qquad \tau_c = 10^{-11} \text{ s} \; .$$

In the analyses presented here, the second value is preferred because the first one has obvious disavantadges from the experimental point of view [104, 105].

It has to be noted that not all the particles that form the hadronic final are hadrons. Leptons and photons may appear in the final state as decay products of some hadrons. These particles are included in the hadronic final state since they were generated as decay products of the partonic final state

4.1.6 Jet energy corrections

Jet energies need to be corrected since the final-state particles may lose energy before the reach the calorimeter. Sometimes the effect of energy loss does not affect significantly the results. For example, the loss in the energy of the scattered positron is important in the reconstruction of the kinematic variables when using the electron method. However, by using the Double Angle method, the energy losses only introduce differences of second order.

In the two analyses presented here, the kinematic variables are well reconstructed without a significant effect from the energy losses. On the other hand, the jet energy has to be corrected because the effects are very large and have a dependence on the polar angle.

The procedure used in the two analyses is briefly described here:

- The standard cuts are applied to the hadron level to select the jets in a Monte Carlo sample of events.

  As described in sections 4.1.3 and 4.1.4, the jets at the detector level are selected using a cut which is smaller than the final one. In the first analysis the cut was 3 GeV (in the Breit frame), while in the second the cut was 10 GeV (in the laboratory frame).

- For each event, the jets at hadron and detector levels are matched, that is, for each pair of jets, one at detector and one at hadron level, the distance in the $\eta - \phi$ plane defined as

  $$\Delta[hd] = \sqrt{(\eta_d - \eta_h)^2 + (\phi_d - \phi_h)^2} \, ,$$

  is calculated; the pair with the minimum distance is defined as a "matched pair" if this distance is smaller than 1. The procedure is repeated until no jet is left or the distances between the remaining pairs is larger than 1.

  It should be noted that for the analysis in the Breit frame the matching is performed in the laboratory to avoid problems in the matching due to the differences between the "true" Breit frame and the reconstructed one. This requires the boost of the four-momenta of the jets at hadron and detector level into the laboratory frame. In what follows, all the variables for the matched jets refer to the laboratory frame.

- For each pair, the energy of the jet at hadron level is taken as the original one and that of the jet at detector level as the reconstructed one. The correction of the jet energy is constructed from the correlation between the reconstructed energy and the original one. This correlation is parameterized with a linear function by fitting the distribution of the reconstructed energy as a function of the original energy. The fitted function has the form

  $$E_{T,jet}^{DET} = m \cdot E_{T,jet}^{HAD} + b \, .$$

  For a given jet at detector level the corrected energy is then obtained by inverting this function:

  $$E_{T,jet}(corr) = \frac{E_{T,jet}(rec) - b}{m}$$

- Since the energy loss depends on the jet pseudorapidity, the actual parametrisation is done separately for each region of η_{jet} by introducing a dependence on η_{jet} of the parameters m and b.

  Furthermore, the parameters could display a dependence on the transverse energy of the jets. For this reason, the parametrisations are perfomed by fitting functions of the mentioned form in several regions of the transverse energy if a global parametrisation was not able to describe the hadron-detector correlations for the whole $E_{T,jet}$ range.

A complete description of the method and detailed plots are presented in the ZEUS internal notes of the corresponding analysis, i.e. in [104] for the analysis of jets in the Breit frame and in [105] for the analysis of the subjet multiplicity.

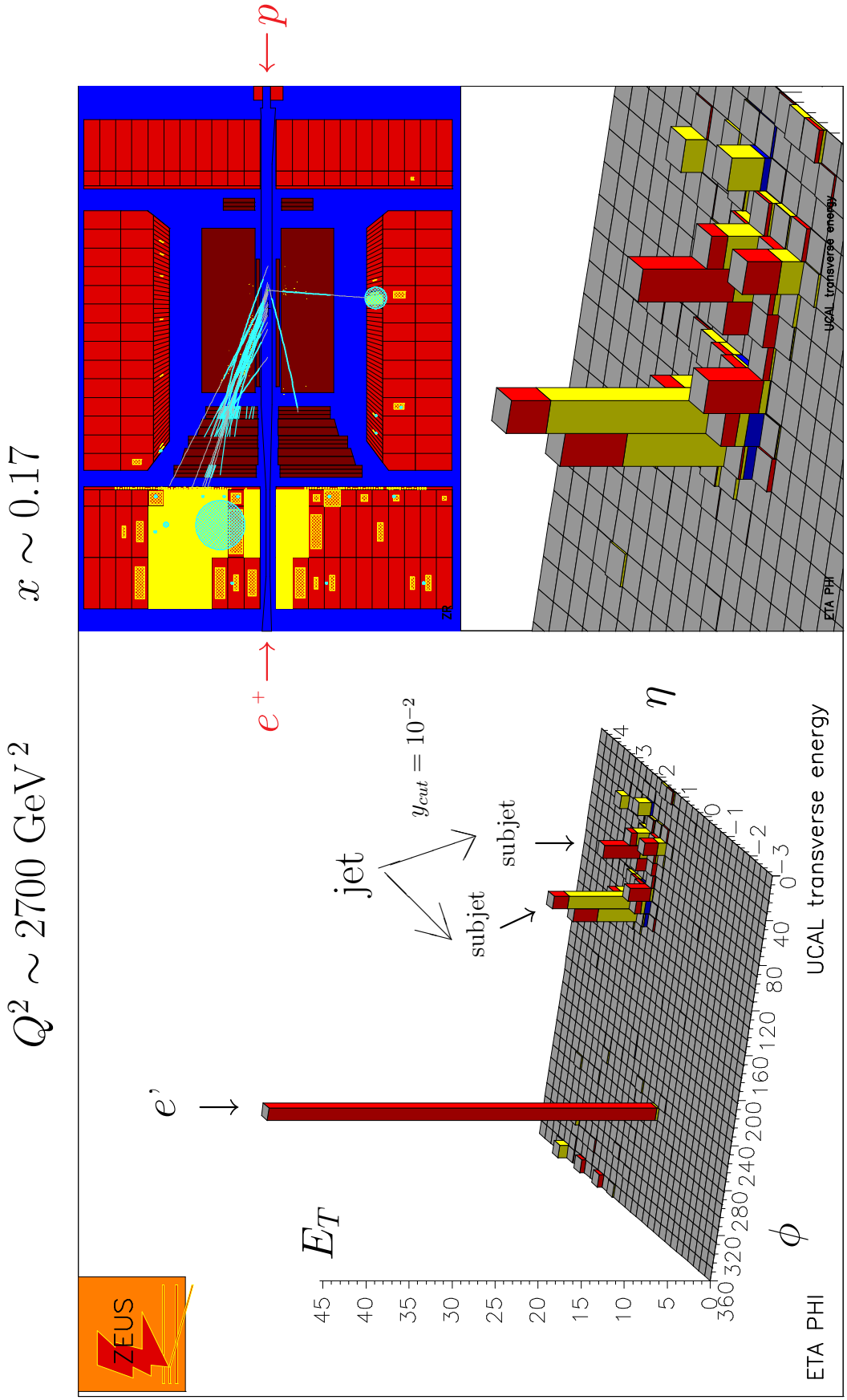

Figure 4.3: An event taken with the ZEUS detector and selected in the analysis of the subjet multiplicity. The small-transverse-size energy deposit is identified as the positron candidate. The additional transverse energy deposit is identified as a jet. It should be noted the presence of large energy deposits close to the direction of the incoming proton. Although these energy deposits, associated to the remnant, are very large, they do not show up in the transverse energy distribution, in which the positron and the jet are clearly observed. Looking at the jet in detail, as shown in the lower figure on the left-hand side, two subjets can be distinguished.

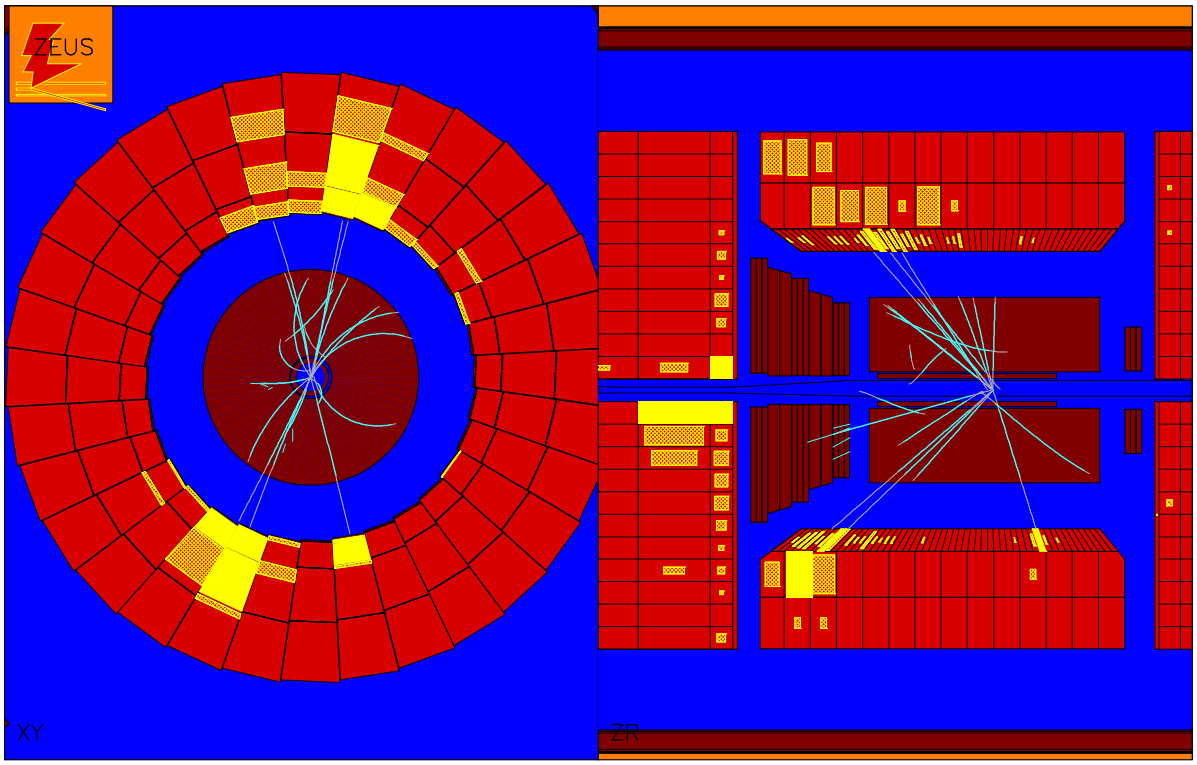

Figure 4.4: An event taken with the ZEUS detector and selected in the analysis of the inclusive jet cross sections in the Breit frame. The small-transverse-size energy deposit is identified as the positron candidate. There are two other clusters of energy deposits in the BCAL, in addition to the deposits associated to the proton remnant (see figure 4.3 and comments in the caption there). They are larger than the one of the positron candidate and are identified as two jets. The kinematic reconstruction of this event gives $Q^2 \sim 622$ GeV^2 and $x \sim 0.011$.

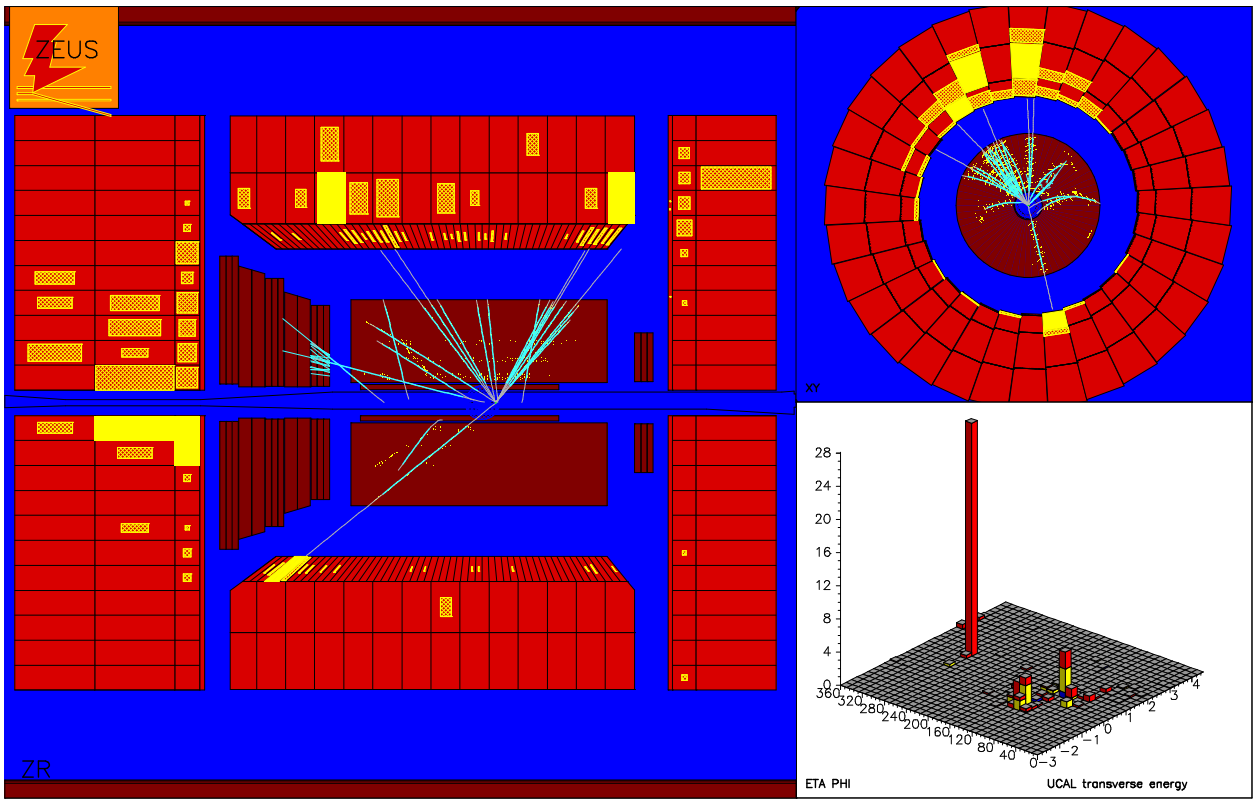

Figure 4.5: Other example of event selected for the analysis of inclusive jet cross sections in the Breit frame. In this case the two jets are partly in the BCAL and partly in the FCAL. The positron candidate is again well isolated. For this event the kinematic reconstruction gives a $Q^2 \sim 5100$ GeV^2 and $x \sim 0.07$. In addition, the distribution of transverse energy in the $\eta - \phi$ plane are also shown in the lower right part of the figure: the two jets and the positron candidate are clearly observed.

In the analysis of the subjet multiplicity, the correction of the jet transverse energy is given by the expression given above. After the correction of the transverse energy of the jet has been applied, the final selection cut on $E_{T,jet}$ is imposed to obtain the final sample of jets, as it was described in section 4.1.3.

In the case of the analysis in the Breit frame, the correction procedure requires two additional steps. First, the jets reconstructed in the Breit frame are boosted into the laboratory to correct the energy in the laboratory frame by using the expression displayed above. Once the energy has been corrected in the laboratory, the factor $E_{T,jet}(corr)/E_{T,jet}(rec)$ is applied to the transverse energy in the Breit frame. After this step, the final selection cut on the transverse energy is performed, as described in section 4.1.4. It should be noted that is not necessary to boost back into the Breit the corrected four-momentum in the laboratory frame.

4.2 Analysis I: Measurement of the inclusive jet cross sections in the Breit frame

In this section the complete description of the experimental results obtained for the first of the two analyses is summarised. Before the results are presented, several studies using the Monte Carlo samples to correct for detector effects are described.

4.2.1 Description of the measurements

In this analysis the aim is to measure the inclusive jet cross sections in the Breit frame. These cross sections are differential in the interesting variables. To obtain the corresponding distribution the following bins are used:

- For the cross section as a function of Q^2 we use the following bin boundaries (in GeV^2):

  $$125, \quad 250, \quad 500, \quad 1000, \quad 2000, \quad 5000, \quad 10^5 \, ,$$

  where it should be noted that the last boundary is above the kinematic limit. The selected value of 10^5 is set to simplify the calculations when calculating the differential cross section.

- For the cross section as a function of $E^B_{T,jet}$ we use the following bin boundaries (in GeV):

  $$8, \quad 10, \quad 14, \quad 18, \quad 25, \quad 35, \quad 100 \, ,$$

  where it should be noted that there could be jets which are counted in the other distributions but not here, if they have $E^B_{T,jet} > 100$ GeV. No jet in the data satisfies this condition.

- For the cross section as a function of η^B_{jet} the following bin boundaries were used:

  $$-2, \quad -1, \quad -0.25, \quad 0.25, \quad 1, \quad 1.8 \, .$$

- For the cross section as a function of ϕ^B_{jet} twelve bins of equal size were used, with the following bin boundaries in degrees:

  $$0, \quad 30, \quad 60, \quad 90, \quad 120, \quad 150, \quad 180, \quad 210, \quad 240, \quad 270, \quad 300, \quad 330, \quad 360 \, .$$

- In addition, the cross section was measured differentially in $E^B_{T,jet}$ for six different regions in Q^2. In this case the regions in Q^2 are exactly the same as for the cross section as a function of this variable. For $E^B_{T,jet}$ we have used similar bins as above, but due to lack of statistics we decided to merge the last two bins; the resulting boundaries (in GeV) are:

$$8, \quad 10, \quad 14, \quad 18, \quad 25, \quad 100\,.$$

To determine the cross sections, we have used the standard definition: after integrating over the entries of each bin to compute the cross section for that bin ($\Delta\sigma$, which will ussually be the ratio of the number of entries in that bin to the luminosity), we divide over the bin width (ΔX) to obtain the differential cross section.

It has to be noted that in the cross section as a function of $E^B_{T,jet}$ in different regions of Q^2 we only divide over the bin width in $E^B_{T,jet}$ and we do not differentiate on Q^2. That is, we are not really measuring a double differential cross section but it will be referred to with this name since in fact the only difference with the double differential cross section is to divide over the bin width in Q^2.

4.2.2 Preliminary studies using Monte Carlo samples

In order to understand the detector effects in the measurements and to correct for them, we use the detector simulation; the effects are quantified by means of simulated events where the information is known before and after the detector effects.

The simulated events are obtained with Monte Carlo programs as described in chapter 3, and the final-state particles are passed through the detector simulation and exactly the same analysis chain as the real data.

Two samples of neutral current DIS events were used to estimate the detector effects. Both were generated using the LEPTO program interfaced to HERACLES via DJANGOH. The HERACLES program includes photon and Z° exchanges and first-order electroweak radiative corrections. The modelling of the QCD cascade is different in each sample. In one of them the ARIADNE program was used, and for this reason in the following this sample will be referred as "ARIADNE sample". The second one, used to estimate the uncertainty in the simulation due to the model used to generate the hadronic final state, was generated using the model of LEPTO based on first-order QCD matrix elements plus parton showers (MEPS). This sample will be referred as "LEPTO-MEPS". In both cases the hadronisation process was performed with the LUND string model as implemented in JETSET. These programs and models were briefly described in section 3.4. Both samples were generated with enough events to reduce the statistical uncertainty in the correction factor much below that of the data.

In a first step, these Monte Carlo samples were used to study the reconstruction of the kinematic variables. Different methods were studied and it has been verified [104] that the Double Angle method is the one which provides the best reconstruction. For this reason this method was the one used in the analysis.

In addition, the samples were used to study the purity and efficiency of the various distributions under investigation. The purity is the percentage of reconstructed jets in the detector which are "real jets", i.e. that are directly related to a jet at the hadron level. The efficiency is the percentage of jets at hadron level which are also reconstructed in the detector. The values of

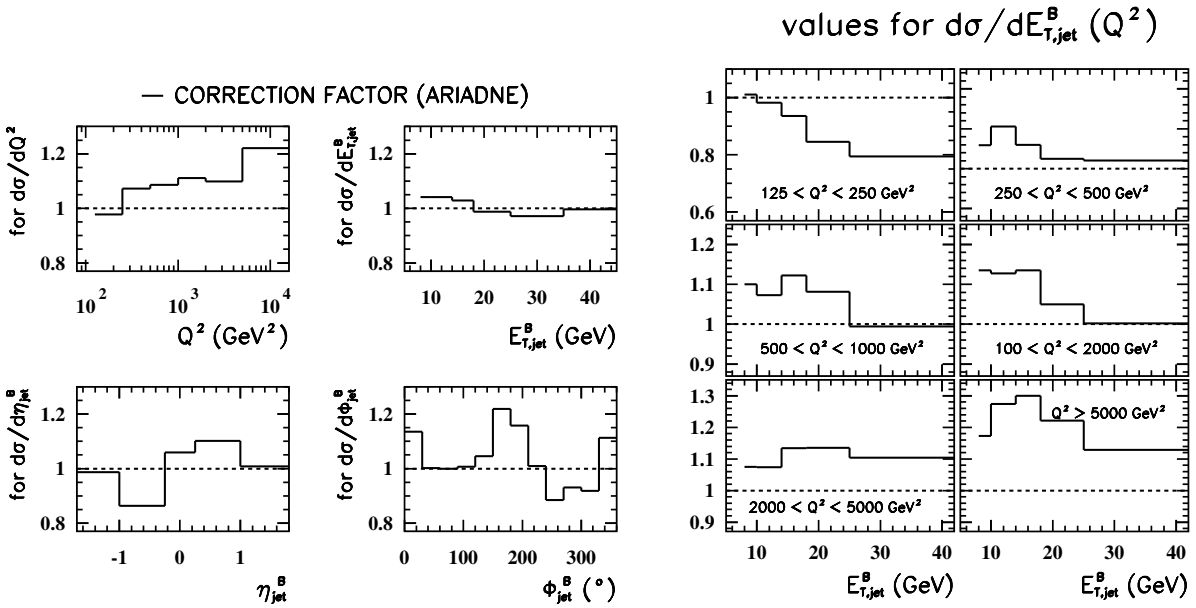

Figure 4.6: Values of the correction factor to be applied to the data to correct for detector effects obtained with the ARIADNE sample.

these two quantities are understood,and well above 50% (40% for the double differential cross section) for all the measured points except for the first bin in $E^B_{T,jet}$.

After verifying that the selection cuts and the response of the detector are reasonable and well under control, the correction factor was obtained. This correction factor is obtained with the Monte Carlo simulations. It is applied to the data in order to correct for the detector effects and acceptance: the inefficiencies introduced are also corrected.

The multiplicative correction factor is obtained as the ratio of the predictions at hadron level and detector level. This *bin-by-bin correction* is only valid if the simulated distributions are in good agreement with the data; this is the case here as it is discussed in section 4.2.3.

The correction factors obtained for the different cross sections are shown in figures 4.6 for the ARIADNE sample and 4.7 for the LEPTO-MEPS. The values are reasonable and the differences observed between the ARIADNE and LEPTO-MEPS predictions are partly due to the different jet energy correction. In fact, this difference is not translated into the systematic error.

It was checked that the correction factor is more similar if the jet energy corrections predicted with ARIADNE are applied to the LEPTO-MEPS sample except for the high-$E^B_{T,jet}$ region, where the two models predict a different behaviour; it is in that region where the systematic uncertainty coming from the model used in the simulation to correct the data is larger.

It should be noted that the correction is always smaller than 20%. Regarding the shape, the azimuthal distribution is the only which needs some explanation. In this case, the shape of the correction factor is similar to the distribution we expect at hadron level. The shape itself is understood in terms of the efficiency and the cleaning cuts used to "tag" and remove the photons reconstructed as jets. A specific check was performed in order to demonstrate that the shape of this correction factor is only related to the cuts and not to the shape at the hadron level of the Monte Carlo used to correct the data (see [104] for details).

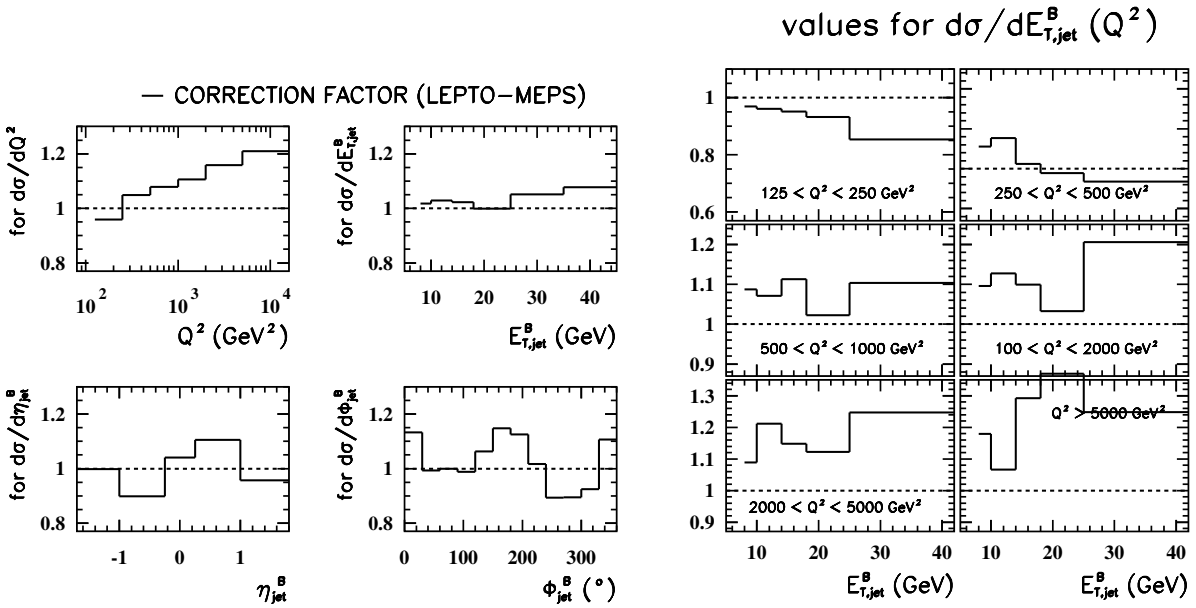

Figure 4.7: Values of the correction factor to be applied to the data to correct for detector effects obtained with the LEPTO-MEPS sample.

4.2.3 Comparison between the data and Monte Carlo predictions

The first step in the real analysis was the comparison of the results at detector level between data and Monte Carlo predictions. This comparison was performed for several global variables of the events and a reasonable description of the data is found. Furthermore, the comparison was extended to the positron candidate and kinematic variables, which are also well described by the ARIADNE and LEPTO-MEPS samples.

After these preliminary checks, the comparison focused on the jet variables. The comparison of the variables of the jets in the Breit and laboratory frames with the predictions by ARIADNE is shown in figure 4.8. The comparison with LEPTO-MEPS is shown in figure 4.9. The variables are well described by both Monte Carlo models; ARIADNE gives a slightly better description of the distribution of the transverse energy in the Breit frame.

The next step is the comparison of the visible (i.e. uncorrected) cross sections in the data with the Monte Carlo predictions of ARIADNE and LEPTO-MEPS (see figures 4.10 and 4.11). The selection of ARIADNE as the main Monte Carlo prediction is based on the slightly better description of the data by ARIADNE.

Regarding the distributions, it should be noted that the cross section falls very rapidly with Q^2 and $E^B_{T,jet}$. In the azimuthal distribution the visible cross section is not similar to the expected $A+B\cos 2\phi^B_{jet}$, but this is understood in terms of the cleaning cuts needed to suppress the presence of jets reconstructed as photons. It should be mentioned that additional checks have been performed in order to demonstrate that the visible cross section is sensitive to the underlying azimuthal distribution. In fact, it was shown that a Monte Carlo sample with a flat distribution at hadron level is not able to describe the distribution observed in the data [104].

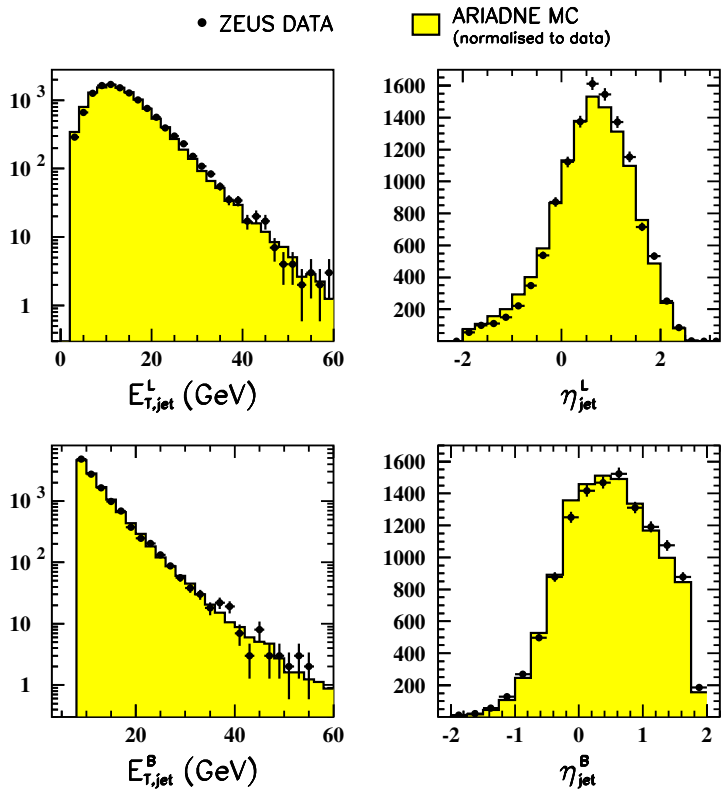

Figure 4.8: Control plots showing the comparison between the data (black dots) and the ARIADNE sample (histograms) for the jet variables in the laboratory and Breit frames. A good description of the data by the simulation is observed for all the quantities shown.

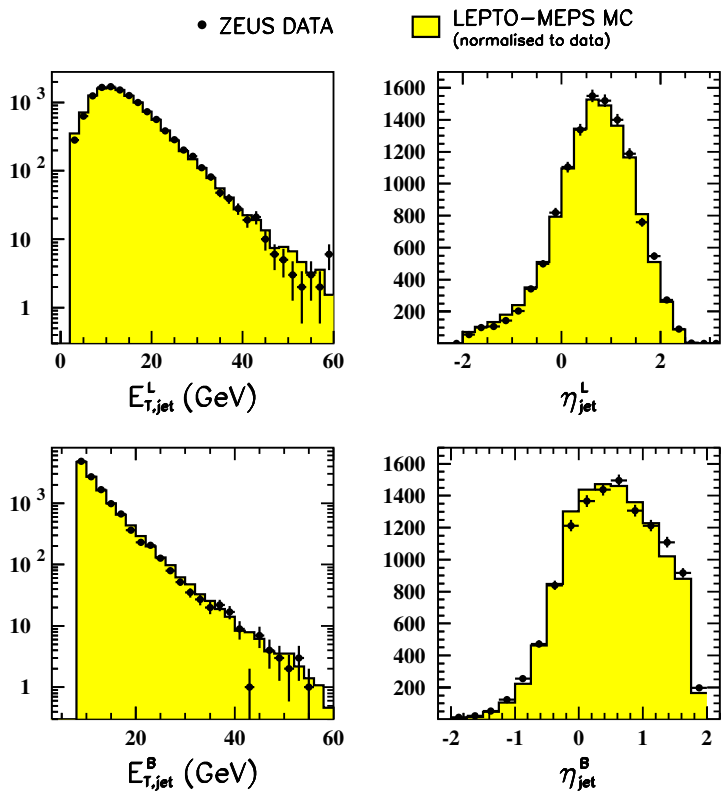

Figure 4.9: Control plots showing the comparison between the data (black dots) and the LEPTO-MEPS sample (histograms) for the jet variables in the laboratory and Breit frames. A good description of the data by the simulation is observed for all the quantities shown.

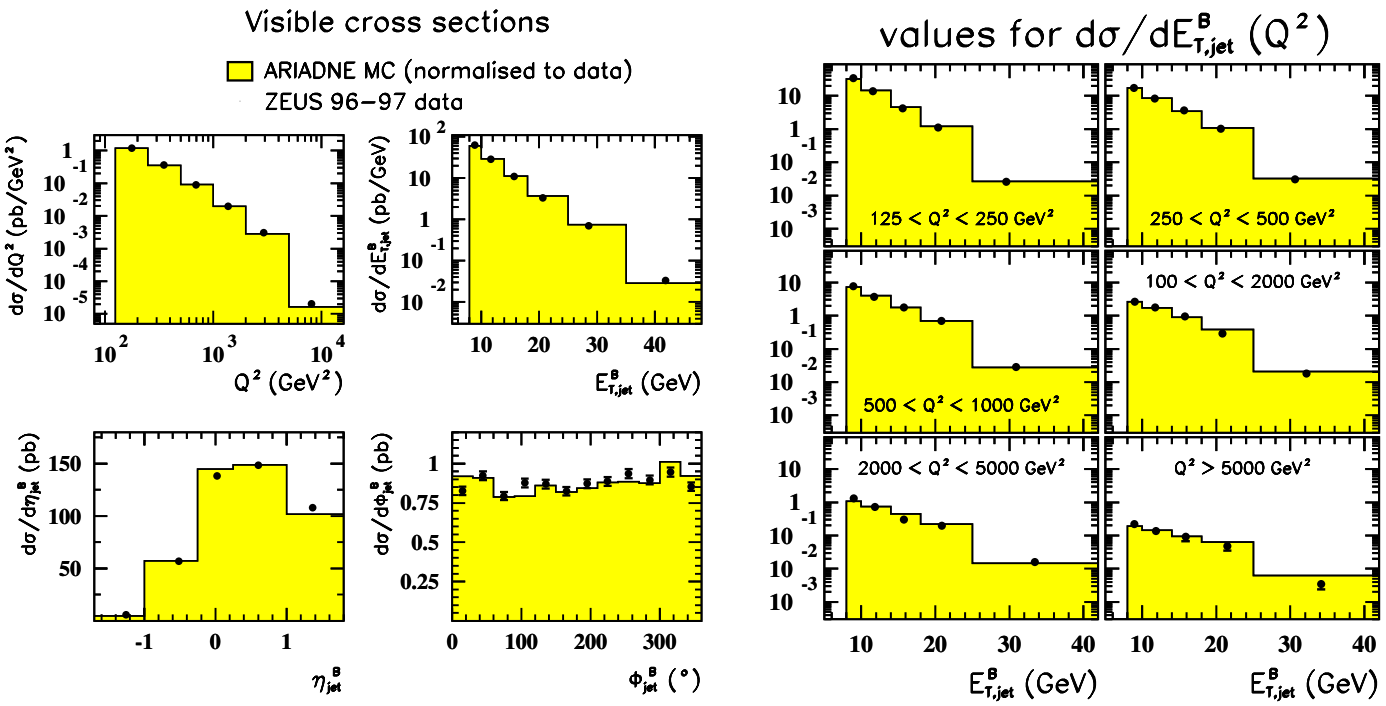

Figure 4.10: Uncorrected (visible) inclusive jet cross sections. The data (dots) are compared with the predictions given by the ARIADNE Monte Carlo sample (histograms) for all the distributions under study. The Monte Carlo predictions are normalised in each plot to the data. A good description of the shape of the distributions in the data is observed.

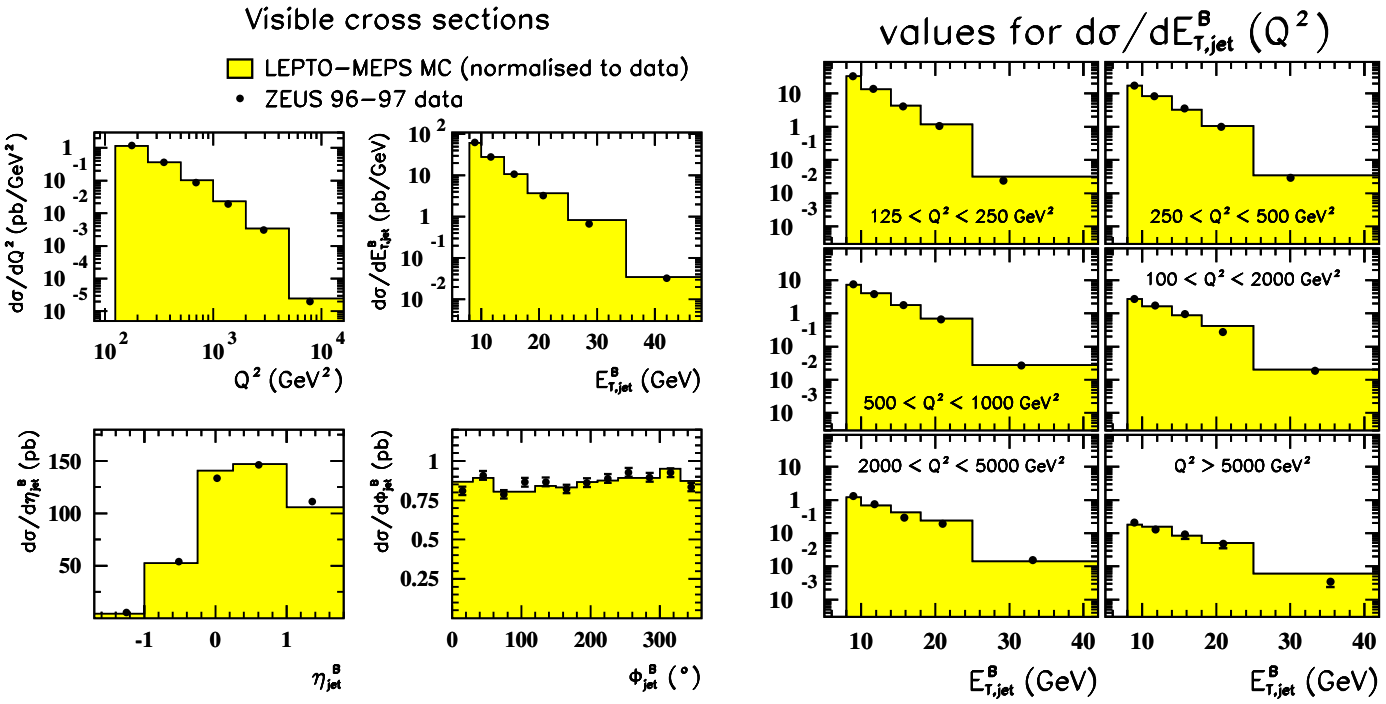

Figure 4.11: Uncorrected (visible) inclusive jet cross sections. The data (dots) are compared with the predictions given by the LEPTO-MEPS Monte Carlo sample (histograms) for all the distributions under study. The Monte Carlo predictions are normalised in each plot to the data. A good description of the shape of the distributions in the data is observed.

4.2.4 Correction for detector and QED effects

Since the Monte Carlo samples give a good description of the data at the detector level, we are confident that it is sensible to correct the data for the detector effects by means of the predictions given by the Monte Carlo and the detector simulation.

In addition, since we are interesting in the comparison with perturbative QCD predictions, it is necessary to correct the data for QED radiative effects, like the radiation of photons by the initial or scattered positron.

The correction for the detector effects is done by using the correction factor described in section 4.2.2, which is directly applied to the measured points.

The correction for the QED effects is obtained in a similar way by using HERACLES. In fact, four additional samples with a very large number of events were generated. Two of these samples are similar to those two used to correct for detector effects, one for ARIADNE and one for LEPTO-MEPS. The other two are the corresponding ones without QED effects, that is, are exactly the same as the previous ones except that neither QED radiation nor the running of α_{em} was included. The predictions given by the different samples are used to compute the QED corrections, defined as the ratio between the prediction without including QED effects and that with those effects included.

It should be mentioned that this correction should be independent of the model used to simulate the parton shower. In fact that is the case, as shown in figure 4.12. However, a small dependence is found because the models predict slightly different shapes of the distributions, in particular for the inclusive jet cross section as a function of Q^2 and $E^B_{T,jet}$.

Regarding the correction for the running of the electromagnetic coupling (α_{em}), it should be noted that the cross sections have been corrected for this running because it is not included in the programs used to compute the perturbative QCD predictions at second order in α_s. To perform a comparison of the data with those predictions the effects of the α_{em} running have to be removed from the measured values.

4.2.5 Systematic uncertainties

The experimental procedure described before is affected by systematic uncertainties. Most of them come from the incomplete knowledge of detector effects and some from the definition and methods used to analyse the data.

In order to take these effects into account, the analysis has been repeated with some modifications. The observed difference for each modification is then considered as the systematic uncertainty coming from the corresponding aspect of the analysis. For example, in the previous sections we have already mentioned the difference in the correction factors between ARIADNE and LEPTO-MEPS.

A complete study of the systematic uncertainties has been done. The following sources of uncertainty have been considered:

- The uncertainty in the absolute energy scale of the jets was estimated to be $\pm 1\%$ for $E^L_{T,jet} > 10$ GeV and $\pm 3\%$ for lower $E^L_{T,jet}$ values. The resulting uncertainty in the cross is less than 5% for $\mathrm{d}\sigma/\mathrm{d}Q^2$;

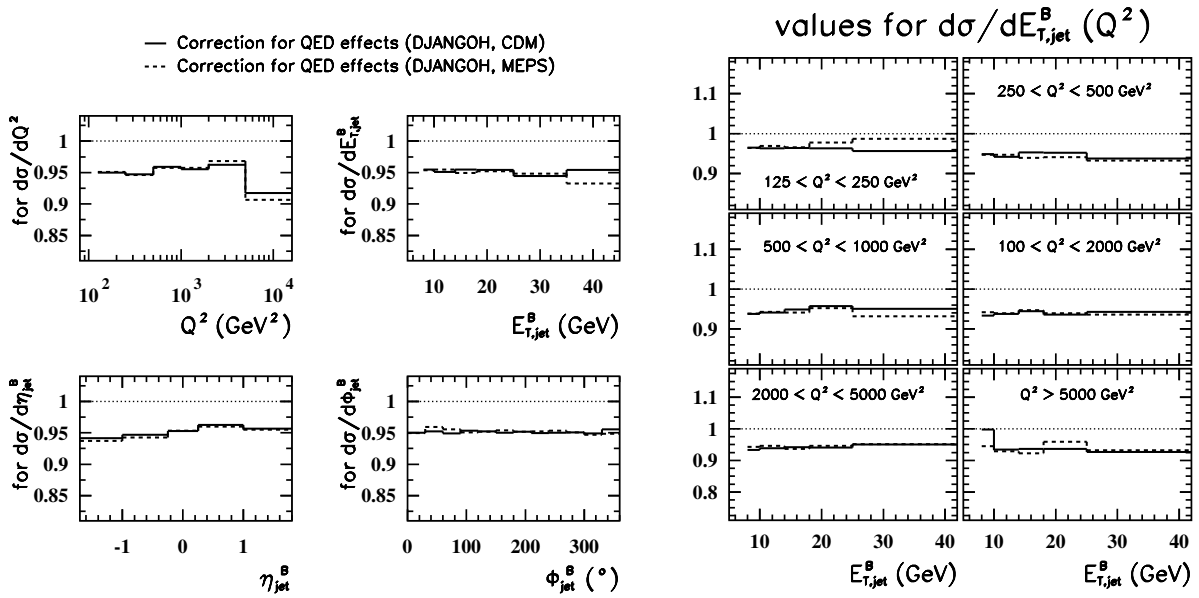

Figure 4.12: Correction factor to apply to the data to correct for QED effects. The lines shows the correction predicted by DJANGOH with ARIADNE (solid line) or LEPTO-MEPS (dashed line). Both are in good agreement.

- The differences in the results by using the ARIADNE or LEPTO-MEPS sample to correct the distributions for detector and QED effects are included as systematic uncertainties. They are typically smaller than 3% except for the high-$E^B_{T,jet}$ region;
- The uncertainty in the CAL absolute energy scale affects the reconstructed value of $E-p_z$. This is taken into account by changing the reconstructed value by $\pm 3\%$. The uncertainty in the cross sections under study is typically less than 3%;
- The analysis was repeated by using an alternative way [108] to select the positron candidate (see [104] for details). The differences in the results are included as systematic uncertainties and amount to less than 2%;
- The uncertainty due to that of the absolute energy scale of the positron candidate was estimated by changing the energy of the candidate by $\pm 1\%$. The uncertainty amounts to less than 1% for all the distributions;
- The $E^L_{T,jet}$ cut was raised to 4 GeV. The differences in the cross sections are $\sim 1\%$;
- The cut in η^L_{jet} used to suppress the contamination due to photons reconstructed as jets in the Breit frame was set to -3 and to -1.5. The uncertainties in the measured cross sections are typically $\sim 1\%$.

For a more detailed description of the systematic uncertainties and other systematic checks performed in the analysis, see the corresponding ZEUS internal note [104].

To obtain the total systematic uncertainty, all the systematic uncertainties are added in quadrature. This procedure assumed that these uncertainties are independent. Since the main contributions satisfy this condition, it is a good approximation.

To obtain the total experimental uncertainty the systematic and the statistical contributions are added in quadrature. This total experimental uncertainty is shown for every point in all

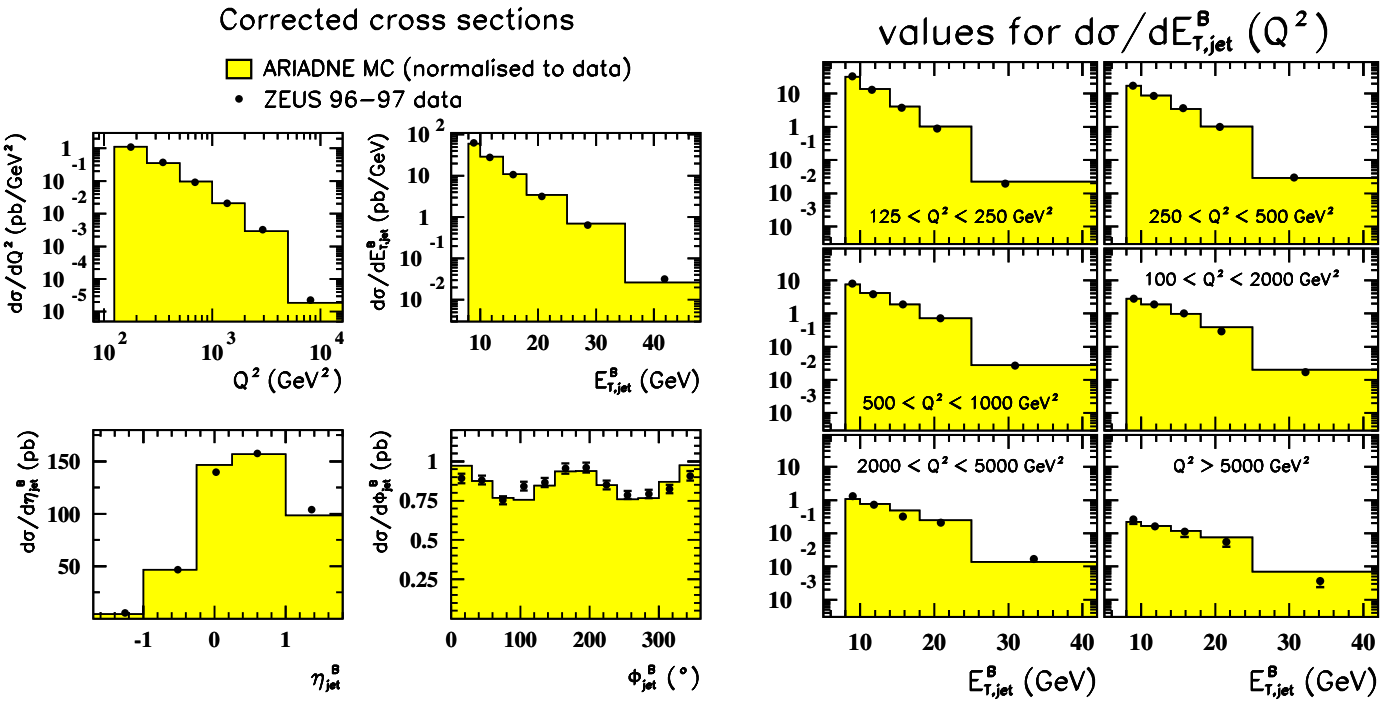

Figure 4.13: Inclusive jet cross sections corrected for detector and QED effects by using the ARIADNE simulations. The data points (dots) are compared with ARIADNE Monte Carlo predictions (histograms) normalised to the data in each plot. A good description of the shape of all the distributions in the data is observed.

the figures showing the distributions with the results of the analysis (see section 5.2). The statistical uncertainty is shown as inner error bars while the complete experimental uncertainty is shown as outer error bars.

On the other hand, the systematic uncertainty coming from that of the jet energy scale is shown separately because it is very correlated between different points and introducing an uncertainty in the normalisation and not in the shape of the distribution. For this reason, in the figures this systematic uncertainty is shown as a shaded band along the points in each distribution.

4.2.6 Measurement of the inclusive jet cross sections

After the data are corrected for detector and QED effects with the ARIADNE simulations, the differential cross sections are obtained. These are shown in figures 4.13 and 4.14, in which the measurements are compared to the predictions from ARIADNE and LEPTO-MEPS. In general, both Monte Carlo models give a reasonable description of the shapes of all the distributions.

It should be noted that in both figures the data points are those corrected with ARIADNE since they are the central values. The values obtained when correcting with LEPTO-MEPS are included as a systematic uncertainty contribution.

The cross section decreases very rapidly with Q^2 and $E^B_{T,jet}$. The decrease in Q^2 is observed over five orders of magnitude, and the phenomenological models describe very well this fall. In the double differential cross section it is observed that the dependence with $E^B_{T,jet}$ is less pronounced as Q^2 increases.

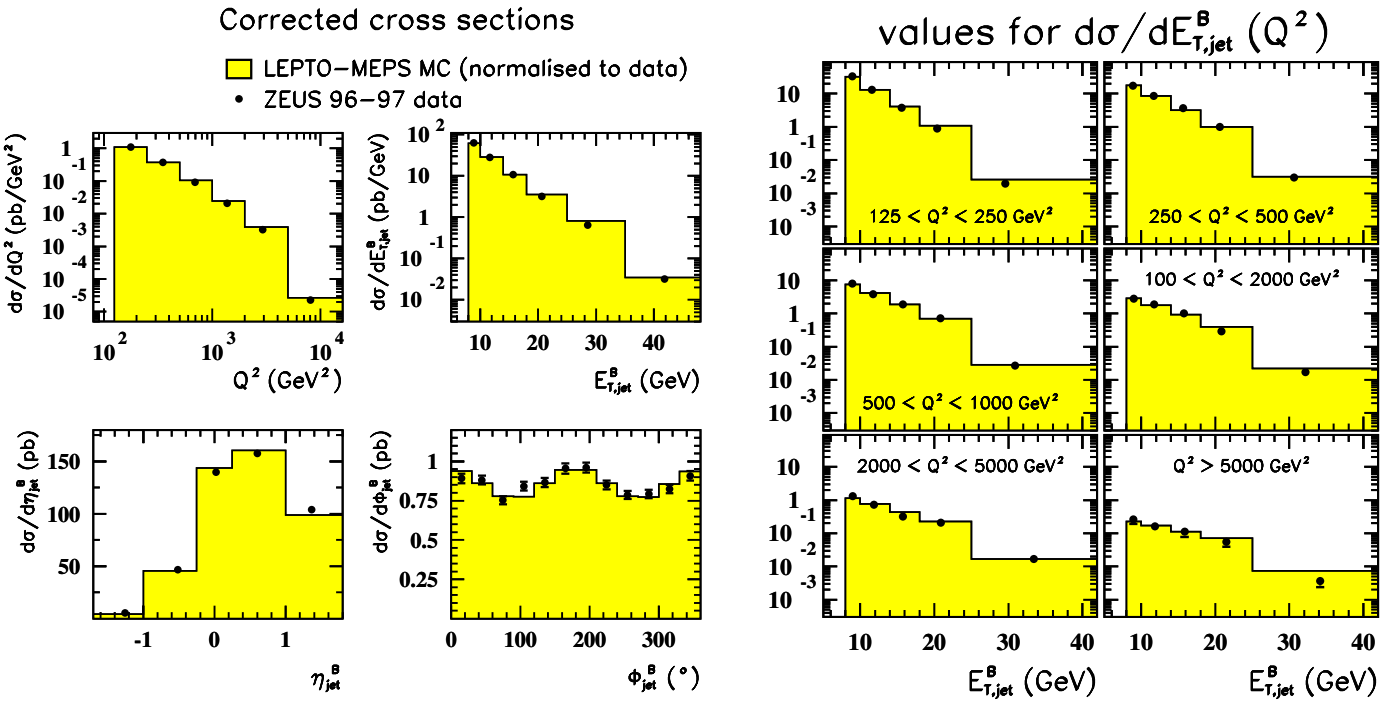

Figure 4.14: Inclusive jet cross sections corrected for detector and QED effects by using the ARIADNE simulations. The data points (dots) are compared with LEPTO-MEPS Monte Carlo predictions (histograms) normalised to the data in each plot. A good description of the shape of all the distributions in the data is observed.

The pseudorapidity distribution displays a significant decrease in the backward region.

It should be emphasised the asymmetric shape of the azimuthal distribution, which is well reproduced by the Monte Carlo models and in aggrement with the $A + B \cos\phi^B_{jet}$ expectation in the Standard Model.

The measurements presented here will be discussed in more detail in section 5.2, where a comparison with NLO QCD predictions allows the extraction of more accurate conclusions regarding the description of the measurements.

4.3 Analysis II: Measurement of the subjet multiplicity in the laboratory frame

In this section the complete description of the experimental results obtained for the analysis of the subjet multiplicity for jets defined in the laboratory frame is given.

The structure of this section is very similar to that of the analysis of inclusive jet production in the Breit frame and for this reason some of the details are not included.

4.3.1 Description of the measurements

After the final selection of jets, we start by studying the subjet multiplicity as resulting from the algorithm described in section 1.4.5. For each jet the number of subjets at each value of y_{cut} is counted and the average value for the sample of jets is computed. In the analysis the following values for the resolution scale were considered

$$y_{cut} = 0.0005,\ 0.001,\ 0.003,\ 0.005,\ 0.01,\ 0.03,\ 0.05,\ 0.1,\ 0.3,\ 0.5\ ,$$

where it should be remarked that the last two are too close to 1 to allow the resolution of any subjet structure.

In this analysis, the jet variables always refer to the laboratory frame and, thus, the label "laboratory" is omitted.

The study of the dependence of the mean subjet multiplicity is done with respect to y_{cut} and to the jet transverse energy and pseudorapidity for a fixed value of y_{cut}. Since for the lower y_{cut} values the perturbative approach might not ne valid and for high values the sensitivity is small, the study is performed for a central value, namely $y_{cut} = 10^{-2}$.

The regions for the kinematic variables of the jets are given by the following boundaries:

$$E_{T,jet} = 15,\ 17,\ 21,\ 25,\ 29,\ 35,\ 41,\ 55,\ 71\ \text{GeV}\ ;$$

$$\eta_{jet} = -1,\ 0,\ 1,\ 1.5,\ 2.$$

In the plots the measured points are plotted at the corresponding average value of the variable in the given bin.

4.3.2 Preliminary studies using Monte Carlo samples

For this analysis, the same Monte Carlo samples used in the previous one (described in section 4.2) were used to perform the study of the detector effects on the variables to be measured.

As for the analysis in the Breit frame, the Double Angle method was used since it provides the best results for the reconstruction of the kinematic variables [105].

In addition, studies of the efficiency and purity were perfomed [105]; it was found that they are well above 40% for all the measured points. It is slightly smaller for the first bin in $E_{T,jet}$ due to the selected Q^2 region since Q^2 is strongly correlated with the value of $E_{T,jet}$ in the laboratory frame.

After verifying that the selection cuts and the response of the detector are under control, the correction factor for the mean subjet multiplicity was obtained. The correction is done in the same way as described for the analysis of jets in the Breit frame (see section 4.2.2).

The correction factors obtained for the mean subjet multiplicities measured in the analysis are shown in figures 4.15 for the ARIADNE sample and 4.16 for that of LEPTO-MEPS. The values are reasonable, especially when the resolution scale is large enough. It should be noted that ARIADNE and LEPTO-MEPS predict similar corrections.

It should be noted that the correction gets smaller as y_{cut} or the jet transverse energy increases for $E_{T,jet}$ high enough. Furthermore, a small dependence on the pseudorapidity is observed in both Monte Carlo predictions.

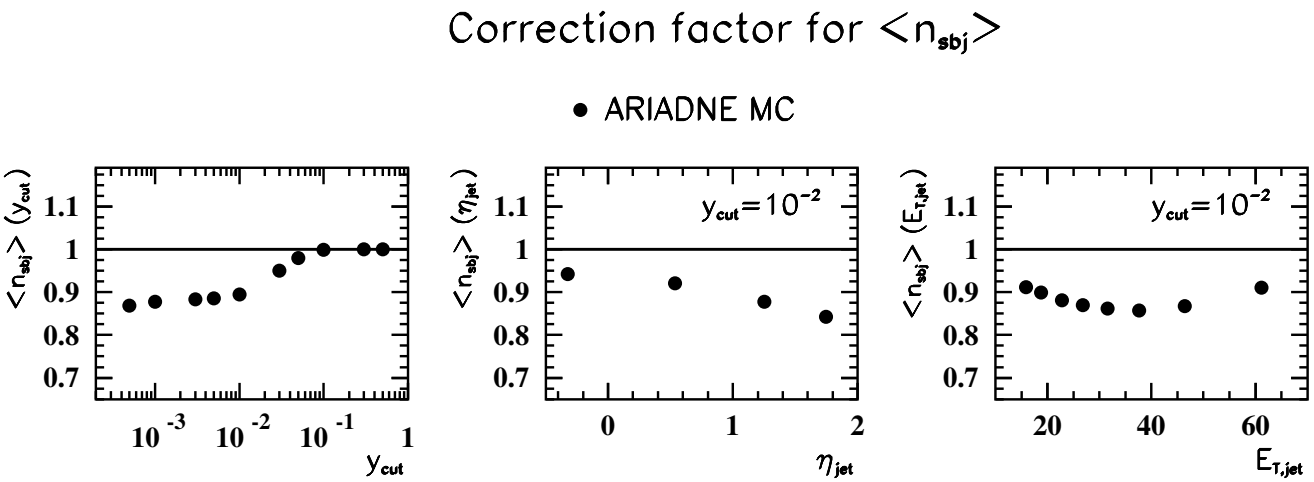

Figure 4.15: Values of the correction factor to be applied to the mean subjet multiplicity measured in the data to correct for detector effects obtained with the ARIADNE sample.

4.3.3 Comparison between data and Monte Carlo predictions

After these preliminary checks, the comparison of the distributions for several variables related to the event and jet reconstruction is performed. The predictions by the ARIADNE and LEPTO-MEPS samples were in good agreement with the data. As an example, figure 4.17 shows the comparison of the jet and positron variables as reconstructed in the data and in the ARIADNE sample. The comparison of the data with LEPTO-MEPS is shown in figure 4.18. The variables are very well described.

The next step is the comparison of the uncorrected distributions of the mean subjet multiplicity in the data with the Monte Carlo predictions. The distributions in the data are compared with ARIADNE and LEPTO-MEPS predictions in figure 4.19. Although the Monte Carlo models predict larger multiplicities, the shape of the distributions are reasonably described. In ARIADNE the discrepancy is mainly in the lower $E_{T,jet}$ region.

The distribution of the number of subjets within a jet must also be studied in detail. The comparison of this distribution between data and Monte Carlo predictions provides a more precise test of those predictions since the comparison is done for the whole distribution and not only for the mean value. The comparison of the data with ARIADNE is shown in figures 4.20 and 4.21 and with LEPTO-MEPS in figures 4.22 and 4.23. In the figures 4.20 and 4.22 the comparison is performed for the whole sample of jets and for different values of the resolution scale. Both Monte Carlo predictions give a reasonable description of the shape of the distributions with a small shift towards higher multiplicities which explains the differences observed in the mean values. In the figures 4.21 and 4.23 the comparison is performed for a fixed resolution scale ($y_{cut} = 10^{-2}$) and different regions of the jet transverse energy. In these distributions a reasonable agreement is also obtained.

4.3.4 Correction for detector and QED effects

Although the Monte Carlo predictions for the mean subjet multiplicity do not reproduce exactly the data, the fair agreement between data and simulations in the distributions for the number

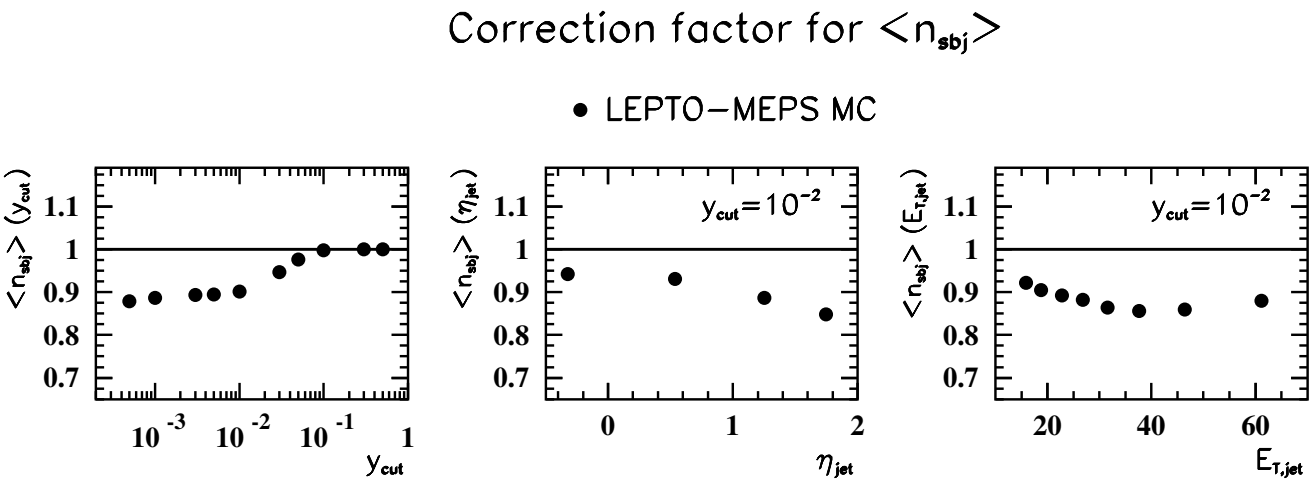

Figure 4.16: Values of the correction factor to be applied to the mean subjet multiplicity measured in the data to correct for detector effects obtained with the LEPTO-MEPS sample.

of subjets makes the correction of the detector effects by using these Monte Carlo samples reliable.

It should be noted that the small shift in the Monte Carlo predictions is not due to a wrong simulation of the detector effects: they predict larger multiplicities at parton and hadron levels when compared with NLO QCD predictions and for this reason a discrepancy with the data was observed at detector level. This shift could be due to various reasons, e.g. some parameter setting in the modelling of the parton showers. Since it is present in all levels of the Monte Carlo samples, it is expected that the detector effects we are correcting for are reasonably well reproduced by the Monte Carlo [105] [4].

The correction for detector effects is done by using the correction factor described in section 4.3.2, which is directly applied to the measured points.

It should be noted that the relatively large diffference in multiplicity between LEPTO-MEPS and ARIADNE is not translated into a visible difference in the correction factor. The difference observed (2% or smaller) is mainly due to the true differences between the models and not to the shift in the mean subjet multiplicity.

The correction for QED effects is obtained by using HERACLES in a similar way as described in section 4.2.4 for the jet cross sections in the Breit frame. In this case, since the observable under study is not a cross section but a ratio, the correction due to QED effects is very small and usually well below 0.5%. As it was the case in the analysis of jets in the Breit frame, the predictions by ARIADNE and LEPTO-MEPS are in good agreement [105].

Regarding the correction for the running of the electromagnetic coupling (α_{em}), the effect is negligible. Anyway, we correct for this effect at the same time we correct for QED radiative events, as described in section 4.2.4.

[4] It should be noted that the detector effects are mainly related to changes in the distribution of the number of subjets. These distributions in the data are well reproduced by the Monte Carlo simulations.

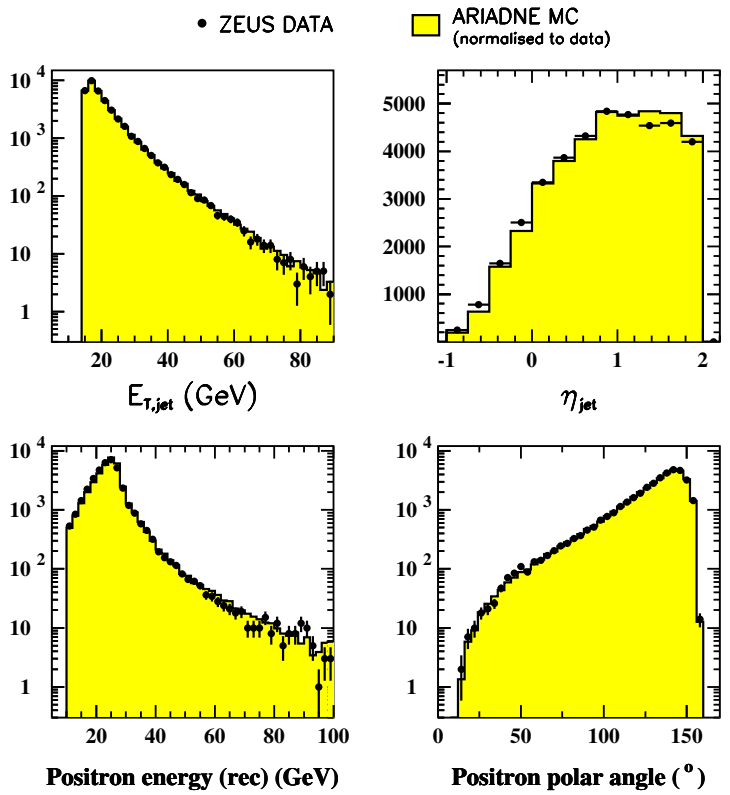

Figure 4.17: Control plots showing the comparison between the data (dots) and the ARIADNE sample (histograms) for the jet and the positron variables reconstructed with the detector. A good description of the data by the simulation is observed for all the quantities.

4.3.5 Systematic uncertainties

Although the observable under study is not very sensitive to modifications of the event selection, the estimation of the systematic uncertainty was performed in a similar way as described for the analysis of jet production in the Breit frame.

The most importat contribution to the systematic uncertainty comes from the differences in the correction predicted by LEPTO-MEPS with respect to ARIADNE. The ARIADNE simulation was considered as the default one to correct the data since it provides a better description of the measurements.

The following sources of uncertainty have also been considered:

- The uncertainty due to that on the energy scale of the calorimeter is estimated by changing the energies of the simulated events. The contribution is separated into the following ones; it should be noted that each contribution is computed independently:
  - The uncertainty due to that of the jet energy scale, estimated to be 1%, induces a relatively large effect, around 0.5%. This effect comes from the dependence of the mean subjet multiplicity on the transverse energy.
  - The $\pm 1\%$ variation of the energy of the positron candidate induces a very small effect in comparison with other contributions.
  - The $\pm 3\%$ variation in the value of $E - p_z$ gives rise to a negligible effect.
- The analysis was repeated by using an alternative method to select the positron candidate (see [105]). The effect in the mean subjet multiplicity is negligible.

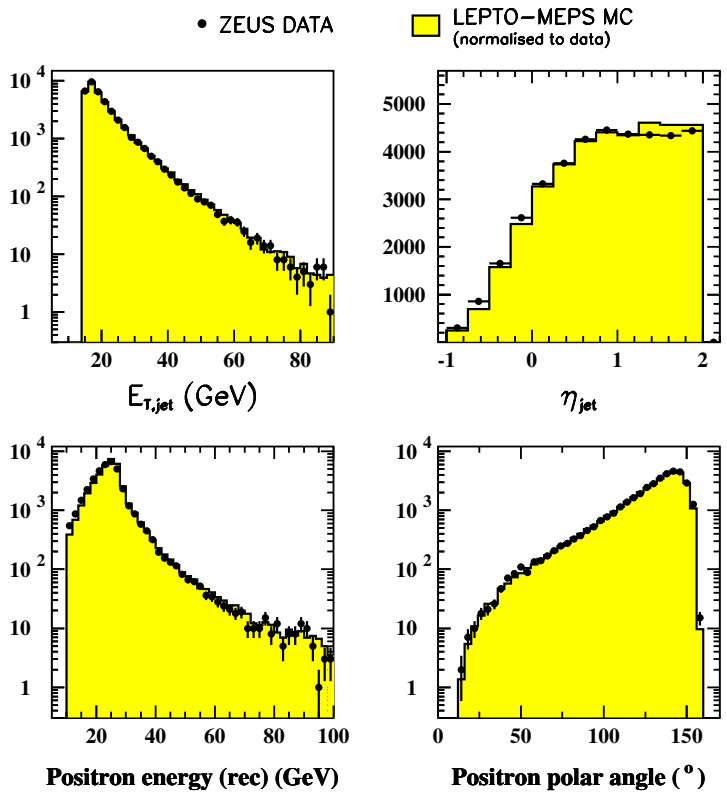

Figure 4.18: Control plots showing the comparison between the data (dots) and the LEPTO-MEPS sample (histograms) for the jet and the positron variables reconstructed with the detector. A good description of the data by the simulation is observed for all the quantities.

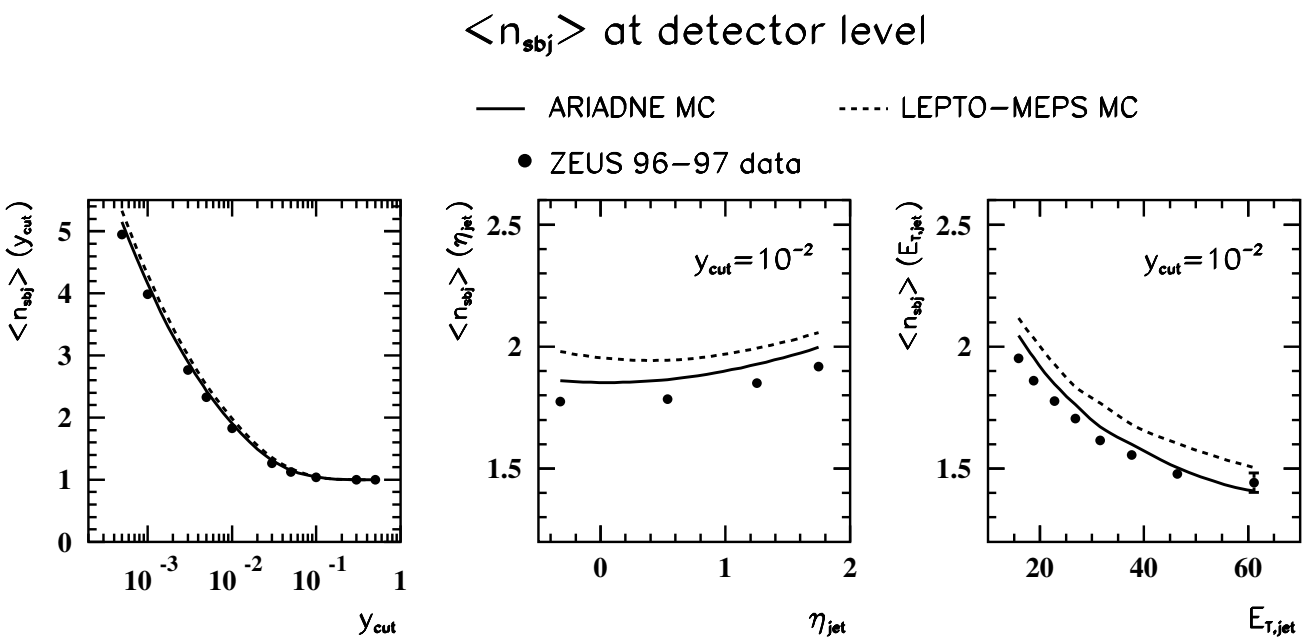

Figure 4.19: Uncorrected distributions for the mean subjet multiplicity (black dots) compared with the predictions given by the ARIADNE and LEPTO-MEPS Monte Carlo sample (lines). A reasonable description of the shape of the distributions is observed, although the simulations predict a larger multiplicity, in particular in the case of LEPTO-MEPS.

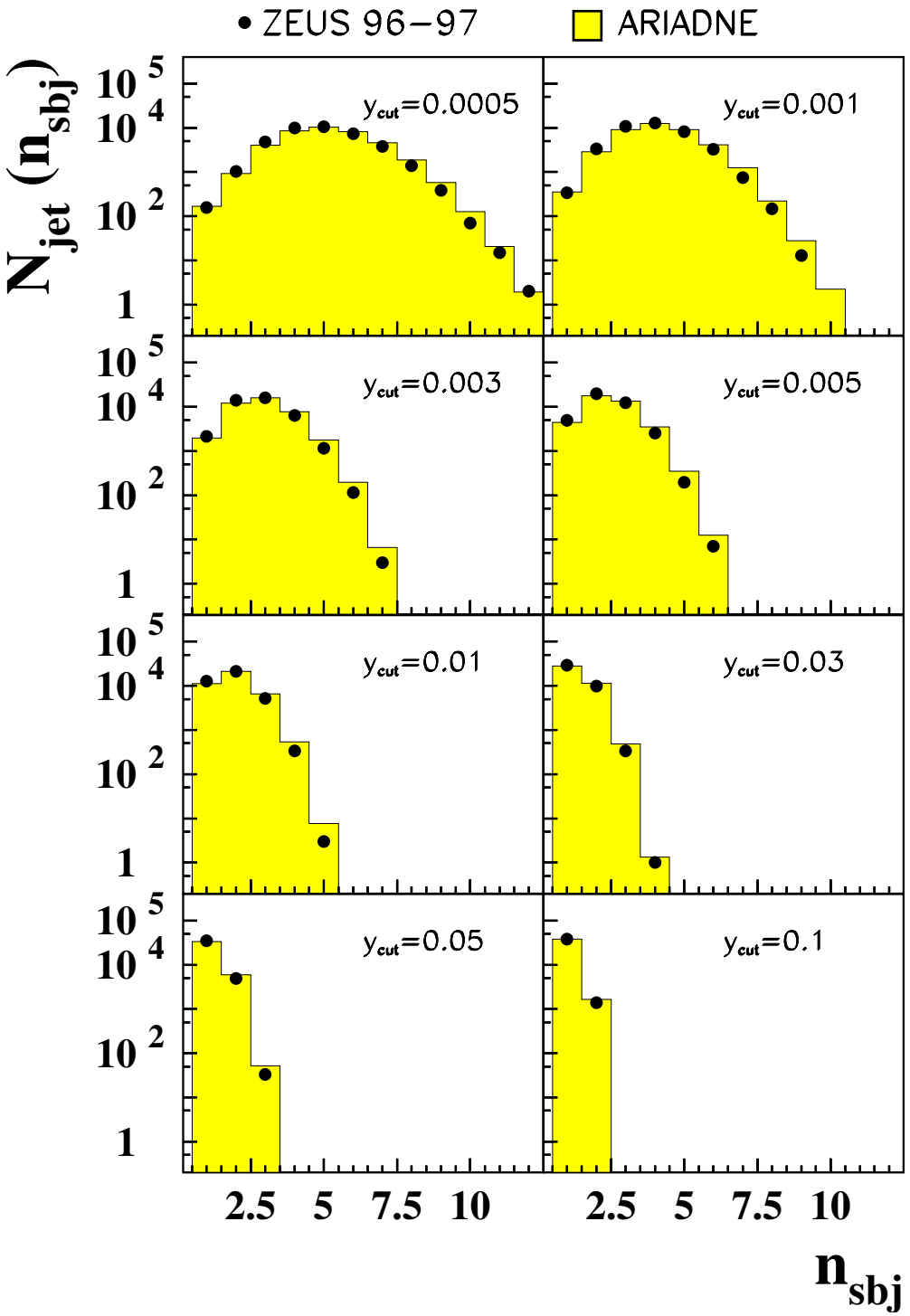

Figure 4.20: Distribution of the number of subjets in the data for different values of y_{cut} (black dots). The predictions of ARIADNE (histograms), normalised to the data, are also shown.

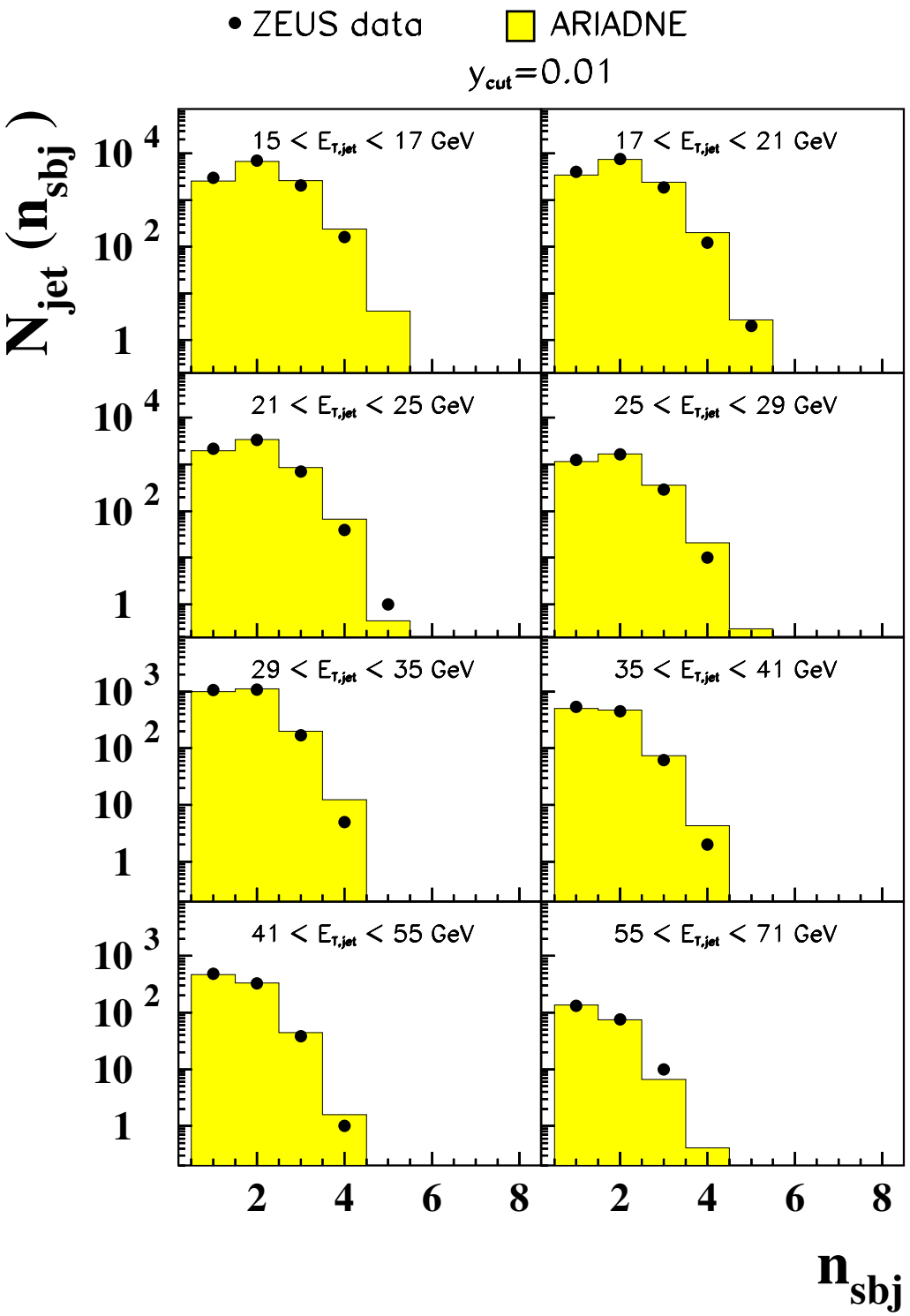

Figure 4.21: Distributions of the number of subjets in the data for $y_{cut} = 10^{-2}$ and different regions in $E_{T,jet}$ (black dots). The predictions of ARIADNE (histogram), normalised to the data, are also shown.

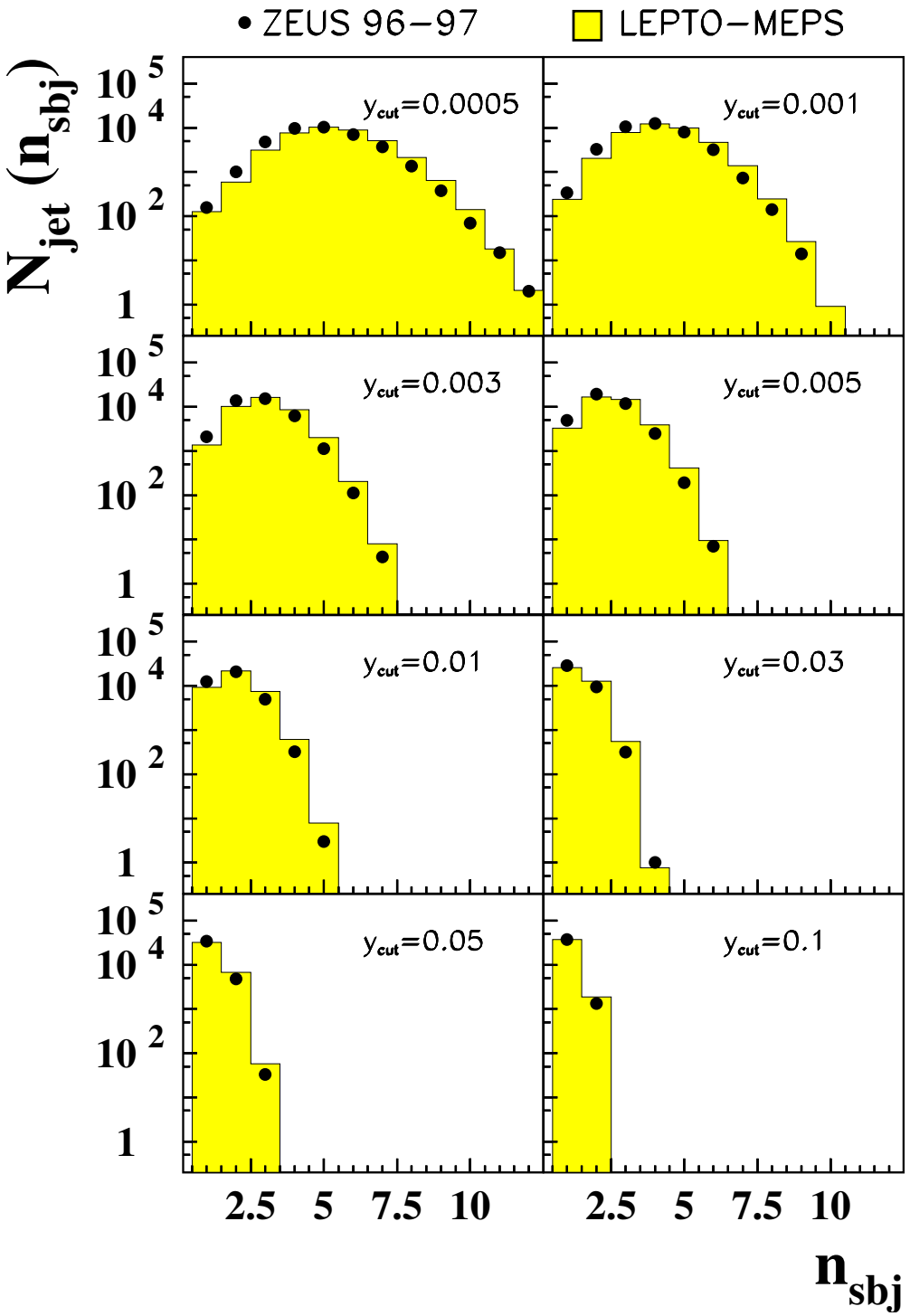

Figure 4.22: Distribution of the number of subjets in the data for different values of y_{cut} (black dots). The predictions of LEPTO-MEPS (histograms), normalised to the data, are also shown.

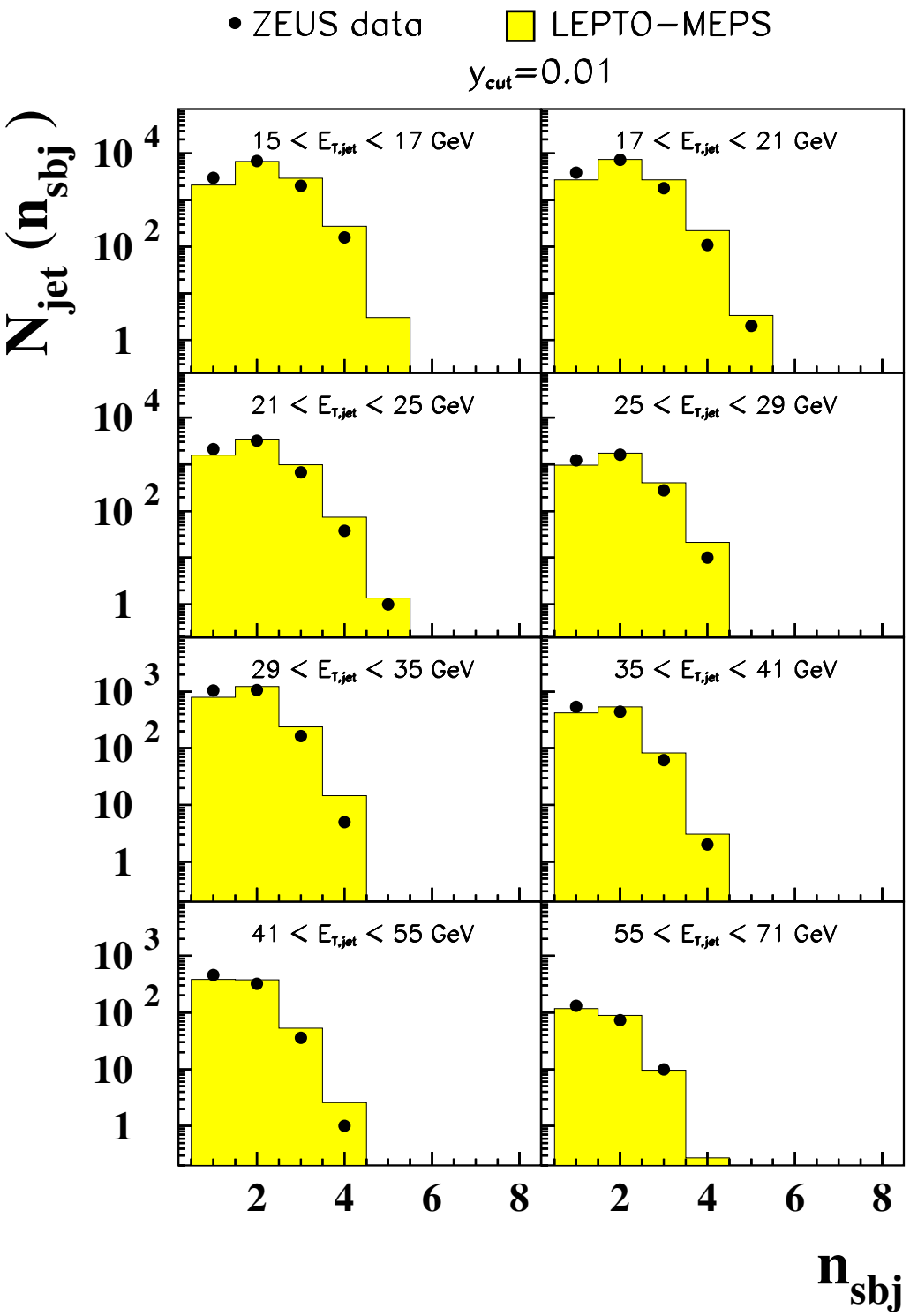

Figure 4.23: Distributions of the number of subjets in the data for $y_{cut} = 10^{-2}$ and different regions in $E_{T,jet}$ (black dots). The predictions of LEPTO-MEPS (histogram), normalised to the data, are also shown.

The total systematic uncertainty is obtained by adding in quadrature all the systematic uncertainties; those related to the uncertainty in the jet energy scale are also included.

To obtain the complete experimental uncertainty, the systematic and statistical uncertainties are added in quadrature. As for the analysis of jets in the Breit frame, this experimental uncertainty is shown for every point in all the figures showing the results of the analysis. The statistical uncertainty is shown as inner error bars while the complete experimental uncertainty is shown as the outer error bars. In this case, the uncertainty due to the jet energy scale is not shown separately and its contribution is included in the outer error bars.

4.3.6 Measurement of the mean subjet multiplicity

After correcting the mean subjet multiplicity in the data by applying the correction factor predicted by ARIADNE, the value thus obtained constitutes the measurement at hadron level.

Figure 4.24 shows the corrected mean subjet multiplicity as a function of y_{cut}. The measured values in the data are compared with the predictions given by the ARIADNE and LEPTO-MEPS samples. The comparison is similar to that at detector level described before. This shows that although the predictions display a relatively large shift with respect to the data, the shift appears both at the hadron and detector levels. In addition, the predictions obtained with a sample generated with HERWIG are shown for comparison. HERWIG is also in reasonable agreement with the data, although it predicts a smaller multiplicity. The differences are more visible for the lower values of y_{cut}.

Figures 4.25 and 4.26 show the measurements at $y_{cut} = 10^{-2}$ as a function of the jet variables.

The mean subjet multiplicity shows a very small dependence on the jet pseudorapidity and this behaviour is well reproduced by the different models. These results are consistent with the QCD prediction that the sample of jets is dominated by quark-initiated jets in the entire η_{jet} range. In the photoproduction regime ($Q^2 \sim 0$), a clear increase with the pseudorapidity of the jets is observed, in agreement with the increase of the fraction of gluon-initiated jets [109, 110].

Regarding the $E_{T,jet}$ dependence, the mean subjet multiplicity decreases as $E_{T,jet}$ increases. This result has been observed in other studies of the jet internal structure [110, 111].

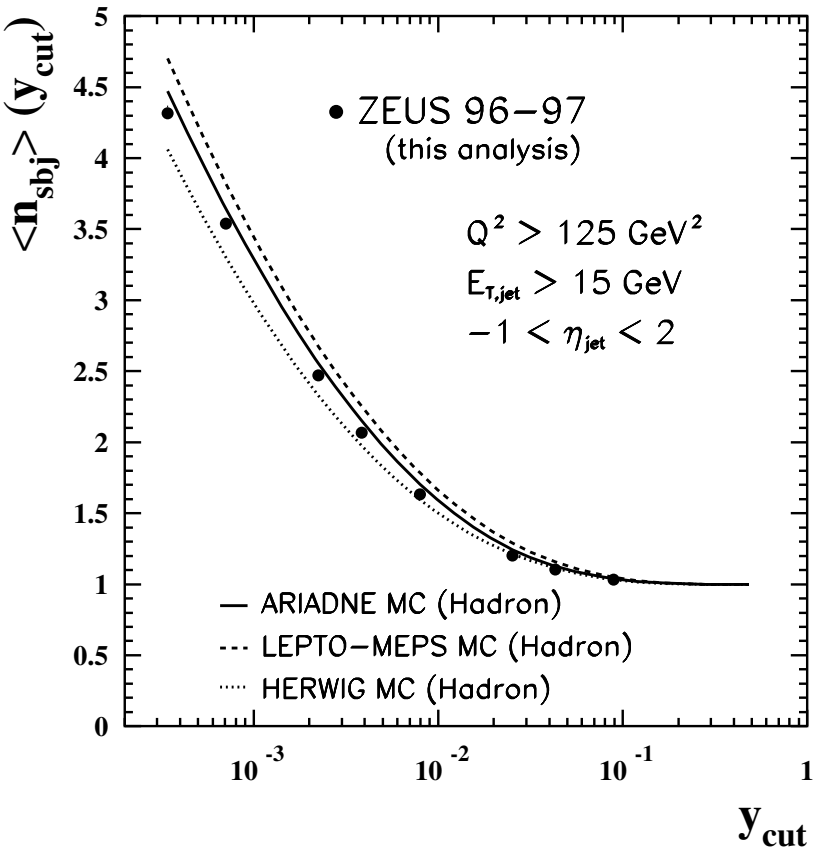

Figure 4.24: Corrected mean subjet multiplicity as a function of y_{cut} (black dots). The predictions of ARIADNE (solid line), LEPTO-MEPS (dashed line) and HERWIG (dotted line) at hadron level are also shown.

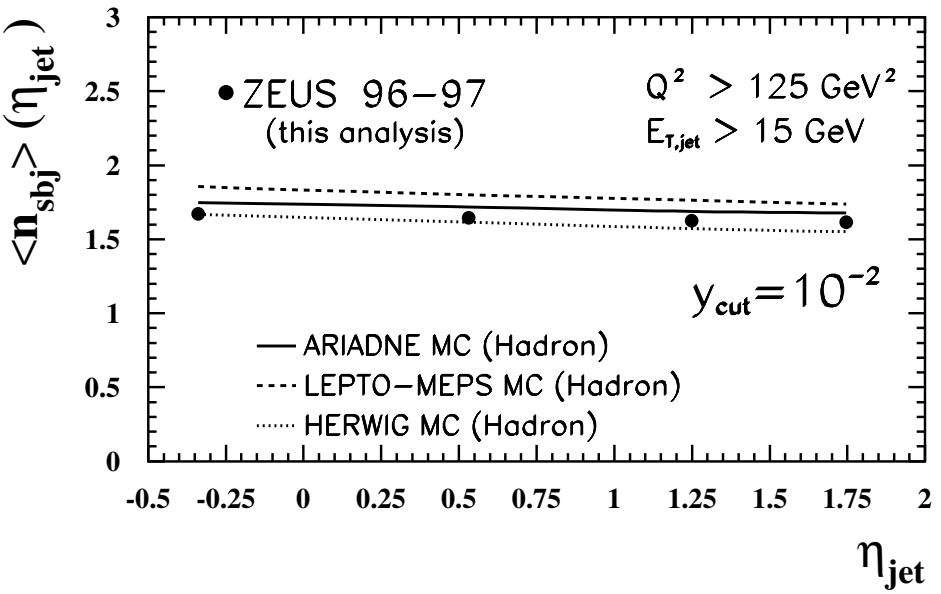

Figure 4.25: Corrected mean subjet multiplicity as a function of η_{jet} for $y_{cut} = 10^{-2}$ (black dots). The predictions of ARIADNE (solid line), LEPTO-MEPS (dashed line) and HERWIG (dotted line) at hadron level are also shown.

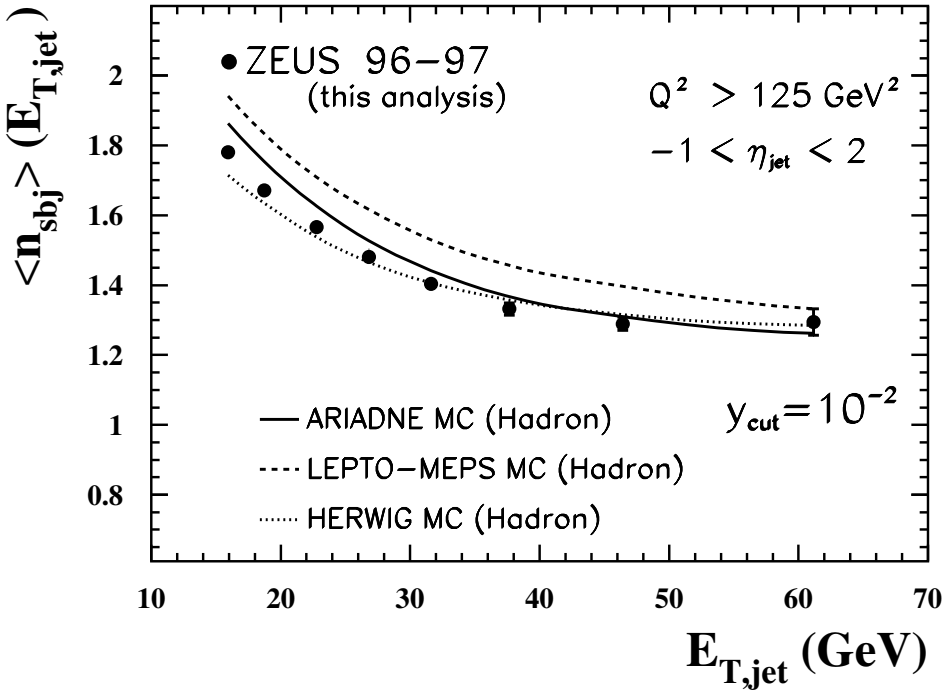

Figure 4.26: Corrected mean subjet multiplicity as a function of $E_{T,jet}$ for $y_{cut} = 10^{-2}$ (black dots). The predictions of ARIADNE (solid line), LEPTO-MEPS (dashed line) and HERWIG (dotted line) at hadron level are also shown.

Chapter 5

Discussion of the results

The results obtained in the previous chapter are discussed in the following sections to draw the final conclusions. In this chapter, the next-to-leading order pQCD predictions are obtained, corrected to hadron level and compared with the data for the two analyses described here. The comparison allows the extraction of the value of α_s.

5.1 NLO QCD predictions

At present, it is possible to make an improved comparison with the theory, since predictions in pQCD are available to the second order in α_s, usually referred as *next-to-leading order* (NLO) predictions. The Monte Carlo models considered earlier only contain the first-order contribution and include the effects of higher orders in an approximate way. On the other hand, these Monte Carlo models are very useful to estimate the corrections and the related uncertainties for the transition from partons to hadrons. These corrections, which have to be applied to the NLO QCD predictions before they are compared to the data, have to be obtained in this way since they are not directly calculable from the theory.

NLO QCD predictions are available both for the inclusive jet cross sections in the Breit frame and for the mean subjet multiplicity for jets defined in the laboratory frame. In this way, we are able to obtain these theoretical predictions and, after correcting them for hadronisation, compared to the measurements described previously.

The way these predictions are obtained and corrected for hadronisation is explained in the following sections. Finally, in sections 5.2 and 5.3, the comparison to the data is presented.

5.1.1 Description of the NLO QCD calculation

The calculation of the theoretical predictions are performed in a similar way as we analysed the hadron level of the Monte Carlo generated events. In this case, the "events" are final states given by the different contributions to the process under study. These events are needed since the calculation of the integrals are only possible by using Monte Carlo integration techniques.

In our particular case, the two kind of measurements we have performed are sensitive to the predictions given by QCD. This means that in both cases, the first contribution is proportional to α_s and the relevant diagrams have to be computed.

The second more important contribution is given by the α_s^2 diagrams and, at present, this is the highest order to which we can make theoretical predictions for both analyses. This implies that the perturbative series is stopped after the second term. For this reason, the most important contribution to the theoretical uncertanty is expected to come from the missing higher orders (see sections 5.2.2 and 5.3.2).

On the other hand, since we include the second order in the theoretical predictions, we are able to make a consistent determination of the α_s value, which is not possible when only the first order is known. To make this determination of α_s, the dependence of the theoretical predictions on the value of α_s must be calculated and then extract the value of α_s which provides the best description of the data by the theory. Although the method we have used is very intuitive, the practical realisation is far from trivial. The description of the method is given in section 5.4.1.

5.1.2 The program DISENT

As mentioned earlier, the theoretical predictions for the measurements we have performed can only be obtained by using Monte Carlo methods. For NLO QCD predictions, there are several programs which contain all the matrix elements needed.

For the results presented here, we have performed the calculations using the program DISENT [112], which has been widely used to obtain predictions for similar analyses within the collaboration and has been proved to give reliable results for the quantities under study. The predictions given by DISENT have been cross-checked with the program DISASTER [113], which is based in the same principles. The agreement between the two programs is good (within 2-3%) and well within the theoretical uncertainties. The plots in figure 5.1 show the relative differences between the two programs and the comparison with the uncertainty due to the dependence on the renormalisation scale. The results for the two analyses are shown. The differences between the two programs are clearly smaller than the uncertainty in the theory. The exceptions can be related to the main limitation of DISASTER: its slow convergence, which means that very long jobs have to be run to get a reasonable precision. This limitation is the main reason why DISASTER was only used to cross-check the DISENT values.

The program DISENT generates different configurations, which correspond to the various terms in the perturbative expansion, for the partons in the initial and final states, each of which has an associated weight. After convoluting each configuration with the parton distribution functions, the total contribution to the cross section is obtained.

The k_T-cluster algorithm is then applied to the partons in the final state in the same way it was applied to the data and simulated events. The selection cuts are applied in the same way as for the hadron level, and finally, if the configuration is accepted, the weight is counted so much times as accepted jets in the given configuration to obtain the corresponding theoretical predictions. See sections 5.1.4 and 5.1.5 for the details of the way this was implemented in each particular analysis.

The calculation of the matrix elements for each configuration is made internally in DISENT. The infrared divergences are removed by using the so-called *Dipole Formalism* [114] and *substraction method* [115].

In addition to the matrix elements, the following ingredients must be included to make a complete calculation:

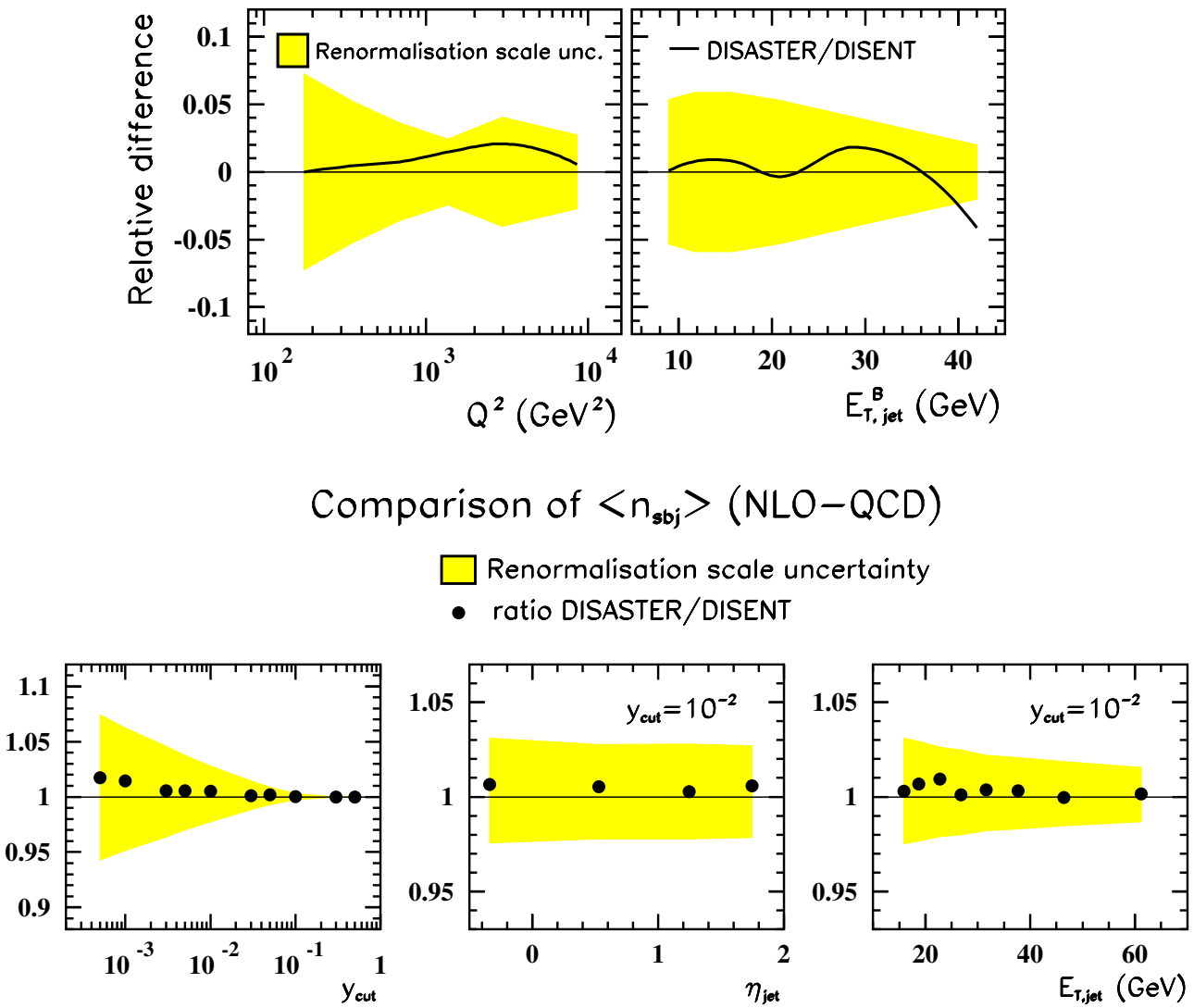

Figure 5.1: Ratio of the NLO QCD predictions obtained with DISASTER and DISENT for the two analyses. In the two plots above, the comparison is performed for the inclusive jet cross sections in the Breit frame as a function of Q^2 (left) and $E^B_{T,jet}$ (right). In the plots below, the comparison refers to the results on $\langle n_{sbj} \rangle$ as a function of y_{cut}, η_{jet} and $E_{T,jet}$. The differences between the two programs are smaller than the theoretical uncertainty

- **The PDF set**: the convolution of the weights given by DISENT with the parton densities in the proton is essential to obtain the final result, since the information given by the PDFs is needed to weight the contribution of the different initial partons coming from the proton.

- **The factorisation scale**: as described in section 1.3.3 the presence of a hadron in the initial state leads to the introduction of a factorisation scale to separate the processes inside and outside the hadron. In the analyses described in this thesis, this scale was set equal to $\sqrt{Q^2}$. It is expected that the results do not depend significantly on this scale and it was checked that the uncertainties coming from the residual dependence on this scale are very small in comparison with other contributions.

- **The renormalisation scale**: as described in section 1.3.2 the mechanisms used to remove the UV divergences in the predictions of perturbative QCD introduce a dependence on the renormalisation scale which, in turn, can be used to estimate the contribution of higher orders to the observable under study. This is done in the analyses presented here and described in the section on the theoretical uncertainties.

The only disavantadge of the use of DISENT is that the calculation is performed for γ-exchange alone, i.e. it doesn't contain the effects due to Z° boson exchange. Although these effects are only observable at high Q^2, they have to be taken into account. In the analyses presented here, the effects due to Z° exchange are included by correcting the NLO QCD predictions given by DISENT. The way this is done is described in section 5.2.1.

To perform the determination of the strong coupling constant from the comparison of the NLO QCD predictions and the measurements, it is necessary to calculate the full dependence of the theoretical predictions on the value of α_s. For this reason, the predictions have been obtained for different values of α_s. This is done by using in each case a set of parton densities which was determined assuming a given value of α_s. In this way, the correlation between the α_s value in the matrix elements and that assumed in the parametrisation of the proton PDFs is taken into account.

5.1.3 Estimation of the theoretical uncertainties

The theoretical predictions which are used in the analyses described here are not free of uncertainties. These should be taken into account, especially to draw quantitative conclusions from the comparison to the data.

Furthermore, the uncertainty in the extracted value of α_s has a theoretical contribution since the theoretical predictions we are using to obtain that value are liable to changes due to these theoretical uncertainties.

In the kind of analyses described here, the following contributions to the theoretical uncertainty have been considered:

- **The dependence on the higher orders**. Since the perturbative expansion in α_s was stopped at the second order, an uncertainty arises from the missing higher orders. As described in section 1.3.2, this uncertainty is estimated by studying the dependence of the predictions on the renormalisation scale.

  The standard procedure for the estimation of this uncertainty is to change the value chosen for the renormalisation scale by a factor of two, i.e. multiply the central value by 2 and by 1/2, and from the observed differences in the predictions, obtain the corresponding uncertainty.

- **The dependence on the parametrisations of the proton PDFs**. The parton densities are obtained from fits to the experimental data. This means that there is some uncertainty in the values used to obtain the theoretical predictions. This uncertainty is coming from that of the data used to fit the PDFs and from the assumptions in the fit procedure.

  The estimation of this uncertainty can be done in two ways. In the simplest naive one, the predictions obtained by using two different parametrisations of the proton PDFs are compared. This have the inconvenience of not considering the real uncertainties.

The second way is to consider the actual uncertainties in the data used in the fits and propagate them to the results. Furthermore, the uncertainty due to the assumptions in the fit procedure can be estimated for those PDFs in which modifications in these assumptions are available. At the time of this thesis, the only way to perform the estimation of these uncertainties by this method was by using the results of the analysis by M. Botje [116].

- **The hadronisation correction**. Since this correction is not calculable in perturbative QCD, it has to be inferred from the different phenomenological models. For this reason, it is very common to estimate the related uncertainty by comparing the predictions of different models of hadronisation.

- **The uncertainty in** α_s. Since the theoretical predictions depend on the assumed value of the strong coupling constant, it is obvious that an uncertainty due to that of this constant has to be included. It should be noted that this uncertainty has not been considered in the extraction of α_s.

All these uncertainties were estimated for the predictions studied in the analyses presented here. The total theoretical uncertainty is computed by adding in quadrature the different contributions.

For detailed comments regarding the theoretical uncertainties in the analyses, see sections 5.2.2 and 5.3.2.

5.1.4 Theoretical predictions for inclusive jet cross sections in the Breit frame

As described in section 1.4.2, high-E_T jet production in the Breit frame is described in the theory by the presence of a QCD process. This means that the theoretical predictions at leading order are directly proportional to α_s. The reason is that any diagram with less than two partons in the final state does not contribute to the production of jets because at least two partons are required to conserve the momentum in the transverse plane of the Breit frame.

The cross sections we have measured are described at leading order by

$$\sigma_{jets} = C_1 \alpha_s + \dots \ , \tag{5.1}$$

which also applies for the differential cross sections.

The next contribution in the perturbative expansion (the next-to-leading order) will be α_s^2, and the calculation of the cross section leads to

$$\sigma_{jets} = C_1 \alpha_s + C_2 \alpha_s^2 + \dots \tag{5.2}$$

All the diagrams needed to compute these two terms are at present available and included in DISENT. We have obtained the theoretical predictions as follows:

- The calculation was performed in the kinematical region of the analysis and with the standard parameters for DISENT, i.e. five flavours and $\mu_F^2 = Q^2$.

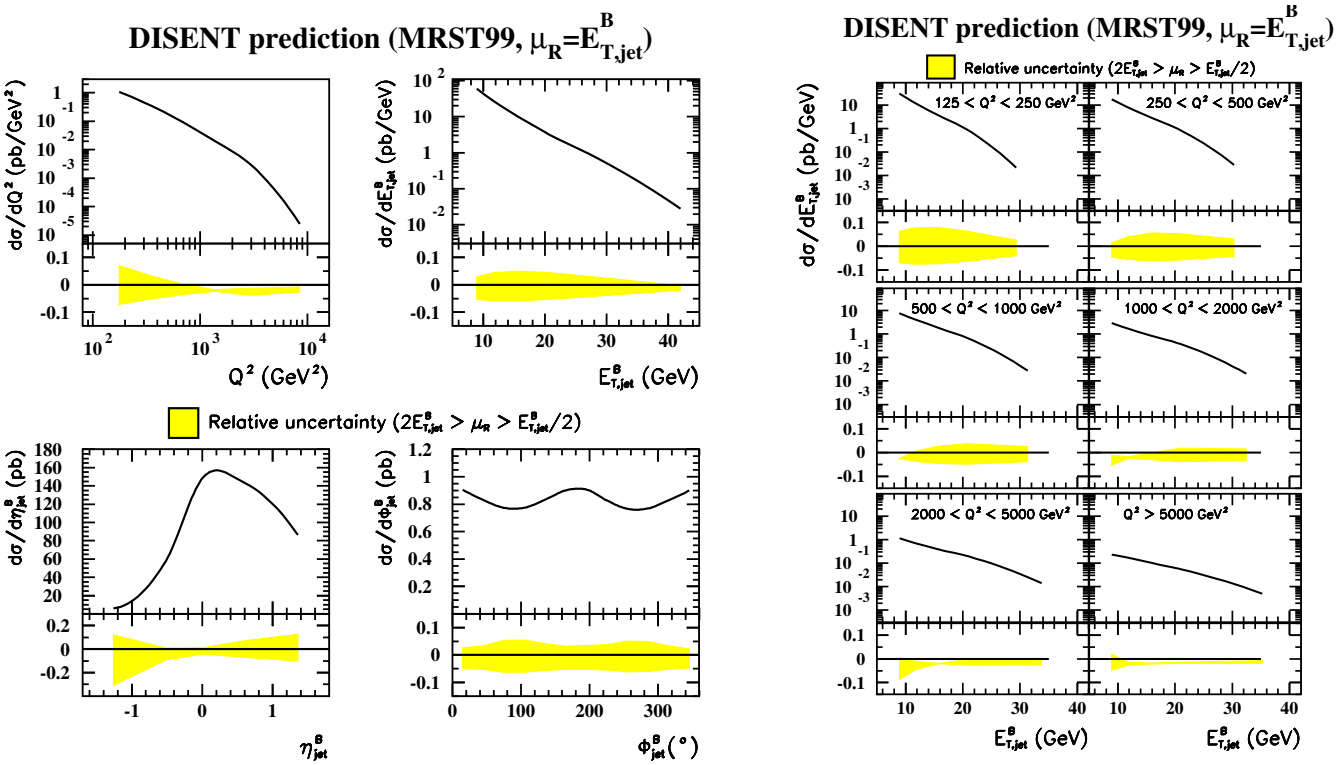

Figure 5.2: NLO QCD predictions for the inclusive jet cross sections in the Breit frame obtained with DISENT using MRST99 central as the set of proton PDFs. For each cross section the uncertainty coming for the residual dependence on the renormalisation scale is shown as a shaded band.

- The renormalisation scale was set equal to $E^B_{T,jet}$ for each of the jets. As an additional check, the predictions were obtained by taking $\mu_R^2 = Q^2$ and were usually within the uncertainty in the theory given by the variation of $E^B_{T,jet}/2 < \mu_R < 2E^B_{T,jet}$.

- The default set of proton PDFs was MRST99 [36], which is the one that gives the best description of the data. The authors provide additional sets of proton PDFs which assume different values of α_s. The uncertainty due to that of the proton PDFs was obtained with Botje's parametrisations [116].

  Furthermore, as a cross-check the predictions were compared with those obtained with the CTEQ5M1 [38] parametrisations of the proton PDFs.

The predictions calculated for this analysis are presented in figure 5.2, where the central values are presented as well as the uncertainties due to the residual dependence on the renormalisation scale. The major comment concerns the shape of the azimuthal distribution, which is predicted to be non-uniform.

As mentioned earlier, before the predictions are compared to the data, they should be corrected for hadronisation and for the effect of Z° exchange. A complete description of the corrections and the comparison with the data is presented in section 5.2.

5.1.5 Theoretical predictions for the subjet multiplicity in the laboratory frame

The mean subjet multiplicity at a fixed order in the perturbative QCD expansion depends upon the number of partons inside a jet. At lowest order the jet is only formed by one parton and the mean subjet multiplicity is exactly 1, independently of the resolution scale. This order is referred to as the *trivial order*.

If two partons are inside a jet, the maximum number of subjets is 2, but depending on how these partons are distributed inside the jet, it will be possible to find 1 or 2 subjets. Therefore, in this case there is a dependence on the resolution scale. The contributions to the configuration in which a jet contains two subjets constitute the first non-trivial contribution to the mean subjet multiplicity. This order is referred to as the leading order.

To calculate this leading order of the mean subjet multiplicity, it is needed to divide the number of jets containig two subjets at the given resolution scale over the number of jets,

$$\left\langle n_{sbj} \right\rangle = 1 + \frac{N_{jets}\,(sbj = 2)}{N_{jets}} + \cdots = 1 + A_1\alpha_s + \ldots \ , \tag{5.3}$$

where both numerator and denominator are calculated to the first non-trivial order.

In the analysis presented here, since jets are reconstructed in the laboratory frame, the first non-trivial contribution to the denominator is that of the Quark-Parton Model diagram, which does not contain any contribution from QCD.

To obtain the next-to-leading order predictions, it is needed to generalise the expression above to the second order. As the order is increased, the number of partons which can be inside a jet increases. To compute $\left\langle n_{sbj} \right\rangle$ we use the following expression

$$\left\langle n_{sbj} \right\rangle - 1 = \frac{\sum_{jets} ({n_{sbj}}^{jet} - 1)}{\sum_{jets} 1} = \frac{a_1\alpha_s + a_2{\alpha_s}^2 + \ldots}{b_0 + b_1\alpha_s + \ldots} \ , \tag{5.4}$$

where the last term is the expression at next-to-leading order. This expression allows the computation to be reduced to the calculation of the number of jets and subjets in a consistent way.

At present the calculation of the mean subjet multiplicity to second order in pQCD is only possible in DIS for jets defined in the laboratory frame; in other frames, terms are required which have not yet been calculated.

To perform the calculation of the previous expression with DISENT, we should calculate two different cross sections: the cross section to produce jets and the cross sections to produce jets with a given number of subjets (different from 1) for a given value of the resolution scale. The final result for $\left\langle n_{sbj} \right\rangle$ is then obtained by dividing both cross sections and adding unity.

Figure 5.3 shows the resulting NLO QCD predictions for $\left\langle n_{sbj} \right\rangle$ as a function of y_{cut}, η_{jet} and $E_{T,jet}$. The predictions have been obtained for different values of α_s. As mentioned earlier this is performed by using in each case a set of parton densities which was determined assuming a given value of α_s. The results shown in the figure were obtained with three of the five sets of the CTEQ4A series [37]. A clear dependence of $\left\langle n_{sbj} \right\rangle$ with the value of α_s is observed.

In addition, calculations have been done using as renormalisation scale $\frac{\sqrt{Q^2}}{2}$ and $2\sqrt{Q^2}$. This is the standard way to quantify the dependence on the renormalisation scale. This dependence

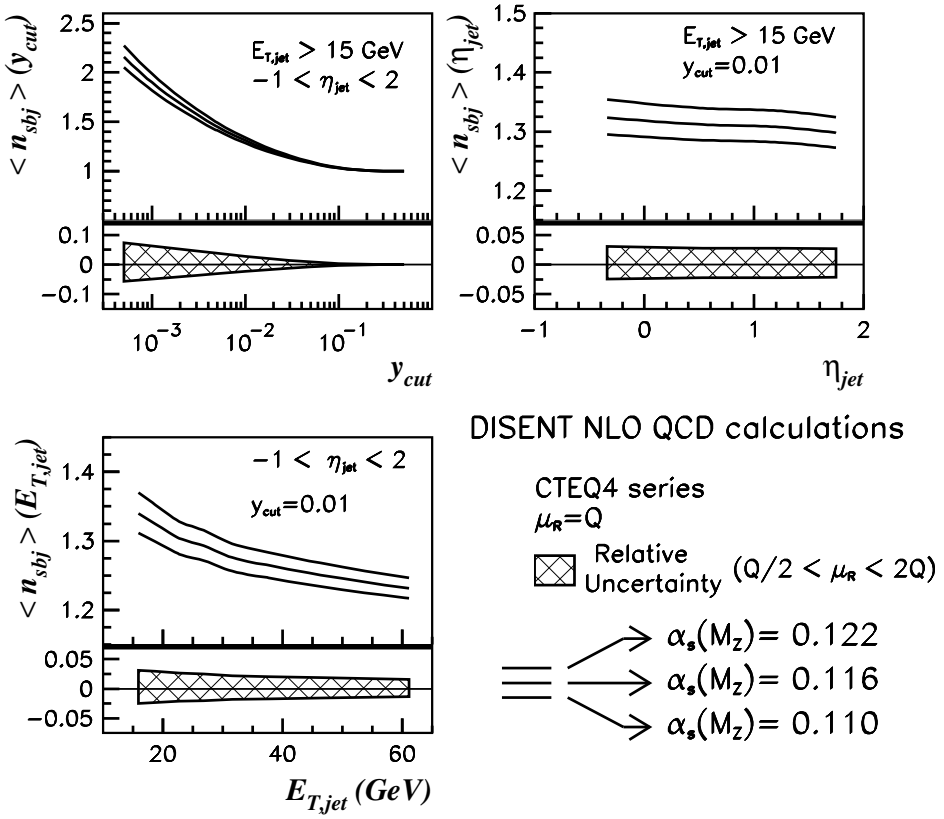

Figure 5.3: NLO QCD predictions for $\langle n_{sbj} \rangle$ as a function of y_{cut} (top left), η_{jet} (top right) and $E_{T,jet}$ (bottom) obtained with DISENT. The three curves in each plot show the predictions for different values of $\alpha_s(M_Z)$. The hatched band below the plot shows the relative uncertainty coming from the residual dependence on the renormalisation scale.

allows the estimation of the uncertainty due to the higher-order terms not included in the calculations and it is shown as a hatched band below each plot. It is observed that the dependence on the renormalisation scale gets smaller when the resolution scale is larger. However, this uncertainty displays only a slight dependence on the transverse energy of the jets or the jet pseudorapidity.

5.2 Comparison of the inclusive jet cross sections with the NLO QCD predictions

In this section we are going to perform the comparison of the theoretical predictions obtained with DISENT (and described in section 5.1.4) with the measurements of the inclusive jet cross sections in the Breit frame (described in section 4.2.6).

5.2.1 Parton-to-hadron and Z° corrections

Before the predictions by DISENT are compared to the data we have to correct the former for hadronisation and Z°-exchange effects.

The correction for Z° exchange is needed because it is not included in DISENT and in the high-Q^2 region its effects are not negligible[1]. Since in the analysis of the inclusive jet cross sections in the Breit frame has been done in a region where Z° exchange is relevant ($Q^2 \gtrsim M_Z^2$), the predictions obtained by DISENT ought to be corrected to have a realistic comparison to the data.

This correction has been obtained by comparing the predictions obtained with LEPTO by including or not Z° exchange. In this case, the program LEPTO was run in stand-alone mode, i.e. the original version and not the one included in DJANGOH since within DJANGOH Z° exchange cannot be switched off. The parton shower was simulated by using ARIADNE. The correction factors has been obtained from the predictions at parton level; it has been checked that the hadron level provides the same correction.

Figure 5.4 shows the comparison of the two predictions for the $\mathrm{d}\sigma/\mathrm{d}Q^2$ and $\mathrm{d}\sigma/\mathrm{d}E^B_{T,jet}$ distributions. Since the effect of Z° exchange is negligible for the lower values of Q^2, it is not observable for $\mathrm{d}\sigma/\mathrm{d}\phi^B_{jet}$; for $\mathrm{d}\sigma/\mathrm{d}\eta^B_{jet}$ is very small except in the backward region, where it is around 5% [104]. It should be noted the the cross section is reduced at high-Q^2 by the effect of the destructive interference; in the case of electrons would be constructive. The effect observed as a function of $E^B_{T,jet}$ is due to some correlation of this variable with Q^2.

In the lower part of each plot in the figure, the ratio of the two predictions is shown. This ratio quantifies the effect of Z° exchange and it is applied to the NLO QCD predictions by DISENT. It should be noted that only for the last point in Q^2 the effect is comparable to the theoretical uncertainties, which are around $5 - 10\%$.

The hadronisation correction gives information about the differences between the system of partons predicted by NLO QCD and the hadronic level arising from it. It is necessary to know these differences to avoid biases in the conclusions when comparing the NLO QCD predictions (parton level) to the measurements, which have been corrected to hadron level.

In this way, the correction of the NLO QCD predictions allows to make a more precise comparison. Since the correction is not calculable in perturbative QCD, it has to be estimated by using phenomenological approaches. These approaches are implemented in the Monte Carlo programs (see chapter 3): the correction is calculated as the ratio of the value obtained at hadron level over that at parton level.

For the present analysis, the estimation of this parton-to-hadron correction was obtained with the models implemented in ARIADNE, LEPTO-MEPS and HERWIG, which allow to have two different models for the simulation of both the parton radiation and hadronisation.

The predictions at hadron level are obtained as described in section 4.1.5. For the parton level, all partons which are produced after the parton radiation takes place are considered. These are the partons that were used as the starting point for the hadronisation procedure. They are handled in the same way as the hadrons: First all, their four-momenta are transformed into the Breit frame by using the same boost that for the hadrons. In a second step, the three-momenta are scaled to obtain massless four-momenta for the partons and the k_T-cluster algorithm is applied to obtain the jets. Finally, the same selection on the kinematic variables and jets as at hadron level is performed.

After obtaining the final sample of jets at the parton level, the cross sections are computed and the parton-to-hadron correction is calculated as mentioned above. Figure 5.5 shows the

[1] In fact, at HERA the observable effect is not coming directly from the Z° exchange itself, but from the $Z^\circ - \gamma$ interference.

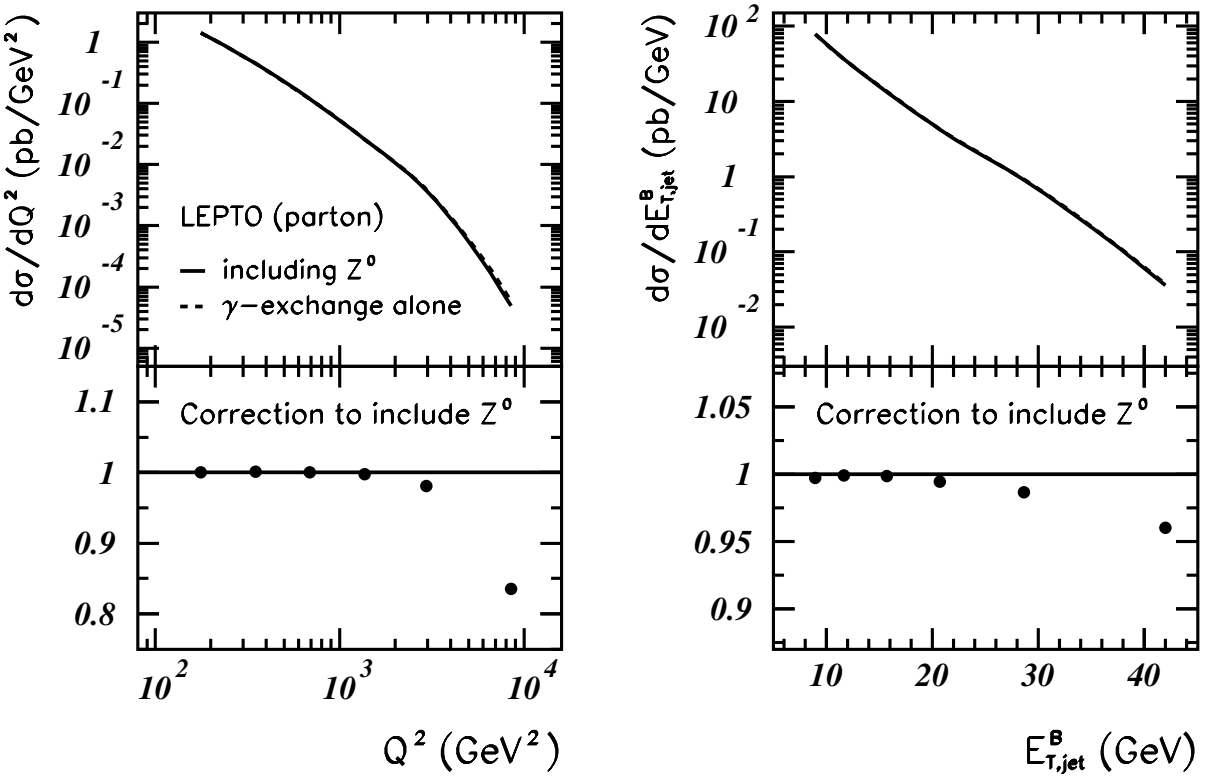

Figure 5.4: Predicted cross sections $\mathrm{d}\sigma/\mathrm{d}Q^2$ and $\mathrm{d}\sigma/\mathrm{d}E^B_{T,jet}$ at parton level by using the Monte Carlo program LEPTO with (solid line) and without (dashed line) Z° exchange. The plot in the lower part of the figure shows the correction to be applied to DISENT predictions to correct for Z° exchange.

corrections applied to the NLO QCD predictions as estimated by using the three Monte Carlo programs. All of them give very similar values in all the distributions under study. It should be noted that the correction is smaller than 10% except for $\mathrm{d}\sigma/\mathrm{d}\eta^B_{jet}$ in the backward (negative η) region. There the correction is large; it should be noted that the cross section is very small, which explains why this large correction does not affect other distributions. On the other hand this correction decreases as η^B_{jet} increases, being very small in the most forward region. It should be mentioned that a similar behaviour of the hadronisation correction has been observed in similar analyses [117].

Since the three estimations of the parton-to-hadron corrections are in good agreement, it was decided to calculate the correction to be applied to the NLO QCD predictions (already corrected by Z° exchange) as the mean value of the three estimations. The uncertainty in this correction was estimated by computing the variance of the three values for each measured point. The corrections obtained as well as the related uncertainties are shown in the final figures, which are discussed in section 5.2.3.

5.2.2 Theoretical uncertainties

To perform a quantitative comparison between the measurements and the theoretical predictions, several sources of theoretical uncertainty have been considered and are briefly described here:

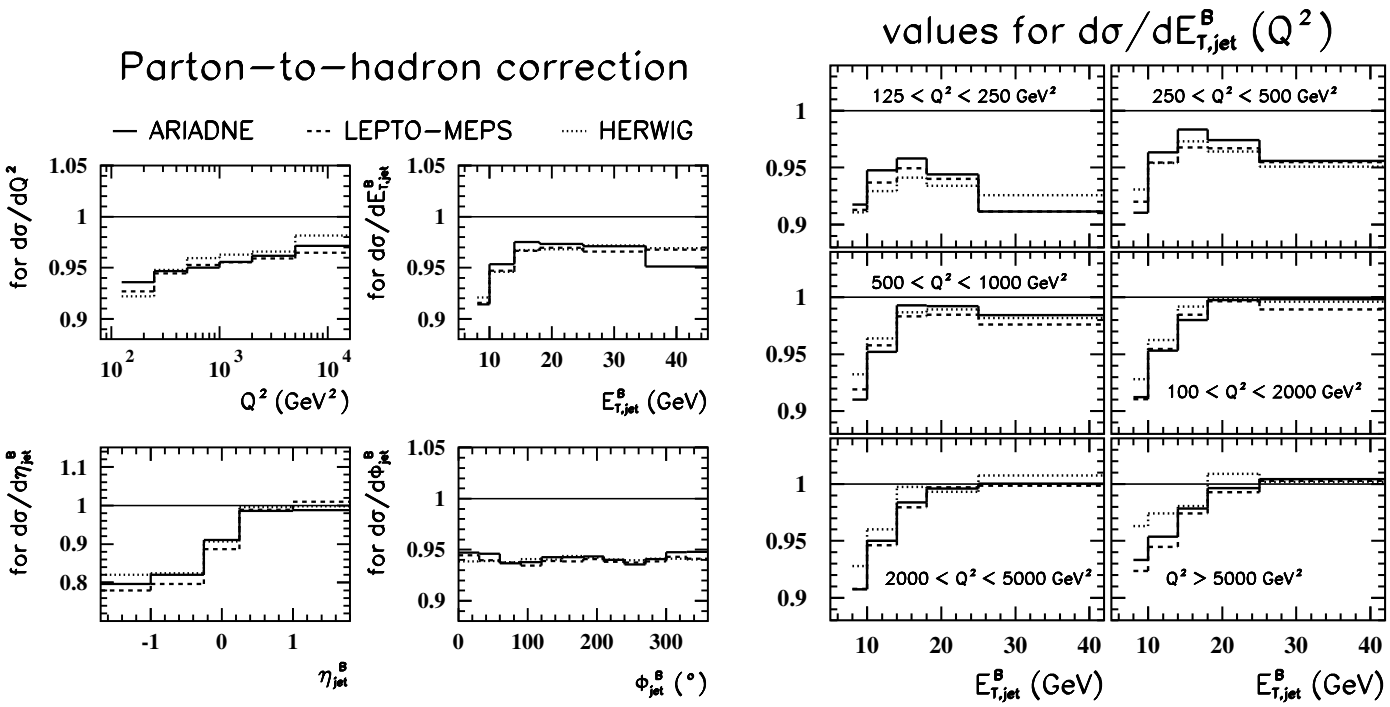

Figure 5.5: Parton-to-hadron correction predicted by the different Monte Carlo programs for the distributions under study. The factor is the ratio of the cross section at hadron level over that at parton level. The three models are in good agreement.

- The uncertainty on the predictions due to terms beyond NLO was estimated by varying μ_R between $E^B_{T,jet}/2$ and $2E^B_{T,jet}$. For some points, the variation induced by the two changes goes in the same direction (usually decreasing the predicted cross section). In that case, the larger variation was considered in both directions. The size of this uncertainty is around 5%.

- The predictions were also obtained by setting the renormalisation scale equal to $\sqrt{Q^2}$. They give a poorer description of the data (see section 5.2.3); the differences are within the uncertainty band estimated by the variation of the renormalisation scale mentioned above.

  It should be mentioned that variations were also considered for this choice, $\sqrt{Q^2}/2$ and $2\sqrt{Q^2}$; the size of the variations in the cross sections are similar to those observed in the variation around $\mu_R = E^B_{T,jet}$.

  For these reasons, these variations were not included in the final uncertainty.

- The uncertainty on the predictions due to that on $\alpha_s(M_Z)$ was estimated by repeating the calculations using two additional sets of proton PDFs, MRST99↑↑ and MRST99↓↓, determined assuming $\alpha_s(M_Z) = 0.1225$ and 0.1125, respectively. The difference between the calculations using these sets and MRST99-central was scaled by a factor 3/5 to refer to the uncertainty on the world average of α_s [118]. The uncertainty in the cross sections amounts to $5 - 10\%$ as a function of Q^2 and $E^B_{T,jet}$;

- the variance of the hadronisation corrections as predicted by the three Monte Carlo programs considered was taken as the uncertainty in this correction; it typically amounts to less than 1%;

- the uncertainty on the NLO QCD calculations due to those of the proton PDFs was estimated by using the sets of proton PDFs obtained by M. Botje [116], who also provides the covariance matrix of the fitted PDF parameters and the derivatives of the PDFs with respect to these parameters as a function of x and Q^2. This information allows the propagation of the uncertainty in the PDFs to the predicted cross sections. This contribution to the theoretical uncertainty amounts to 3%, reaching 5% in the high $E^B_{T,jet}$ region;

- an additional contribution to the theoretical uncertainty comes from the fit procedure used in the determination of the PDFs. This is computed by taking into account the systematic effects on this procedure; its calculation was possible by using the sets of PDFs given by M. Botje [116], which provide the variations induced in the proton PDFs by the variations in the fit procedure. The uncertainty in the cross sections amounts to 3%.

- As a cross-check, the predictions were compared to those obtained by using the set of PDFs called CTEQ5M1 [38] and the central Botje's set [116]. The observed differences are within the theoretical uncertainties and, in the case of CTEQ5M1, the predictions agree with the ones obtained with MRST99 at the 1-2% level. The differences observed in these comparisons were not included in the final uncertainties.

- The factorisation scale was set equal to $\mu_F = \sqrt{Q^2}/2$ and $\mu_F = 2\sqrt{Q^2}$ in order to estimate the dependence on this scale. The observed variations are very small in comparison with the dependence on the renormalisation scale except in the high $E^B_{T,jet}$ region, where both uncertainties are comparable. The observed differences were not included in the final uncertainties.

All the considered uncertainties have been added in quadrature to compute the total theoretical uncertainty, which is the one used when analysing the comparison between the data and the theoretical predictions, described in the following section.

5.2.3 Final results

At this point, the theoretical predictions are compared to the measurements obtained previously (see section 4.2.6). This comparison is shown in figures 5.6 to 5.11 for all the cross sections we have measured in the data, described in section 4.2.1.

To study the scale dependence, NLO QCD calculations using $\mu_R = \mu_F = \sqrt{Q^2}$ are also compared to the data in the figures; overall they provide a poorer description of the data than those using $\mu_R = E^B_{T,jet}$.

The ratios of the measured differential cross sections over the NLO QCD calculations are shown in the central plot of each figure except for the azimuthal distribution. The NLO QCD calculations describe reasonably well the measured differential cross sections.

The size and uncertainty of the hadronisation correction are shown in each figure as the shaded band in the bottom plot. As described previously (section 5.2.1), this correction is smaller than 10% except for the η^B_{jet} distribution.

At low Q^2 and low $E^B_{T,jet}$, the measurements of inclusive jet cross sections are above the calculations by $\sim 10\%$. The differences between the measurements and calculations are of the same size as the theoretical uncertainties.

The η^B_{jet} distribution is reasonably described by NLO QCD. An excess in the forward region is observed; the ratio plot shows that the NLO QCD predictions display a slightly different shape than that observed in the data. The disagreement between the measurements and the theoretical predictions increases with the pseudorapidity, but the theoretical uncertainty, mostly the dependence on the renormalisation scale, is also increasing. The disagreement observed in the most forward region is of the same size as the theoretical uncertainty.

In the case of the azimuthal distribution, shown in figure 5.9, since we are interested in the comparison of the shapes, the measured and predicted cross sections have been area normalised. The NLO QCD calculations describe the shape of the measured $d\sigma/d\phi^B_{jet}$ well and show that the observed azimuthal dependence is compatible with that expected in the Standard Model. This is the first time that the azimuthal asymmetry has been observed by using jets.

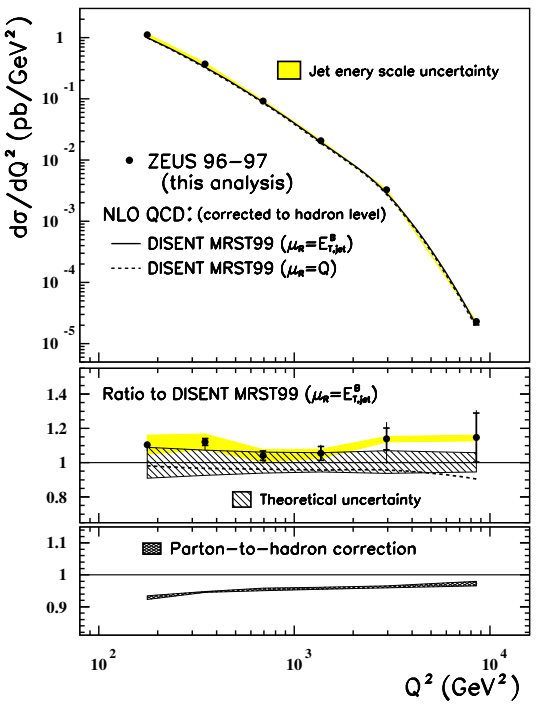

Figure 5.6: The differential cross-section $\mathrm{d}\sigma/\mathrm{d}Q^2$ for inclusive jet production (black dots). The inner error bars represent the statistical uncertainty. The outer error bars show the statistical and systematic uncertainties not associated with the uncertainty in the absolute energy scale of the jets added in quadrature. The shaded band displays the uncertainty due to the absolute energy scale of the jets. The NLO QCD calculations corrected for hadronisation effects and using the MRST99 parametrisations of the proton PDFs are shown for two choices of the renormalisation scale. The plot in the middle shows the fractional difference between the measured $\mathrm{d}\sigma/\mathrm{d}Q^2$ and the NLO QCD calculation; the hatched band displays the total theoretical uncertainty. The shaded band in the lower plot shows the magnitude and the uncertainty of the parton-to-hadron correction used to correct the NLO QCD predictions.

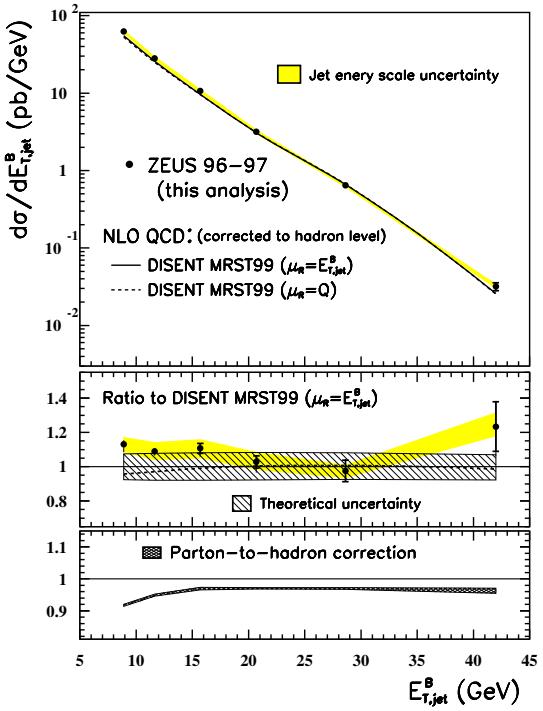

Figure 5.7: The differential cross-section $\mathrm{d}\sigma/\mathrm{d}E^B_{T,jet}$ for inclusive jet production with $E^B_{T,jet} > 8$ GeV and $-2 < \eta^B_{jet} < 1.8$ (black dots). Other details are as described in the caption to figure 5.6.

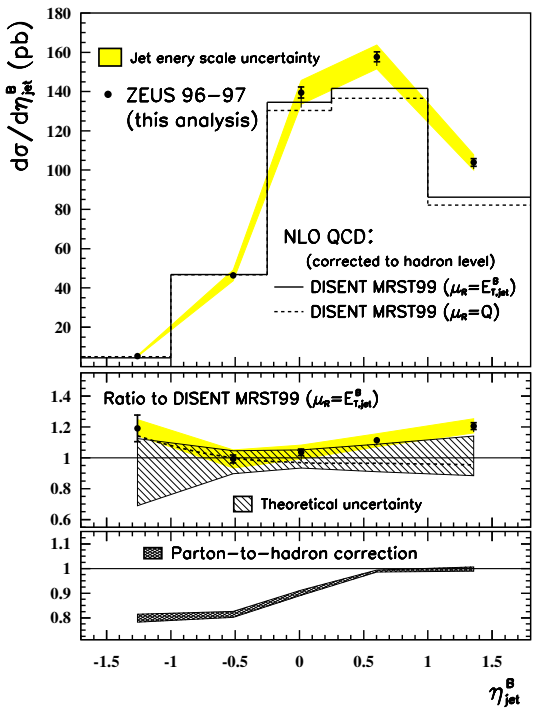

Figure 5.8: The differential cross-section $\mathrm{d}\sigma/\mathrm{d}\eta^B_{jet}$ for inclusive jet production with $E^B_{T,jet} > 8$ GeV and $-2 < \eta^B_{jet} < 1.8$ (black dots). Other details are as described in the caption to figure 5.6.

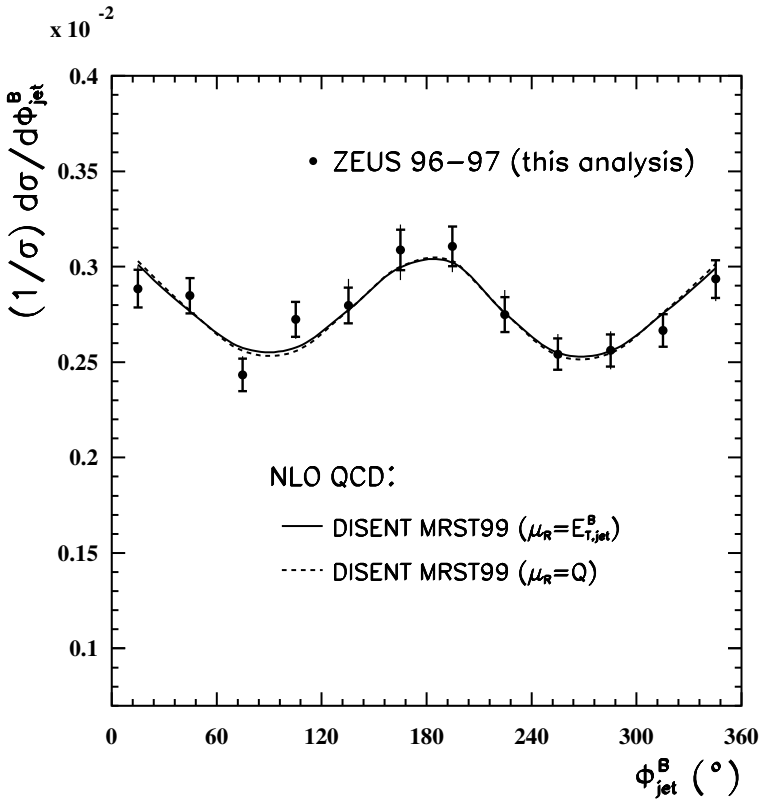

Figure 5.9: The normalized differential cross-section $(1/\sigma)\,\mathrm{d}/\mathrm{d}\phi^B_{jet}$ for inclusive jet production with $E^B_{T,jet} > 8$ GeV and $-2 < \eta^B_{jet} < 1.8$ (black dots). The inner error bars represent the statistical uncertainty. The outer error bars show the statistical and systematic uncertainties not associated with the uncertainty in the absolute energy scale of the jets added in quadrature. The NLO QCD calculations using the MRST99 parametrisations of the proton PDFs are shown for two choices of the renormalisation scale.

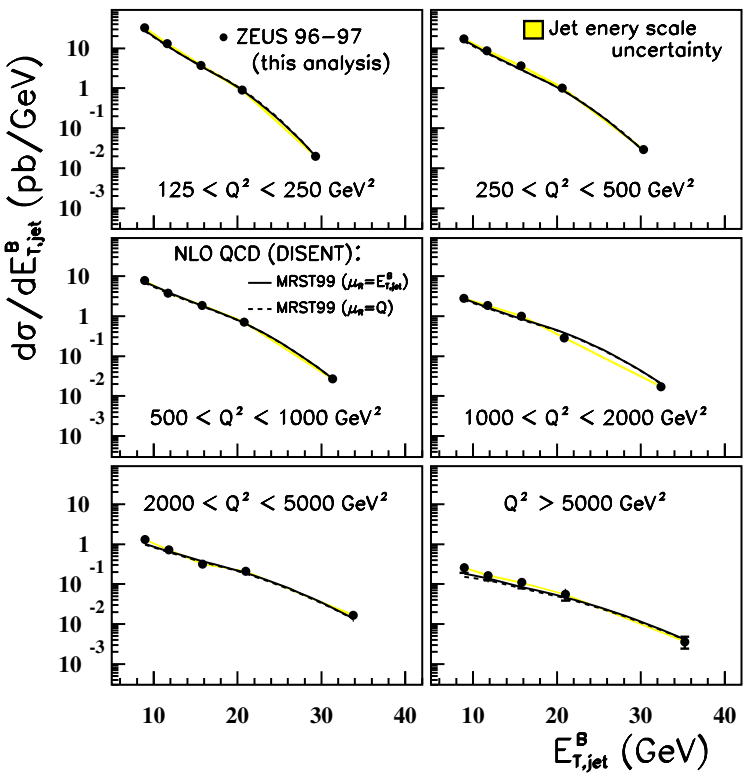

Figure 5.10: The differential cross-sections $\mathrm{d}\sigma/\mathrm{d}E^B_{T,jet}$ for inclusive jet production with $E^B_{T,jet} > 8$ GeV and $-2 < \eta^B_{jet} < 1.8$ in different regions of Q^2 (black dots). Other details are as described in the caption to figure 5.6.

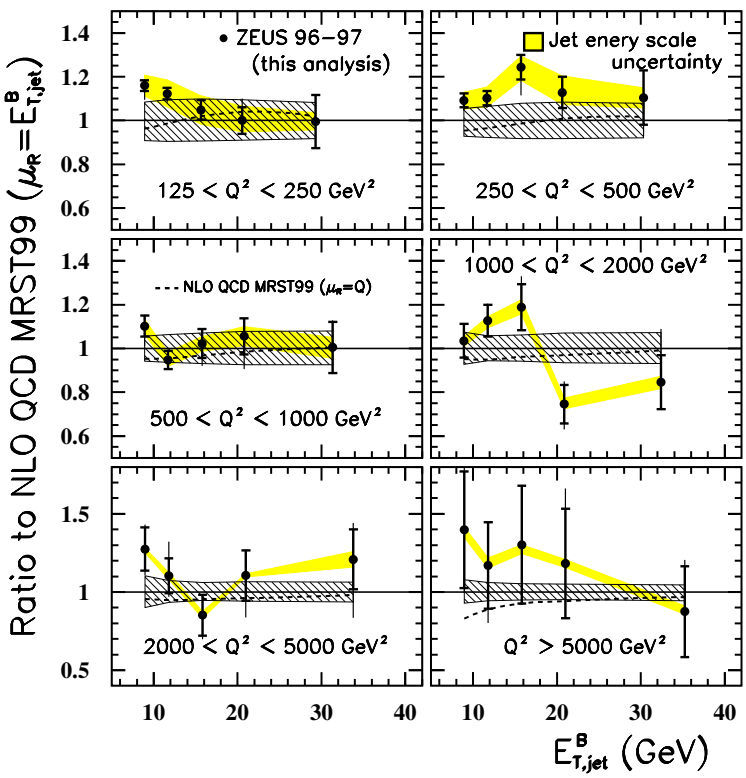

Figure 5.11: Ratios between the differential cross-sections $\mathrm{d}\sigma/\mathrm{d}E^B_{T,jet}$ presented in figure 5.10 and NLO QCD calculations using the MRST99 parametrisations of the proton PDFs and $\mu_R = E^B_{T,jet}$ (black dots). Other details are as described in the caption to figure 5.6.

5.3 Comparison of the subjet multiplicity with the NLO QCD predictions

In this section we are going to perform the comparison of the theoretical predictions obtained with DISENT (and described in section 5.1.5) with the measurements of the mean subjet multiplicity which were described in section 4.3.6.

5.3.1 Parton-to-hadron and Z° corrections

As mentioned earlier, before the predictions by DISENT are compared to the data we have to correct them for hadronisation and Z°-exchange effects. In this analysis the effect of the Z° has been calculated and found to be negligible for all the distributions. For this reason, the correction was not applied. On the other hand, the hadronisation corrections for the mean subjet multiplicity are large, especially for small values of y_{cut} or $E_{T,jet}$. It is preferred not to use those regions to extract conclusions from the comparison between the corrected NLO QCD and the data since the uncertainty in the hadronisation correction is expected to be also large.

As in the analysis of jets in the Breit frame (see section 5.2.1), the hadronisation correction was computed by dividing the predictions at hadron level over those obtained at parton level. The values of these factors, as predicted by ARIADNE, LEPTO-MEPS and HERWIG, are shown in figure 5.12; the predicted corrections are shown as a function of the resolution scale and of the transverse energy of the jets. The plots in that figure show that the correction is very large for the lower values of y_{cut}. For a fixed value of this scale, the correction becomes smaller as the jet transverse energy increases. Furthermore, the uncertainty in this correction, which is estimated by the differences between the different models, decreases when the correction itself decreases. This is valid for the three Monte Carlo models, although it should be noted that the predictions obtained with HERWIG are in disagreement with those of ARIADNE and LEPTO-MEPS, especially in the region in which these two models are in good agreement. This difference makes unreliable the correction predicted by HERWIG. It was checked that the problem was that although HERWIG was in fair agreement with the data, its parton level predictions were in clear disagreement with the values predicted by NLO QCD . In the case of ARIADNE and LEPTO-MEPS, the disagreement is just coming from a global shift in the mean subjet multiplicity at all levels, which has a small effect in the correction themselves because they are obtained as ratios. In fact, the NLO QCD predictions corrected with ARIADNE and LEPTO-MEPS gives a reasonable description of the data; this is not the case when the HERWIG correction is used [105].

Due to this problem with HERWIG, it was decided to correct the NLO QCD directly by using the prediction of ARIADNE and estimate the uncertainty by computing the difference between ARIADNE and LEPTO-MEPS in each point. With this criterion and for $y_{cut} = 10^{-2}$, the correction is smaller than 15% in the region $E_{T,jet} > 25$ GeV. It is in this region where a reliable comparison between the data and the corrected NLO QCD predictions can be performed.

5.3.2 Theoretical uncertainties

A detailed study of the uncertainties in the theoretical predictions has been performed and is described here. The sources of uncertainty considered are listed below:

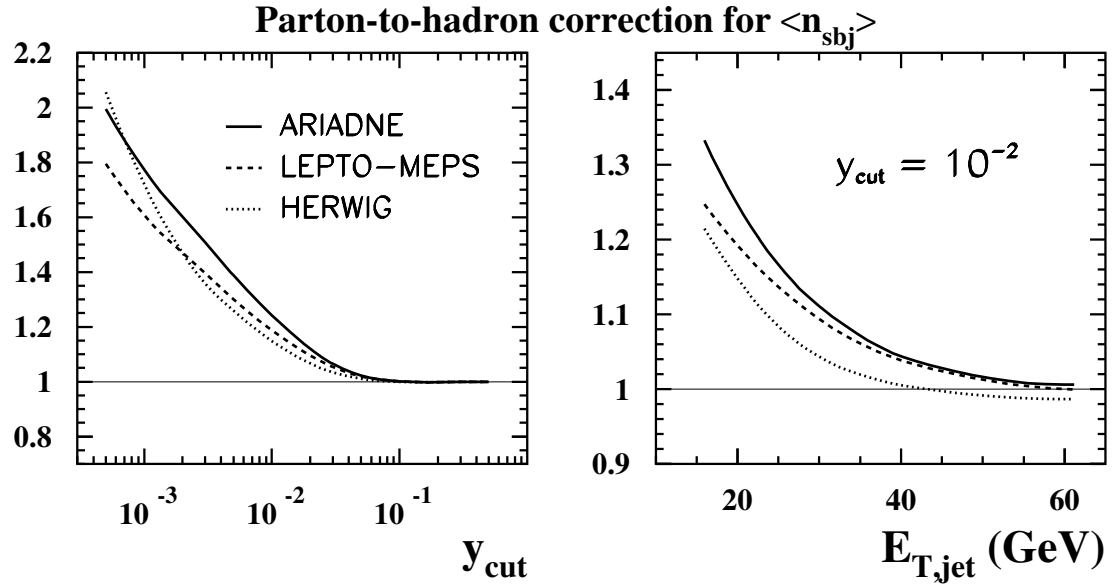

Figure 5.12: Parton-to-hadron correction factor as estimated by using ARIADNE (solid lines), LEPTO-MEPS (dashed lines) and HERWIG (dotted line) as a function of y_{cut} (left) and $E_{T,jet}$ (right).

- Higher-order effects: they have been estimated by varying the renormalisation scale between $\frac{\sqrt{Q^2}}{2}$ and $2\sqrt{Q^2}$. This represents the largest source of uncertainty.

- The hadronisation correction: it was estimated by comparing the corrections obtained with ARIADNE and LEPTO-MEPS, as described previously. It should be noted that the difference is considered as the uncertainty in both directions.

- The renormalisation scale was set equal to the transverse energy of each jet in the event. The results are very similar to those using $\sqrt{Q^2}$ and always within the uncertainty of varying the renormalisation scale by a factor of 2. For this reason, this variation is not considered as an additional source of uncertainty.

- The calculations were repeated using the MRST99 parametrisations [36] of the parton densities. No significant difference was found with respect to the predictions obtained using the CTEQ4M set [37].

- The uncertainty due to that on the gluon content of the proton was estimated by repeating the calculations with sets of parton densities which make different assumptions on the gluon content of the proton. Three sets of the MRST99 series (central, $g\uparrow$ and $g\downarrow$) permit to make this check. Differences smaller than 0.1% are observed .

It should be emphasised the small uncertainty in $\langle n_{sbj} \rangle$ coming from that of the parton distribution functions. This represents an advantage of this analysis for studying QCD.

5.3.3 Final results

Once the NLO QCD predictions have been corrected to the hadron level, it is possible to compare them directly to the data.

Figure 5.13 shows the comparison of the predictions and the measurements of the mean subjet multiplicity for the entire sample as a function of y_{cut}. It should be noted that the NLO QCD predictions give a good description of the data even in the region where the parton-to-hadron corrections are very large, which is indicated in the plot as the shaded region. On the other hand, leading order predictions are clearly below the measurements.

The plot also shows the predictions for different values of $\alpha_s(M_Z)$, which have been obtained as described in section 5.1.5.

Figure 5.14 shows the comparison of the NLO QCD predictions and the measurements for the mean subjet multiplicity at a given resolution scale ($y_{cut} = 10^{-2}$) as a function of the transverse energy of the jets. The agreement between data and NLO QCD is very good. The predictions using different values of $\alpha_s(M_Z)$ show that the measurements are sensitive to its value.

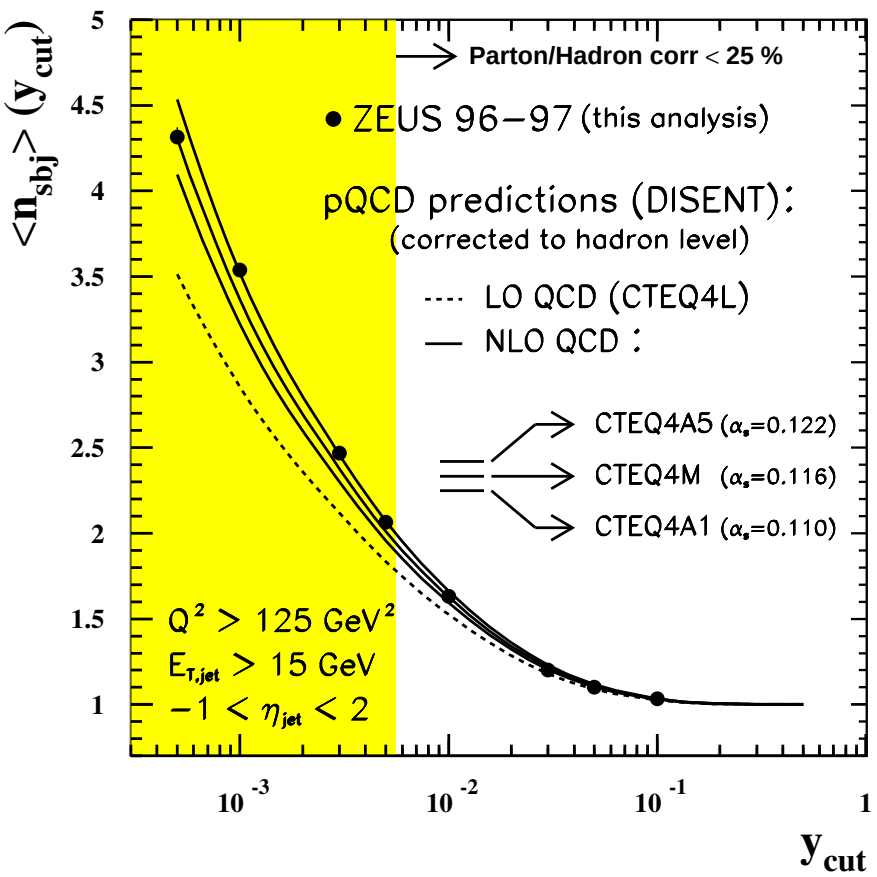

Figure 5.13: The measured mean subjet multiplicity corrected to the hadron level $\langle n_{sbj} \rangle$ as a function of y_{cut} for inclusive jet production in NC DIS (black dots). For comparison, NLO QCD calculations corrected for hadronisation effects and obtained using three different CTEQ4 sets of the proton parton densities are shown (solid lines). LO QCD calculations corrected for hadronisation effects and obtained with the CTEQ4L set of proton parton densities are also shown (dashed line).

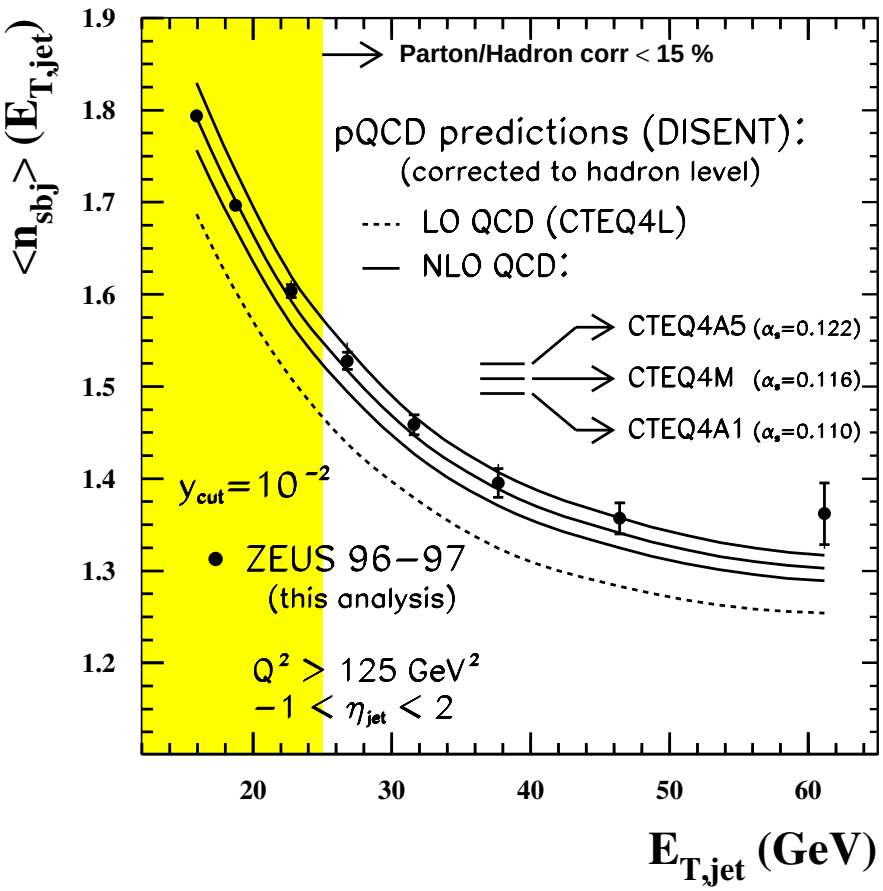

Figure 5.14: The measured mean subjet multiplicity corrected to the hadron level $\langle n_{sbj} \rangle$ as a function of $E_{T,jet}$ at $y_{cut} = 10^{-2}$ for inclusive jet production in NC DIS (black dots). The inner error bars represent the statistical uncertainties of the data. The outer error bars show the statistical and systematic uncertainties added in quadrature. Other details are as described in the caption to figure 5.13.

5.4 Extraction of $\alpha_s(M_Z)$ from the measurements

The reasonable description of the measurements given by the NLO QCD predictions confirms the validity of QCD as the theory to describe jet production in NC DIS. We have gone a step further and from the comparison between data and theory, and the sensitivity of the measurements to the value of α_s, the comparisons have been used to determine its value. The value of α_s is not predicted by the theory and has to be determined from experimental measurements like the ones performed in this thesis.

In this section, the method used to extract the value of α_s is described as well as the result of this extraction.

5.4.1 Description of the method

As described previously, it is possible to obtain the theoretical predictions for different values of the strong coupling contant in a consistent way, i.e. taking into account the correlations

between the value of α_s used in the matrix elements and that assumed in the parametrisation of the proton PDFs. To make this, sets of parton densities determined by assuming different values of α_s have to be considered in the calculations. Furthermore, these sets have to be comparable in the sense that the only difference in the fit is the value of α_s.

By computing the predictions for different values of α_s, we obtained the dependence on α_s of the predicted observables, in one case the inclusive jet cross sections in the Breit frame and in the other the mean subjet multiplicity. Since in fact the complete calculation can be done for a finite number of values, the α_s-dependence has to be parameterised to have a continuum functional dependence. This parametrisation is done for the observable $\mathcal{O}$ (which is σ or $\langle n_{sbj} - 1 \rangle$) by fitting the predicted values to the analytical expression:

$$\mathcal{O} = \alpha_s(M_Z) \cdot a_1 + \alpha_s^2(M_Z) \cdot a_2 \ , \tag{5.5}$$

being (a_1, a_2) the parameters of the fit.

As an example, figure 5.15 shows the parametrisations as obtained for the analysis of the mean subjet multiplicity. In this case, as described in section 5.1.5, the predictions are known for five different values of the strong coupling constant. The parametrisations are shown for the regions in $E_{T,jet}$ where the parton-to-hadron corrections are small. It should be noted that the fitted function is in perfect agreement with each individual prediction. This is also the case for the parametrisations obtained in the analysis of the inclusive jets cross sections in the Breit frame. The figure also shows the way the measured values of $\langle n_{sbj} \rangle$ are translated into values of $\alpha_s(M_Z)$. At the same time, the statistical error of the measurement is propagated into the statistical contribution to the uncertainty of α_s.

In the following sections, a more detailed description of the determination of α_s by using this method in the two analyses is given.

5.4.2 $\alpha_s(M_Z)$ from the inclusive jet cross sections

To determine the value of α_s, we only consider the measured cross sections $\mathrm{d}\sigma/\mathrm{d}Q^2$ and $\mathrm{d}\sigma/\mathrm{d}E^B_{T,jet}$. In principle, one value could be extracted from each measured point in all the cross sections considered. However, these two distributions are the most convenient ones. In fact, we have extracted not only one value for each measured point but also combined values which allow the reduction of the uncertainties.

The method used in the analysis to extract the value of α_s is the one described above. The parametrisations are computed for twelve points: six for the $\mathrm{d}\sigma/\mathrm{d}Q^2$ distribution and six for $\mathrm{d}\sigma/\mathrm{d}E^B_{T,jet}$. The fits are performed by using the predictions obtained with three sets of proton PDFs (and the related values of α_s) from the MRST99 sets [36]. These three sets are: the one we used for the comparison with the data (MRST99 central), one with a larger value of α_s (MRST99$\uparrow\uparrow$) and another with a smaller value of α_s (MRST99$\downarrow\downarrow$). The corresponding values of $\alpha_s(M_Z)$ are 0.1175, 0.1225 and 0.1125, respectively. From the parameterised function we extract the value of $\alpha_s(M_Z)$ corresponding to the measured data point. This is done for the twelve points mentioned above.

Furthermore, four combined values are obtained by a χ^2-fit to the measured values in the distributions. The fit is performed in order to find the $\alpha_s(M_Z)$ value which provides the best description of the measurements.

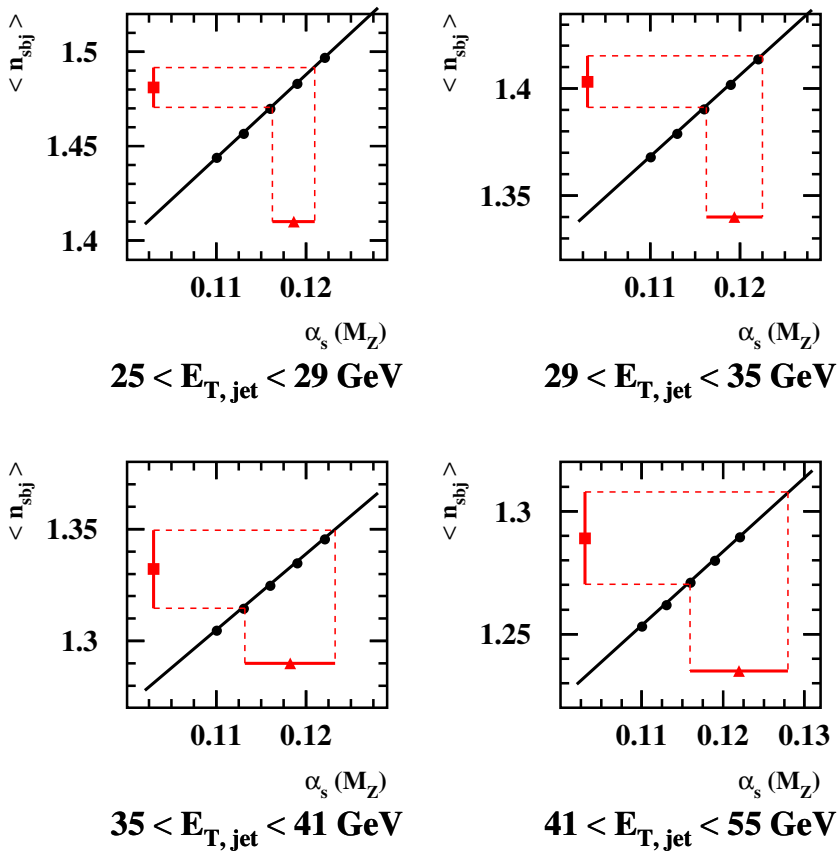

Figure 5.15: NLO QCD calculations of $\langle n_{sbj} \rangle$ for different values of $\alpha_s(M_Z)$ (black dots) in various $E_{T,jet}$ regions. The parametrisations (solid lines) according to Eq. (5.5) are also shown. The measured $\langle n_{sbj} \rangle$ values (solid squares) are used to extract a value of α_s (solid triangles) in each plot.

The same sources of experimental uncertainty we have included in the cross sections have been considered in the the extracted values of α_s constant. The estimation of each uncertainty was done by repeating the determination of α_s in each point. The difference with respect to the central one defines the given uncertainty.

The uncertainty in the luminosity value, estimated to be 1.6%, is included as an additional source of uncertainty. This uncertainty was computed by increasing or decreasing the measured cross sections by 1.6%.

To calculate the total experimental systematic uncertainty on the extracted α_s values, all the different contributions were added in quadrature. In this case, the contribution coming from the uncertainty in the jet energy scale was also added in quadrature with the others.

Regarding the theoretical uncertainties, the extraction is repeated for each central point, but now the predicted points that are parameterised are slightly different due to the theoretical variations. In this case, we include all the theoretical uncertainties considered in the analysis except that coming from the uncertainty on α_s.

As we did for the cross sections, if the variations in the value of α_s when changing the renormalisation scale by 2 or by 1/2 go into the same direction, the error is symmetrised by taking

the largest variation in both directions. Finally, the total theoretical uncertainty on α_s was computed by adding in quadrature all the contributions.

The following sixteen values of the strong coupling constant have been obtained:

- Six values extracted from the experimental points in the measured $\mathrm{d}\sigma/\mathrm{d}Q^2$. These values are presented in figure 5.16;
- six values extracted from the experimental points in the measured $\mathrm{d}\sigma/\mathrm{d}E^B_{T,jet}$. These values are presented in figure 5.17;
- a value is extracted from the whole sample of jets by fitting the experimental points in the measured $\mathrm{d}\sigma/\mathrm{d}Q^2$. The value, presented in figure 5.16, is

$$\alpha_s(M_Z) = 0.1243 \pm 0.0007\ (\text{stat.})^{+0.0034}_{-0.0041}\ (\text{syst.})^{+0.0055}_{-0.0039}\ (\text{th.});$$

- a value is extracted from the whole sample of jets by fitting the experimental points in the measured $\mathrm{d}\sigma/\mathrm{d}E^B_{T,jet}$. The value, presented in figure 5.17, is

$$\alpha_s(M_Z) = 0.1239 \pm 0.0007\ (\text{stat.})^{+0.0034}_{-0.0030}\ (\text{syst.})^{+0.0055}_{-0.0038}\ (\text{th.});$$

- a value is extracted from the measurements of $\mathrm{d}\sigma/\mathrm{d}Q^2$ in the $Q^2 > 500$ GeV^2 region, where the uncertainties are smaller:

$$\alpha_s(M_Z) = 0.1212 \pm 0.0013\ (\text{stat.})^{+0.0023}_{-0.0031}\ (\text{syst.})^{+0.0027}_{-0.0027}\ (\text{th.}).$$

  This value is also shown in figure 5.16 and used as a reference there;

- a value is extracted from the measurements of $\mathrm{d}\sigma/\mathrm{d}E^B_{T,jet}$ in the $E^B_{T,jet} > 14$ GeV region, where the uncertainties are smaller:

$$\alpha_s(M_Z) = 0.1211 \pm 0.0012\ (\text{stat.})^{+0.0030}_{-0.0036}\ (\text{syst.})^{+0.0041}_{-0.0030}\ (\text{th.}).$$

  This value is also shown in figure 5.17 and used as a reference there.

The main value of α_s is that extracted from the high-Q^2 region. The reason is that this value is the most precise one. In any case, the four combined values agree within the errors. In fact, the four values are in agreement with the current PDG world average of $\alpha_s(M_Z) = 0.1181 \pm 0.0020$ [119].

Regarding the twelve values obtained from the individual experimental points, only the one in the last bin in $E^B_{T,jet}$ is slightly above the four combined values, but its statistical uncertainty is very large.

To give an idea of the different contributions to the uncertainty, figure 5.18 shows the complete list of uncertainties for the combined value extracted from $\mathrm{d}\sigma/\mathrm{d}Q^2$ for $Q^2 > 500$ GeV^2. Furthermore, in that figure we have the values obtained by using different sets of proton PDFs or $\sqrt{Q^2}$ as the renormalisation scale.

It should be noted that the theoretical uncertainty is clearly dominated by the residual dependence on the renormalisation scale. On the other hand, most of the contributions to the experimental uncertainty are smaller than the statistical error. The comparison with the values extracted using other sets of PDFs shows differences, but they are within the theoretical uncertainties. For the points extracted as cross-checks, only the statistical error of the data is shown, and not the systematic uncertainties.

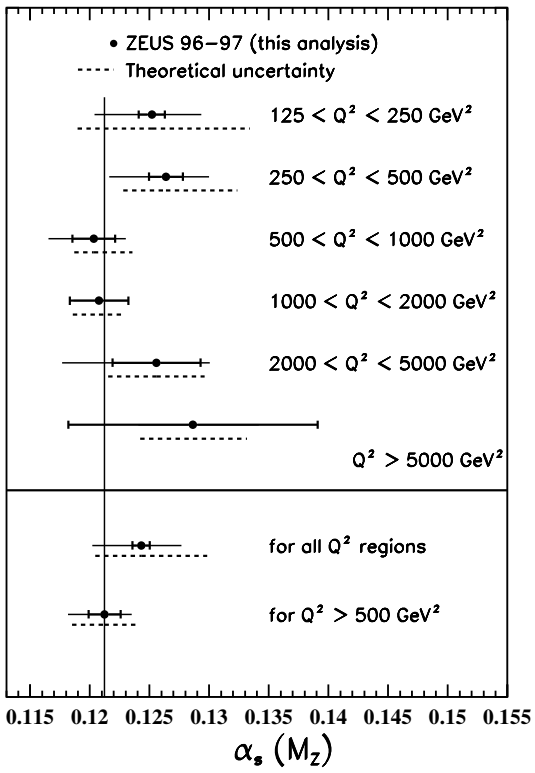

Figure 5.16: Values of the strong coupling contant extracted from the $\mathrm{d}\sigma/\mathrm{d}Q^2$ distribution (black dots). The six values of the upper part of the figure are those extracted by directly inverting the parametrisations of the theoretical predictions. The two values below the horizontal line are extracted from a χ^2 fit to the data of the parametrisations in the given regions. All α_s values are in agreement within the uncertainties.

5.4.3 $\alpha_s(M_Z)$ from the subjet multiplicity

For this analysis, the mean subjet multiplicity in the high-$E_{T,jet}$ ($E_{T,jet} > 25$ GeV) region and for $y_{cut} = 10^{-2}$ has been considered as the most reliable to determine the value of α_s. The main criteria was the size of the hadronisation correction, which suggests to avoid the region of low-$E_{T,jet}$ or very small y_{cut} values. In addition, the final region was selected such that a strong sensitivity to α_s was achieved.

To obtain the parametrisation of the α_s-dependence of the NLO QCD calculations, the five sets of the CTEQ4A-series [37] which assume different values of α_s have been used. The parametrisation mentioned above in Eq. (5.5) has been obtained for each measurement at $E_{T,jet} > 25$ GeV and for each data point a value of α_s has been determined.

Figure 5.15 shows the parametrisations for four regions in $E_{T,jet}$ and the way the measured values of $\langle n_{sbj} \rangle$ are translated into values of $\alpha_s(M_Z)$. At the same time, the statistical error of the measurement is propagated into the statistical contribution to the uncertainty on α_s. Figure 5.19 presents the five extracted values of $\alpha_s(M_Z)$. It should be emphasised the good agreement among the five determinations. The extracted values are completely independent from the experimental point of view. The systematic uncertainties shown in the figure are discussed below.

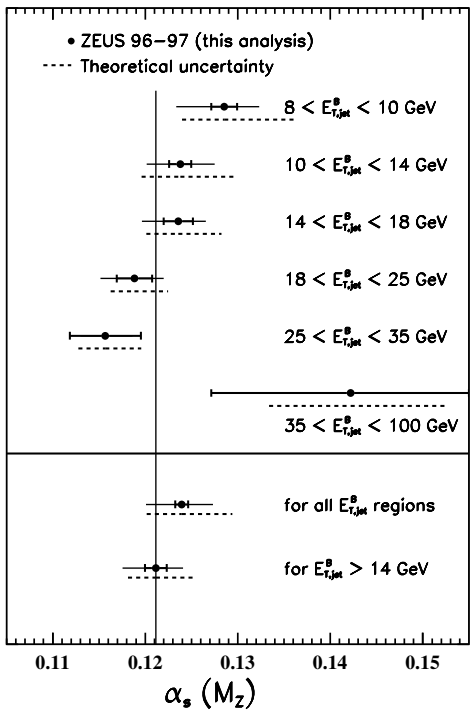

Figure 5.17: Values of the strong coupling contant extracted from the $\mathrm{d}\sigma/\mathrm{d}E^B_{T,jet}$ distribution (black dots). The six values of the upper part of the figure are those extracted by directly inverting the parametrisations of the theoretical predictions. The two values below the horizontal line are extracted from a χ^2 fit to the data of the parametrisations in the given regions. All the values are in agreement within the uncertainties.

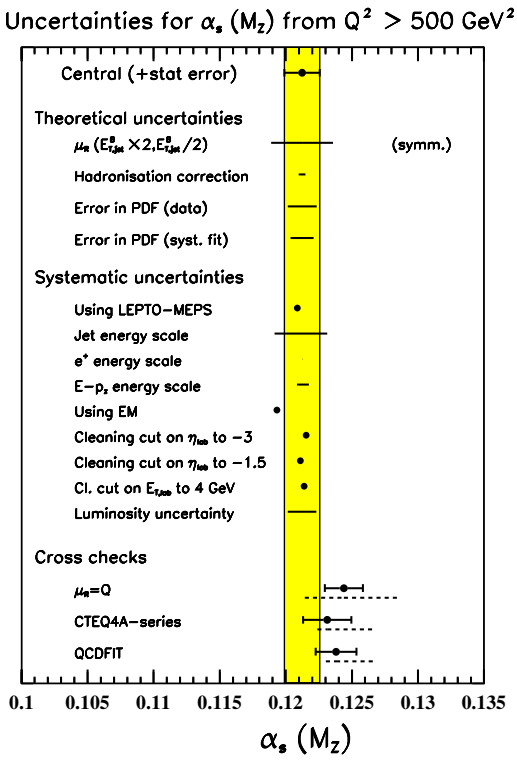

Figure 5.18: Schematic representation of the different contributions to the total uncertainty in the extracted value of $\alpha_s(M_Z)$ from the $\mathrm{d}\sigma/\mathrm{d}Q^2$ distribution for $Q^2 > 500$ GeV ^{2}. In this case the uncertainty due to the residual dependence on the renormalisation scale has been symmetrised. The values extracted with $\mu_R^2 = Q^2$ and other parametrisations of the proton PDFs are shown for comparison. In that case the error bars represent the statistical error in the data. The dashed lines below represent the uncertainties due to the variation of the renormalisation scale by a factor of two.

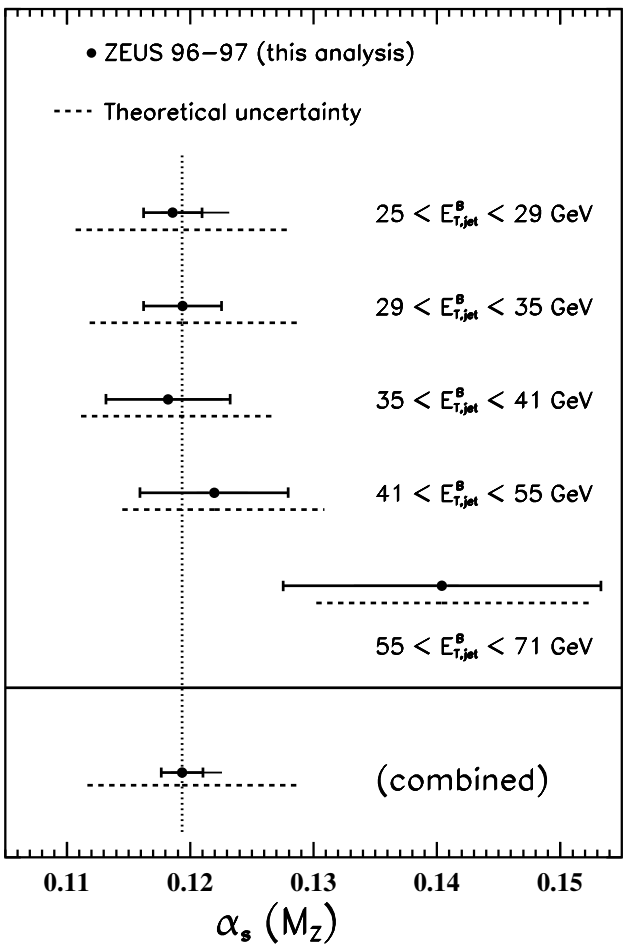

Figure 5.19: The $\alpha_s(M_Z)$ values determined from the QCD fit of the measured mean subjet multiplicity $\langle n_{sbj} \rangle$ at $y_{cut} = 10^{-2}$ in the different $E_{T,jet}$ regions (black dots). The combined value of $\alpha_s(M_Z)$ obtained by using all the $E_{T,jet}$ regions is shown (black dot at the bottom). The inner error bars represent the statistical error of the data. The outer error bars show the statistical and systematic uncertainties added in quadrature. The dashed line below each point shows the theoretical uncertainty.

To obtain a combined value, an additional χ^2 fit is performed to the five values considering only the statistical uncertainties. The error obtained from the fit is taken as the statistical uncertainty on the final value of α_s. This value, which is presented in figure 5.19 and used as a reference there, is

$$\alpha_s(M_Z) = 0.1194 \pm 0.0017\ (\text{stat})^{+0.0032}_{-0.0009}\ (\text{syst.})^{+0.0094}_{-0.0077}\ (\text{th.})\ .$$

The systematic and theoretical uncertainties on the different α_s values are obtained by repeating the entire procedure, but making the corresponding variation either in the measured value or the theoretical assumption.

All sources of systematic uncertainty considered for the measurements are propagated into α_s in this way. The most important contribution is the uncertainty on the use of LEPTO-MEPS instead of ARIADNE to correct the data for detector effects.

Regarding the theoretical uncertainty, all the sources described in section 5.3.2 have been taken into account. However, only the contributions due to the hadronisation correction and the

dependence with the renormalisation scale are considered in the final theoretical uncertainty. The reason is that other theoretical uncertainties are either negligible with respect to the two mentioned above or are considered as cross-checks and not as additional sources of uncertainty.

The theoretical uncertainties in the value of α_s are listed below:

- Variation of the renormalisation scale by a factor of 2:

$$\Delta\alpha_s(M_Z) = ^{+0.0091}_{-0.0072}$$

- The uncertainty on the modelling of the parton-to-hadron correction has been estimated by comparing the corrections with ARIADNE and LEPTO-MEPS and amounts to

$$\Delta\alpha_s(M_Z) = \pm 0.0027$$

- The whole procedure was repeated using the following sets of parton densities of MRST99: central, $\alpha_s\uparrow\uparrow$ and $\alpha_s\downarrow\downarrow$. The difference in the resulting $\alpha_s(M_Z)$ value is less than 0.3%. This uncertainty was neglected.

- All NLO QCD calculations were repeated using as renormalisation scale the $E_{T,jet}$ of each jet in the event. The difference of the resulting $\alpha_s(M_Z)$ with respect to the central value is less than 0.3%. It was not considered as an additional contribution to the theoretical uncertainty because this variation is already included in the uncertainty arising from the variation of $\mu_R = \sqrt{Q^2}$ by a factor of 2.

- Since the depencence of the extracted value of α_s on the gluon content of the proton, estimated by using the corresponding MRST99 sets (section 5.3.2) is very small, this uncertainty was not considered as an additional contribution to the theoretical uncertainty on α_s.

As for the values of α_s extracted for the inclusive jet cross sections, all the contributions to the theoretical uncertainty were added in quadrature to compute the total theoretical error on α_s. The same has been done for the systematic uncertainties.

All the uncertainties affecting the combined value of the strong coupling constant are shown in figure 5.20. Furthermore, the results of the cross checks (by using MRST99, $\mu_R = E_{T,jet}$ or $y_{cut} = 0.03$ or 0.005) are also shown for comparison. This figure shows that the uncertainty in the determination on the strong coupling constant is dominated by far but the uncertainty due to the missing higher orders in the perturbative series. The large residual dependence on the renormalisation scale clearly indicates that terms beyond NLO are needed to reduce the uncertainty in the determination of the strong coupling constant by means of the subjet multiplicity.

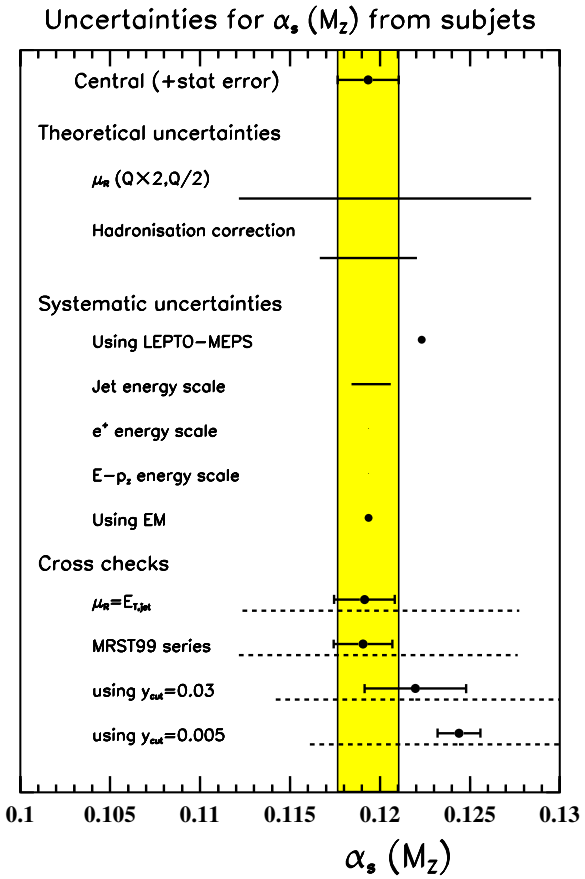

Figure 5.20: Schematic representation of the different contributions to the uncertainty in the extracted value for $\alpha_s(M_Z)$ from the subjet multiplicities for jets with $E_{T,jet} > 25$ GeV. The values extracted with $\mu_R = E_{T,jet}$, other parametrisations of the proton PDFs and the use of different resolution scales for the subjets are shown for comparison. In the latter cases the error bars represent the statistical errors in the data. The dashed lines below show the variations of the renormalisation scale by a factor of two.

Chapter 6

Summary and conclusions

This document presents the description and discussion of two different analyses related to the study of the strong interactions and the determination of the strong coupling constant. These analyses are: an analysis of jet production in the Breit frame and an analysis of the jet internal structure. Both analyses were performed using 38.6 pb^{-1} of data taken with the ZEUS detector at HERA.

The first of the analysis consisted of measuring the inclusive jet cross section in the Breit frame in neutral current deep inelastic positron-proton scattering at $Q^2 > 125$ GeV^2. This cross section was studied as a function of various jet variables in order to perform a wide comparison with the theory. The measurements were compared to NLO QCD predictions, which give a reasonable description of the data points for all the distributions under study. The differences observed, around 10%, are of the same order as the theoretical uncertainties.

In addition, the azimuthal distribution of jets in the Breit frame was measured. It was found that the azimuthal distribution is not uniform but peaks in the direction along and opposite to that of the scattered positron in that frame. The NLO QCD calculations show that the observed azimuthal asymmetry is compatible with that expected in the Standard Model. This is the first time this asymmetry has been observed by using hadronic jets.

The second analysis consisted of measuring the mean subjet multiplicity in an inclusive sample of jets produced in the laboratory frame in neutral current deep inelastic positron-proton scattering at $Q^2 > 125$ GeV^2. This observable has been studied as a function of the resolution scale y_{cut} as well as a function of the jet variables. The measurements have been compared with the next-to-leading order QCD predictions, which give a very good description of the measurements, especially when the hadronisation corrections are small enough, which is the case if the scale to resolve subjets and the transverse energy of the jets are large.

From the comparison between the NLO QCD calculations and the data in the two analyses, the value of the strong coupling constant was extracted by means of the dedicated QCD analyses.

Several determinations of $\alpha_s(M_Z)$ were performed in the analysis of the inclusive jet cross sections in the Breit frame. One of them, extracted from $\mathrm{d}\sigma/\mathrm{d}Q^2$ for $Q^2 > 500$ GeV^2, has very competitive uncertainties when compared to other determination of this constant:

$$\alpha_s(M_Z) = 0.1212 \pm 0.0013\ (\text{stat})^{+0.0023}_{-0.0031}\ (\text{syst.})^{+0.0027}_{-0.0027}\ (\text{th.})\ ,$$

where it should be emphasised the smallness of the theoretical uncertainty.

In the case of the analysis of the subjet multiplicities, the combined value of $\alpha_s(M_Z)$ has relatively large theoretical uncertainties, but it still represents a competitive determination:

$$\alpha_s(M_Z) = 0.1194 \pm 0.0017\ (\text{stat})^{+0.0032}_{-0.0009}\ (\text{syst.})^{+0.0094}_{-0.0077}\ (\text{th.})\ ,$$

It should be mentioned that this value was extracted in a different kind of analysis than those used previously at HERA.

The values of $\alpha_s(M_Z)$ obtained in the two analyses are in good agreement with the world average value and their uncertainties are competitive with the most precise determinations of this quantity around the world.

Appendix A

Some remarks on conventions

This appendix presents some of the conventions used in the thesis. Some additional remarks are given.

System of physical units

During this thesis, natural units, which are the standard ones in high-energy physics, are used. The velocity of light in vacuo, c and the reduced Planck's constant $\hbar$ are taken to be exactly one. The values of these quantities in the units of the International System are [119]:

$$c = 2.99792458 \cdot 10^{8}\ \mathrm{m/s}$$
$$\hbar = \frac{h}{2\pi} = 1.05457160 \cdot 10^{-34}\ \mathrm{J \cdot s}$$

Fixing these two constants to 1, the complete set of units is given by using the unit of energy. In the present case, the "GeV" is the most used due to the usual energy values present at HERA.

Dimensional analysis allows to reconstruct the correct dimension of the relevant quantities. The following list gives some examples and useful relations when transforming to more usual quantities.

$$1\ \mathrm{kg} = 10^{3}\ \mathrm{g} \qquad = 5.61 \cdot 10^{26}\ \mathrm{GeV}/c^{2}$$
$$1\ \mathrm{m} = 10^{2}\ \mathrm{cm} = 10^{-3}\ \mathrm{km} \qquad = 5.07 \cdot 10^{15}\ \hbar c\ \mathrm{GeV}^{-1}$$
$$1\ \mathrm{s} = \tfrac{1}{3600}\ \mathrm{h} = 10^{9}\ \mathrm{ns} \qquad = 1.52 \cdot 10^{24}\ \hbar\ \mathrm{GeV}^{-1}$$
$$1\ \mathrm{J} = \tfrac{1}{e}\ \mathrm{eV} = 0.624151 \cdot 10^{10}\ \mathrm{GeV}$$

Since in high-energy physics is very common the use of fractions of "barns" as units for cross sections, the relations of this unit with the corresponding ones in natural units and those of the International System are summarised here:

$$\begin{aligned} 10^{-2}\ \mathrm{barns} &= 10\ \mathrm{mb} = 10^{10}\ \mathrm{pb} \\ &= 1\ \mathrm{fm}^2 = 10^{-26}\ \mathrm{cm}^2 = 10^{-30}\ \mathrm{m}^2 \\ &= 25.705\ \mathrm{GeV}^{-2} \quad \text{in fact} \quad (\hbar c\ \mathrm{GeV}^{-1})^2 \end{aligned}$$

Finally, although in the whole description of the analysis the angles have been quoted in degrees, the units used in the expressions are radians. This is not important when the angular variable

is inside a trigonometric function, but in the analysis presented here is very important for the expressions used to calculate distances in the $\eta - \phi$ plane. The angular unit which should be used in combination with the adimensional pseudorapidity is the radian, and not the degree.

Laboratory and Breit frames

One of the analysis presented in the previous chapters has been performed in the laboratory frame. In this reference system the proton and the positron collide head-on with energies $E_p = 820$ GeV and $E_e = 27.5$ GeV, respectively. The other analysis was performed in the Breit frame, which was completely described in section 1.2.4. In this frame, the proton collides head-on with the exchanged boson, which is purely space-like with 3-momentum $\mathbf{q} = (0, 0, -Q)$.

Since the data, or the final states in simulated events, are known in the laboratory frame, it is necessary to make a boost into the Breit frame (see section 4.1.4). Furthermore, once the jet variables have been reconstructed in that frame, they are boosted back into the laboratory frame, since some cuts (at the detector level) are applied in this frame.

On the other hand, the final-state partons which are provided by the program DISENT (see section 5.1.2) have their four-momenta as seen in the Breit frame. For this reason, to obtain the NLO QCD predictions of $\langle n_{sbj} \rangle$ for jets in the laboratory frame, it is necesary to transform the four-momenta of the partons into the laboratory frame. This is very simple if the exchanged boson is known in the laboratory frame. Since the kinematic variables (for example, x and Q^2) are Lorentz-invariant, the reconstruction of this four-momentum is straightforward, and the components are

$$\begin{aligned} q_0 &= y \cdot (E_e - x\, E_p) \\ q_1 &= \sqrt{Q^2 \cdot (1-y)} \\ q_2 &= 0 \\ q_3 &= -y \cdot (E_e + x\, E_p) \ , \end{aligned}$$

where the second component is set to zero by convention. A rotation in the first two spatial components (here q_1 and q_2) does not modify the results.

With this four-momentum, the transformation from the laboratory to the Breit frame is performed by using the following relation for any four-momentum $p_{_L}$:

$$p_{_B} = \mathcal{L}_{lb}\, p_{_L} \ ,$$

whilst the transformation from the Breit to the laboratory frame is given by

$$p_{_L} = \mathcal{L}_{bl}\, p_{_B} = (\mathcal{L}_{lb})^{-1}\, p_{_B} \ .$$

The matrices needed for the transformations are the following 4x4 matrices,

$$\mathcal{L}_{lb} = \begin{bmatrix} \frac{q_0}{Q} + \frac{Q}{q_0 - q_3} & -\frac{q_1}{Q} & -\frac{q_2}{Q} & -\frac{q_3}{Q} - \frac{Q}{q_0 - q_3} \\ \frac{q_T}{q_0 - q_3} & -\frac{q_1}{q_T} & -\frac{q_2}{q_T} & -\frac{q_T}{q_0 - q_3} \\ 0 & \frac{q_2}{q_T} & -\frac{q_1}{q_T} & 0 \\ \frac{q_0}{Q} & -\frac{q_1}{Q} & -\frac{q_2}{Q} & -\frac{q_3}{Q} \end{bmatrix}$$

and

$$\mathcal{L}_{bl} = \begin{bmatrix} \frac{q_0}{Q} + \frac{Q}{q_0 - q_3} & -\frac{q_T}{q_0 - q_3} & 0 & -\frac{q_0}{Q} \\ \frac{q_1}{Q} & -\frac{q_1}{q_T} & \frac{q_2}{q_T} & -\frac{q_1}{Q} \\ \frac{q_2}{Q} & -\frac{q_2}{q_T} & -\frac{q_1}{q_T} & -\frac{q_2}{Q} \\ \frac{q_3}{Q} + \frac{Q}{q_0 - q_3} & -\frac{q_T}{q_0 - q_3} & 0 & -\frac{q_3}{Q} \end{bmatrix},$$

where the first row and column are those related to the time component, $Q = \sqrt{Q^2}$ and $q_T = \sqrt{{q_1}^2 + {q_2}^2}$. It is very simple to demonstrate that the second matrix is the inverse of the first one.

Thus, upon application of these matrices to the four-momenta of the particles (cells, hadrons or partons), the jets can be reconstructed in the frame we are interested in: the Breit frame in the first of the analyses described in this thesis and the laboratory frame in the second one.

Appendix B

Resumen en castellano

En éste apéndice se resumen en castellano los principales aspectos de la tesis. En él se cubren todos los aspectos tratados durante la parte en inglés pero únicamente en líneas muy generales con el propósito de dar una visión global de los análisis descritos en la tesis, así como situar el contexto tanto teórico como experimental.

En todo caso, debe indicarse que los capítulos precedentes contienen los detalles que aquí se omiten. No se considera necesario su inclusión en este resumen en castellano ya que suponemos que cualquier persona que tuviera necesidad de dichos detalles probablemente sea capaz de entender la versión en inglés, tal vez incluso mejor que el resumen en castellano de este apéndice.

Básicamente, durante el resumen se va a seguir la misma estructura que durante la tesis.

B.1 Introducción teórica

En esta sección se resume el capítulo dedicado a la introducción teórica. En concreto se da un breve resumen del Modelo Estándar y se destacan los aspectos de la teoría directamente relacionados con los análisis de la tesis.

B.1.1 El Modelo Estándar de las interacciones fundamentales

Actualmente, los resultados experimentales relacionados con nuestra comprensión de la Naturaleza a nivel sub-atómico son explicados teóricamente por el Modelo Estándar de las interacciones fundamentales. En el mismo, las interacciones entre las partículas elementales se describen en el contexto de la Teoría Cuántica de Campos, la cual surge a partir de la descripción relativista de procesos cuánticos.

El Modelo Estándar es sin duda el gran éxito científico dentro de la Física de la segunda mitad del siglo XX, al ser capaz de explicar las interacciones que observamos entre las partículas fundamentales. En esta teoría, las partículas interaccionan a través de tres clases de interacciones, la fuerte o de color, la electromágnetica y la débil. Esta descripción es el resultado a energías "bajas" (menores o del orden de 100 GeV) del comportamiento a energías grandes, donde la interacción electromagnética y la débil aparecen mezcladas y proviniendo de otras dos interacciones, una asociada al isospín débil y otra a la hipercarga débil de las partículas fundamentales.

En el Modelo Estándar, las tres interacciones son construidas a partir de simetrías existentes en la naturaleza. A partir de estas simetrías se definen números cuánticos que tienen asociados principios de conservación. El tratamiento de estos número cuánticos (las *cargas*) dentro de la Teoría Cuántica de Campos permite introducir las interacciones a partir de los siguientes principios:

- Las partículas con una carga no nula van a ser capaces de interaccionar a través de dicha interacción. Normalmente partimos de una serie de fermiones y posteriormente se añade la interacción a través de bosones, las propiedades de los cuales dependen principalmente del tipo de simetría asociada a la interacción.

- La interacción se describe a partir de acoplamientos de los bosones con los fermiones. Dependiendo del tipo de simetría los propios bosones pueden tener acoplamientos entre ellos mismos, como ocurre con los gluones.

- Los acoplos permiten entender los diferentes procesos que pueden ocurrir entre las partículas. Así, por ejemplo, la radiación de bosones por parte de fermiones, como ocurre cuando un electrón emite un fotón.

  Así mismo, los procesos de interacción entre las partículas cargadas se entienden como el intercambio de los bosones correspondientes. Por ejemplo, la fuerza de atracción o repulsión entre cargas eléctricas es descrita a través del intercambio de fotones.

De esta forma, el Modelo Estándar describe la naturaleza a nivel fundamental a través de una serie de fermiones, divididos en quarks y leptones, y las interacciones entre ellos, que dan origen a los bosones de gauge: los ocho gluones (para la interacción fuerte), los tres bosones W (para la interacción de isospín débil) y el bosón B (para la interacción de hipercarga débil). Estas son las únicas partículas necesarias para explicar satisfactoriamente la gran mayoría de los resultados experimentales.

A energías menores de 100-200 GeV, las simetrías asociadas a la hipercarga débil y la de isospín débil no son verdaderas simetrías, y ésa es la razón por la que dichas interacciones no se observan como tales. En su lugar aparece una interacción asociada a una simetría exacta y al principio de conservación de la carga eléctrica, que es la eletromagnética, y una interacción llamada débil y que no se asocia a ninguna simetría. En este límite de energías pequeñas, los bosones W y B aparecen modificados, y en su lugar se observan los bosones cargados $W^{\pm}$, el neutro Z° y el fotón.

Debido a que la interacción débil no está asociada a una simetría, el Modelo Estándar recurre a un mecanismo para eliminar las simetrías presentes a energías grandes. Este mecanismo, conocido como *rotura espontánea de simetría*, permite eliminar las simetrías además de proporcionar masa a los bosones débiles, tal como se observa experimentalemente. Este mecanismo, tal y como se introduce en el Modelo Estándar, requiere para ser válido la existencia de un nuevo bosón conocido como bosón de Higgs, que es la única partícula predicha por el Modelo Estándar que aún no ha sido observada experimentalmente.

La tabla 1.3 muestra un esquema de las propiedades de los diferentes bosones asociados a las interacciones. Debe notarse que a pesar de existir ocho gluones diferentes, en realidad, la diferencia es únicamente el valor de la carga de color, la cual resulta inobservable experimentalemte. Es por eso que es muy normal hablar como si sólamente hubiera un único tipo de gluón, aunque en los cálculos se tenga en cuenta los diferentes valores de dicha carga.

Una vez descrita la parte de las interacciones, pasamos a la denominada parte de materia del Modelo Estándar. En ella tenemos partículas muy diversas, todas de espín 1/2 y por lo tanto fermiones. Estos fermiones se agrupan en tres generaciones que son estructuralmente idénticas, siendo la única diferencia entre generaciones las masas de las partículas. Además, todas las generaciones están duplicadas, existiendo las correspondientes antipartículas, que se distribuyen de la misma manera.

La primera generación es la formada por las partículas más ligeras y contiene todos los componentes de la materia ordinaria, es decir los átomos. La estructura formal de esta generación es la siguiente:

$$\begin{pmatrix} \nu_e \\ e_L^- \end{pmatrix} , \; e_R^- , \; \begin{pmatrix} u_L \\ d_L \end{pmatrix} , \; u_R , \; d_R ,$$

siendo e el electrón, ν_e el neutrino asociado al electrón (que sólo tiene componente levógira), y u y d los quarks de la generación. Las partículas que se dan como vectores se agrupan de esta manera indicando la forma en que se acoplan con la interacción débil cargada, que relaciona la partícula superior y la inferior. Las partículas que no aparecen como vectores no sienten la interacción débil.

Por otra parte, la distinción entre leptones y quarks se introduce a partir de la interacción fuerte: los leptones no tienen carga de color y por lo tanto no se acoplan a través de dicha interacción. Además, los neutrinos, al ser eléctricamente neutros tampoco interaccionan electromagnéticamente.

La segunda generación es idéntica a la primera pero el muón (μ) toma el lugar del electrón, el neutrino muónico (ν_μ) el lugar del neutrino electrónico y los quarks c y s el lugar de los quarks u y d. Para la tercera generación, el tauón o leptón tau (τ) y su neutrino ocupan la parte leptónica y los quarks t y b la parte correspondiente a los quarks. No existe ningún indicio experimental de que exista alguna generación o partícula adicional en este sector.

La tabla 1.2 muestra las propiedades de los diferentes fermiones del modelo estándar. Debe notarse que, al igual que con los gluones, la carga de color de los quarks no se indica ya que es igual para todos y aunque puede tomar tres posibles valores, suelen ignorarse las diferencias entre quarks en este sentido al ser experimentalemente inobservable, aunque en los cálculos debe tenerse en cuenta que cada quark puede tener tres valores diferentes de esta carga.

Desde el punto de vista experimental, este esquema de partículas e interacciones no resulta suficiente debido a que en la práctica, no todas esas partículas se observan en los detectores. Así, mientras los leptones sí pueden ser observados como tales, o a través de sus productos de desintegración, disponiéndose de los dispositivos adecuados, los quarks no se observan como partículas libres, sino formando partículas más complejas llamadas hadrones.

Esta característica de los quarks se puede entender a partir de la interacción fuerte. Esta interacción se hace muy intensa con el aumento de la distancia, lo que impide la existencia de estados en el que haya cargas netas de color lo suficientemente separadas para ser observadas. Por otra parte, a distancias cortas la interacción es muy débil, lo que permite que los quarks y tal vez los gluones formen estados ligados que son los hadrones. Por razones obvias, la carga de color neta de estos hadrones tiene que ser cero, lo que únicamente se puede conseguir con tres cargas diferentes o con una carga y su anticarga. Esta propiedad, dicho sea de paso, es lo que le da el nombre de "color" que se usa en este contexto: con tres colores diferentes se puede lograr el color blanco. Aunque teóricamente se han predicho partículas compuestas por gluones, no hay evidencia experimental de su existencia.

Por lo tanto, los hadrones están formados o por un quark y un antiquark o por tres quarks o tres antiquarks. Debido a que la interacción fuerte es igual para todos los tipos de quarks, independientemente del sabor (es decir, que sea un u, un d o un t), todas las combinaciones serían posibles. Esto da origen a una gran variedad de hadrones, que son estudiados en lo que se llama espectroscopía de hadrones y cuyo estudio siempre ha proporcionado numerosos aportes al conocimiento de la interacción fuerte.

En la espectroscopía de hadrones, los mismos se dividen en dos grupos: bariones y mesones. Los mesones son los formados por un quark y un antiquark, mientras que los bariones están formados por tres quarks (y, cómo es lógico, los antibariones por tres antiquarks). El protón, por ejemplo, es el barión de menor masa y está formado por dos quarks u y un d. Esta forma de entender la estructura interna de los hadrones se suele denominar Modelo Quark, y fue introducido de forma independiente por Gell-mann y Zweig en 1964 [8, 9].

El Modelo Quark resulta muy conveniente para la espectroscopía pero no para estudios dinámicos de la interacción fuerte, para lo cual es necesario introducir la Cromodinámica Cuántica en donde se describe la interacción entre quarks y gluones. Añadiendo la presencia de los gluones, el Modelo Quark se transforma en el llamado Modelo Partónico de Quarks (QPM, de sus siglas en inglés) introducido a partir de las deducciones teóricas de Bjorken y Feynman [17, 18]. En este modelo los hadrones están formados por una serie de partones, de los cuales unos están cargados eléctricamente (quarks) y otros son neutros (gluones).

El siguiente paso es añadir las interacciones entre estos partones, las cuales permiten no sólo describir el comportamiento observado dentro de los propios hadrones (como las desviaciones con respecto al Modelo Partónico de Quarks) sino incluso procesos que involucran a los propios partones como partículas fundamentales, como la formación de hadrones como pruductos de una colisión. Los experimentos de las últimas décadas relacionados con estas interacciones han establecido que la Cromodinámica Cuántica es la teoría más conveniente para describir la interacción fuerte, a pesar de que actualmente no existe una manera conveniente de obtener predicciones para procesos de energías pequeñas debido a que la intensidad de la interacción es tan grande que no es posible realizar cálculos perturbativos.

El éxito del Modelo Estándar al explicar con una asombrosa precisión los resultados experimentales de las últimas dos décadas es un gran logro de la física de partículas en su objetivo por describir las interacciones fundamentales. Sin embargo, no se puede olvidar que este modelo aún tiene algunas dificultades, y sobre todo que la interacción gravitatoria no está aún incluida dentro de ese marco. En todo caso, los buenos resultados obtenidos con el Modelo Estándar permiten considerarlo como una teoría muy bien establecida, y experimentalmente es utilizada para medir los parámetros de la misma con cada vez mayor precisión, así como para continuar realizando pruebas que confirmen la validez de este modelo en regiones aún no estudiadas.

B.1.2 Procesos de dispersión profundamente inelástica

Uno de los experimentos más fructíferos para conocer la estructura interna de los hadrones es el estudio de la dispersión de leptones en procesos de colision con hadrones, normalmente protones o núcleos. Cuando las transferencias de momento en estas colisiones son muy grandes, tenemos un proceso de dispersión profundamente inelástica (DIS, de las siglas en inglés). En este caso, el hadrón pierde su identidad y los productos resultantes consisten en estados de diversas partículas cuyo estudio permite aumentar el conocimiento sobre la estructura del hadrón inicial.

De esta forma, un proceso de dispersión profundamente inelástica puede describirse como la reacción:

$$l(k) + h(p) \rightarrow l'(k') + X(p') \ ,$$

donde las partículas del estado inicial (el leptón l y el hadrón h) están fijadas por el experimento que se considere. Las partículas del estado final (el leptón l' y el llamado sistema hadrónico X) vienen dadas por los procesos que ocurren en la colisión. Debe notarse que X indica cualquier configuración de partículas.

En HERA las partículas iniciales son electrones (o positrones) y protones, por lo que a partir de ahora nos centraremos en este tipo de experimento, aunque hay que mencionar que la mayoría de las deducciones que se hagan pueden ser generalizadas para cualquier proceso similar.

Cuando un electrón es dispersado por un protón, podemos distinguir dos tipos generales de procesos dependiendo del tipo de bosón que es intercambiado en la interacción (véase la figura 1.3). Si esa partícula es eléctricamente neutra, el proceso se denomina *dispersión profundamente inelástica mediada por interacciones neutras*. Por otra parte, si está cargada, el proceso se dice que está *mediado por interacciones cargadas*. Para diferenciar entre los dos la única información necesaria es el tipo de leptón en el estado final. Si es del mismo tipo que el inicial, el proceso ha sido mediado por interacciones neutras. Si es mediado por una interacción cargada, la carga del leptón final e inicial deben ser diferentes y por lo tanto la naturaleza del leptón debe cambiar en la interacción; el electrón (positrón) se transforma en un neutrino (antineutrino) a través del intercambio de un bosón $W^{\pm}$.

Considerando las propiedades de la interacción en el contexto de la teoría cuántica de campos, la interacción entre un electrón o positrón con un protón viene dada a través de una parametrización de la estructura interna del protón. Esta parametrización se construye en términos de una serie de funciones que describen cómo el protón reacciona ante diversos procesos y que se denominan *funciones de estructura del protón*.

En 1968, Bjorken había predicho que estas funciones de estructura sólo dependerían de una variable adimensional en el límite de energías grandes, siempre que dicha variable adimensional, x se mantuviera finita. Esta propiedad de las funciones de estructura, que se puede caracterizar como

$$F_i(x, Q^2) \rightarrow F_i(x) \ \text{ for } Q^2 \rightarrow \infty, \tag{B.1}$$

es normalmente conocida como *invariancia con la escala de Bjorken* (o simplemente *escalado de Bjorken*) [17, 18].

Por otra parte, el aumento del valor del momento transferido (Q^2) lleva consigo un aumento de la capacidad de resolución de la estructura interna del protón: cuanto mayor es el momento transferido, más pequeña es la distancia que podemos resolver. Sin embargo, si el protón consiste de partículas puntuales, debería ser posible observar la invariancia con la escala escala de Bjorken incluso con Q^2 finito. Los resultados experimentales obtenidos en SLAC [19] demostraron que la idea de Bjorken era acertada, al observarse claramente la invariancia con la escala, como se muestra en la figura 1.4.

La interpretación del escalado de Bjorken resultaba entonces sencillo para un modelo teórico de la estructura interna del protón. Dicho modelo fue introducido por Feynman [20] y consiste en describir el protón como un conglomerado de partículas libres llamados partones. De esta manera la interacción del protón y el electrón se interpreta como la adición de las interacciones entre el electrón y los diferentes partones.

En este modelo la variable x de Bjorken se interpreta como la fracción de momento lineal del protón que corresponde al partón que participa en la interacción. Algunas predicciones de este modelo permiten identificar los partones de Feynman con los quarks de la espectroscopía de hadrones. En concreto, se comprobó que los partones que interaccionan con el electrón (normalmente a través de la interacción electromagnética) eran fermiones de espín 1/2 y con las cargas predichas en el modelo quark.

Por otra parte, si el protón consistiera únicamente de quarks, la suma de las fracciones de momento debería ser igual a 1, pero experimentalmente se encuentra que una fracción grande del momento corresponde a partones que no interactúan con el electrón. Estos partones neutros se denominan gluones y la evidencia directa de su existencia es la observación de formación de sucesos de tres jets de hadrones (ver la sección B.1.3) en procesos de aniquilación entre electrones y positrones.

La descripción de la estructura interna de los hadrones en términos de partones libres, en concreto quarks, se denomina usualmente el Modelo Partónico de Quarks. Este modelo da una descripción muy razonable a primer orden de la interacciones que ocurren en la dispersión profundamente inelástica. Sus principales inconvenientes son que no es capaz de explicar cómo los partones se mantienen juntos dentro de los hadrones ni tampoco el porqué los partones no se observan experimentalmente, sino que se produce rápidamente la formación de nuevos hadrones.

La necesidad de introducir una interacción que permita explicar estos comportamientos de los partones lleva a completar el Modelo Partónico con una interacción entre los quarks mediada por los gluones. Esta teoría es la Cromodinámica Cuántica (QCD de las siglas en inglés) que describe la estructura del protón como dada por los tres quarks del Modelo Quark ligados a través de la interacción fuerte (descrita por QCD). Estos quarks pueden radiar gluones que a su vez pueden excitar del vacío nuevos partones, como por ejemplo parejas quark-antiquark. De esta forma la estructura interna del protón resulta bastante complicada y en concreto actualmente no puede ser calculada teóricamente, aunque cálculos usando teoría de perturbaciones basados en QCD (lo que se conoce como *QCD pertubativa*) permiten predecir la evolución con la escala de energía de dicha estructura en términos de las densidades partónicas de los quarks y los gluones.

La principal propiedad de QCD que permite hacer cálculos perturbativativamente y obtener predicciones es que a cortas distancias la intensidad de la interacción se hace muy pequeña. Esta intensidad viene dada por la *constante de acoplamiento fuerte* (α_s), que a escalas de energías grandes se hace muy pequeña debido a las propiedades de la teoría. Esta característica de QCD se denomina *libertad asintótica*.

Por otra parte para energías pequeñas, asociadas a distancias grandes, la fuerza de la interacción se hace más fuerte. Este comportamiento, que se relaciona con el crecimiento del valor de α_s, permite justificar el porqué los quarks y los gluones no pueden ser observados en libertad: la fuerza de la interacción fuerte (también llamada de color) aumenta tanto con la distancia que las partículas con carga de color, es decir que sienten esta interacción, no pueden "escapar" y quedar en libertad. Esta propiedad de QCD se denomina *esclavitud infrarroja*. La idea asociada a esta propiedad es que dos partones que se separan sufren una interacción tan fuerte a ciertas distancias que es energéticamente favorable la generación de nuevos partones a partir del vacío. La creación de nuevos partones conduce finalmente a una reorganización de los mismos en estados ligados que no tienen carga neta de color y que son los hadrones observados experimentalmente.

Debe notarse que los partones que interaccionan pueden ser separados físicamente, aunque cada uno de ellos aparezca confinado dentro de un hadrón diferente. Los que no se observan como partículas libres son los partones con carga de color, aunque los partones en sí, igual que sus números cuánticos (excepto la carga de color), pueden ser estudiados experimentalmente.

B.1.3 Producción de jets de hadrones

Las características de QCD relacionadas con el confinamiento de las partículas que presentan carga neta de color impide la observación directa de quarks y gluones en los experimentos. En su lugar se produce la formación de conjuntos de hadrones que generalmente reciben el nombre de *sistema hadrónico*.

Cuando los partones producidos experimentalmente tienen una energía grande, los hadrones producidos a partir de ellos se detectan como chorros muy energéticos y colimados que reciben el nombre de *jets*. A partir de los hadrones es posible reconstruir las propiedades cinemáticas de los jets y de esta forma obtener información que está directamente relacionada con los partones originales producidos en la interacción. En la práctica, para hacer una comparación cuantitativa entre las medidas experimentales, realizadas con hadrones, y las predicciones teóricas, realizadas con partones, hay que profundizar en la definición de "jet" y utilizar un algoritmo que permita definir los jets de forma más cuantitativa.

En la actualidad, existen diversos tipos de algoritmos de jets, debiéndose indicar que los resultados experimentales dependen ligeramente de la definición usada. Por otra parte existe una serie de criterios que deben ser verificados por cualquier algoritmo para poder ser considerado como aceptable. Entre estos criterios, los principales son que debe ser capaz de definir los jets sin ambigüedad, debe ser aplicable tanto en los cálculos teóricos como en los estados finales medidos experimentalmente y debe evitar los problemas asociados a las divergencias infrarrojas (esto es, distancias grandes) que pudieran aparecer en la teoría tanto en los estados finales como iniciales. Debido a estas propiedades, los algoritmos utilizados en cada tipo de experimento pueden ser ligeramente diferentes.

En los análisis presentados en esta tesis se ha utilizado el algoritmo de jets conocido como *algoritmo de agrupamiento* k_T [42, 43] en su modo de invariancia longitudinal [45] que es el que resulta conveniente para procesos con hadrones en el estado inicial, como ocurre en HERA. La idea básica de este algoritmo es que las partículas se van emparejando utilizando un criterio de distancia. En cada iteración se emparejan las partículas que están más cercanas y el producto de su unión se utiliza en la siguiente iteración en vez de las dos partículas que se han unido. Por otra parte, si en una iteración una partícula está más cerca de lo que sería el hadrón inicial, esa partícula forma un protojet y no se vuelve a considerar. Cuando el proceso iterativo ha finalizado, se seleccionan los jets entre los protojets imponiendo un corte en la energía transversal con respecto a la dirección del hadrón inicial.

Debe notarse que en este contexto las *partículas* sobre las que se aplica el algoritmo pueden ser hadrones, partones o cualquier forma de reconstruir experimentalemente el estado hadrónico final, como por ejemplo las celdas del calorímetro.

La utilización de este algoritmo en los análisis está justificado porque se ha demostrado que es el más conveniente para el tipo de estudios realizados en esta tesis. En concreto, se ha comprobado que el uso de algoritmos de agrupamiento reduce las correcciones hadrónicas además de permitir explotar el uso de diversas escalas de resolución al definir los jets, lo que permite una

generalización directa al concepto de subjet (ver la sección siguiente) y un estudio "natural" de la estructura interna de los jets.

Respecto al análisis de producción de jets en el sistema de referencia de Breit, se ha demostrado que el uso del algoritmo de agrupamiento k_T presenta ventajas desde el punto de vista teórico [47]. Este sistema de referencia se define como aquél en el que los procesos de dispersión profundamente inelástica son interpretados como una colisión frontal del protón con el bosón virtual intercambiado a lo largo del eje z. Además, no existe transferencia de energía entre el positrón y el protón, es decir, el bosón intercambiado no tiene energía, aunque sí momento lineal.

Debido a esta característica del sistema de referencia de Breit, la producción de jets con energía transversal grande respecto a la dirección del bosón y protón que colisionan (el eje z) no se puede producir en el Modelo Partónico de Quarks, donde el quark que interacciona con el bosón simplemente "rebota" contra el bosón sin abandonar el eje z donde estaba inicialmente. En cambio, si se produce un proceso con radiación de QCD, entonces los partones del estado final pueden generar jets con energías transversales grandes. Esto significa que la descripción teórica para la producción de jets en el sistema de referencia de Breit está dada principalmente por procesos de QCD. Esta es la razón por la que en esta tesis se estudia la producción de jets en el sistema de referencia de Breit: la comparación con las predicciones teóricas permite la realización de pruebas de la validez de QCD para describir la interacción fuerte.

Una de estas pruebas, realizada por primera vez en el análisis presentado en esta tesis, es la medida de la distribución azimutal de los jets producidos en el sistema de referencia de Breit. En QCD se predice que esta distribución no es uniforme y que según los tipos de procesos que puedan ocurrir se tienen distribuciones diferentes, como se muestra en la figura 1.13. En el caso de medirse la distribución inclusiva, sin distinguir el tipo de partón inicial, tenemos que en QCD se predice una distribución para la sección eficaz dada a primer orden por:

$$\frac{\mathrm{d}\sigma}{\mathrm{d}\phi^B_{jet}} = A + C\ \cos 2\phi^B_{jet}\ . \tag{B.2}$$

que es una predicción muy concreta y dominada por el primer orden. Por lo tanto la medida de esta sección eficaz proporciona una prueba muy exigente de la validez del Modelo Estándar, concretamente de QCD.

B.1.4 La estructura interna de los jets

La estructura interna de los chorros de hadrones, que en el contexto de QCD perturbativa se atribuye a la emisión de partones adicionales, es una propiedad que está determinada principalmente por la estructura de dicha radiación en el proceso considerado. Además, el estudio de la estructura interna de los jets proporciona información relacionada con los procesos que ocurren en la transición de los partones obtenidos como productos finales de una colisión y los hadrones que se observan en los detectores. De esta manera, la comparación con las predicciones teóricas es una prueba rigurosa para la validez de QCD perturbativa.

La manera más tradicional de estudiar la estructura interna de los jets de hadrons consiste en medir la distribución de energía (o de energía transversal) alrededor de la dirección marcada por el eje del jet. El observable utilizado se denomina la *forma del jet* (del inglés "jet shape"), que se relaciona con la cantidad relativa de energía transversal alrededor del eje del jet. Cerca

de este eje, en el núcleo del jet, la forma está determinada principalmente por la emisión de gluones colineales al partón emisor, lo cual puede ser calculado perturbativamente.

Sin embargo, los algoritmos de agrupamiento como el k_T sugieren de manera natural una alternativa a esta manera de estudiar la estructura interna de los jets, que está más relacionada con la imagen intuitiva de cómo surge dicha estructura. Dentro de cada jet se resuelven objetos más pequeños pero formalmente idénticos a los jets y que se denominan *subjets*. La descripción de la estructura interna dentro de este contexto vendría dada por la asociación de los subjets a los partones radiados en el interior del jet por parte del partón inicial.

El observable utilizado en este caso se denomina *multiplicidad de subjets* y se define como el número de subjets existente dentro de un jet. Para poder resolver los subjets es necesario fijar una escala de resolución, caracterizada por un número entre 0 y 1, de forma que cuando es muy pequeña es posible encontrar muchos subjets, y cuando se aproxima a 1, no se resuelve la estructura interna del jet sino el jet en su totalidad

Normalmente, la estructura interna de los jets se estudian con métodos estadísticos, considerándose valores promedios referidos a un conjunto de jets con unas propiedades dadas. En el caso de utilizarse los subjets, se define la *multiplicidad media de subjets* como el valor medio de subjets en el conjunto de jets considerado para una escala de resolución (y_{cut}) dada:

$$\langle n_{sbj} \rangle (y_{cut}) = \frac{1}{N_{jets}} \sum_{jets} n_{sbj}^{jet}(y_{cut}) \ .$$

Ésta es precisamente la cantidad que se ha estudiado en el segundo análisis de esta tesis.

En QCD perturbativa, el valor medio del número de hadrones contenidos en un jet viene determinado de manera esencial por el tipo de partón que dió origen a dicho jet. En concreto, se predice que la multiplicidad promedio de cualquier tipo de objetos dentro de un jet (como podrían ser los subjets) es mayor para jets iniciados por gluones que en aquéllos iniciados por quarks. La razón es que la intensidad de la interacción entre gluones es mayor que la correspondiente a la interacción entre quarks y gluones. Esta predicción ha sido verificada experimentalmente de forma cualitativa en experimentos de aniquilación de electrones y positrones.

B.1.5 Medida de la constante de acoplamiento fuerte

Debido a que tanto la producción de jets de hadrones en el sistema de referencia de Breit como el análisis de la estructura interna de los jets producidos en el laboratorio están relacionados con procesos gobernados por la interacción fuerte, su estudio permite la realización de pruebas de la validez de QCD para describir dicha interacción.

Además, debido a que las predicciones de QCD perturbativa para los observables asociados a dichos estudios son muy sensibles al valor de la constante de acoplamiento fuerte α_s, es posible utilizar la comparación de las medidas experimentales con la teoría para realizar una medida del valor de esta constante de acoplamiento.

La realización de esta medida sólo puede hacerse de manera consistente cuando las predicciones teóricas de los observables que medimos se conocen al menos hasta segundo orden en el desarrollo perturbativo en α_s.

En el primero de los análisis que se incluyen en esta tesis, la medida de las secciones eficaces de producción de jets de hadrones en el sistema de referencia de Breit, las predicciones teóricas

que necesitamos están disponibles, y por lo tanto es posible realizar la medida de α_s a partir de estas secciones eficaces.

En el caso de la multiplicidad de subjets, debe notarse que la obtención de una comparación razonable con las predicciones de QCD perturbativa sólo se puede realizar en los puntos experimentalmente medidos en los cuales las energías relacionadas con el proceso de formación de subjets no sean demasiado pequeñas, de forma que los subjets se relacionen con procesos duros de QCD, que son los que podemos describir perturbativamente.

Esta característica impone la limitación de que la medida de α_s no se puede realizar para escalas de resolución de subjets o energías transversales de los jets demasiado pequeñas.

Respecto a las predicciones teóricas, debe mencionarse que actualmente se conocen todos los términos que nos hacen falta para calcular las predicciones de la multiplicidad media de subjets a segundo orden en α_s. Este punto es cierto únicamente para describir la estructura interna de los jets producidos en el sistema de referencia del laboratorio y no, por ejemplo, para los producidos en el de Breit.

De esta forma, los dos análisis presentados en esta tesis posibilitan la realización de medidas de α_s de una manera totalmente consistente.

B.2 Dispositivo experimental

Los resultados experimentales descritos en esta tesis han sido obtenidos con el análisis de los datos tomados con el detector ZEUS, con el que se estudian los productos de las colisiones de positrones (o electrones) y protones acelerados en HERA, situado en el centro de investigación DESY (Deutsches Electronen-Synchrotron), sito en Hamburgo (Alemania).

B.2.1 El acelerador HERA

HERA [54] es el primer acelerador del mundo donde se aceleran simúltaneamente electrones (o positrones) y protones antes de hacerlos colisionar. Está construido bajo tierra en un túnel cuya longitud es de 6.3 Km. Está formado por cuatro arcos circulares y cuatro segmentos (ver figura 2.1) donde están situados los cuatro experimentos que utilizan los haces de partículas acelerados en HERA.

Otra de las particularidades de HERA que lo distinguen de anteriores aceleradores de partículas, es que las energías de los haces de partículas no son simétricas. En concreto, HERA se diseñó para acelerar electrones (o positrones) y protones hasta unas energías de 30 GeV y 820 GeV respectivamente, lo que supone una energía total disponible en cada colisión de 300 GeV aproximadamente. Para alcanzar tales energías existe un sistema de pre-aceleradores, mostrados en la figura 2.2. Después de esas etapas, los electrones se inyectan en HERA con una energía de 14 GeV y los protones con 40 GeV, siendo en éste acelerador donde se alcanzan las energías finales a las que se producen las colisiones.

Tal y como se muestra en la figura 2.3, los protones y los electrones están agrupados en paquetes que se cruzan en los diferentes puntos de interacción para producir las colisiones, habiendo un cruce cada 96 ns. Por otra parte, algunas de las posiciones asociadas a los paquetes se dejan vacías para permitir una estimación de posibles "sucesos" observados en los detectores, pero

cuyo origen no es una colisión entre las partículas del acelerador. Estos "sucesos" pueden estar producidos por rayos cósmicos (muones) o por interacciones de las partículas aceleradas con las moléculas del gas residual presente dentro del tubo "de vacío" que contiene los haces de partículas.

Además de las energías de las partículas, otra cantidad importante para caracterizar el funcionamiento de un acelerador es **la luminosidad**. Esta cantidad indica la cantidad de colisiones que ocurren. En concreto, dada la luminosidad (L) y la sección eficaz de un proceso concreto (σ), el número de sucesos obtenidos con el acelerador está dado por

$$N = L \cdot \sigma \ . \tag{B.3}$$

La luminosidad que un acelerador es capaz de proporcionar depende de sus características. Por otra parte, desde el punto de vista del análisis de los datos, la cantidad que resulta de interés es la luminosidad integrada durante un periodo de tiempo dado, que es el asociado a los datos utilizados.

La figura 2.4 muestra la luminosidad integrada proporcionada por HERA en diferentes periodos de tiempo. La separación en tres grandes grupos se asocia a diferentes tipos de partículas (electrones o positrones) y diferentes energías del haz de protones, ya que desde 1998 dicha energía es de 920 GeV, lo que supone un aumento del 5% en la energía total disponible.

Durante los años en que se tomaron los datos utilizados en los análisis descritos en esta tesis, 1996 y 1997, HERA proporcionó colisiones entre positrones y protones. Por esta razón, en lo sucesivo únicamente consideraremos el caso de positrones, aunque muchos de los comentarios se podrían aplicar para el caso de electrones.

B.2.2 Descripción del detector ZEUS

ZEUS es uno de los cuatro experimentos realizados en el acelerador HERA. En el mismo se estudian los productos finales de las colisiones de los positrones y protones de HERA. El experimento consiste en un detector de propósito múltiple situado en una de las zonas de interacción de HERA (ver figura 2.1). Ha sido construído y es utilizado y mantenido por una colaboración internacional formada por 50 institutos pertenecientes a 12 países (entre los cuales se encuentran U.S.A., Canadá, Alemania, Japón y España). El número total de físicos que forman la colaboración es de unos 450. España está representada por el Grupo de Altas Energías de la Universidad Autónoma de Madrid.

Las figuras 2.5 y 2.6 muestran unos diagramas esquemáticos de la estructura del detector. En la primera, se presenta el detector visto a lo largo del movimiento de las partícualas aceleradas en HERA. En la segunda, se muestra una sección transversal. En este caso las partículas aceleradas se moverían en la dirección perpendicular a la figura.

Desde la parte más interna (el punto de interacción) hacia fuera, la estructura de ZEUS [55] es la siguiente:

- En la zona interior están situados los detectores de trazas que permiten medir las trayectorias y momentos lineales de las partículas cargadas. El sistema de detectores se divide en las cámaras central (CTD), delantera (FTD) y trasera (RTD) de trazas.

  De estas diversas componentes, únicamente la cámara central de trazas es utilizada en los análisis descritos en esta tesis. Este detector [56] es una cámara de hilos cilíndrica con

un radio interior de 16.2 cm y otro exterior de 85 cm. Su longitud es de 241 cm. Está situada a la largo del tubo de vacío correspondiente a los haces de HERA. La cámara está llena de un gas que es ionizado con el movimiento de las partículas cargadas. Los electrones libres obtenidos en este proceso de ionización son atraídos por los hilos de la cámara (ánodos) y así se genera una señal eléctrica asociada al paso de las partículas. Debe notarse que el movimiento de los propios electrones hacia los ánodos induce nuevas ionizaciones, generándose un fenómeno de avalancha que amplifica la señal.

Los sensores situados en los ánodos permiten detectar en cada punto el paso de partículas cargadas. Posteriormente, las señales medidas en diferentes puntos permiten reconstruir las trayectorias de dichas partículas que dan información muy variada sobre el suceso. En concreto, la proyección de las trayectorias de las partículas hacia la zona de interacción permite obtener con mucha precisión la posición del punto (vértice) donde se produjo la colisión del positrón y el protón. Si las partículas medidas no provienen de una colisión de este tipo, las trayectorias reconstruidas permiten muchas veces identificar el suceso, y rechazarlo en el momento de realizar el análisis.

- Las cámaras de trazas están rodeadas por un solenoide que genera un campo magnético a lo largo de la dirección de las partículas de HERA. Este campo magnético curva las trayectorias de las partículas cargadas y por ende las trazas que se miden con los detectores mencionados anteriormente. Dicha curvatura resulta fundamental para medir el momento lineal asociado a las partículas cargadas.

- Englobando a todas las componentes anteriores, está situado el calorímetro [73] de uranio (UCAL), que es la principal componente de ZEUS. Está dividido en tres partes, tal como se muestra en la figura 2.8. La parte central (BCAL) tiene forma cilíndrica. En las zonas delantera y trasera están situadas las otras dos partes (FCAL y RCAL), que tienen una forma aproximadamente cuadrada y actúan de tapas del cilindro. En las partes delantera y trasera existen sendos huecos para dejar paso a las partículas de HERA. Debido a estos huecos, el calorímetro no tiene una cobertura del 100% (4π) en ángulo sólido, sino del 99.7%. En la próxima sección se dan más detalles sobre la estructura del calorímetro y su uso en el análisis de los sucesos.

- Detrás del calorímetro están situadas las componentes exteriores. Debido a que el calorímetro principal es capaz de absorber totalmente la energía de casi todas las partículas, las componentes exteriores están orientadas hacia propósitos más concretos. Por ejemplo, la detección de muones, que debido a sus propiedades son capaces de atravesar el calorímetro. Es por eso que de las componentes exteriores las más importantes son las cámaras de detección de muones divididas en tres partes, al igual que el calorímetro. Cada una de esas partes se divide en dos, una interior y otra exterior. Entre las partes interior y exterior está situado un calorímetro auxiliar (BAC) de baja resolución.

- Las cámaras de muones permiten detectar trazas de partículas cargadas y medir su momento y posición. Las trazas pueden ser asociadas con trayectorias reconstruidas en las cámaras centrales de trazas y detectar de esta forma la producción de muones en la interacción. Debe notarse que la únicas partículas cargadas de la interacción que pueden ser detectadas en las cámaras de muones son los muones, debido a que son las únicas que son capaces de atravesar el calorímetro conservando su naturaleza y la mayor parte de su energía.

- El calorímetro auxiliar tiene dos misiones. La primera es medir la energía no absorbida por el calorímetro principal, lo cual puede ocurrir en sucesos en los que hay una gran cantidad de energía en el estado final. Para absorver esta energía se utiliza hierro, que puede ser magnetizado y así servir de blindaje magnético del campo generado por el solenoide mencionado anteriormente. Ésta es la segunda misión de esta parte del detector, servir de retorno de las líneas de campo magnético generado en el interior del detector, actuando como "yugo" (yoke) de las componentes interiores.

- Una componente fundamental del detector es la dedicada a la medida de la luminosidad. Esta medida resulta fundamental para la realización de medidas de secciones eficaces, ya que es la cantidad que necesitamos para, una vez contado el número de sucesos de cierto tipo, convertir ese número en una sección eficaz, que es la cantidad predicha por la teoría.

  La forma más simple de medir la luminosidad es seleccionar un tipo de proceso que tenga una sección eficaz muy grande para obtener gran cantidad de sucesos en poco tiempo, lo que aumenta la precisión de la medida. También se necesita que sea un proceso cuya sección eficaz sea bien conocida, para poder extraer sin error la luminosidad tras contar el número de sucesos que ocurren.

  En HERA, el proceso elegido para medir la luminosidad es el de radiación de frenado descrito por

  $$e \, + \, p \, \rightarrow \, e' \, + \gamma \, + \, p \, ,$$

  debido a que cumple las propiedades anteriormente mencionadas y además es fácil de identificar experimentalmente.

  En ZEUS, el monitor [77] de luminosidad (LUMI) es utilizado para detectar el positrón y el fotón, que salen a través del tubo de vacío. El positrón es desviado por el campo magnético de HERA y detectado a unos 35 m. del punto de interacción. El fotón es detectado a 107 m. de distancia del punto de interacción. La detección en coincidencia de las dos partículas y la condición de que las energías de las mismas sumen la correspondiente al haz de positrones permite el contaje de sucesos de radiación de frenado producidos.

  Tras corregir ese número por efectos de aceptancia y de posibles sucesos cuyo origen no es una colisión del positrón con un protón de HERA, se obtiene el valor de la luminosidad a través del valor de la sección eficaz, del proceso considerado, obtenida con la fórmula de Bethe-Heitler [75].

- Aparte de las descritas, ZEUS contiene otras componentes que no serán mencionadas debido a que su propósito es muy específico y no han sido utilizadas en los análisis, salvo en algunos casos en los que la información proporcionada por estas partes del detector permiten eliminar la presencia de sucesos no relacionados con interacciones de los positrones y protones de HERA, o al menos no relacionadas con los sucesos en los que estamos interesados.

Además de estas componentes "visibles", ZEUS dispone de un sistema de selección de sucesos automático que permite discriminar los sucesos de interés para el análisis de los que no son interesantes, principalmente los que se relacionan a sucesos producidos por otras interacciones, como muones cósmicos atravesando el detector o interacciones con el gas residual existente en las trayectorias de los haces de HERA. Este sistema debe ser capaz de decidir si cada vez que se produce un cruce ha habido una colisión. Debido a la frecuencia de HERA, la frecuencia de cruces/sucesos a considerar es de 10 MHz. ZEUS usa un sistema de decisión ("trigger") en tres

niveles [79] para reducir dicha frecuencia a 5 Hz (ver figura 2.11), lo que permite almacenar la información proporcionada por el detector sobre los sucesos de interés y su posterior análisis.

B.2.3 El calorímetro central de ZEUS

Los procesos que ocurren cuando las partículas atraviesan un medio material son la clave que permite la detección de las mismas. Estos procesos dependen de la naturaleza de la partícula, de su energía y del material que atraviesa.

Un calorímetro es un dispositivo experimental que permite medir la energía de las partículas aprovechando que las interacciones que la partícula sufre permite absorber su energía y transformarla, normalmente de manera parcial, en una señal detectable. En la práctica, la absorción de la energía se realiza utilizando materiales muy densos (plomo, uranio,...) con objeto de absorber grandes candidades de energía en un espacio reducido. Por otra parte, esos materiales no son convenientes a la hora de convertir la energía absorbida en señales.

Por esta razón es muy común el empleo de lo que se denomina *calorímetros de muestreo* en los que se alternan capas de material "absorbente" y capas de un material centelleador que permite detectar parte de las partículas que lo atraviesan y medir su energía. Debe notarse que en este tipo de dispositivo, la señal medida no proviene de la conversión de la energía de la partícula incidente, sino de un muestreo estadístico del proceso de absorción. Debido a ello, la señal medida es una variable estadística cuyo valor medio es proporcional a la energía de la partícula incidente. Esto permite conocer el valor de dicha energía (E) y además con un resolución relativa según la ley $1/\sqrt{E}$, es decir que la resolución es mejor cuanto mayor es la energía medida.

Los diferentes procesos que una partícula puede sufrir en un material y sobre todo su intensidad dependen de las características de la misma. Así, las partículas de tipo electromagnético (fotones, electrones y positrones) generan una cascada que está mucho más localizada que la generada por hadrones. Por su parte, los muones muy energéticos son capaces de atravesar un calorímetro perdiendo sólamente una pequeña fracción de su energía. Es por eso que en ZEUS su detección se realiza con cámaras especializadas situadas más exteriormente que el calorímetro principal.

El calorímetro principal de ZEUS es un calorímetro de muestreo compensado[1] de gran resolución formado por placas alternas de uranio empobrecido y de material centelleador plástico. Los fotones generados por el material centelleador en la fase de detección se transmiten a través de un sistema de guías de onda a los fotomultiplicadores, que a partir de los fotones generan señales eléctricas que son registradas por el sistema de lectura de señales para su procesamiento.

El calorímetro consiste en tres partes: la parte central, que tiene forma de barril situado a lo largo de la dirección que llevan las partículas en HERA; y dos partes con forma cuadrada perpendiculares a dicha dirección y que sirven como bases o tapas del barril. Las tres partes tienen una estructura similar. Están divididas longitudinalmente en una parte electromágnetica y otra hadrónica. Las dos son formalmente idénticas, aunque las señales generadas se leen separadamente. Los nombres que reciben proceden de su propósito: la parte electrómagnetica,

[1] Un calorímetro compensado es aquél que reacciona igual ante partículas electromagnéticas o hadrones. Es decir, que proporciona en promedio una señal de igual valor para una partícula electromagnética que para un hadrón con la misma energía.

que es más interna, es capaz de absorber toda la cascada generada por una partícula electromagnética, mientras que la generada por un hadrón depositará energía parcialmente en la parte hadrónica (externa).

La lectura de las señales se realiza separadamente para cada estructura con forma de paralelepípedo llamada celda. Cada celda está formada por una parte del material que forma el calorímetro y la energía depositada en la misma es procesada por dos fotomultiplicadores, cada uno de ellos asociado a la medida de la señal en caras opuestas de la celda. La estructura de celdas es ligeramente diferente para cada parte del calorímetro, aunque globalmente es la siguiente:

- Cada parte está subdividida en *módulos*, siendo su ancho de 20 cm. En la tapas los 23 módulos se localizan como estructuras verticales, mientras en la parte central los 32 módulos se sitúan paralelos al eje z.

- Cada uno de los módulos se divide en un número dado de *torres* de 20 cm de altura. El número de torres en cada módulo depende de su posición. En el caso de la parte central, cada módulo tiene 14 torres.

- Una torre se subdivide longitudinalmente en dos partes, que son la electromagnética y la hadrónica. En el caso de la tapa trasera, la parte hadrónica no presenta más subdivisiones mientras que la electromágnetica se divide transversalmente en dos celdas de 10 cm. de altura, y así se tienen tres celdas por torre. En las partes central y delantera, la parte hadrónica se divide longitudinalmente en dos celdas de 20x20 cm^2, mientras que la electromagnética se divide transversalmente en 4 celdas de 5 cm. de altura, teniéndose por lo tanto 6 celdas por torre[2].

Debe notarse que el menor tamaño de las celdas en la parte electromagnética permite obtener una mejor resolución, en concreto al reconstruir la posición de las partículas electromagnéticas, como es el caso del positrón dispersado en procesos de interacciones neutras.

Debido a la velocidad de procesado de las señales medidas en el calorímetro, es posible distinguir perfectamente las señales provenientes de cruces consecutivos de los haces de HERA. En la práctica, dicha velocidad es tan grande que es posible usar el calorímetro para medir de forma precisa el tiempo en el que se detectó la señal en cada celda. La resolución de este tiempo es del orden de 1 ns. La medida de este tiempo resulta muy útil, especialmente a la hora de eliminar sucesos producidos por procesos diferentes del de una colisión entre partículas de HERA.

B.3 Simulación de procesos y cálculos teóricos

Debido a la complejidad de los detectores de partículas actuales, resulta muy complejo entender el efecto que tienen los dispositivos de medida sobre los sistemas de partículas que se desean estudiar. Es por eso que para cuantificar dichos efectos y corregir los resultados en la medida de lo posible es muy común el uso de simulaciones.

[2]Hay excepciones de esta estructura general para ciertas posiciones especiales, como el borde de la parte con forma de barril o la zona de las tapas que solapa con la parte central, pero las diferencias son meramente estructurales.

La base de este estudio es tener una simulación del detector lo más precisa posible. Dicha simulación permite comprender el efecto del detector sobre unos estados finales que son conocidos y que deben ser construidos a partir de las predicciones teóricas. Por razones de eficiencia, la construcción de estos estados finales se realiza utilizando técnicas de integración de Monte Carlo. Es decir, se generan de forma aleatoria sucesos similares a los que se esperan en las colisiones reales, dentro de la teoría considerada. Posteriormente se observa el efecto del detector sobre estos sucesos. Si la presencia de cada tipo de suceso está dada en una proporción similar a la que se predice en la teoría y se espera en los datos, entonces si la teoría es "correcta" y la simulación del detector razonable, los sucesos observados en la realidad y los simulados darán resultados similares, lo que permite corregir los mismos usando la información proporcionada por los sucesos simulados, debido a que en éstos conocemos el resultado que obtendríamos sin los efectos introducidos por el detector.

Debe notarse que la obtención de sistemas de partículas que sean similares a los observados en el detector conlleva necesariamente el uso de modelos fenomenológicos para simular ciertos aspectos de la teoría que no son calculables en la actualidad. En concreto, la generación de sucesos requiere la simulación de la radiación de partones y la posterior conversión de dichos partones en hadrones, proceso denominado *hadronización* o *fragmentación*.

La radiación de partones tiene como objetivo técnico la introducción de órdenes superiores del desarrollo perturbativo que o bien no han sido aún calculados, o bien su complejidad impide su implementación práctica en programas de generación de sucesos.

La hadronización es un proceso genuinamente no perturbativo y por lo tanto debe ser calculado de forma fenomenológica. Su objetivo es transformar los estados de partones en estados de hadrones, ya que para comparar con las medidas experimentales se necesitan predicciones a nivel hadrónico. Por otra parte, el proceso de hadronización permite la generación de sucesos simulados para ser utilizados en el estudio de la respuesta del detector a los estados finales de interés.

En la actualidad, existen diversos programas de generación de sucesos simulados, aunque la mayoría se basan en un reducido número de modelos de simulación de la radiación de partones y de la hadronización. En las siguientes secciones se da una breve descripción de estos modelos y la manera en que han sido utilizados en los análisis.

B.3.1 Modelos de simulación de la radiación de partones

El primer paso en la generación de sucesos es la simulación de la radiación de partones. Su objetivo es tener una aproximación a los cálculos de orden superiores en el desarrollo perturbativo y que aún no han sido calculados. Esto es posible a partir de modelos fenomenológicos que de esta forma permiten obtener estados de un número de partones que no está fijado por el número de términos del desarrollo perturbativo que hayan sido calculados.

En los programas de generación empleados en los análisis de esta tesis, disponemos de dos modelos diferentes para simular la radiación de partones: el Modelo de Cascadas Partónicas [86], basado en los procesos de radiación en los órdenes más inferiores en QCD perturbativa, y el Modelo de Dipolos de Color [87], en el que los partones son radiados a partir de los campos de color generados por dipolos, lo cuales se definen a partir de los partones existentes en la etapa previa.

Estos dos modelos generan la radiación de partones a partir de procesos sucesivos de radiación de partones. Ambos son capaces de describir las medidas realizadas sobre los estados hadrónicos finales en aniquilaciones entre electrones y positrones, aunque en dispersión profundamente inelástica la situación es más complicada debido a la presencia de hadrones en el estado inicial.

B.3.2 Modelos de simulación de la hadronización

Una vez que la cascada de partones ha finalizado, el estado final está formado por una serie de partones que deberán ser transformados en hadrones si los sucesos generados van a ser utilizados para estimar las correcciones debidas a la hadronización o simplemente para estudiar la reacción del detector a los estados finales hadrónicos.

El proceso de hadronización es puramente no perturbativo y, en la actualidad únicamente puede hacerse un cálculo aproximado utilizando modelos fenomenológicos. Estos modelos permiten obtener una estimación de los efectos en las variables estudiadas introducidos por el proceso de hadronización. Por otra parte, su empleo es la única manera de obtener estados hadrónicos finales que puedan ser procesados en la simulación del detector.

Durante los análisis presentados en esta tesis, dos modelos diferentes para simular la hadronización han sido utilizados y se describen brevemente a continuación.

En el primero de ellos, conocido como el Modelo de Cuerda de Lund [92], los hadrones son generados a partir de una cuerda de color que une los diferentes partones siguiendo las cargas de color. Es decir, los gluones unirán dos cuerdas diferentes al tener dos colores (mejor dicho, un color y anticolor) mientras que los quarks y antiquarks solo pueden aparecer en los extremos de las cuerdas. Una vez construidas las cuerdas de color a partir del estado partónico, se produce un proceso de fraccionamiento de las mismas generándose de esta forma los diferentes hadrones que posteriormente son considerados como el estado hadrónico final.

Por otra parte, en el Modelo de Fragmentación de Conglomerados [94, 95] se realiza un pre-agrupamiento de partones para crear conglomerados sin carga neta de color, que posteriormente se desintegran en los hadrones correspondientes. Normalmente la generación de los conglomerados es realizada a partir de la unión de quarks y antiquarks lo que suele requerir una fase anterior al agrupamiento en la que los gluones son transformados en pares quark-antiquark a través de procesos de desintegración no perturbativos.

En los análisis realizados para esta tesis, se han utilizado tres programas para generar los sucesos simulados. El primero es LEPTO [96] combinado con ARIADNE [101] para generar la radiación de partones. En este programa se simula la cascada partónica usando el Modelo de Dipolos de Color, y los partones son hadronizados con el Modelo de Cuerda de Lund. El segundo programa también utiliza LEPTO para generar la interacción dura, aunque la cascada partónica es simulada con el Modelo de Cascadas Partónicas. La hadronización en este caso también se realiza con el Modelo de Cuerda de Lund. Estos dos programas son utilizados para corregir por los efectos del detector, para lo cual es necesario utilizar el programa adicional HERACLES [98, 99] que calcula las correciones debidas a radiación de fotones por parte del positrón, un tipo de proceso que ocurre simultáneamente que las interacciones positrón-protón, y que modifican ligeramente tanto la dinámica de la interacción como la respuesta del detector y deben ser tenidas en cuenta.

Para hacer predicciones con una alternativa al Modelo de Cuerda de Lund, el programa HERWIG [102] ha sido utilizado para estimar la correción hadrónica. Debido a que HERWIG

normalmente da una descripción peor de los datos y a que no es posible incluir las correciones debidas a la radiación de fotones, este programa no se utilizó para corregir los datos de los efectos introducidos por el detector. En HERWIG la radiación de partones se simula con el Modelo de Cascadas Partónicas, mientras que la posterior hadronización se realiza con el Modelo de Fragmentación de Conglomerados mencionado anteriormente.

B.3.3 Cálculo de predicciones NLO en QCD perturbativa

Los programas de generación de sucesos simulados descritos anteriormente son suficiente para estudiar los efectos del detector sobre los estados finales que queremos estudiar. Por otra parte, para una comparación más precisa con las predicciones teóricas, en concreto de QCD perturbativa, es posible realizar los cálculos teóricos exactos hasta un orden superior en α_s que el incluido en dichos programas.

Este cálculo tiene el inconveniente de que hasta la fecha no ha sido posible implementarlo dentro de programas que nos permitan obtener los estados finales a nivel hadrónico que necesitamos para entender los efectos introducidos por el detector y por lo tanto deben ser considerados separadamente.

Aunque el cálculo teórico puede hacerse analíticamente en algunos casos, en general resulta muy complejo cuando se tienen en cuenta los criterios de selección de los sucesos que son necesarios experimentalmente. Es por ello que las predicciones teóricas frecuentemente se obtienen con programas de integración por técnicas de Monte Carlo.

Uno de estos programas, DISENT [112], es el utilizado en los análisis de esta tesis. Para la realización de las integrales que permiten calcular las secciones eficaces hasta segundo orden en α_s, este programa genera configuraciones de partones que se corresponden con las distintas contribuciones de la serie pertubativa, teniendo cada una su correspondiente "peso" necesario para la realización del cálculo.

El algoritmo de jets se aplica entonces sobre los partones del estado final al igual que hicimos con los hadrones y partones de los programas de simulación de sucesos. Tras aplicar los cortes de selección, se cuentan los sucesos y se atribuye el correspondiente peso a cada jet. De esta forma podemos obtener las predicciones para las secciones eficaces de jets.

En el caso del análisis de subjets, se aplica el algoritmo usado para definir los subjets sobre los partones pertenecientes a cada jet. De esta forma es posible tener la predicción de la sección eficaz de jets con un número dado de subjets a una escala de resolución dada. Con esta cantidad, y con la predicción de la sección eficaz total de jets es posible obtener la predicción a segundo orden en α_s para la multiplicidad media de subjets.

Hay que mencionar que si bien DISENT permite calcular las predicciones teóricas a segundo orden en α_s, tiene el inconveniente que no nos da los valores a nivel hadrónico, y por lo tanto no es comparable directamente con los datos. Es necesario corregir las predicciones de DISENT por efectos de hadronización, lo que actualmente solo puede obtenerse con modelos fenomenológicos. La comparación de los valores para las correcciones dados por diferentes modelos permite calcular el valor de la corrección, además de estimar la incertidumbre en la misma. Esta incertidumbre ha sido incluida en el error de la medida como parte del error teórico.

De manera similar, actualmente DISENT únicamente describe los procesos de interacción positrón-protón a través de la interacción electromagnética. Es decir, este programa no in-

cluye la contribución debida a la interacción débil neutra, mediada por el bosón Z°. El efecto de esta contribución es despreciable para valores pequeños de Q^2, pero para valores grandes debe ser tenida en cuenta, aunque para ciertos observables (como la multiplicidad media de subjets) no sea apreciable.

B.4 Descripción de los análisis

A continuación se comentan los principales resultados de los análisis, incluyendo cómo se realiza la selección de los sucesos en los datos y en la simulación.

B.4.1 Selección de los sucesos

En ambos análisis se han utilizado la muestra de sucesos tomados con el detector ZEUS durante los años 1996 y 1997. La luminosidad total integrada correspondiente es de 38.6 ± 0.6 pb^{-1}.

Con respecto a los sucesos simulados, dos muestras diferentes han sido generadas y posteriormente procesadas por los códigos de simulación del detector. La primera de las muestras fue generada con LEPTO y la cascada partónica simulada con el Modelo de Dipolos de Color de ARIADNE. Esta muestra de sucesos es la que da una mejor descripción de los datos y por lo tanto es utilizada para las correcciones principales del análisis.

La segunda muestra fue generada con LEPTO usando el Modelo de Cascadas Partónicas del mismo (LEPTO-MEPS). Aunque la descripción no es tan buena como la obtenida usando ARIADNE, las predicciones, principalmente de los factores de corrección son muy similares y han sido utilizados para estimar la incertidumbre en las correcciones debidas al modelo usado para generar los sucesos.

Además de estas muestras de LEPTO, otras muestras adicionales fueron generadas para calcular las correcciones aplicadas a las predicciones de QCD perturbativa dadas por DISENT. Estas correcciones se pueden calcular sin necesidad de procesar las muestras en el código de simulación del detector, lo que permite generar muestras con un número muy grande de sucesos y lograr así una mayor precisión. Básicamente estas muestras fueron generadas con ARIADNE y LEPTO-MEPS como las usadas para corregir los datos. También, para estimar la incertidumbre en el proceso de hadronización se utilizó el programa HERWIG, donde se recurre al Modelo de Fragmentación de Conglomerados, a diferencia de LEPTO que utiliza el Modelo de Cuerda de Lund, tal como se describió en la sección B.3.2.

Cortes de selección de sucesos

Una vez que tenemos las muestras de sucesos a utilizar en el análisis, es necesario realizar una selección concreta de los sucesos de interés. Ésta se hace aplicando una serie de cortes de selección, los cuales son diferentes a nivel detector que a nivel generador.

Nivel detector significa que se aplican los cortes de selección utilizando la información proporcionada por el detector. Por lo tanto se refiere tanto a los datos reales como a los valores proporcionados por la simulación del detector para cada suceso. A este nivel se aplican dos tipos de cortes. El primero consiste en los cortes de selección de la región cinemática a estudiar: cortes en los jets, en Q^2, etcétera. Es decir los correspondientes a la medida a realizar. El segundo tipo corresponde a los cortes de limpieza, cuyo objetivo es seleccionar los sucesos con

suficiente calidad y desechar aquéllos que probablemente no sean realmente sucesos de interés, sino producidos por otro tipo de procesos distintos a los de colisiones de positrones y protones.

Nivel generador significa el nivel de los sucesos simulados anterior a su procesamiento en la simulación del detector. Este nivel contiene los mismos cortes de selección a los que se refiere la medida a realizar. No es necesario la aplicación de cortes de limpieza de la muestra debido a que no hay posibilidad de que el suceso sea de un tipo diferente al que estamos interesados y a que la reconstrucción del mismo se realiza de forma exacta, a diferencia de lo que ocurre en los datos reales.

Respecto a los cortes de limpieza aplicados en los análisis descritos en esta tesis, los principales se refieren a una selección muy precisa de sucesos en los que se detecta la presencia de un positrón. Dado que estamos interesados en sucesos en los que hay un positrón en el estado final y con un ángulo de dispersión suficiente para ser detectado en el calorímetro principal, la presencia de dicho positrón es necesaria para la selección de los sucesos.

Es por eso que se ha puesto un especial cuidado en la búsqueda de un depósito de energía cuyas características sean claramente las propias de un positrón: un depósito lo suficientemente pequeño y aislado. La búsqueda de estos depósitos se realiza con una red neuronal que proporciona una serie de candidatos a cada uno de los cuales asocia una probabilidad. Posteriormente, se selecciona el candidato más conveniente y se aplican una serie de cortes adicionales para mejorar la pureza de la muestra.

Además de la selección de un buen candidato a ser el positrón dispersado, se aplican otros cortes de limpieza orientados a eliminar la presencia de sucesos en los que casualmente se ha encontrado un depósito que aparenta ser un positrón. Normalmente estos cortes tienen mucho menos efecto que la propia selección del positrón, pero resultan muy importantes para eliminar sucesos que no son realmente del tipo en el que estamos interesados.

Selección de sucesos para el análisis de jets en el sistema de referencia de Breit

Una vez que se ha seleccionado una muestra de sucesos de procesos de dispersión profudamente inelástica mediados por interacciones neutras, se pasa a la segunda fase de selección de la región cinemática. Esta ya depende del análisis que se está realizando y, en concreto, para el análisis de jets en el sistema de referencia de Breit, se siguieron los siguientes pasos:

- Se reconstruyen las variables cinemáticas y se seleccionan los sucesos que están en la región donde se va a realizar la medida. Para este análisis se seleccionó la región con $Q^2 \geqslant 125$ GeV^2 y $-0.7 \leqslant \cos\gamma_h \leqslant 0.5$, siendo γ_h el ángulo polar correspondiente al quark extraído del protón en el Modelo Partónico de Quarks. La fórmula para calcular este ángulo está dada en la ecuación (2.9).

- Se aplica una tranformación de Lorentz para calcular los cuadrimomentos de las diferentes celdas del calorímetro en el sistema de referencia de Breit. Esto es necesario porque posteriormente se aplica el algoritmo de jets sobre dichos cuadrimomentos.

  Debe notarse que los cuadrimomentos de las celdas en el laboratorio se construyen utilizando para cada celda su centro geométrico para definir la dirección y la energía medida en la misma. Se considera que los cuadrimomentos no tienen masa.

- Una vez aplicado el algoritmo de jets en el sistema de referencia de Breit, se aplican los cortes de selección sobre los jets. Sólamente se consideran como tales los jets cuya energía

transversal en el sistema de referencia de Breit sea mayor que 8 GeV y estén en la región de pseudorapidez[3] en dicho sistema entre -2.0 y 1.8.

- Hay que mencionar que aparte de estos cortes de selección se realizan otros de limpieza para eliminar sucesos en los que uno de los jets no es realmente un chorro de hadrones, sino un fotón radiado por el positrón. Estos sucesos son muy problemáticos y deben ser rechazados.

Una vez seleccionados los jets que nos interesan, se realizan las medidas relacionadas con los mismos, como se describe en la siguiente sección. Debe notarse que la figura 4.1 muestra la distribución en el plano $x - Q^2$ de todos los sucesos (en total 8523) que han sido seleccionados. Debe notarse que el estudio no se hace realmente sobre los sucesos, sino sobre los 12167 jets que han sido seleccionados.

Selección de sucesos para el análisis de la multiplicidad de subjets

Para el análisis de la multiplicidad de subjets la selección de los sucesos se realiza de forma similar, aunque más simple debido a que no es necesario hacer la transformación al sistema de referencia de Breit. Los pasos seguidos son los siguientes:

- Tras reconstruir las variables cinemáticas, se seleccionan los sucesos con $Q^2 \geqslant 125$ GeV^2.
- El algoritmo de jets se aplica de forma directa a los cuadrimomentos reconstruídos en el detector, sin necesidad de hacer la transformación de Lorentz.
- De todos los jets proporcionados por el algoritmo, se seleccionan aquéllos que tengan una energía transversal mayor que 15 GeV y una pseudorapidez entre -1.0 y 2.0.

El análisis definitivo se realiza sobre los jets seleccionados, a los que se vuelve a aplicar el algoritmo de jets pero a una escala de resolución menor que 1 para definir los subjets. La cantidad de importancia es el número de subjets que contiene cada jet para cada una de las escalas de resolución consideradas en el análisis.

La distribución de todos los sucesos seleccionados en esta análisis en el plano $x - Q^2$ se muestra en la figura 4.2. En total se tienen 39650 jets de hadrones repartidos en 38779 sucesos.

Selección a nivel generador

A nivel generador se aplican los mismos cortes de selección que a nivel detector, aunque en este caso la selección se realiza sobre las cantidades generadas, es decir, sin efectos introducidos por el detector. Tras seleccionarse la región cinemática con los cortes sobre las variables correspondientes (Q^2 y $\cos\gamma_h$), se aplica el algoritmo de jets en el sistema de referencia de Breit (en el caso del primer análisis) o en el laboratorio (en el caso del segundo) sobre los cuadrimomentos de las partículas que correspondan.

Estas partículas son las asociadas al nivel hadrónico o al nivel partónico. El nivel hadrónico del que se dispone en los sucesos generados tras el proceso de hadronización. El nivel partónico es del que se dispone justo antes de que el proceso de hadronización tenga lugar, y que es el que se puede comparar con la teoría.

[3]La pseudorapidez es una variable que se define a partir del ángulo polar como ($\eta = -\ln(\tan(\theta/2))$ y que tiene la ventaja que se transforma de forma aditiva bajo transformaciones de Lorentz a lo largo del eje z.

Es necesario aplicar el algoritmo de jets sobre las partículas de los dos niveles por separado para obtener las predicciones relacionadas con las medidas en los dos niveles. Dichas predicciones son imprescindibles para poder corregir los datos de los efectos del detector (a partir de las predicciones de la simulación a nivel detector y hadrónico) y para poder corregir las predicciones teóricas a un nivel comparable a los datos (a partir de las predicciones de los generadores a nivel partónico y hadrónico).

Una vez obtenidas estas predicciones para los diferentes tipos de muestras de sucesos simulados se tiene toda la información que nos hace falta para realizar las medidas y la comparación con la teoría.

B.4.2 Descripción de las medidas experimentales

Después de seleccionar los sucesos se realizan las medidas en cada uno de los niveles para poder obtener los resultados tal y como se observan en el detector así como los valores de las diferentes correcciones que tenemos que aplicar a los datos o a la teoría antes de poderlos comparar.

Las medidas realizadas en cada uno de los análisis se describen brevemente a continuación:

Medidas para el análisis de producción de jets en el sistema de referencia de Breit.

En este análisis se han medido las secciones eficaces para $Q^2 \geqslant 125\ \mathrm{GeV}^2$ y $-0.7 \leqslant \cos\gamma_h \leqslant 0.5$ de la producción inclusiva de jets en el sistema de referencia de Breit con una energía transversal de más de 8 GeV y con una pseudorapidez entre -2 y 1.8.

Las secciones eficaces son estudiadas de forma diferencial para diferentes variables. Estas son Q^2, $E^B_{T,jet}$, η^B_{jet} y ϕ^B_{jet}. Para cada una de ellas se ha obtenido la dependencia de la sección eficaz. Además se ha estudiado la dependencia de la sección eficaz con $E^B_{T,jet}$ para diferentes regiones de Q^2.

Todas estas medidas permiten la realización de un estudio muy completo de la producción de jets a partir de procesos duros mediados por la interacción fuerte.

Medidas para el análisis de la multiplicidad de subjets

Para el segundo de los análisis se ha estudiado la dependencia de la multiplicidad media de subjets como función de la escala de resolución, de la energía transversal y de la psedorapidez del jet. Para realizar las medidas se han utilizado 10 valores diferentes de la escala de resolución que cubren el rango de $5 \cdot 10^{-4} - 1$, aunque para valores superiores a 0.25 no se resuelve ninguna estructura interna de los jets.

En el caso de la dependencia con las propiedades de los jets se ha elegido una escala de resolución para los subjets fija ($y_{cut} = 0.01$). El valor considerado se eligió de forma que no fuera demasiado pequeño para evitar correcciones muy grandes debidas a la hadronización y a los efectos del detector. Por otra parte tampoco se eligió demasiado grande para evitar realizar medidas poco sensibles a los efectos de QCD. Además, el aumento de la escala de resolución para los subjets conlleva problemas en la aplicación de correcciones y los errores sistemáticos son mayores.

B.4.3 Correcciones aplicadas a las medidas

Una vez realizadas las medidas a los diferentes niveles se calculan las correcciones que correspondan y se aplican a los datos o a las predicciones teóricas calculadas con DISENT.

En el análisis de producción de jets en el sistema de referencia de Breit se han aplicado las siguientes correcciones a las diferentes distribuciones:

- La corrección debida a los efectos experimentales se calcula como el cociente entre el valor a nivel hadrónico de una muestra simulada y el correspondiente valor a nivel detector. El factor de corrección obtenido se aplica a los datos para eliminar los efectos introducidos por la reconstrucción o los cortes de selección.

- Un factor adicional aplicado a los datos es la corrección de efectos introducidos por procesos de radiación electromagnética. La radiación de fotones por parte del positrón introduce efectos importantes en la medida de secciones eficaces. Para estimar el valor de esta corrección se utilizan muestras de sucesos para calcular las predicciones a nivel hadrónico por técnicas de Monte Carlo. Estas predicciones se calculan ora sin incluir estos efectos ora incluyéndolos y el cociente de estos valores nos dan la corrección que debemos aplicar a los datos.

  Al calcular esta corrección se corrigieron los efectos de la radiación de fotones así como los introducidos por la variación del valor de la constante de acoplamiento electromagnético (α_{em}) con la distancia (usualmente conocido como "running"), debido a que DISENT realiza las predicciones sin tener en cuenta esta dependencia.

  En total la corrección debido a todos estos efectos de órdenes superiores de QED perturbativa son del orden del 5%.

- La primera corrección aplicada a las predicciones teóricas obtenidas con DISENT es el efecto debido a la presencia del bosón débil Z°. En DISENT únicamente se contempla el intercambio del fotón, lo que es exacto para valores de Q^2 mucho menores que la masa al cuadrado del bosón Z° (que es aproximadamente 91 GeV). Dado que las medidas de las secciones eficaces realizadas aquí incluyen la región de Q^2 donde los efectos son apreciables, es necesario corregir las predicciones de DISENT.

  La corrección se calcula con un factor obtenido como el cociente de la sección eficaz cuando se incluye el bosón Z° y cuando no se incluye. El programa utilizado para obtener esta corrección fue LEPTO (usando ARIADNE para simular la cascada partónica). Los valores calculados (para positrones pues para electrones es diferente) se aplican a la predicción de DISENT antes de comparar con los datos. La corrección es despreciable para $Q^2 < 2000$ GeV^2, pero alcanza el 17% para las medidas realizadas en la región de $Q^2 > 5000$ GeV^2.

- La última corrección que se necesita aplicar a las predicciones de DISENT es la debida a los procesos de hadronización. Como se ha mencionado anteriormente (sección B.3.2), el efecto introducido por estos procesos sólo puede estimarse con los modelos fenomenológicos existentes. Para este análisis se han comparado las predicciones obtenidas con ARIADNE, LEPTO-MEPS y HERWIG, que están en muy buen acuerdo. La corrección se obtiene con el cociente de los valores obtenidos a nivel hadrónico y a nivel partónico.

Las medidas realizadas en el análisis de la multiplicidad media de subjets requieren un número menor de correcciones debido a que estamos utilizando un observable que, al ser un cociente, es insensible (a un nivel del 0.5%) a los efectos introducidos por varias de estas correciones. Por otra parte es más sensible a las correcciones hadrónicas. En este análisis las únicas correcciones que se aplican son las debidas al detector (aplicadas a los datos), a los órdenes superiores de

QED y las correcciones de hadronización (aplicadas a las predicciones de DISENT). Los efectos introducidos por las correciones de QED son muy pequeñas, pero aún así se aplicaron por razones de consistencia.

Las correciones hadrónicas fueron calculadas comparando LEPTO-MEPS y ARIADNE. En esta ocasión HERWIG no pudo ser utilizado porque la corrección obtenida no era consistente.

B.4.4 Comparación de las medidas con las predicciones teóricas

Tal como se describió en la sección B.3.3, las predicciones teóricas a segundo orden en QCD no pueden calcularse analíticamente y deben realizarse mediante técnicas de Monte Carlo. El programa DISENT, utilizado en los análisis, proporciona diversas configuraciones de partones en el estado final con su correspondiente peso y la selección de las configuraciones de interés permiten realizar los cálculos.

Por razones de consistencia, las predicciones teóricas se obtienen usando el mismo algoritmo de jets que se aplicó sobre los datos y se realiza la misma selección que la mencionada anteriormente sobre el nivel generador de los programas de generación de sucesos.

Debido a que los cálculos teóricos no se conocen con toda exactitud, es necesario realizar una estimación de las incertidumbres teóricas. La principal contribución viene dada por el hecho de que la serie perturbativa ha sido truncada en el segundo término.

Tras corregir los valores calculados con DISENT por los efectos de hadronización y del intercambio del bosón débil Z°, las predicciones pueden ser comparadas con las medidas experimentales, lo que se ha hecho para los dos análisis:

- La comparación para la medida de la secciones eficaces inclusivas de jets en el sistema de referencia de Breit se discute en la sección 5.2.3. La conclusión principal es que las predicciones teóricas a segundo orden en QCD describen bien los datos, siendo las dirferencias observadas del mismo orden que las incertidumbres teóricas.

- La comparación de las medidas de la multiplicidad de subjets con las predicciones se discute en la sección 5.3.3. La conclusión principal es que las predicciones teóricas dan una descripción muy buena de las medidas experimentales, incluso en la región en la que los efectos debidos a la hadronización son muy grandes. La dificultad principal de este análisis a la hora de comparar con la teoría es que la incertidumbre en la misma es mayor que en otros casos. Esto nos indica que es necesario el cálculo de órdenes superiores del desarrollo perturbativo para la realización de pruebas de mayor precisión de las predicciones teóricas.

  Por otra parte, como la comparación de este tipo de observable con las predicciones de los modelos fenomenológicos resulta interesante, la misma ha sido realizada en la sección 4.3.6. Mientras HERWIG da una descripción razonable de las multiplicidades observadas en los datos, tanto ARIADNE como LEPTO-MEPS predicen multiplicidades mayores que las observadas en los datos. Para energías transversales de los jets grandes, ARIADNE tiende a parecerse más a las medidas experimentales.

De esta forma, la conclusión general es que las predicciones de QCD a segundo orden describen de forma razonable la producción de jets en el sistema de referencia de Breit así como la estructura interna de los jets producidos en la dispersión profundamente inelástica.

B.4.5 La asimetría azimutal

Una mención especial merece la distribución mostrada en la figura 5.9. En ella se compara la distribución azimutal de los jets medida en los datos con las predicciones del Modelo Estándar. Dado que lo interesante es la comparación de la forma de la distribución, la sección eficaz se presenta normalizada. Además ello permite una comparación más directa debido a la cancelación de muchas incertidumbres que afectan principalmente al valor absoluto de la sección eficaz.

Puede notarse que los datos muestran una distribución claramente asimétrica, en buen acuerdo con la distribución predicha por el Modelo Estándar. De hecho, las predicciones de DISENT describen perfectamente la forma de la distribución (como se describe en la sección 5.2.3).

La observación de la asimetría azimutal ha sido realizada por primera vez usando jets en el análisis presentado aquí. El resultado obtenido proporciona una confirmación adicional de la validez de QCD en su descripción de los procesos de producción de jets en el sistema de referencia de Breit.

B.4.6 Determinación de α_s

Dado el buen acuerdo existente entre las medidas experimentales y las predicciones teóricas, se han utilizado las medidas realizadas para realizar medidas del valor de la constante de acoplamiento fuerte (α_s). El método utilizado en ambos análisis fue el siguiente:

- El primer paso fue calcular la dependencia de las predicciones teóricas con el valor de α_s. Esta dependencia se obtuvo teniendo en cuenta que las predicciones teóricas dependen del valor de α_s de dos formas diferentes: la primera, de forma directa debido a su presencia en los elementos de matriz; la segunda, de forma indirecta, porque las densidades partónicas se calculan suponiendo un valor dado de α_s.

- Una vez calculada esta dependencia, cada una de las medidas experimentales permite obtener un valor para α_s. Basta ver a qué valor de α_s corresponde el valor medido.

- En realidad para aumentar la precisión de las medidas, además de extraer los valores de α_s de las medidas experimentales, se realizaron una serie de medidas combinadas asociadas a varias medidas. Estas medidas combinadas se calculan por medio de un ajuste de tipo χ^2 para encontrar el valor de α_s que mejor se corresponde con las medidas experimentales.

Los valores de la constante de acoplamiento fuerte están referidos a la escala dada por la masa del bosón Z°. Se han obtenido los siguientes:

- En el caso de la medida de secciones eficaces de la producción de jets se determinó un valor de α_s para cada punto medido en las secciones eficaces diferenciales como función de Q^2 y $E^B_{T,jet}$. Para cada una de las secciones eficaces se obtienen seis valores, que son los mostrados en las figuras 5.16 y 5.17.

  Además se obtuvo un valor global ajustando en cada distribución los seis puntos tal y como se mencionó anteriormente. Debido a que para valores de Q^2 grandes y/o $E^B_{T,jet}$ grandes las incertidumbres teóricas son menores, se obtuvieron valores combinados a partir de los cuatro últimos puntos de cada distribución. Estos cuatro valores combinados son también mostrados en las figuras.

Debe notarse que el valor de $\alpha_s(M_Z)$ obtenido a partir de la sección eficaz $\mathrm{d}\sigma/\mathrm{d}Q^2$ para $Q^2 > 500$ GeV^2 tiene una precisión muy buena:

$$\alpha_s(M_Z) = 0.1212 \pm 0.0013\ (\text{estad.})^{+0.0023}_{-0.0031}\ (\text{sist.})^{+0.0027}_{-0.0027}\ (\text{teor.}).$$

Siendo una de las medidas individuales de α_s más precisas realizadas hasta la fecha. Esto es debido principalmente a que el error teórico es pequeño.

- En el caso de la medida de α_s a partir de la multiplicidad media de subjets, aunque sería posible determinar un valor a partir de cada punto experimental, se ha considerado que se deben evitar las regiones donde la corrección debida a los procesos de hadronización sea grande. Por eso se utilizaron únicamente las medidas con $E_{T,jet} > 25$ GeV a una escala de resolución de $y_{cut} = 10^{-2}$. Los cinco valores obtenidos se muestran en la figura 5.19 donde también se muestra el valor combinado obtenido como describimos antes. Este valor combinado es:

  $$\alpha_s(M_Z) = 0.1194 \pm 0.0017\ (\text{estad.})^{+0.0032}_{-0.0009}\ (\text{sist.})^{+0.0094}_{-0.0077}\ (\text{teor.})\ ,$$

  y, tal como se muestra en la figura, está en buen acuerdo con las cinco medidas individuales. Debe notarse que en esta determinación el error teórico es mucho mayor que el estadístico o al sistemático. Aún así la medida tiene una precisión comparable a la mayoría de las medidas individuales de este acoplo.

Todos los valores de la constante de acoplamiento fuerte medidos en esta tesis están en buen acuerdo, dentro de los errores, con las otras medidas existentes de la constante de acoplamiento fuerte y también con el valor considerado actualmente como el promedio global [119].

B.5 Conclusiones

En esta tesis se presentan y comentan dos análisis cuyo objetivo es el estudio de las interacciones fuertes y la medida de la constante de acoplamiento fuerte. En el primero de ellos se estudia la producción de jets en el sistema de referencia de Breit, mientras que en el segundo se analiza la estructura interna de los jets a través de los llamados subjets. Los dos análisis han sido realizados con el uso de 38.6 pb^{-1} de colisiones ep producidos en HERA y estudiados con el detector ZEUS.

En el primero de los análisis se ha medido la sección eficaz de producción inclusiva de jets en el sistema de referencia de Breit en colisiones positrón-protón en el régimen de dispersión profundamente inelástica mediado por interacciones neutras. Concretamente, se ha estudiado la dependencia de esta sección eficaz con respecto a diferentes variables de los jets con objeto de realizar una comparación detallada con la teoría. Las medidas han sido comparadas con predicciones teóricas a segundo orden en QCD perturbativa. Estas predicciones describen de forma razonable las medidas experimentales teniendo las diferencias observadas, del orden del 10%, de un tamaño similar al de las incertidumbres teóricas.

Además, en el análisis se ha medido la distribución azimutal de los jets en el sistema de referencia de Breit. La misma no es uniforme y presenta máximos en la dirección paralela a la del positrón dispersado en dicho sistema de referencia. Las predicciones teóricas demuesran que la asimetría observada es compatible con la predicha por el Modelo Estándar. Esta es la primera vez que esta asimetría ha sido observada utilizando jets de hadrones.

El segundo análisis se realizó con la medida de la multiplicidad media de subjets para una muestra de jets producidos en el sistema de referencia del laboratorio en el mismo tipo de proceso. El estudio se ha centrado en la dependencia de este observable con la escala de reolución de los subjets y con respecto a las variables del jet. Las medidas realizadas han sido comparadas con predicciones a segundo orden en QCD perturbativa, los cuales describen muy bien los resultados, especialmente en la regiones donde las correcciones debidas a la hadronización son lo suficientemente pequeñas. Ésta es la situación cuando la escala de resolución y la energía transversal de los jets son suficientemente grandes.

Usando la comparación con las predicciones a segundo orden en QCD perturbativa y con el desarrollo de un análisis en QCD, se ha realizado la medida de la constante de acoplamiento fuerte α_s en ambos análisis.

En el primero de los dos análisis se han obtenido diversas extracciones, entre las cuales, la medida realizada a partir de $\mathrm{d}\sigma/\mathrm{d}Q^2$ en la región $Q^2 > 500$ GeV^2 tiene una precisón que es de las mejores obtenidas hasta la fecha. Este valor es

$$\alpha_s(M_Z) = 0.1212 \pm 0.0013\ (\text{estad.})^{+0.0023}_{-0.0031}\ (\text{sist.})^{+0.0027}_{-0.0027}\ (\text{teo.})\ ,$$

debiéndose indicar que el error teórico pequeño es el que permite tener una medida tan precisa.

En el caso del análisis de la multiplicidad de subjets, el valor final obtenido para α_s tiene un error teórico más grande, pero aún así el valor resulta competitivo en comparación con otras medidas de este acoplo. Por otra parte, hay que destacar que el valor ha sido obtenido en un nuevo tipo de análisis experimental. En este caso el valor obtenido es:

$$\alpha_s(M_Z) = 0.1194 \pm 0.0017\ (\text{estad.})^{+0.0032}_{-0.0009}\ (\text{sist.})^{+0.0094}_{-0.0077}\ (\text{teo.})\ .$$

Las medidas de $\alpha_s(M_Z)$ realizadas son completamente compatibles con el valor promedio de todas las medidas existentes y la precisión obtenida es comparable a las mejores medidas de esta constante realizadas en todo el mundo.

Bibliography

[1] J. Balmes, *El criterio* (1845).

[2] O. González, *Determination of α_s using subjet multiplicities*, to be published in the Proceedings of the 9^{th} International Workshop on Deep Inelastic Scattering (ed. G. Bruni, G. Iacobucci and R. Nania), Bologna, Italy, 27^{th} April - 1^{st} May, 2001.

[3] ZEUS Collab., *Measurements of jet substructure in NC DIS and determination of α_s at HERA*. Contributed paper to the International Europhysics Conference on High Energy Physics, Budapest, Hungary (2001). Abstract 641.

[4] ZEUS Collab., *Inclusive jet cross sections in neutral current DIS in the Breit frame and determination of α_s at HERA*. Contributed paper to the International Europhysics Conference on High Energy Physics, Budapest, Hungary (2001). Abstract 637.

[5] ZEUS Collab., *Inclusive jet cross sections in neutral current DIS in the Breit frame*. Contributed paper to the International Conference on High Energy Physics, Osaka, Japan (2002). Abstract 890.

[6] F. Halzen and A.D. Martin, *Quarks and Leptons: An Introductory Course in Modern Particle Physics*. John Wiley & Sons, Inc. (1984).

[7] B.H. Bransden and C.J. Joachain, *Physics of atoms and molecules*. Addison Wesly Longman Limited (1983).

[8] Y. Ne'eman, Nucl. Phys. **26** (1961) 222;
M. Gell-Mann, Phys. Rev. **125** (1962) 1067.

[9] M. Gell-Mann, Phys. Lett. **8** (1964) 214;
G. Zweig, CERN-8192/TH 401 (1964); CERN-8419/TH 412 (1964).

[10] O.W. Greenberg, Phys. Rev. Lett. **13** (1964) 598;
M.Y. Han and Y. Nambu, Phys. Rev. **139** (1965) B1006.

[11] N. Cabibbo, Phys. Rev. Lett. **10** (1961) 531;
M. Kobayashi and T. Maskawa, Prog. Theor. Phys. **49** (1973) 652.

[12] S. Glashow, Nucl. Phys. B**22** (1961) 579.

[13] S. Weinberg, Phys. Rev. Lett. **19** (1967) 1264;
A. Salam, in *Elementary Particle Theory*, ed. N. Svartholm, Almquist and Forl, Stockholm (1968).

[14] R.K. Ellis, W.J. Stirling and N.R. Webber, *QCD and Collider Physics*. Cambridge University Press (1996).

[15] P.W. Higgs, Phys. Lett. **12** (1964) 132; Phys. Rev. Lett. **13** (1964) 508; Phys. Rev. **145** (1966) 1156;
R. Brout and F. Englert, Phys. Rev. Lett. **13** (1964) 321.

[16] J. Goldstone, Nuovo Cim. **19** (1961) 154.

[17] J.D. Bjorken, Phys. Rev. **179** (1969) 1547.

[18] R.P. Feynman, *Photon Hadron Interactions*, W.A. Benjamin, New York (1972).

[19] SLAC-MIT collaboration, E.D. Bloom et al., Phys. Rev. Lett. **23** (1969) 930;
SLAC-MIT collaboration, E.D. Bloom et al., Phys. Rev. Lett. **23** (1969) 935;
SLAC-MIT collaboration, G. Miller et al., Phys. Rev. D**5** (1972) 528.

[20] R.P. Feynman, Phys. Rev. Lett. **23** (1969) 1415.

[21] C.G. Callan and D. Gross, Phys. Rev. Lett. **22** (1969) 156.

[22] Gargamelle Neutrino Collab., H. Deden et al., Nucl. Phys. B**85** (1975) 269.

[23] TASSO Collab., R. Bradelick et al., Phys. Lett. B**86** (1979) 243.

[24] A. Quadt, *Measurement and QCD Analysis of the Proton Structure Function F_2 from the 1994 HERA Data using the ZEUS Detector.* Doctoral Thesis. Christ Church, University of Oxford (1996).

[25] ZEUS Collab., M. Derrick et al., Phys. Lett. B**316** (1993) 412;
H1 Collab., I. Abt et al., Nucl. Phys. B**407** (1993) 515.

[26] ZEUS Collab., S. Chekanov et al., Eur. Phys. J. C**21** (2001) 443.

[27] K.H. Streng, T.F. Walsh and P.M. Zerwas, Z. Phys. C**2** (1979) 237.

[28] G. Parisi, *Proc.* 11$^{\text{th}}$ *Rencontre de Moriond*, J. Tran Tranhm (ed.), ed. Fronties (1976) 83;
G. Altarelli and G. Parisi, Nucl. Phys. B**126** (1977) 298;
G. Altarelli, Nucl. Phys. B**81** (1981) 1.

[29] V.N. Gribov and L.N. Lipatov, Sov. J. Nucl. Phys. **15** (1972) 438;
L.N. Lipatov, Sov. J. Nucl. Phys. **20** (1975) 96;
Y.L. Dokshitzer, Sov. Phys. JETP **46** (1977) 641.

[30] Y. Balitzki and L.N. Lipatov, Phys. Rev. Lett. **28** (1978) 822;
E.A. Kuraev, L.N. Lipatov and V.S. Fadin, Phys. Rev. Lett. **44** (1976) 443; Phys. Rev. Lett. **45** (1977) 199.

[31] M. Ciafaloni, Nucl. Phys. B**296** (1988) 49;
S. Catani, F. Fiorani and G. Marchesini, Phys. Lett. B**234** (1990) 339; Nucl. Phys. B**336** (1990) 18.

[32] J. Kwiecinski, A.D. Martin and P.J. Sutton, Phys. Rev. D**52** (1995) 1445.

[33] M.G. Ryskin and E.M. Levin, Phys. Rep. **189** (1990) 267;
A.H. Mueller, Nucl. Phys. B**335** (1990) 115.

[34] L.V. Gribov, E.M. Levin and M.G. Ryskin, Phys. Rep. **100** (1983) 1; Nucl. Phys. B**188** (1981) 155;
A.H. Mueller and J. Qiu, Nucl. Phys. B**260** (1986) 427.

[35] A.D. Martin et al., Eur. Phys. J. C**4** (1998) 463.

[36] A.D. Martin et al., Eur. Phys. J. C**14** (2000) 133.

[37] H.L. Lai et al., Phys. Rev. D**55** (1997) 1280.

[38] H.L. Lai et al., Eur. Phys. J. C12 (2000) 375.

[39] M. Glück, E. Reya and A. Vogt, Z. Phys. C**49** (1991) 501;
M. Glück and E. Reya, Dortmund DO-TH 93/27 (1993);
M. Glück, E. Reya and A. Vogt, Phys. Lett. B**306** (1993) 391;
M. Glück, E. Reya and A. Vogt, Z. Phys. C**67** (1995) 433; Eur. Phys. J.**5** (1998) 461.

[40] M. Milite, *The Internal Structure of Charmed Jets in Photoproduction at HERA*. Doctoral Thesis, University of Hamburg. DESY-THESIS-2001-050 (2001).

[41] G. Sterman and S. Weinberg, Phys. Rev. Lett. **39** (1977) 1436.

[42] JADE Collab., W. Bartel et al., Z. Phys. C**33** (1986) 23;
JADE Collab., S. Bethke et al., Phys. Lett. B**213** (1988) 235.

[43] S. Catani, Yu.L. Dokshitzer and B.R. Webber, Phys. Lett. B**285** (1992) 291;
S. Catani et al., Nucl. Phys. B**406** (1993) 187.

[44] UA1 Collab., G. Arnison et al., Phys. Lett. B**123** (1983) 115.

[45] S.D. Ellis and D.E. Soper, Phys. Rev. D**48** (1993) 3166.

[46] J. Huth et al. *Proc. of the 1990 DPF Summer Study on High Energy Physics*, Snowmass, Colorado. E.L. Berger (ed.), World Scientific, Singapore (1992) p. 134.

[47] B.R. Webber, J. Phys. G**19** (1993) 1567.

[48] H. Georgi and H.D. Politzer, Phys. Rev. Lett. **70** (1978) 3;
V. Hedberg et al., *Asymmetries in Jet Azimuthal Angle Distributions as a Test of QCD*, Proceedings of the Workshop "Physics at HERA" (ed. W. Buchmüller and G. Ingelman), Vol. I, (1991) pg. 331.

[49] E. Mirkes and S. Willfahrt, Phys. Lett. B**414** (1997) 205.

[50] ZEUS Collab., J. Breitweg et al., Phys. Lett. B**481** (2000) 199.

[51] S. Catani et al., Nucl. Phys. B**377** (1992) 445; Nucl. Phys. B**383** (1992) 419;
M.H. Seymour, Nucl. Phys. B**421** (1994) 545; Phys. Lett. B**378** (1996) 279.

[52] S.D. Ellis, Z. Kunszt and D.E. Soper, Phys. Rev. Lett. **69** (1992) 3615.

[53] OPAL Collab., G. Abbiendi et al., Eur. Phys. J. C**17** (2000) 373;
ALEPH Collab., D. Buskulic et al., Z. Phys. C**76** (1997) 1991.

[54] *HERA: A Proposal for a Large Electron Proton Colliding Beam Facility at DESY*, DESY-HERA 81-10 (1981).

[55] ZEUS Collaboration, "The ZEUS Detector", Status Report 1993, U. Holm (ed.), DESY (1993) (unpublished).
Available on http://www-zeus.desy.de/bluebook/bluebook.html.

[56] C.B. Brooks et al. (ZEUS-UK Collab.), *Development of the ZEUS central tracking detector*. Nucl. Instr. and Meth. A**283** (1989) 477;
B. Foster et al., *The design and construction of the ZEUS central tracking detector*. Nucl. Instr. and Meth. A**338** (1994) 254.

[57] O. Deppe, *Measurement of $D^{*\pm}$ Electroproduction at HERA*. Doctoral Thesis. DESY-THESIS-2000-006 (2000).

[58] J.A. Blissett et al., *Development of a tapered cell drift chamber II: Operation of high magnetic fields and different gas pressures*. Nucl. Instr. and Meth. A**245** (1986) 291.

[59] R. Hall-Wilton et al., *The CTD tracking resolution*. ZEUS-Note 99-024 (1999)

[60] I. Redondo, *Charm electroproduction at HERA*. Doctoral Thesis, U. Autónoma de Madrid. DESY-THESIS-2001-037 (2001).

[61] W.R. Leo, *Techniques for Nuclear and Particle Physics Experiments*. Springer-Verlag, New York (1997).

[62] D.H. Perkins, *Introduction to High Energy Physics*. Addison-Wesley (1982).

[63] E. Lohrmann, *Hochenergiephysik*. Teubner (1990).

[64] U. Amaldi, *Fluctuations in Calorimetry Measurements*. Physica Scripta **23** (1981) 409.

[65] Y. Iga and S. Schlendstedt, *Status and Improvement of the ZEUS Calorimeter Simulation*. ZEUS-Note 97-019 (1997).
C. Catterall and Y. Iga, *Improved Simulation of Hadronic Cascades in the Uranium Calorimeter*. ZEUS-Note 98-077 (1998).

[66] T. Woeniger, *Influence of Calorimeter Calibration Errors on the Measurement of Deep Inelastic Scattering*. Doctoral Thesis, University of Hamburg (1991).
I. Bohnet, *Investigations on Uniformity, Radiation Resistance and Calibration of ZEUS Calorimeter Components at HERA*. Doctoral Thesis. DESY-THESIS-1999-041 (1999).

[67] C.W. Fabjan, *Calorimetry in High-Energy Physics*, CERN-EP-85-54 (1985).

[68] A. Fürtjes, *Kalibration des ZEUS Vorwärts- und Rückwärtskalorimeters*. Doctoral Thesis, University of Hamburg. DESY-THESIS-93-03 (1992).

[69] C.W. Fabjan et al., Nucl Instr. Meth. **141** (1977) 61.
H. Brückman, U. Behrens and B. Anders, *Hadron Sampling Calorimetry - A Puzzle of Physics*. DESY 86-155 (1986).

[70] E. Bernardi et al. (ZEUS Collab.), Nucl. Instr. and Meth. A**262** (1987) 229;
G. García López, *Two Different Cases of Calorimetry in High Energy Physics: the ATLAS Liquid Argon Electromagnetic End Cap and the ZEUS Forward Plug Calorimeter*. Doctoral Thesis, U. Autónoma de Madrid. DESY-THESIS-2000-10 (2000).

[71] J.A. Straver, *Design, Construction and Beam Test of the High Resolution Uranium Scintillator Calorimeter for ZEUS*. Doctoral Thesis, University of Amsterdam (1991). RX-1336 (Amsterdam, 1991).

[72] J. Krüger, *The Uranium Scintillator Calorimeter for the ZEUS Detector at the Electron-Proton Collider HERA*. DESY-Report, DESY F35-92-02 (1992).

[73] M. Derrick et al., Nucl. Instr. and Meth. A309 (1991) 77;
A. Andresen et al., Nucl. Instr. and Meth. A309 (1991) 101;
A. Caldwell et al., Nucl. Instr. and Meth. A321 (1992) 356;
A. Bernstein et al., Nucl. Instr. and Meth. A336 (1993) 23.

[74] L. Hervás, *The Pipelined Readout for the ZEUS Calorimeter*. Doctoral Thesis, U. Autónoma de Madrid (1991). DESY F35D-91-01.

[75] H. Bethe and W. Heitler, Proc. Roy. Soc. A**146** (1934) 83.

[76] M. van der Horst, *Theoretical Calculations for Electron-Proton Scattering*. Doctoral Thesis, University of Amsterdam (1990). RX-1278 (Amsterdam, 1990)

[77] ZEUS Luminosity Monitor Group, J. Andruszkow et al., DESY-92-066 (1992);
ZEUS Luminosity Monitor Group, J. Andruszkow et al., DESY-01-041 (2001).

[78] A. Bamberger et al., *The Small Angle Rear Track Detector for ZEUS*. ZEUS-Note 95-095 (1995).

[79] W.H. Smith et al., Nucl. Instr. and Meth. A**335** (1995) 278.

[80] L.A.T. Bauerdick et al. *The Physics Analysis Enviroment of the ZEUS Experiment*. DESY 95-236 (1995).

[81] R. Brun et al., CERN DD/EE/81-1 (1987).

[82] F. Jacquet and A. Blondel, *Proceedings of the study for an ep facility for Europe*. DESY 79-48 (1979) p. 391.

[83] S. Bentvelsen, J. Engelen and P. Kooijman, *Proceedings of the 1991 Workshop on Physic at HERA*, Vol. 1, p.23. W. Buchmüller and G. Ingelman (ed.) (DESY, Hamburg, 1992).

[84] U. Bassler, G. Bernardi, Nucl. Instr. and Meth. A**361** (1995) 197.

[85] J.C. Collins, D.E. Soper and G. Sterman, Nucl. Phys. B**308** (1988) 833.

[86] M. Bengtsson and T. Sjöstrand, Phys. Lett. B**185** (1987) 435; Nucl. Phys. B**289** (1987) 810.

[87] Y. Azimov et al., Phys. Lett. B**165** (1985) 147;
G. Gustafson, Phys. Lett. B**175** (1986) 453;
G. Gustafson and U. Petersson, Nucl. Phys. B**306** (1988) 746;
B. Andersson et al., Z. Phys. C**43** (1989) 625.

[88] A. Petersen et al., Phys. Rev. D**37** (1988) 1;
OPAL Collab., M.Z. Akrawy et al., Phys. Lett. B**246** (1990) 285.

[89] V.V. Sudakov, Zh.E.F.T. **30** (1956) 87; Sov. Phys. JETP **30** (1956) 65.

[90] A.H. Mueller, Phys. Lett. B**104** (1981) 161;
B.I. Ermolaev and V.S. Fadin, JETP Lett.**33** (1981) 269;
A. Bassetto, M. Ciafaloni and G. Marchesini, Phys. Rep. **100** (1983) 201.

[91] R.D. Field and R.P. Feynman, Phys. Rev. D**15** (1977) 2590; Nucl. Phys. B**136** (1978) 1.

[92] B. Andersson, G. Gustafson and B. Söderberg, Z. Phys. C**20** (1983) 317; Nucl. Phys. B**264** (1986) 29;
B. Andersson et al., Phys. Rep. **97** (1983) 33.

[93] B. Andersson et al., Phys. Rep. **97** (1983) 31.

[94] D. Amati and G. Veneziano, Phys. Lett. B**83** (1979) 87;
A. Bassetto, M. Ciafaloni and G. Marchesini, Phys. Lett. B**83** (1979) 207;
G. Marchesini, L. Trentadue and G. Veneziano, Nucl. Phys. B**181** (1980) 335.

[95] R.D. Field and S. Wolfram, Nucl. Phys. B**213** (1983) 65.

[96] G. Ingelman, A. Edin and J. Rathsman, Comp. Phys. Comm. **101** (1997) 108; version used: 6.5.

[97] H. Plothow-Besch, Comput. Phys. Commun. **75** (1993) 396; versions used: 7.08 and 7.09.

[98] K. Kwiatkowski, H. Spiesberger and H.-J. Möhring, Comp. Phys. Comm. **69** (1992) 155;
H. Spiesberger, *HERACLES - An Event Generator for ep Interactions at HERA Including Radiative Processes (Version 4.6)*, 1996, available on `http://www.desy.de/~hspiesb/heracles.html`

[99] K. Charchula, G.A. Schuler and H. Spiesberger, Comp. Phys. Comm. **81** (1994) 381;
H. Spiesberger, *DJANGO6 version 2.4 - A Monte Carlo Generator for Deep Inelastic Lepton Proton Scattering Including QED and QCD Radiative effects*, 1996, available on `http://www.desy.de/~hspiesb/django6.html`

[100] T. Sjöstrand, Comp. Phys. Comm. **39** (1986) 347;
T. Sjöstrand and M. Bengtsson, Comp. Phys. Comm. **43** (1987) 367; version used: 7.4.

[101] L. Lönnblad, Comp. Phys. Comm. **71** (1992) 15; Z. Phys. C**43** (1995) 285; version used: 4.08.

[102] G. Marchesini et al., Comp. Phys. Comm. **67** (1992) 465; hep-ph/9607939;
G. Corcella et al., JHEP **0101** (2001) 010; hep-ph/0107071; versions used: 5.9 and 6.3

[103] H. Abramowicz, A. Caldwell and R. Sinkus, *Neural network Based Electron Identification in the ZEUS Calorimeter*, DESY 95-054;
R. Sinkus, Nucl. Instr. and Meth. A**361** (1995) 290.

[104] O. González, H. Raach and J. Terrón, *Measurements of the inclusive jet cross sections in NC DIS in the Breit frame and determination of* α_s, ZEUS-Note 02-007 (2002).

[105] O. González and J. Terrón, *Measurement of the subjet multiplicity in neutral current deep inelastic scattering and determination of* α_s, ZEUS-Note 02-008 (2002).

[106] J. Edmonds, J. Grosse-Knetter and A. Quadt, *Neutral Current Cross Sections at High* Q^2, ZEUS-Note 99-016 (1999).

[107] O. González and J. Terrón, *Analyses in the Breit frame and the related problems*, ZEUS-Note 02-006 (2002).

[108] ZEUS Collab., J. Breitweg et al., Eur. Phys. J. C**11** (1999) 427.

[109] O. González, *Measurement of the subjet multiplicity in neutral current DIS and determination of* α_s *at HERA*. Memoria del trabajo de iniciación a la investigación. U. Autónoma de Madrid (2001).

[110] ZEUS Collab., *Measurements of Jet Substructure in Photoproduction at HERA*, Contributed paper to ICHEP'99 (Tampere, July 1999) N-530.

[111] ALEPH Collab., D. Buskulic et al., Phys. Lett. B**346** (1995) 389;
D0 Collab., B. Abbott et al., Nucl. Phys. Proc. Suppl. **79** (1999) 494.

[112] S. Catani and M.H. Seymour, Nucl. Phys. B**485** (1997) 291, *and Erratum* B510 (1997) 503.

[113] D. Graudenz in *Proceedings of the Ringberg Workshop on New Trends in HERA physics*, Ringberg Castle, Germany, 25-30 May 1997. PSI-PR-97-20.
hep-ph/9708362.
D. Graudenz, hep-ph/9710244.

[114] S. Catani and M.H. Seymour, Phys. Lett. B**378** (1996) 287.

[115] R.K. Ellis, D.A. Ross and A.E. Terrano, Nucl. Phys. B**178** (1981) 421.

[116] M. Botje, Eur. Phys. J. C**14** (2000) 285;
M. Botje, ZEUS-Note 99-048 (for use of EPDFLIB, version 2.0).

[117] ZEUS Collaboration, J. Breitweg et al., Phys. Lett. B507 (2001) 70.

[118] S. Bethke, J. Phys. G26 (2000) R27.

[119] D.E. Groom et al., Eur. Phys. J. C**15** (2000) 1.

Acknowledgments

The analysis presented here would not have been performed without the work of the HERA machine group and the people who constructed the ZEUS detector and make possible the data taking.

I would like to mention that the analyses were developed with the essential help of different people of the ZEUS collaboration, especially those belonging to the Hadronic Final States (QCD) Working Group. I thank them all for their comments and useful discussions, and even for their own work, from which my analysis has benefited a lot, mainly in the use of programs and methods which were used and developed before I have need of them.

Finally, I would like to thank the HEP group of the Universidad Autónoma de Madrid to give me the opportunity of joining in the efforts of the ZEUS experiment and analysing the data taken in a high-energy collider. Especially, I wish to emphasize the enormous support and guiding I receive from Juan Terrón, my thesis supervisor. Without his guidance and teaching, this work probably would never have reached the end or even started at all. I would like to mention also Ignacio Redondo for his comments and suggestions and his help to solve a lot of important tasks in DESY and Hamburg.

It was a very fruitful experience to work for the CAL DQM group. I want to thanks all the people who belongs to the same group for their help and support. Especially I want to mention Roberto Sacchi, Tatsu Tsurugai, Pat Saull and Maurício Barbi which taught me everything I know about the ZEUS UCAL and the readout.

Especial thanks to the different people at DESY and Hamburg with whom I share many activities outside physics. It has been a pleasure to come to Hamburg not only for doing physics, but also enjoying these years of my phD and especially to meet people from different countries which have been a very pleasant and friendly company.

Finalmente, querría agradecer todo el apoyo y ayuda que he recibido de mi familia y amigos en España. Gracias sobre todo por su compañía, a pesar de la distancia, por medio de las nuevas y viejas tecnologías. Sin su presencia las estancias en Hamburgo, y sobre todo los viajes entre Alemania y España, habrían sido algo menos agradables de lo que fueron.